Escola Universitària d'Enginyeria
Tècnica Industrial de Barcelona
Consorci Escola Industrial de Barcelona
UNIVERSITAT POLITÈCNICA DE CATALUNYA

Volume I
Project report

TREBALL DE FI DE GRAU

IMPLEMENTATION AND CHARACTERIZATION OF AN EJECTOR BASED HYDROGEN RECIRCULATION SYSTEM FOR A PEM FUEL CELL

TFG presentat per obtenir el títol de GRAU en ENGINYERIA MECÀNICA

Per **Xavier Corbella Coll**

Barcelona, 9 de Juny de 2015

Director: Ricardo Torres Cámara
Departament de MF
Universitat Politècnica de Catalunya (UPC)

Codirector: Miguel Allué Fantova
Departament Automatic Control
Institut de Robòtica i Informàtica Industrial (IRI/CSIC)

GENERAL CONTENTS

VOLUME I

Project report

Contents I
Abstract V
Resum V
Resumen VI
Acknowledgements VII
List of figures IX
List of tables XV
Nomenclature XVII
Chapter 1: Introduction and objective 1
1.1. Introduction 1
1.2. Objective 3
Chapter 2: Introduction to PEM fuel cells 5
2.1. Fuel cells 5
2.2. PEM fuel cells 7
2.2.1. Basic chemistry and thermodynamics 7
2.2.2. Theoretical potential 8
2.2.3. Efficiency 9
2.2.4. Voltage losses 9
2.3. Hydrogen supply 11
Chapter 3: Test Station 4 13
3.1. Characteristics of Test Station 4 13
3.2. Control and data acquisition system 16
3.3. Experimental Test 17
Chapter 4: Compressible Flow and Ejectors 23
4.1. Compressible flow 24
4.1.1. Ideal gas law and perfect gases 24

4.1.2. Isentropic relations for perfect gases 25
4.1.3. Speed of Sound 25
4.1.4. Stagnation properties 25
4.1.5. Sonic properties 27
4.1.6. Velocity changes due to area changes 27
4.1.7. Choking phenomena 29
4.1.8. Normal shock waves 30
4.1.9. Oblique shock waves 31
4.1.10. Expansion waves 34
4.1.11. Nozzles 35
4.2. Ejectors 37
4.2.1. Geometrical parameters of an ejector 39
4.2.2. Flow behavior within the ejector 41
Chapter 5: Ejector Modelling 43
5.1. 1D Mathematical Models 43
5.2. Introduction to the CFD model 45
5.2.1. Reynolds-averaged and Favre-averaged Navier-Stokes equations 45
5.2.2. The standard k-ε turbulence model 49
5.2.3. Wall functions 50
5.3. COMSOL model 51
5.3.1. Governing equations 52
5.3.2. Geometry 53
5.3.3. Boundary conditions and initial values 54
5.3.4. Solver 55
5.3.5. Mesh 56
5.3.6. Cluster computation 58
5.3.7. Example 58
5.3.8. Modeling an experimental nozzle 62
Chapter 6: Experimental validation of the CFD model 67
6.1. Layout of the experimental set-up 67
6.2. Geometry of the experimental ejector 73
6.2.1. Initial solution 73
6.2.2. Chosen geometry 76
6.3. Data acquisition and control 81

6.3.1. FPGA program 81
6.3.2. RTOS program 81
6.3.3. Host program 82
6.3.4. Mass flow meter/controller 82
6.4. Results 82
6.4.1. Primary mass flow 83
6.4.2. Normal mode 83
6.4.3. Recirculation mode 86
Chapter 7: Geometry of the ejector for TS4 89
7.1. Parametrical studies to find the optimal geometrical parameters 89
7.1.1. Diameter of the throat 89
7.1.2. Diameter of the mixing chamber 91
7.1.3. Length of the mixing chamber 92
7.1.4. Nozzle position 92
7.1.5. Pressure drop 93
7.2. Final Geometry 94
Chapter 8: Conclusions 97
8.1. Conclusions 97
8.2. Future work 98
Bibliography 99

VOLUME II

Appendices

APPENDIX A: Implementation of the model in COMSOL 3
A.1. Preprocessing 3
A.1.1. Space Dimension, physics and study type. 3
A.1.2. Parameters 3
A.1.3. Geometry 5
A.1.4. Isotropic diffusion. 8
A.1.5. Material. 8
A.1.6. Initial Values 8
A.1.7. Boundary Conditions 10
A.1.8. Mesh. 11
A.2. Processing. 11

A.2.1. Study 1 11
A.2.2. Study 2 13
A.2.3. Computation 13
A.3. Postprocessing. 14
A.3.1. Computation of the mass flow 15
APPENDIX B: LabVIEW programs..... 17
B.1. FPGA 18
B.2. RTOS 19
B.3. HOST 21

Budget

Part 1: Budget broken down into sections..... 1
1.1. Valves and piping 1
1.1.1. Valves 1
1.1.2. Piping and fittings 2
1.2. Data acquisition system 2
1.3. Sensors and actuators 3
1.4. Electronics 3
1.5. Gases 3
1.6. Computer and software 4
1.6.1. Computational costs 4
1.6.2. Licenses and software 4
1.7. Support Structures 5
1.8. Ejector 5
1.9. Professional fees 6
Part 2: Total budget 7

VOLUME III

Technical Drawings

Contents

Drawing 1: Experimental Ejector
Drawing 2: Body
Drawing 3: Outlet 1
Drawing 4: Nozzle Support
Drawing 5: Nozzle 1
Drawing 6: Hexagonal Nut
Drawing 7: TS4 Ejector
Drawing 8: Outlet 2
Drawing 9: Nozzle 2

Escola Universitària d'Enginyeria
Tècnica Industrial de Barcelona
Consorci Escola Industrial de Barcelona
UNIVERSITAT POLITÈCNICA DE CATALUNYA

Project report

IMPLEMENTATION AND CHARACTERIZATION OF AN EJECTOR BASED HYDROGEN RECIRCULATION SYSTEM FOR A PEM FUEL CELL

TFG presentat per optar al títol de GRAU en
ENGINYERIA MECÀNICA
per **Xavier Corbella Coll**

Barcelona, 9 de Juny de 2015

Director: Ricardo Torres Cámara
Departament de MF
Universitat Politècnica de Catalunya (UPC)

Codirector: Miguel Allué Fantova
Departament Automatic Control
Institut de Robòtica i Informàtica Industrial (IRI/CSIC)

CONTENTS

Contents I
Abstract V
Resum V
Resumen VI
Acknowledgements VII
List of figures IX
List of tables XV
Nomenclature XVII
Chapter 1: Introduction and objective 1
1.1. Introduction 1
1.2. Objective 3
Chapter 2: Introduction to PEM fuel cells 5
2.1. Fuel cells 5
2.2. PEM fuel cells 7
2.2.1. Basic chemistry and thermodynamics 7
2.2.2. Theoretical potential 8
2.2.3. Efficiency 9
2.2.4. Voltage losses 9
2.3. Hydrogen supply 11
Chapter 3: Test Station 4 13
3.1. Characteristics of Test Station 4 13
3.2. Control and data acquisition system 16
3.3. Experimental Test 17
Chapter 4: Compressible Flow and Ejectors 23
4.1. Compressible flow 24
4.1.1. Ideal gas law and perfect gases 24
4.1.2. Isentropic relations for perfect gases 25
4.1.3. Speed of Sound 25
4.1.4. Stagnation properties 25
4.1.5. Sonic properties 27
4.1.6. Velocity changes due to area changes 27

4.1.7. Choking phenomena 29
4.1.8. Normal shock waves 30
4.1.9. Oblique shock waves 31
4.1.10. Expansion waves 34
4.1.11. Nozzles 35
4.2. Ejectors 37
4.2.1. Geometrical parameters of an ejector 39
4.2.2. Flow behavior within the ejector 41
Chapter 5: Ejector Modelling 43
5.1. 1D Mathematical Models 43
5.2. Introduction to the CFD model 45
5.2.1. Reynolds-averaged and Favre-averaged Navier-Stokes equations 45
5.2.2. The standard k-ε turbulence model 49
5.2.3. Wall functions 50
5.3. COMSOL model 51
5.3.1. Governing equations 52
5.3.2. Geometry 53
5.3.3. Boundary conditions and initial values 54
5.3.4. Solver 55
5.3.5. Mesh 56
5.3.6. Cluster computation 58
5.3.7. Example 58
5.3.8. Modeling an experimental nozzle 62
Chapter 6: Experimental validation of the CFD model 67
6.1. Layout of the experimental set-up 67
6.2. Geometry of the experimental ejector 73
6.2.1. Initial solution 73
6.2.2. Chosen geometry 76
6.3. Data acquisition and control 81
6.3.1. FPGA program 81
6.3.2. RTOS program 81
6.3.3. Host program 82
6.3.4. Mass flow meter/controller 82
6.4. Results 82
6.4.1. Primary mass flow 83
6.4.2. Normal mode 83

6.4.3. Recirculation mode 86
Chapter 7: Geometry of the ejector for TS4 89
7.1. Parametrical studies to find the optimal geometrical parameters 89
7.1.1. Diameter of the throat 89
7.1.2. Diameter of the mixing chamber 91
7.1.3. Length of the mixing chamber 92
7.1.4. Nozzle position 92
7.1.5. Pressure drop 93
7.2. Final Geometry 94
Chapter 8: Conclusions 97
8.1. Conclusions 97
8.2. Future work 98
Bibliography 99

ABSTRACT

One of the issues that needs to be studied in order to improve the durability of a PEM fuel cell system is the management of the hydrogen feeding procedure. It has been demonstrated that its efficiency and durability are improved when using a hydrogen recirculation system.

In this work, an ejector has been designed and manufactured to be implemented in the PEM fuel cell Test Station 4 of the IRI's Fuel Cell Control Laboratory to analyze how ejector based hydrogen recirculation systems affect PEM fuel cells. The proper design of an ejector must take into account several geometrical parameters that can only be studied using Computational Fluid Dynamics (CFD). Thus, a CFD model has been implemented with a 2D axisymmetric geometry and the standard k-ε model to solve Favre-averaged Navier-Stokes equations. An experimental ejector has been designed using the model and manufactured. Then, it has been tested experimentally to validate the CFD model.

Results showed that the model is capable of capturing the mass flows obtained for different operative conditions. Then, a parametric study has been done to find the optimum geometrical parameters for the ejector to be implemented in Test Station 4.

RESUM

L'estudi del sistema d'alimentació d'hidrògen és un dels camps de recerca necessaris per a allargar la vida útil de les piles de combustible PEM. Estudis anteriors han demostrat que la vida útil i l'eficiència d'aquestes piles milloren amb l'ús d'un sistema de recirculació d'hidrogen.

En aquest treball s'ha dissenyat i fabricat un ejector per a ser implementat a l'estació de proves 4 del laboratori de control de piles de combustible de l'IRI amb la finalitat d'analitzar l'efecte que els sistemes de recirculació d'hidrogen basats en ejectors tenen sobre aquestes piles. En el disseny de la geometria d'un ejector s'han de considerar diferents paràmetres que només es poden estudiar mitjançant CFD (Computational Fluid Dynamics). Per tant, s'ha desenvolupat un model 2D axisimètric utilitzant el model de turbulència k-ε estàndard per a resoldre les equacions de Navier-Stokes amb una mitjana de Favre. El model s'ha utilitzat per a dissenyar i fabricar un ejector experimental amb la finalitat de validar-lo.

Els resultats obtinguts mostren que el model és capaç d'obtenir els fluxos màssics que apareixen en un ejector per a diferents condicions operatives. Un cop validat el model, s'ha fet servir per a fer un estudi paramètric per a trobar els paràmetres geomètrics òptims que ha de tenir l'ejector dissenyat per a l'estació de proves 4.

RESUMEN

El estudio del sistema de alimentación de hidrógeno es uno los campos de investigación necesarios para alargar la vida de las pilas de combustible PEM. Estudios anteriores han demostrado que la vida útil y la eficiencia de estas pilas mejoran con el uso de sistemas de recirculación de hidrógeno.

En este trabajo se ha diseñado y fabricado un eyector para ser implementado en la estación de pruebas 4 del laboratorio de control de pilas de combustible del IRI con la finalidad de analizar el efecto que los sistemas de recirculación de hidrógeno basados en eyectores tienen sobre dichas pilas. El correcto diseño de la geometría de un eyector debe tener en consideración diferentes parámetros que solo pueden ser estudiados utilizando CFD (Computational Fluid Dynamics). Para ello, se ha desarrollado un modelo 2D asimétrico utilizando el modelo de k-ε estándar para resolver las ecuaciones de Navier-Stokes con un promediado de Favre. El modelo ha sido utilizado para diseñar y fabricar un eyector experimental con la finalidad de validar-lo.

Los resultados obtenidos muestran que el modelo es capaz de obtener los flujos másicos que aparecen en un eyector para diferentes condiciones operativas. Una vez validado el modelo, se ha utilizado para hacer un estudio paramétrico para encontrar los parámetros geométricos óptimos para el eyector diseñado para la estación 4.

ACKNOWLEDGEMENTS

I would like to express my gratitude to all those who made the realization of this project possible. First and foremost, I want to thank the Fuel Cell Control Laboratory of the Institut de Robòtica i Informàtica Industrial (IRI) of the Spanish Council for Scientific Investigation (CSIC) and the Escola Universitària d'Enginyeria Tècnica Industrial de Barcelona (EUETIB) of the Universitat Politècnica de Catalunya (UPC) for giving me permission to accomplish this project and carry out the necessary work in their institutions.

Furthermore I would like to thank Dr. Ricardo Torres for encouraging me to go ahead with my Degree Final Project, helping me to understand the concepts that appeared in the it and providing me with valuable resources.

I want to thank my colleagues from IRI for their support, help and interest. I am deeply indebted to Miguel Allué and Vicente Roda for their help and knowledge and for providing me with the possibility of working in a friendly and stimulating environment.

I would also like to thank the Spanish Ministry of Education Sport and Culture and the Fluid Mechanics Department of the UPC for their finantial support. Furthermore, I would like to thank the EUETIB Fluid Mechanics Department and Professor Joan Grau for letting me use their computational resources and advising me in how to use them.

I am also grateful to the Mechanical Engineering Laboratory of the Escola Tècnica Superior d'Enginyeria Industrial de Barcelona (ETSEIB) and to Rafael Bermúdez for making possible the manufacturing of the ejector.

Finally I would like to give my most sincere thanks to my partner for her patience, incalculable knowledge and useful support, to my friends, for their tireless sense of humor, and to my family, for their continuous support and encouragement throughout my entire studies.

LIST OF FIGURES

Fig. 2. 1- a) Electrolysys of water. b) A small current flows. The oxygen and hydrogen are recombining (Larminie and Dicks 2003).....6

Fig. 2. 2- Different types of fuel cells, their reactions and operating temperatures (Barbir 2005).....6

Fig. 2. 3- The basic principle of operation of a PEM fuel cell (Barbir 2005). 7

Fig. 2. 4- Voltage losses in the fuel cell (Barbir 2005). 10

Fig. 2. 5- Representation of the polarization curve including voltage losses (Strahl 2010). 11

Fig. 3. 1- Pictures of the Test Station 4 (Rojas Fernández 2011). 14

Fig. 3. 2- Polarization curve of stack UBzM BZ 100. Image from the Operational Manual of PEM-FC-Stack BZ 100. 14

Fig. 3. 3- Layout of Test Station 4. 15

Fig. 3. 4- Logical supervisory diagram for the FC station based on LabVIEW FPGA and Real Time components (Rojas Fernández 2011). 16

Fig. 3. 5- Flow rates of hydrogen and oxygen. 18

Fig. 3. 6- Temperature of the water, the fuel cell and at the outlet of hydrogen. 18

Fig. 3. 7- Voltage, current and power of the load. 19

Fig. 3. 8- Pressure of anode and cathode at the inlet. The pressure at the outlet is 1 bar_{abs}. 19

Fig. 3. 9- Efficiency vs current for different stoichiometry without recirculation. 20

Fig. 3. 10- Expected efficiency vs current for different stoichiometry with recirculation. 21

Fig. 3. 11- Power vs current for different stoichiometry without recirculation. ... 21

Fig. 4. 1- Flow through a throat section and a bulge section. (White 1999) 28

Fig. 4. 2- Area ratio versus Mach number for air. 29

Fig. 4. 3- A fixed normal shock wave. (White 1999) 31

Fig. 4. 4- Oblique Shock analysis. (White 1999) 32

Fig. 4. 5- Supersonic flow over a concave corner. (Anderson 2004) 32

Fig. 4. 6- Supersonic wave pattern emanating from a projectile moving at Ma=2. Heavy lines are oblique-shock waves and light lines are Mach waves. (White 1999) 33

Fig. 4. 7- Oblique-shock deflection versus wave angle for different Mach numbers. 33

Fig. 4. 8- Attached and detached shocks. (White 1999) 34

Fig. 4. 9- Shock reflection from a solid boundary. (Anderson 2004) 34

Fig. 4. 10- Supersonic flow over a convex corner. (Anderson 2004) 35

Fig. 4. 11- Operation of a converging nozzle: a) nozzle geometry showing characteristic pressures; b) Pressure distribution caused by various back pressures; c) Mass flow versus back pressure. (White 1999) 36

Fig. 4. 12- Operation of a converging diverging Nozzle, (3); a) Converging-Diverging Nozzle; b) Pressure distribution caused by various back pressures; c)mass flow versus back pressure. (White 1999) 36

Fig. 4. 13- Geometry of an ejector. (Liao 2008) 38

Fig. 4. 14- Geometry of a convergent-divergent nozzle ejector. (B. Huang 1999) 39

Fig. 4. 15- Operational modes of an ejector.(Zhu and Li 2009) 41

Fig. 4. 16- Flow pattern in the mixing chamber of a rectangular ejector (see Fig. 4. 17). (Koita and Iwamoto 2009) 41

Fig. 4. 17- Rectangular ejector used by Koita el al. (Koita and Iwamoto 2009) . 42

Fig. 4. 18- Shadowgraph pictures for different NPR (nozzle pressure ratio, P_{p0}/P_b) with entrainment flow. (Koita and Iwamoto 2009) 42

Fig. 5. 1- Typical point velocity measurement in turbulent flow (Versteeg and Malalasekera 2007). 47

Fig. 5. 2- Geometry of the model. a) 2D geometry for axisymmetric calculus. b) 3D geometry obtained from the revolution of the 2D geometry. 53

Fig. 5. 3- Wall distance. (Comsol: The CFD module user's guide, 2012) 54

Fig. 5. 4- Relative error respect to the finest mesh vs number of elements of the mesh. 57

Fig. 5. 5- Relative error respect to the finest mesh vs time. 57

Fig. 5. 6- Chosen mesh. 58

Fig. 5. 7- Mass flows obtained for the different values of P_{p0} analyzed. 59

Fig. 5. 8- Results for P_{p0}=1.75 bar_{abs}. a) Temperature. b) Pressure. c) Mach Number 60

Fig. 5. 9- Results for P_{p0}=2.25 bar_{abs}. a) Temperature. b) Pressure. c) Mach Number 60

Fig. 5. 10- Results for P_{p0}=3.25 bar_{abs}. a) Temperature. b) Pressure. c) Mach Number 61

Fig. 5. 11- Results for P_{p0}=4.5 bar_{abs}. a) Temperature. b) Pressure. c) Mach Number..... 61

Fig. 5. 12- Geometry of the experimental convergent-divergent nozzle. (EUETIB, Manual de Prácticas de Ingeniería de Fluidos: Flujo Compresible en Toberas, 2010) 62

Fig. 5. 13- Layout of the experimental set-up. (EUETIB, Manual de Prácticas de Ingeniería de Fluidos: Flujo Compresible en Toberas, 2010)..... 62

Fig. 5. 14- Experimental set-up. (EUETIB, Manual de Prácticas de Ingeniería de Fluidos: Flujo Compresible en Toberas, 2010) 62

Fig. 5. 15- Pressure along the axis of the nozzle for a stagnation pressure of 3.8 bar_{abs} and three different back pressures. 63

Fig. 5. 16- Pressure along the axis of the nozzle for a stagnation pressure of 6 bar_{abs} and three different back pressures. 63

Fig. 5. 17- Geometries used in the simulation. a) First attempt (Real geometry). b)Second attempt. c)Third attempt..... 64

Fig. 5. 18- Results obtained with the second geometry (P_0=3.8 bar abs, P_b=1 bar abs). There are strong oblique shock waves that perturb the solution. a)Pressure (Pa). b) Mach number. 64

Fig. 5. 19- Mesh..... 65

Fig. 5. 20- P_p=3.8 bar abs, P_b=3.1 bar abs. 65

Fig. 5. 21- P_p=3.8 bar abs, P_b=1.9 bar abs. 65

Fig. 5. 22- P_p=3.8 bar abs, P_b=1 bar abs..... 65

Fig. 5. 23- P_p=6 bar abs, P_b=5.4 bar abs..... 65

Fig. 5. 24- P_p=6 bar abs, P_b=2.7 bar abs..... 66

Fig. 5. 25- P_p=6 bar abs, P_b=1.2 bar abs..... 66

Fig. 5. 26- Mach number for P_p=3.8 bar_{abs} and P_b=1.9 bar_{abs}. A shock wave appears near the outlet of the nozzle. 66

Fig. 6. 1- Picture of the assembly of the experimental validation. 68

Fig. 6. 2- Picture of the experimental set-up. 69

Fig. 6. 3- Picture of the experimental set-up. 69

Fig. 6. 4- Layout of the experimental set-up. 70

Fig. 6. 5- Initial solution. a)Ejector assembled. b)Exploded view. 73

Fig. 6. 6- Sectional view of the initial solution. 74

Fig. 6. 7- Parts of the initial ejector. a) Nozzle b)Outlet c)Hexagonal nut d) Connector e) Body 74

Fig. 6. 8- Sectional view of the initial ejector with some of its dimensions..... 75

Fig. 6. 9- Geometry used in the CFD simulations of the initial ejector..... 75

Fig. 6. 10- Mass flows obtained with COMSOL for the initial ejector (P_{s0}=P_b=1 bar_{abs} and T_{s0}=T_{p0}=298 K). 75

Fig. 6. 11- Solid Works exploded view of the chosen geometry for the experimental ejector. 76

Fig. 6. 12- Pieces of the experimental ejector. 77

Fig. 6. 13- Sectional view of the ejector. 79

Fig. 6. 14- Sectional view of the ejector with some of its dimensions. 79

Fig. 6. 15- Mass flows obtained with COMSOL for the experimental ejector (P_{s0}=P_b=1 bar abs and T_{s0}=T_{p0}=298 K)..... 80

Fig. 6. 16- Results for P_{p0}=4 bar abs. a) Temperature. b) Pressure. c) Mach Number..... 80

Fig. 6. 17- Primary mass flow without recirculation. The experimental results are compared with 1D predictions and COMSOL results. 83

Fig. 6. 18- Comparison of the mass flows and stoichiometry obtained experimentally and with COMSOL (Normal Mode and P_b=P_{s0}=1.2 bar_{abs}, NXP=1.5 mm)..... 84

Fig. 6. 19- Comparison of the mass flows and stoichiometry obtained experimentally and with COMSOL (Normal Mode and P_b=P_{s0}=1.2 bar_{abs}, NXP=2.5 mm)..... 85

Fig. 6. 20- Comparison of the mass flows and stoichiometry obtained experimentally and with COMSOL (Normal Mode and P_b=P_{s0}=1.2 bar_{abs}, NXP=3.5 mm)..... 85

Fig. 6. 21- Comparison of the mass flows and stoichiometry obtained experimentally and with COMSOL (Normal Mode and P_b=P_{s0}=1.5 bar_{abs}, NXP=1.5 mm)..... 86

Fig. 6. 22- Comparison of the mass flows and stoichiometry obtained experimentally and with COMSOL (Recirculation Mode and P_b=1.2 bar_{abs}, NXP=1.5 mm)..... 87

Fig. 6. 23- Comparison of the mass flows and stoichiometry obtained experimentally and with COMSOL (Recirculation Mode and P_b=1.5 bar_{abs}, NXP=1.5 mm)..... 87

Fig. 7. 1- Primary mass flow for different diameters of the throat using the isentropic 1D theory..... 90

Fig. 7. 2- Primary mass flow for Dt=0.4 mm obtained using COMSOL's model.. 90

Fig. 7. 3- Stoichiometry obtained for different diameters of the mixing chamber when Pb=Ps0=1 bar_{abs}..... 91

Fig. 7. 4- Stoichiometry obtained for different diameters of the mixing chamber when Pb=Ps0=1.1 bar_{abs}..... 91

Fig. 7. 5- Stoichoimetry obtained for different lengths of the mixing chamber when Pb=Ps0=1.1 bar abs. 92

Fig. 7. 6- Stoichiometry obtained for different nozzle positions. 93

Fig. 7. 7- Stoichiometry, primary and secondary mass flows with the chosen geometrical parameters and a drop of pressure of 0.1 bar_{abs}..... 94

Fig. 7. 8- Stoichiometry, primary and secondary mass flows with the chosen geometrical parameters and $P_b=P_{s0}$..... 94
Fig. 7. 9- Sectional view of the ejector designed for TS4 with some of it dimensions. 95
Fig. 7. 10- Sectional view of the designed ejector. 95
Fig. 7. 11- Outlet 2..... 96
Fig. 7. 12- Nozzle 2 96
Fig. 7. 13- Parts of the Ejector for TS4..... 96
Fig. 7. 14- Parts of the Ejector for TS4..... 96
Fig. 7. 15- Parts of the Ejector for TS4..... 96

LIST OF TABLES

Table 6. 1- Elements used in the experimental validation. 71
Table 6. 2- Parts of the experimental ejector 77

NOMENCLATURE

a	Speed of Sound
c	Velocity
C_k and δ_{id}	Tuning parameters for crosswind diffusion and isotropic diffusion
C_p	Specific Heat Capacity at Constant Pressure
c_τ	Friction velocity
C_v	Specific Heat Capacity at Constant Volume
$C_{1\varepsilon}, C_{2\varepsilon}, C_\mu, \sigma_k, \sigma_\varepsilon$	Constants of the k- ε model
δ_{ij}	Kronecker delta
δ_w	Distance from a wall
E	Theoretical Potential
g	Gravity
G	Gibb's Free Energy
H	Enthalpy
I_T	Turbulence intensity
γ	Specific Heat Ratio
Γ_t	Turbulent diffusivity
η	Efficiency
k	Turbulent kinetic energy per unit mass
k_t	Thermal conductivity
k_v	Constant of Von Karman
L_T	Turbulence length scale
λ	Constant that relates stresses to the volumetric deformation
$\dot{m}$	Mass flow
$\bar{M}$	Molecular Weight
Ma	Mach Number
μ	Dynamic viscosity
$\boldsymbol{n}$	Normal vector

n_e	Number of electrons per molecule
P	Pressure
Ψ	Mass flow function
r	Radius
R	Specific Gas Constant
R_u	Universal Gas Constant
ρ	Density
s	Entropy
S_{ij}	Deformation rate
S_i, S_M, S_E	Source terms in the Navier-Stokes equations
S_{H_2}	Hydrogen stoichiometry ratio
σ_t	Turbulent Prandtl number
t	Time
T	Temperature
τ_{ij}	Reynolds stresses
u	x component of the velocity vector
u_i	Internal energy
v	y component of the velocity vector
w	z component of the velocity vector
W_{el}	Electrical Work

CHAPTER 1: INTRODUCTION AND OBJECTIVE

1.1. Introduction

The continuous and exponential increase in energy demand makes it necessary to develop alternative energy production methods that can substitute fossil fuels. The fact that the availability of these fuels is finite and that they have a harmful effect over the environment makes mandatory the investigation of new and more sustainable energy sources.

A good alternative to replace fossil fuels is hydrogen. Hydrogen provides higher efficiency than fossil fuels and is environmentally friendly. A high advantage of hydrogen is that it is fully recyclable since it produces water that can be used as the raw material for hydrogen generation. Moreover, it can be used to produce energy by several different ways: by burning it, using it in a combustion engine or producing electricity through fuel cells.

When properly designed, fuel cell systems can be a reliable and durable method to produce efficient and environmentally friendly energy for various applications. Amongst the various fuel cell technologies, Proton Exchange Membrane (PEM) fuel cells are considered the best candidate to replace the combustion engine because of their capability of high power densities, relatively high efficiency, low operating temperatures, quick startup, zero pollution and relatively long lifetime (J. He, Choe, and Hong 2008). For the last years, significant progress has been made in means of achieving the optimum balance of cost, efficiency and durability. Fuel lifetime requirements vary significantly, ranging from 3000 to 40000 operating hours. In order to optimize the lifetime and efficiency of a PEM fuel cell, several conditions must be taken into account. Some of them are: reactant flow rates and composition, operating and environmental temperature

and pressure, humidification levels, peak load requirements and required rate of transient responses(Knights et al. 2004).

A very important issue that has to be studied to improve the efficiency of a PEM fuel cell system is the management of the hydrogen feeding procedure. Two different designs can be considered regarding the hydrogen feeding system: The dead-end mode and the flow-through mode. In the dead-end mode, the amount of hydrogen provided to the fuel cell stack is equal to the amount consumed by the fuel cell. This procedure leads to accumulation of impurities and water, fuel starvation and catalyst corrosion that makes it necessary to purge the anode with hydrogen. In the flow-through mode, the amount of hydrogen provided to the fuel cell stack is larger than the amount consumed by the fuel cell. An excessive ratio of hydrogen has positive effects: It improves efficiency, helps to maintain the pressure difference between anode and cathode, provides better water management, increases the lifetime of the membrane and reduces the response time to an increased power demand. However, unconsumed hydrogen means a decrease in the efficiency of the fuel cell since it is a waste of energy. Thus, hydrogen must be recirculated.

Hydrogen recirculation systems can be designed by using either a compressor or an ejector. Compressors can work for a wide range of flow rates, but they require energy and need maintenance and they usually use lubricants that can produce catalyst poisoning. Ejectors are more suited for PEM fuel cells. They have no moving parts, need almost no maintenance and have a very simple mechanical structure. Ejectors use the energy of the hydrogen which is stored in a high pressurized tank to recirculate the anodic exhaust, so they have no parasitic power.

One of the research areas of the Automatic Control group of the "Institut de Robòtica i Informàtica Industrial" (IRI) is the validation and testing of control strategies of fuel cell based energy conversion systems. This project is a contribution to their work by means of designing an ejector that will be used in the future as the core of an ejector based hydrogen recirculation system in the Station TS4 of the Fuel Cell Control Laboratory. In order to design the ejector, a lot of previous work has been needed. In first place, a literature review of fuel cells (Chapter 2), compressible flow and ejectors (Chapter 4) has been carried out. Then, a CFD model was developed using COMSOL to model ejectors(Chapter 5). The next step was to validate this model using an experimental ejector, in the Fuel Cells Control Laboratory (Chapter 6). This experimental ejector was designed and then manufactured in the Laboratory of Mechanical Engineering of the ETSEIB. Last step of this work has been the utilization of the COMSOL model to design a final ejector with optimal geometrical parameters to be implemented in Test Station 4 (Chapter 7). Station TS4 and its operative conditions are described in Chapter 3.

1.2. Objective

The main objective of this work is to design and manufacture an ejector to recirculate hydrogen in Station TS4. To achieve this goal, it will be necessary to acquire certain knowledge related to fuel cells, compressible flow and computational fluid dynamics. The manufacture of the ejector will be done by the technics working in the laboratory of mechanical engineering of the ETSEIB (Escola Tècnica Superior d'Enginyeria Industrial de Barcelona) following the technical drawings developed in this project.

A secondary objective is to develop a CFD model using COMSOL Multiphysics that can be used to evaluate the behavior of the flow and the mass flows that appear in an ejector for certain conditions of pressure and temperature. This model needs to be validated experimentally, and therefore an experimental set-up will have to be implemented.

CHAPTER 2: INTRODUCTION TO PEM FUEL CELLS

In this chapter fuel cells are briefly introduced and the basics about PEM fuel cell are explained. The last part of the chapter is devoted to explain different modes of hydrogen supply and the advantages of using an ejector based hydrogen recirculation system. More information about PEM fuel cells can be found in more specialized bibliography (Barbir 2005)(Larminie and Dicks 2003).

2.1. Fuel cells

A fuel cell is an electrochemical energy converter that converts chemical energy of fuel directly into DC electricity (Barbir 2005). The operational principle of a fuel cell refers to an experiment of Sir William Grove in 1839. First, he electrolyzed water into hydrogen and oxygen by applying an electrical current through it (Fig. 2. 1 a). Then, he replaced the power supply with an ammeter and measured a small current produced by the reversing of the electrolysis (Fig. 2. 1 b). This small current is produced by the chemical reaction that takes places in the recombining of hydrogen and oxygen.

A fuel cell is composed of two electrodes, the anode (negative) and the cathode (positive). The chemical reactions that produce electricity take place at the electrodes. Fuel cells also have an electrolyte, which carries the electrically charged particles (ions) from one electrode to the other, and usually use a catalyst to speed the reactions at the electrodes. The electrons released in the

chemical reaction that takes place at the anode travel through an external circuit where they perform electrical work and come back at the cathode.

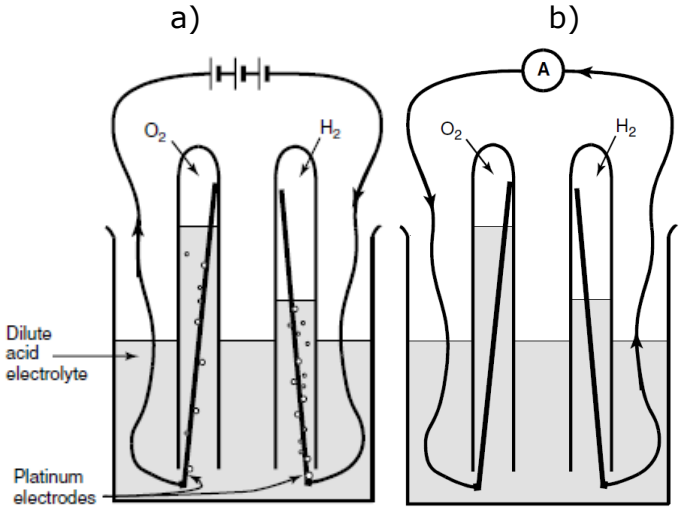

Fig. 2. 1- a) Electrolysys of water. b) A small current flows. The oxygen and hydrogen are recombining (Larminie and Dicks 2003).

There are different types of fuel cells which can be grouped by the type of the electrolyte they use (Barbir 2005). Amongst them (Fig. 2. 2):

- Alkaline Fuel Cells (AFC).
- Proton Exchange Membrane Fuel Cells (PEMFC).
- Phosphoric Acid Fuel Cells (PAFC).
- Molten Carbonate Fuel Cells (MCFC).
- Solid Oxide Fuel Cells (SOFC).

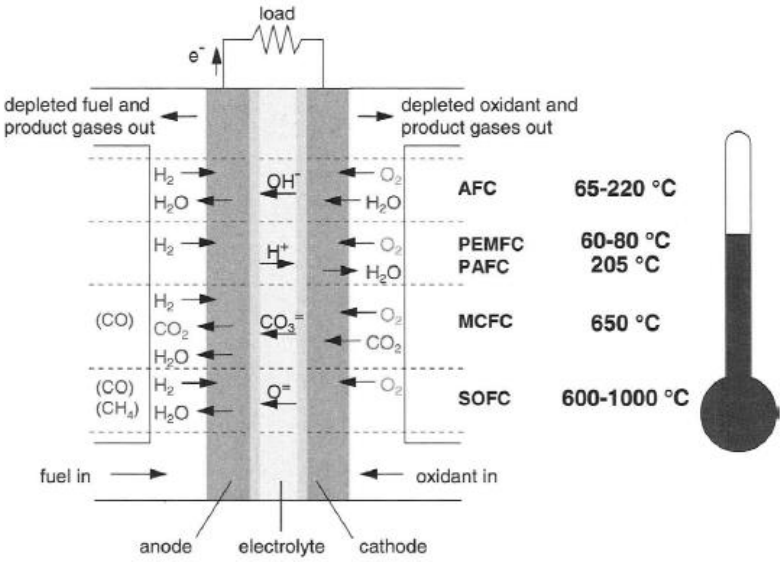

Fig. 2. 2- Different types of fuel cells, their reactions and operating temperatures (Barbir 2005).

2.2. PEM fuel cells

PEM fuel cells use hydrogen and oxygen as the reactant gases, a proton conductive polymer membrane as the electrolyte and, typically, platinum as the catalyst. Their major advantages are their low operating temperatures, short start-up time, high efficiency and compactness (Strahl 2010). These advantages make them serious candidates for automotive applications, small-scale distributed stationary power generation and portable power applications.

The proton conductive polymer membrane is the main component of a PEM fuel cell due to its unique capabilities. It is impermeable to gases and electrically insulated but conductive to protons. The membrane is situated between two porous electrodes (Fig. 2. 3). A layer with catalyst particles (platinum) is inserted at the membrane-electrode interface. Hydrogen is fed on the anode side of the membrane and oxygen on the cathode.

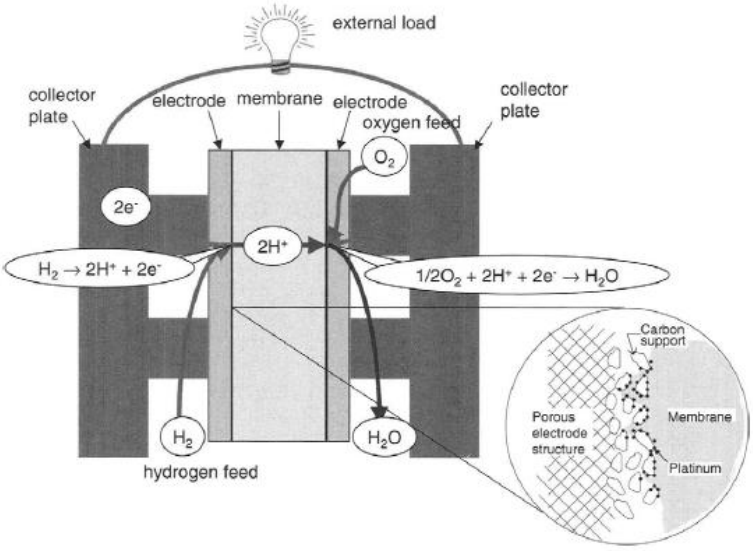

Fig. 2. 3- The basic principle of operation of a PEM fuel cell (Barbir 2005).

2.2.1. Basic chemistry and thermodynamics

The electrochemical reactions happen simultaneously on both cathode and anode. At the anode, hydrogen is split into protons and electrons:

$$\mathrm{H}_2 \rightarrow 2H^+ + 2e^- \qquad \textbf{Eq. 2. 1}$$

The protons resulting from Eq. 2. 10 permeate through the membrane, whereas the electrons travel from the anode to the cathode through an external circuit.

At the cathode, the oxygen combines with the protons and the electrons from the anode producing water:

$$2H^+ + \frac{1}{2}O_2 + 2e^- \rightarrow H_2O \qquad \textbf{Eq. 2. 2}$$

The overall reaction is the same as the reaction of hydrogen combustion, which is an exothermic process:

$$\mathrm{H}_2 + \frac{1}{2}O_2 \rightarrow H_2O + \Delta H \qquad \textbf{Eq. 2. 3}$$

The enthalpy of the reaction can be calculated as the difference between the heats of formation of products and reactants (Barbir 2005):

$$\Delta H = \left(h_f\right)_{H_2O} - \left(h_f\right)_{H_2} - \frac{1}{2}\left(h_f\right)_{O_2} = -286\,\frac{kJ}{mol} \qquad \textbf{Eq. 2. 4}$$

The latter result has been obtained by using the higher heating value of hydrogen at 25ºC and at atmospheric pressure. It can be considered as the maximum amount of energy that may be extracted from hydrogen.

As in every chemical reaction, not all the energy can be converted into useful work since there are some irreversible loses due to creation of entropy (ΔS). The portion of hydrogen's higher heating value that can be converted into electricity correspond to Gibbs free energy (Barbir 2005):

$$\Delta \mathrm{G} = \Delta \mathrm{H} - \mathrm{T}\Delta S \qquad \textbf{Eq. 2. 5}$$

The created entropy formed is the difference between the entropies of products and reactants, similar to Eq. 2. 4. At 25ºC, 237.34 kJ/mol can be converted into electrical energy and the remaining 46.68 kJ/mol is converted into heat (Barbir 2005).

Gibbs free energy is not only a function of temperature but also of pressure, which is described by adding the Nernst equation (Strahl 2010):

$$\Delta \mathrm{G} = \Delta \mathrm{H} - \mathrm{T}\Delta \mathrm{S} + \mathrm{RT}\ln\left(\frac{p_{H_2O}}{p_{H_2}p_{O2}^{0.5}}\right) \qquad \textbf{Eq. 2. 6}$$

Where p_{H_2O}, p_{H_2} and p_{O_2} are partial pressures and R is the gas constant.

2.2.2. Theoretical potential

Electrical work can be calculated as a product of charge and potential. It can be expressed as (Barbir 2005):

$$\mathrm{W_{el}} = n_e F E \qquad \textbf{Eq. 2. 7}$$

Where n_e is the number of electrons per molecule, which for H_2 is 2, and F is the Faraday's constant (96.485 Coulombs/electron·mol). Using Gibb's free energy as the maximum amount of electrical work that can be generated in a fuel cell, the theoretical potential can be described as:

$$\mathrm{E} = -\frac{\Delta \mathrm{G}}{\mathrm{n_e F}} = -\frac{\Delta \mathrm{H}}{\mathrm{n_e F}} - \frac{\mathrm{T}\Delta \mathrm{S}}{\mathrm{n_e F}} + \frac{\mathrm{RT}}{\mathrm{n_e F}}\ln\left(\frac{p_{H_2}p_{O2}^{0.5}}{p_{H_2O}}\right) \qquad \textbf{Eq. 2. 8}$$

The theoretical potential at 25ºC and 1 atm is 1.23V (Strahl 2010). This theoretical potential is low. If more voltage is desired, then the solution is

working with multiple cells electrically connected in series. The assembly of multiple cells connected in series is called a fuel cell stack.

2.2.3. Efficiency

The efficiency of an energy conversion device is defined as the ratio between useful energy output and energy input. The maximum possible efficiency of a PEM fuel cell is (Barbir 2005):

$$\eta_{max} = \frac{237.34 \frac{\text{kJ}}{\text{mol}}}{286.02 \frac{kJ}{mol}} = 83\% \qquad \textbf{Eq. 2. 9}$$

The efficiency of a fuel cell can be expressed as a ratio of two potentials (Strahl 2010):

$$\eta_{max} = \frac{\text{V}_{\text{cell}}}{\left(\frac{286.02 \frac{kJ}{mol}}{n_e F}\right)} = \frac{V_{cell}}{1.482\ V} \qquad \textbf{Eq. 2. 10}$$

If hydrogen is supplied to the cell in excess, this excess will leave the fuel cell unused. This unused fuel must be added to the efficiency using the fuel utilization parameter:

$$\eta_{\text{fu}} = \frac{1}{S_{H2}} \qquad \textbf{Eq. 2. 11}$$

Where S_{H2} is the hydrogen stoichiometry ratio, that is the ratio between the amount of hydrogen supplied to the fuel cell and that consumed in the electrochemical reaction (Barbir 2005):

$$S_{H2} = \frac{\dot{m}_{H_2 consumed}}{\dot{m}_{H_2 supply}} \qquad \textbf{Eq. 2. 12}$$

The fuel efficiency is then:

$$\eta_{max} = \frac{V_{cell}}{1.482\ V}\eta_{\text{fu}} \qquad \textbf{Eq. 2. 13}$$

2.2.4. Voltage losses

If a fuel cell is supplied with reactant gases and is not connected to an external circuit, it will not generate any current and one would expect the cell potential to be close to the theoretical cell potential. However, in practice this potential is much lower. When the fuel cell is connected to an external load, the potential drops even further. This suggests that there are voltage losses in the fuel cell even when no external current is generated (Barbir 2005). There are four major voltage losses (Strahl 2010):

1) Activation polarization losses: A certain proportion of the generated voltage is needed to get the electrochemical reaction going. These losses

are called activation polarization, and occur at both anode and cathode. However, activation polarization of hydrogen oxidation reaction is much smaller than activation polarization of oxygen reduction reaction, and therefore can be neglected.

2) Internal currents and fuel crossover losses: Although the membrane is not electrically conductive and theoretically impermeable to gases, a small amount of hydrogen diffusion (fuel crossover) and electron transport through the membrane (internal currents) is possible.

3) Resistive (Ohmic) losses: These losses occur because of resistance to the flow of electrons through the electrically conductive components and to the flow of ions through the membrane.

4) Concentration polarization losses: The consumption of reactant gases at the electrode leads to concentration gradients which change the partial pressure of reactants affecting the fuel cell potential. Reactant concentration at the catalyst depends on current density, therefore the higher the current density the lower the reactant concentration at the catalyst layer. The current density at which the reactant concentration reaches zero is the maximum current density that can be generated by a fuel cell.

The magnitude of the different voltage losses as a function of current density is shown in Fig. 2. 4. Activation losses are by far the largest losses at any value of current density.

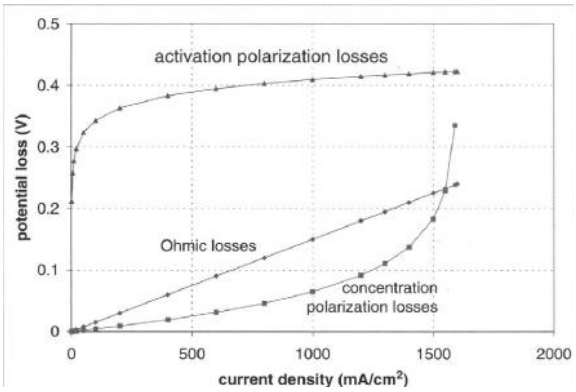

Fig. 2. 4- Voltage losses in the fuel cell (Barbir 2005).

The result of combining all voltage losses and subtracting them from the theoretical potential is the actual voltage of the fuel cell. When this voltage is expressed as a function of current density it is called the polarization curve (Fig. 2. 5). The polarization curve is the most important characteristic of a fuel cell.

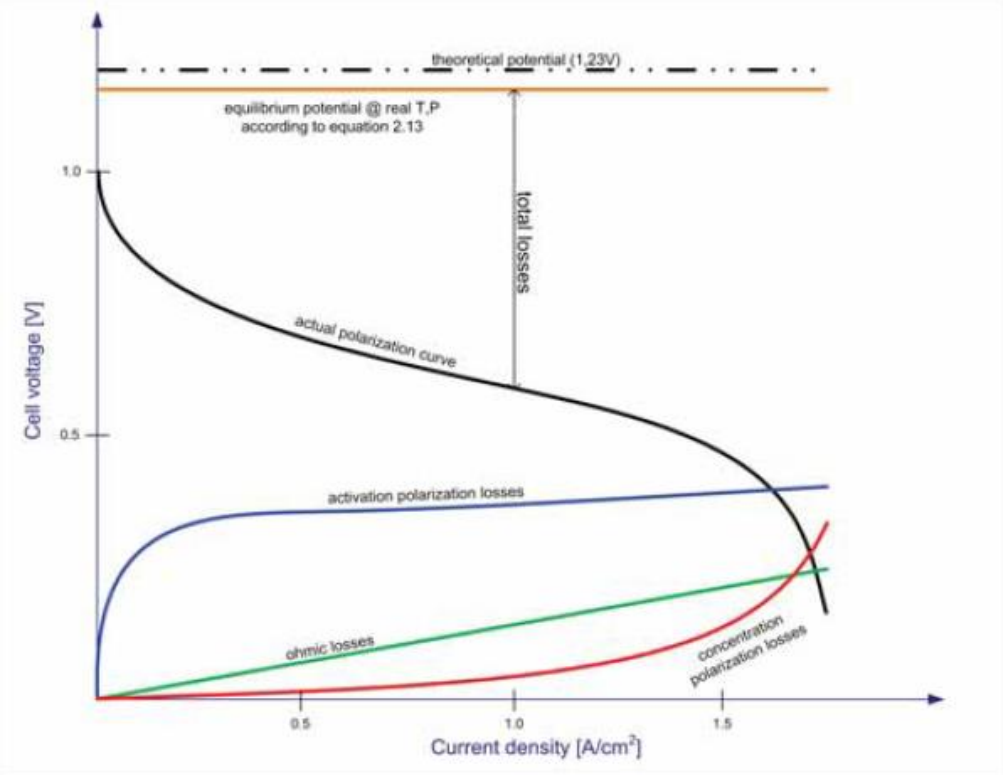

Fig. 2. 5- Representation of the polarization curve including voltage losses (Strahl 2010).

2.3. Hydrogen supply

The simplest way to supply hydrogen is the so-called dead-end mode. In this mode, hydrogen is supplied at the exact rate at which it is being consumed. This mode is optimal in terms of fuel utilization and power consumption of auxiliary devices. In PEM fuel cell systems, the stored hydrogen is commonly under pressure and the supply of hydrogen to a PEM fuel cell is achieved through a pressure regulator. However, when working in the dead-end mode, any impurity in hydrogen that may remain in the anode side will eventually accumulate in the fuel cell (Maghsoodi, Afshari, and Ahmadikia 2014). These impurities can poison the catalyst and decrease the life of the fuel cell and its performance. Another issue related to the dead-end mode is the accumulation of water in the anode. The accumulation of both impurities and water can produce hydrogen starvation on the whole stack or just in some cells.

Therefore, when working in the dead-end mode the anode must be periodically purged even when highly pure hydrogen is used. The frequency of purges depends on purity of hydrogen, the rate of nitrogen permeation through membrane and water net transport (Barbir 2005). In calculating the efficiency, the loss of hydrogen due to purging must be taken into account through fuel utilization:

$$\eta_{\mathrm{fu}} = \frac{\dot{m}_{H_2 cons}}{\dot{m}_{H_2 cons} + \dot{m}_{H_2 loss} + \dot{m}_{H_2 prg}\, \tau_{prg}\, f_{prg}} \qquad \textbf{Eq. 2. 14}$$

Where $\dot{m}_{H_2 loss}$ accounts for hydrogen loss due to crossover permeation or internal currents, τ_{prg} is the duration of hydrogen purge and f_{prg} is the frequency of purges.

Instead of purging, hydrogen may be supplied in excess. This is called the flow-through mode. This mode has demonstrated to have a better impact over the durability and performance of the system than the dead-end mode with purges (Migliardini, Capasso, and Corbo 2014). However, the efficiency obtained will be lower due to the higher fuel consumption.

In case of pure hydrogen, the flow-through mode can be improved using a recirculation mode. In the recirculation mode, the unused gas is returned to the inlet by a pump or a compressor or using a passive device such as an ejector. The use of ejectors present some advantages compared to compressors. Their main advantage is that they use the energy of the hydrogen stored in the highly pressurized tank to suck the anodic exhaust and do not need to consume part of the energy produced by the fuel cell. Moreover, ejectors do not have moving parts, do not use lubricants and require less maintenance.

CHAPTER 3:

TEST STATION 4

In this chapter, Test Station 4 is presented and the characteristics of the stack, hardware and software are described.

The Test Station 4 is placed in the Laboratory of Fuel Cell Control of the "Institut de Robòtica i Informàtica Industrial" (Institute of Robotics and Industrial Informatics). This laboratory is used for the validation and testing of control strategies of fuel cell based energy conversion systems. It has five test stations provided with oxygen, hydrogen, nitrogen and air inlets in order to work with fuel cells, and a sixth test station which is used for electrical power generation with special-machines. Each of the five test stations working with fuel cells is provided with sensors and actuators to work in a safe and automated way, as well as to modify the working conditions that affect a fuel cell. The laboratory is equipped with a supervisor system which monitors necessary safety conditions to prevent gas leaks, manages power failure alarms, automatic air extraction and safe shutdown routines for the test station in case of emergency.

3.1. Characteristics of Test Station 4

Test Station 4 (Fig. 3. 1 and Fig. 3. 3) is composed by several sections:

- **Fuel Cell Stack**: It is a PEM fuel cell stack of 600 W with membranes made of Nafion and with a single cell voltage of 0.6V. It is the model BZ100, built by UBzM. It consists of 20 cells with 100 cm^2 of active area and with an open voltage of approximately 0.95 V/cell. According to the manufacturer, the maximum theoretical current is 80 A. The nominal temperature is 55ºC and the stack can work with temperatures ranging from 20ºC to 65ºC. Hydrogen flow rate range goes from 1 Nl/min to 20 Nl/min with a maximum pressure of 1.5 bar_{abs} and a stoichiometry between 1.1 and 2.5 (gas utilization between 40% and 90%). Air flow rate range goes from 4 Nl/min to 116 Nl/min with a maximum pressure of 1.6 bar_{abs} and a stoichiometry between 2.5 and 5 (gas utilization between 25%

and 40%). The operating pressure at the stack should be near atmospheric pressure, with a maximum differential pressure between cathode and anode of 0.5 bar. The current-voltage curve provided by the manufacturer in the operational manual is shown in Fig. 3. 2.

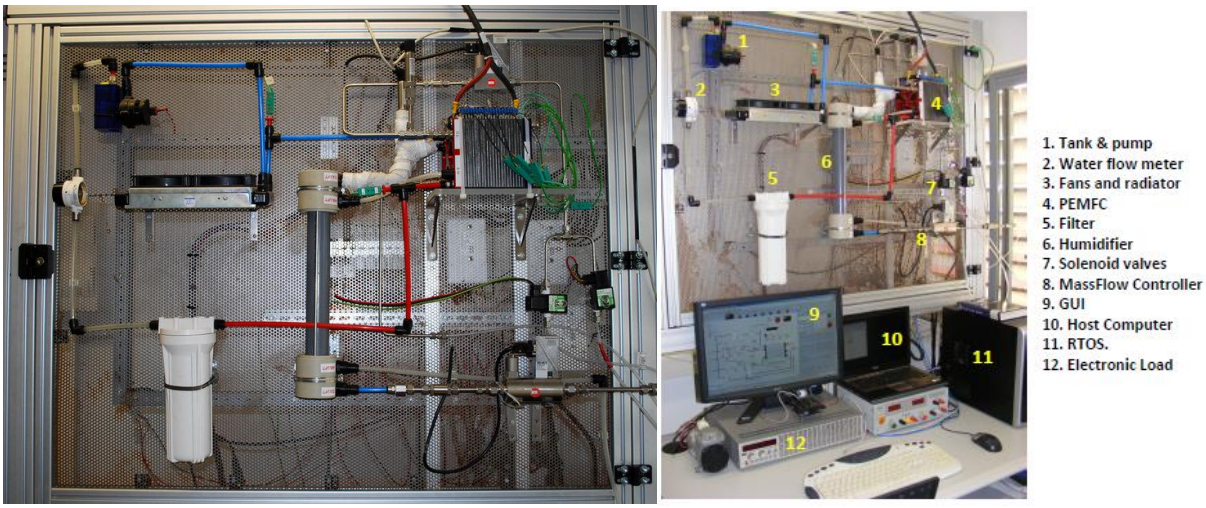

Fig. 3. 1- Pictures of the Test Station 4 (Rojas Fernández 2011).

- **Hydrogen Pipeline**: It consists of a gas filter, a Bronkhorst High-Tech B.V. mass flow controller, an anti-return check valve and a pressure transducer which can measure up to 1 bar. The pipeline is made of stainless steel of ½ inch and it has two normally-closed electro-valves that allow the user to select either hydrogen, for normal operation of the stack, or nitrogen, to purge the stack.

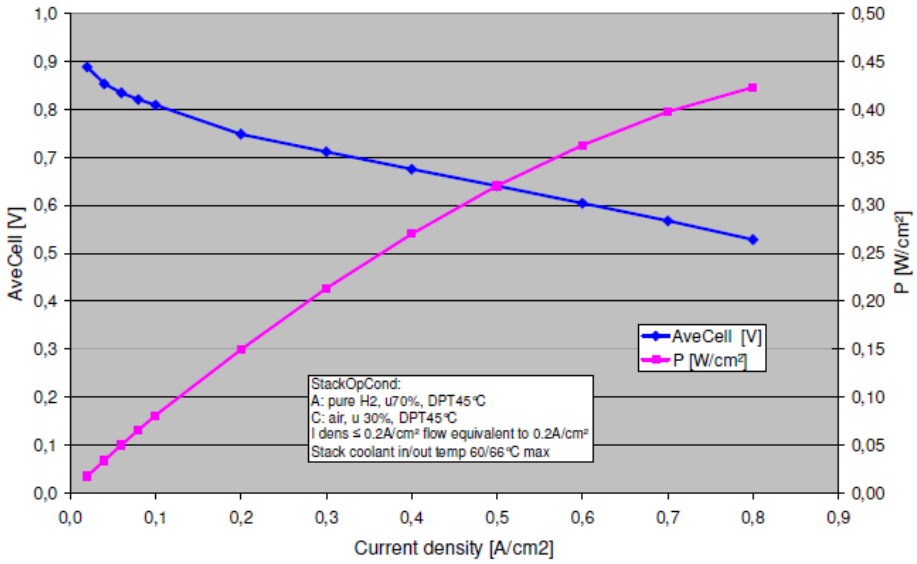

Fig. 3. 2- Polarization curve of stack UBzM BZ 100. Image from the Operational Manual of PEM-FC-Stack BZ 100.

- **Air Pipeline**: It consists of a gas filter, a Bronkhorst High-Tech B.V. mass flow controller, an anti-return check valve, a humidifier and a pressure transducer which can measure up to 1 bar. The humidifier is a membrane humidifier which uses the water at the output of the cathode to humidify

the air entering the stack. The pipe is a plastic tube of 10 mm. The section of the tube between the outlet of the humidifier and the inlet of the cathode is thermally insulated.

- **Cooling System**: Bz 100 PEM fuel cell stack requires an active cooling system to control the temperature. The cooling system is composed of a water flow meter, a deposit tank, an electric pump, a heat exchanger with two fans, a deionization system and two temperature transducers.
- **Programmable Load**: The programmable load is the model PL1006 manufactured by Höcherl and Hackl GmbH. The maximum current is 100 A with a maximum power of 1000 W. The maximum voltage is 60 V, with a rise and fall time of 75 µs.

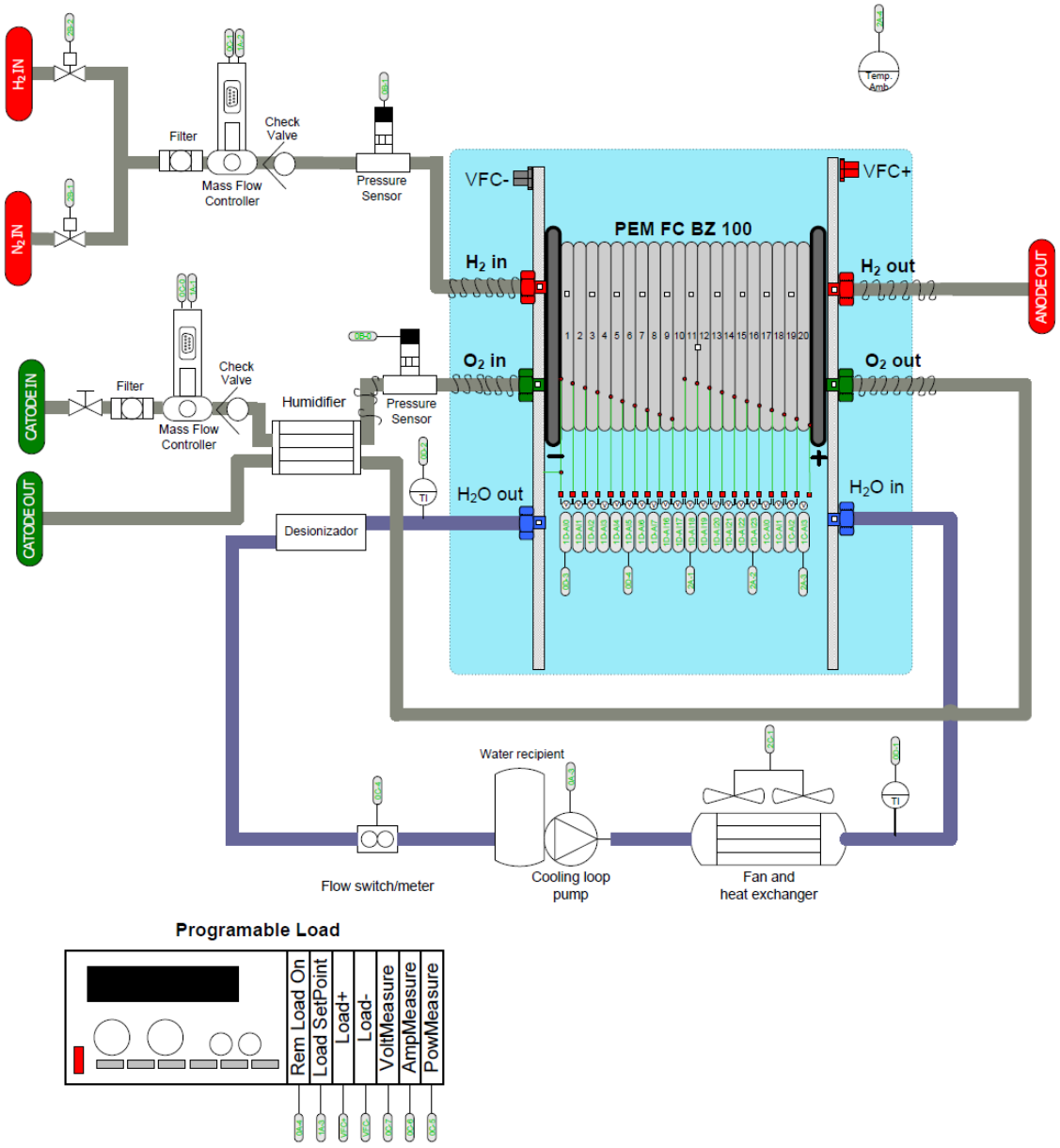

Fig. 3. 3- Layout of Test Station 4.

3.2. Control and data acquisition system

The control and data acquisition is achieved using LabVIEW. The logical hierarchy of the system is depicted in Fig. 3. 4. In the lowest level, all the measured signals are connected to the Programmable Automation Controller (PAC) CompactRIO. The communication with the signal is achieved thanks to a series of I/O Modules that transform the electrical signals into binary data which can be read by the Field Programmable Gate Array (FPGA) connected to a PCI bus in the Real Time Operating System (RTOS) computer. The programming and monitoring of the complete system is done in the Host Computer, which is connected to the RTOS via Ethernet. The programming is done in the Host computer and, when ready, the program is deployed to the RTOS and the FPGA. The main Graphical User Interface (GUI) is programed in the HOST computer and is where the data is visualized and the user has access to control the system. The hardware and software used is briefly described below. More information can be found in the master thesis written by J.D. David Rojas Fernández (Rojas Fernández 2011).

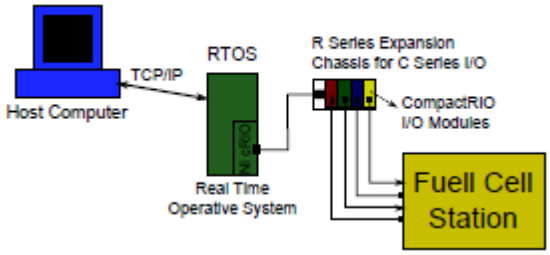

Fig. 3. 4- Logical supervisory diagram for the FC station based on LabVIEW FPGA and Real Time components (Rojas Fernández 2011).

The NI cRIO (National Instruments CompactRIO) is a reconfigurable control and acquisition system designed for applications that require high performance and reliability and is powered by reconfigurable I/O FPGA technology. This FPGA acquires data at a high sampling rate ($10\mu s$) and provides this information to the RTOS. The FPGA code deals with the I/O signals and performs two tasks: calibration, which is done at the beginning of the program, and data acquisition, which is a while loop controlled by a stop variable. This while loop stores the values from the I/O modules into variables that can be read by the RTOS.

There are several modules, called cRIO I/O modules, connected to the FPGA. These modules perform the input/output conversion task. There are three chassis and each one contains 4 modules:

- Chassis 0
    - NI9481: 4 Channel, SPST Relay Module.
    - NI9203: 8 Channel, ±20mA, 16 Bit Analog Input Module.
    - NI9201: 8 Channel, 12 Bit Analog Input Module (±10V).
    - NI9211: 4 Channel, Thermocouple Input Module.

- Chassis 1
    - NI9263: 4 Channel, ±10V, 16 Bit Analog Voltage Output Module.
    - NI9423: 8 Channel, Digital Input Module.
    - 2 x NI9206: 16 Channel Analog Input Module for Fuel Cells.
- Chassis 2
    - NI9211
    - NI9481
    - 2xNI9505

The RTOS is a computer that has the Pharlap ETS Real Time Operative System (RTOS), as well as the Lab-VIEW real-time modules. The code developed in this computer is more complex than the FPGA program and handles the control, initialization, emergency alarms and the raw data coming from the FPGA. It also stores the global variables used by the Host computer and creates the file with the data.

The Host computer is where the different LabVIEW programs are developed and also contains the Graphical User Interface. The code deployed in this computer allows the user to control and interact with the station and it is the link between the user and the RTOS. It also presents the state of the system and plots the variation and state of the different signals measured.

3.3. Experimental Test

An experimental test was done in order to know the behavior of the station and its working conditions. This consisted on running the station and study the results obtained for different flow rates and loads. The results obtained are shown in Fig. 3. 5, Fig. 3. 6, Fig. 3. 8 and Fig. 3. 7.

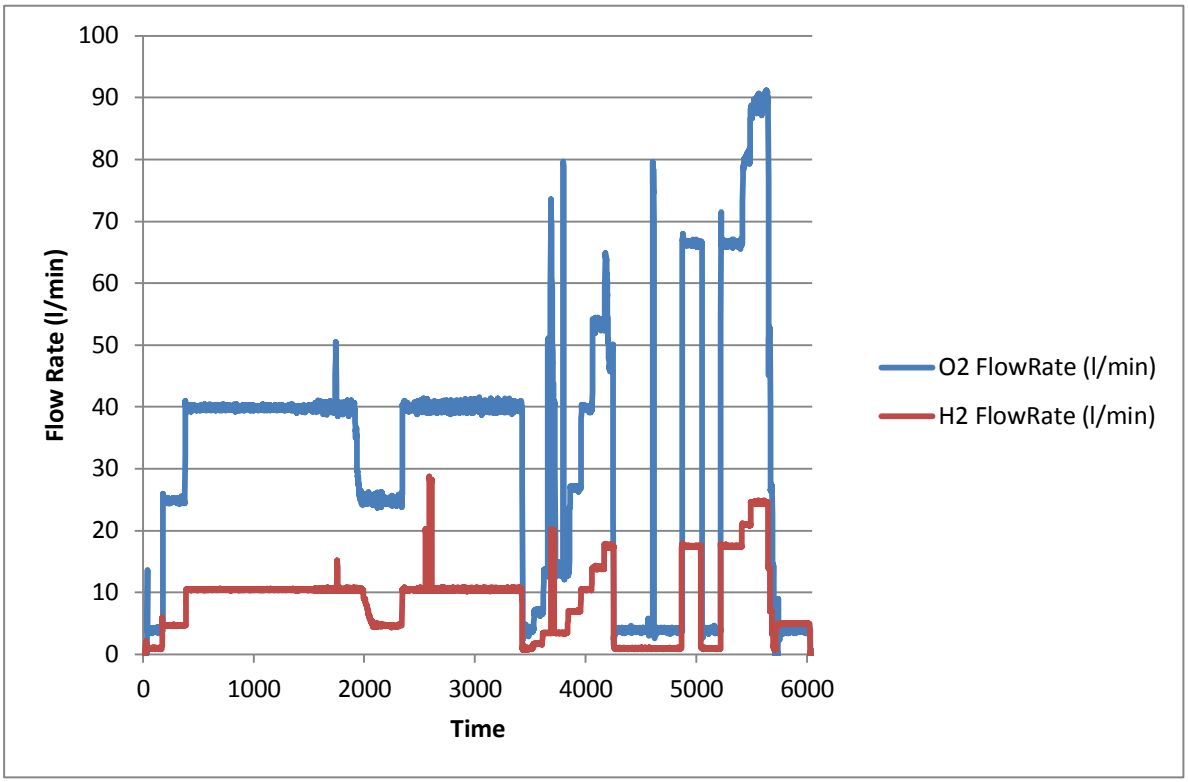

Fig. 3. 5- Flow rates of hydrogen and oxygen.

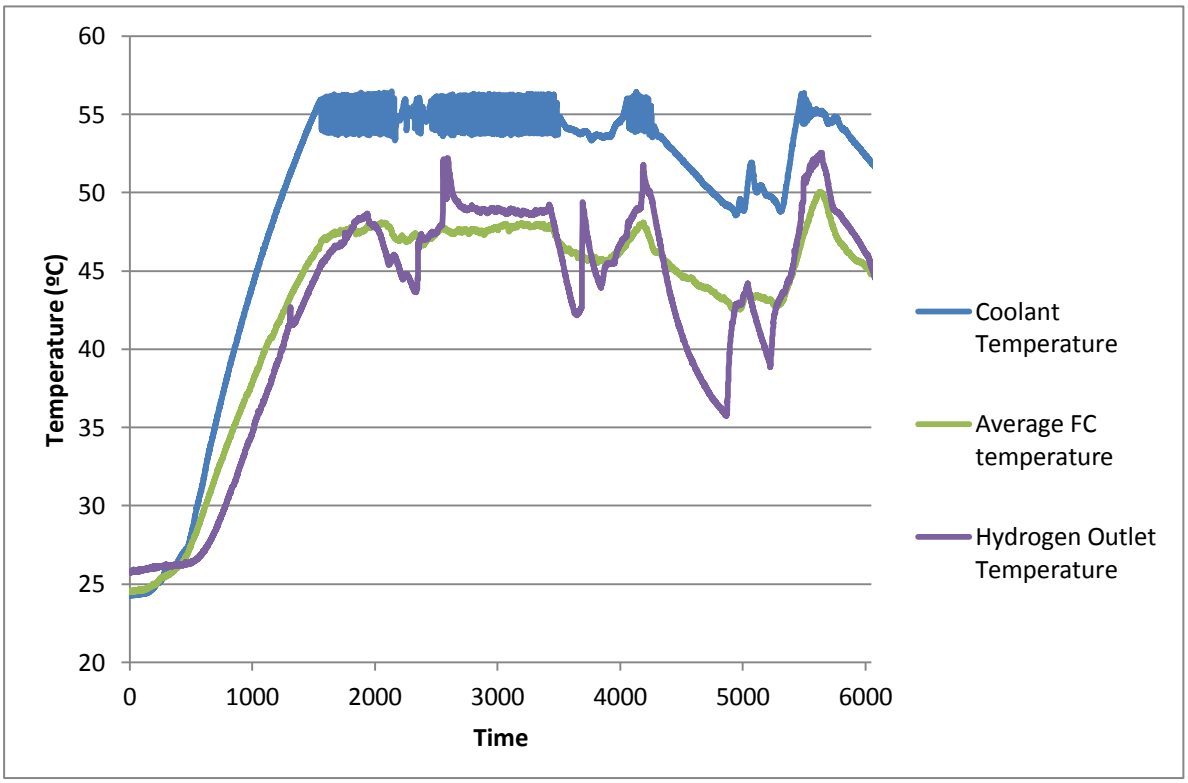

Fig. 3. 6- Temperature of the water, the fuel cell and at the outlet of hydrogen.

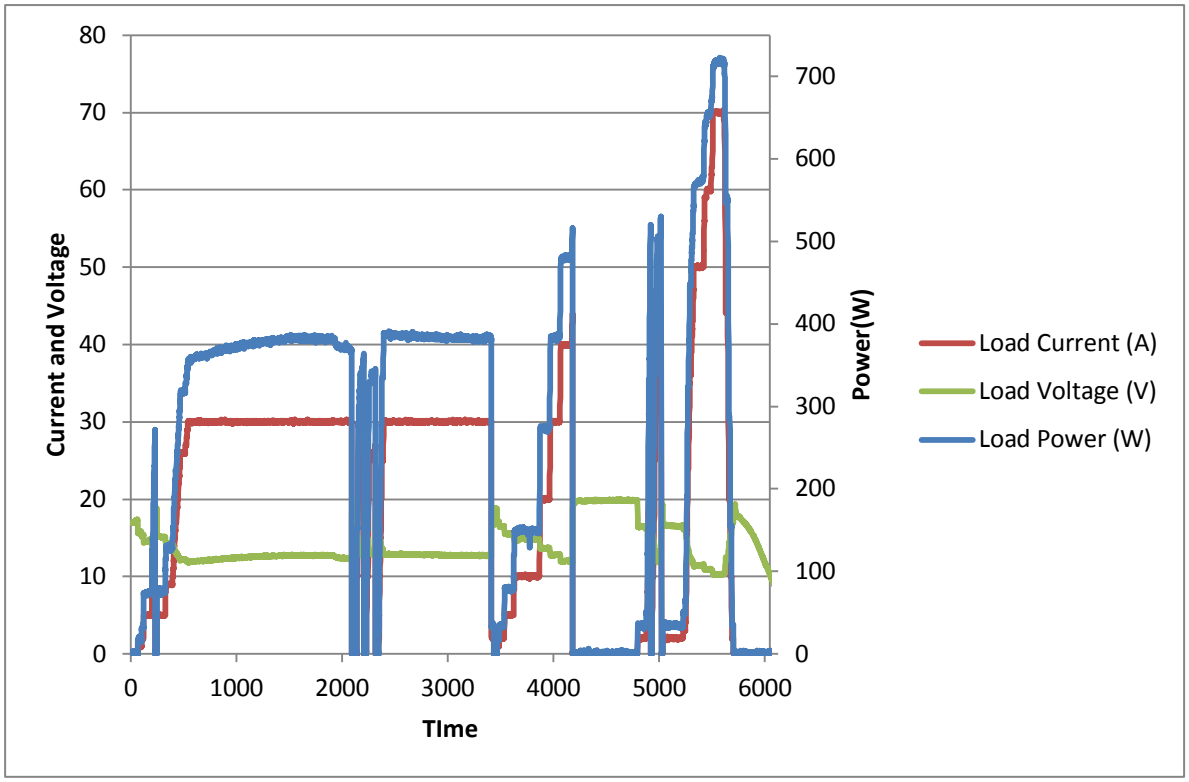

Fig. 3. 7- Voltage, current and power of the load.

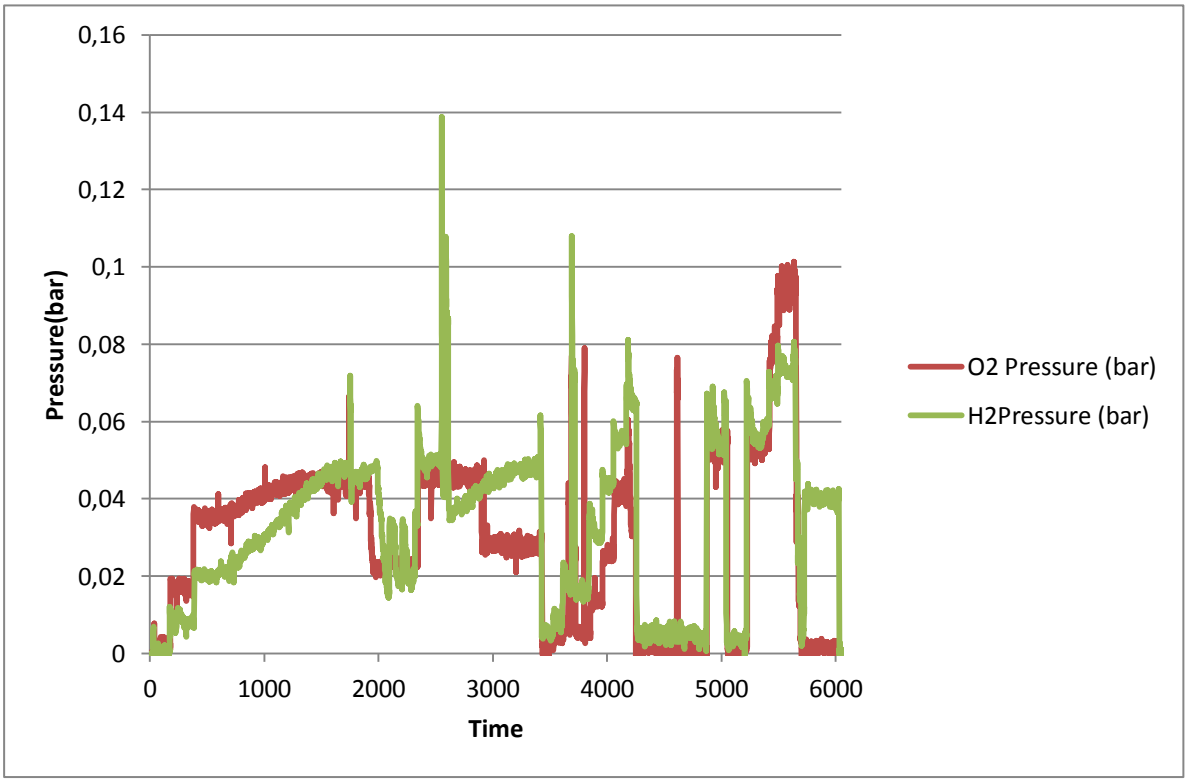

Fig. 3. 8- Pressure of anode and cathode at the inlet. The pressure at the outlet is 1 bar_{abs}.

The results obtained show that the station works with a hydrogen flow rate between 0 and 20 Nl/min and a pressure at the inlet of the anode between 1 and 1.1 bar abs. The temperature of the stack ranges from 45ºC to 50ºC, and the temperature of the hydrogen at the outlet can be considered to be 50ºC. These results can be useful to define the conditions at which the ejector will work, and therefore they will be used in Chapter 7 to design the final ejector.

It is also useful to study the efficiency and power obtained with the dead-end mode (S=1.11) and the flow-through mode for different stoichiometry Fig. 3. 9. In this figure it is clear that the flow-through mode has a strong impact over the efficiency of the fuel cell. So, recirculation is mandatory. The expected efficiency when adding recirculation is shown in Fig. 3. 10. This last picture is an approximation as it is obtained calculating the efficiency as in Fig. 3. 9, but using a value of fuel utilization equal to one.

Apart from improving operating conditions and lifetime of the fuel cell, working with the flow-through mode also induces a small improvement in the amount of power obtained (Fig. 3. 11).

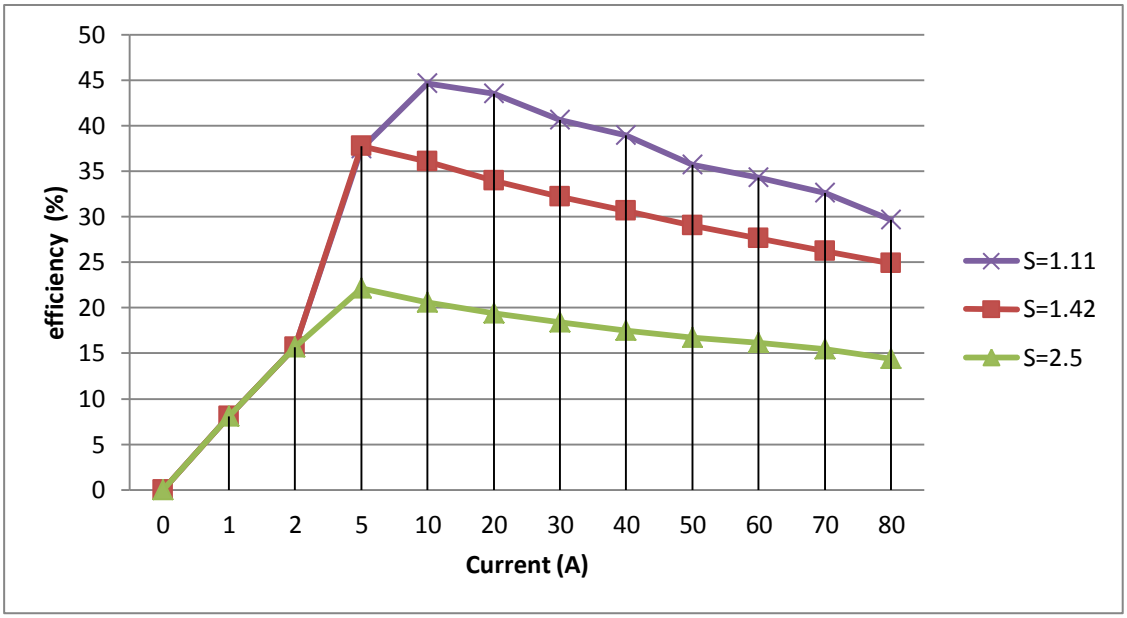

Fig. 3. 9- Efficiency vs current for different stoichiometry without recirculation.

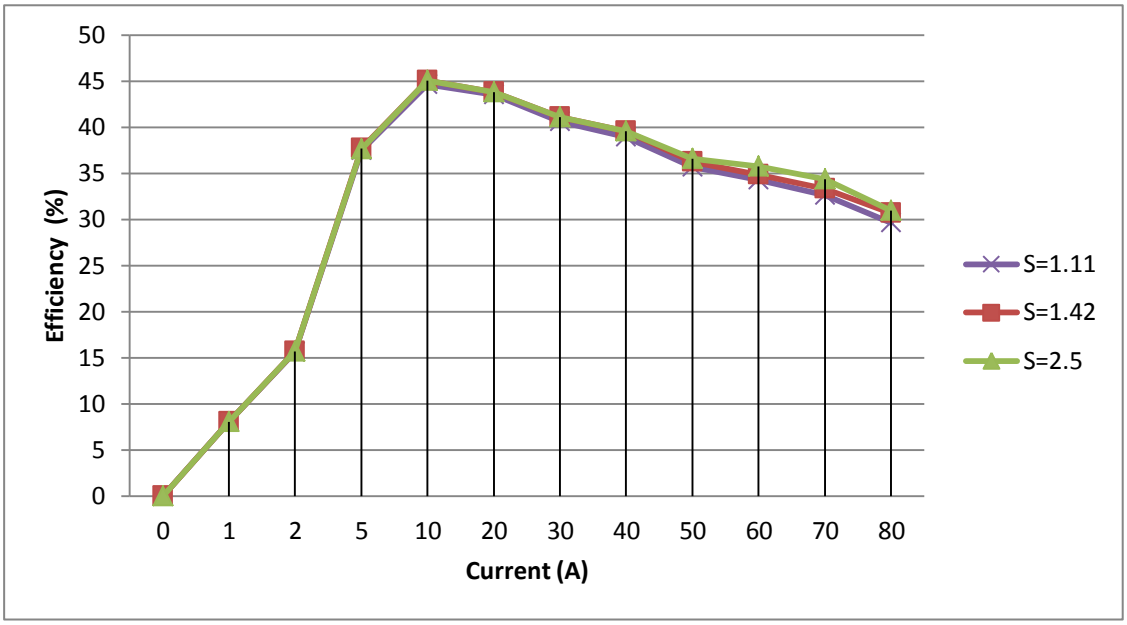

Fig. 3. 10- Expected efficiency vs current for different stoichiometry with recirculation.

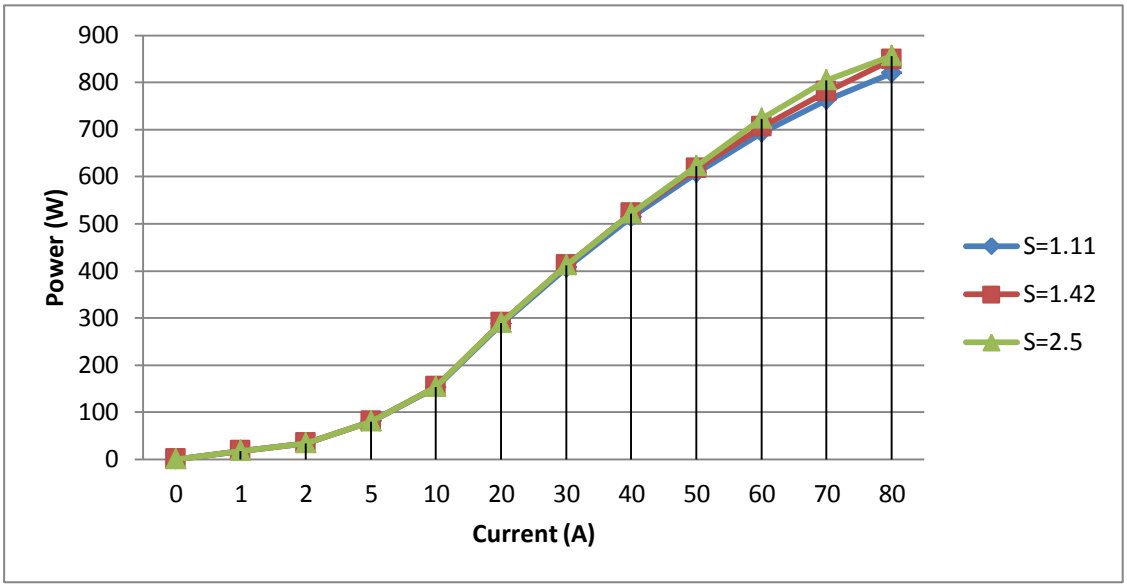

Fig. 3. 11- Power vs current for different stoichiometry without recirculation.

CHAPTER 4: COMPRESSIBLE FLOW AND EJECTORS

When a fluid moves at speeds comparable to its speed of sound, its density changes significantly and can be considered a compressible flow. Liquids do not tend to generate compressible flow since they need really high pressures to obtain sonic velocities. However, in gases, a pressure ratio of 2 can generate sonic flow.

Compressibility introduces two important effects: Choking and shock waves. Choking occurs when the mass flow through a duct is limited by the sonic condition, while shock waves are discontinuous changes in the properties of a supersonic flow.

In this chapter, the 1D theory of compressible flow is introduced and is used to explain shock waves and the behavior of subsonic and supersonic flow inside a nozzle. Then, ejectors are introduced and explained from the point of view of compressible flow.

4.1. Compressible flow

One of the most important parameters in compressible-flow analysis is Mach number, which relates the velocity "c" of the flow with the speed of sound "a" of the fluid:

$$Ma = \frac{c}{a} \qquad \textbf{Eq 4. 1}$$

Depending on the Mach number, the flow can be classified as:

- *Ma<0.3: Incompressible flow.* The density of the flow can be considered constant and temperature effects can be ignored. An incompressible flow can be solved using two equations: Continuation equation and Momentum equation.
- *Ma>0.3: Compressible flow.* The density of the flow cannot be considered constant, and the effects of temperature and pressure change must be taken into account. Energy equation and an equation of state must be added to analyze flow. Compressible flow can be classified as:
  - *Ma<1: Subsonic flow.* No shock waves appear.
  - *Ma=1: Sonic flow.*
  - *Ma>1: Supersonic flow*. Shock waves appear.

Another important parameter is the specific heat-ratio of a gas (γ), which relates the heat capacity of the gas at constant pressure to its heat capacity at constant volume:

$$\gamma = \frac{C_p}{C_v} \qquad \textbf{Eq 4. 2}$$

For air and diatomic gasses, γ=1.4.

4.1.1. Ideal gas law and perfect gases

The most common equation of state used to analyze compressible flow is the ideal gas law:

$$\frac{P}{\rho} = RT \qquad \textbf{Eq 4. 3}$$

Where R is the specific gas constant, which is related to the universal gas constant:

$$R = \frac{R_u}{\overline{M}} \qquad \textbf{Eq 4. 4}$$

$$R_u = 8314 \frac{m^2}{s^2 \cdot K} \qquad \textbf{Eq 4. 5}$$

$$R = C_p - C_v \qquad \textbf{Eq 4. 6}$$

If the heat capacities of an ideal gas at constant pressure and constant volume are constant, the gas is said to be a perfect gas. The enthalpy of a perfect gas can be expressed as:

$$h = C_p T \qquad \textbf{Eq 4. 7}$$

4.1.2. Isentropic relations for perfect gases

The analysis of compressible flows is usually made using the isentropic approximation. When a compressible flow is analyzed using the isentropic approximation and the perfect gas assumption, a really useful power-law relation is obtained:

$$\frac{P}{\rho^k} = constant \rightarrow \frac{P_b}{P_a} = \left(\frac{T_b}{T_a}\right)^{\frac{\gamma}{\gamma-1}} = \left(\frac{\rho_b}{\rho_a}\right)^{\gamma} \qquad \textbf{Eq 4. 8}$$

4.1.3. Speed of Sound

The speed of sound is a thermodynamic property of a fluid, and it is the rate of propagation of a pressure pulse of infinitesimal strength through a still fluid. The speed of sound of a fluid can be expressed as:

$$a^2 = \left.\frac{\partial p}{\partial \rho}\right|_S \qquad \textbf{Eq 4. 9}$$

To evaluate this derivative, the thermodynamic process related to the wave must be known. Assuming an adiabatic process:

$$a = \sqrt{\frac{\partial p}{\partial \rho}} = \sqrt{\gamma \left.\frac{\partial p}{\partial \rho}\right|_T} \qquad \textbf{Eq 4. 10}$$

This equation is correct for any fluid (White 1999). Using the ideal gas law:

$$a = \sqrt{\gamma \left.\frac{\partial p}{\partial \rho}\right|_T} = \sqrt{\gamma R T} \qquad \textbf{Eq 4. 11}$$

4.1.4. Stagnation properties

When a compressible fluid is flowing at high speed, its potential energy can be neglected if compared with its kinetic energy and enthalpy terms. Outside the boundary layer, the viscous-work and heat-transfer terms are 0. Thus, the total energy of the flow can be expressed as the sum of its enthalpy and kinetic energy, and it will be constant if no friction or heat transfer is considered:

$$h_a + \frac{1}{2} c_a^2 = constant \qquad \textbf{Eq 4. 12}$$

The constant value in *Eq 4. 12* is called the stagnation enthalpy (or total enthalpy) of the flow, and it is the maximum enthalpy achieved by the fluid if brought to rest isentropically:

$$h_0 = h + \frac{1}{2}c^2 = constant \qquad \textbf{Eq 4. 13}$$

The stagnation, or total, properties of the flow are important properties used to define the energy of the flow. The stagnation temperature, or total temperature, of a perfect gas can be obtained as:

$$\frac{T_0}{T} = 1 + \frac{c^2}{2c_pT} \qquad \textbf{Eq 4. 14}$$

The stagnation values of the speed of sound, pressure and density of the flow can be obtained from the stagnation temperature:

$$a_0 = \sqrt{\gamma R T_0} \qquad \textbf{Eq 4. 15}$$

$$\frac{P_0}{P} = \left(\frac{T_0}{T}\right)^{\frac{\gamma}{\gamma-1}} \qquad \textbf{Eq 4. 16}$$

$$\frac{\rho_0}{\rho} = \left(\frac{T_0}{T}\right)^{\frac{1}{\gamma-1}} \qquad \textbf{Eq 4. 17}$$

The total properties of the flow can also be expressed related to the Mach number. From *Eq 4. 2* and *Eq 4. 6*:

$$C_p = \frac{\gamma R}{\gamma - 1} \qquad \textbf{Eq 4. 18}$$

So:

$$\frac{T_0}{T} = 1 + \frac{c^2}{2c_pT} = 1 + \frac{(\gamma-1)c^2}{2a^2} = 1 + \frac{\gamma-1}{2}Ma^2 \qquad \textbf{Eq 4. 19}$$

$$\frac{P_0}{P} = \left(\frac{T_0}{T}\right)^{\frac{\gamma}{\gamma-1}} = \left(1 + \frac{\gamma-1}{2}Ma^2\right)^{\frac{\gamma}{\gamma-1}} \qquad \textbf{Eq 4. 20}$$

$$\frac{\rho_0}{\rho} = \left(\frac{T_0}{T}\right)^{\frac{1}{\gamma-1}} = \left(1 + \frac{\gamma-1}{2}Ma^2\right)^{\frac{1}{\gamma-1}} \qquad \textbf{Eq 4. 21}$$

$$\frac{a_0}{a} = \sqrt{\frac{T_0}{T}} = \sqrt{1 + \frac{\gamma-1}{2}Ma^2} \qquad \textbf{Eq 4. 22}$$

T_0, h_0 and a_0 are constant when the flow is adiabatic, even if the flow is non-isentropic. However, the relations to obtain P_0 and ρ_0 are obtained using isentropic assumptions, so P_0 and ρ_0 are not constant when the entropy changes due to friction or shock waves.

4.1.5. Sonic properties

The sonic, or critical, properties of the flow are the properties of the flow when it is sonic (Ma=1). The sonic properties of the flow can be related to its stagnation properties. From Eq. 4.19 to 4.22:

$$\frac{T_0}{T^*} = 1 + \frac{\gamma - 1}{2} \quad \textbf{Eq 4. 23}$$

$$\frac{P_0}{P^*} = \left(1 + \frac{\gamma - 1}{2}\right)^{\frac{\gamma}{\gamma - 1}} \quad \textbf{Eq 4. 24}$$

$$\frac{\rho_0}{\rho^*} = \left(1 + \frac{\gamma - 1}{2}\right)^{\frac{1}{\gamma - 1}} \quad \textbf{Eq 4. 25}$$

$$\frac{a_0}{a^*} = \sqrt{1 + \frac{\gamma - 1}{2}} \quad \textbf{Eq 4. 26}$$

Other interesting relations can be obtained from the latter equations:

$$\frac{T^*}{T} = \frac{T^*}{T_0}\frac{T_0}{T} = Ma^2 \quad \textbf{Eq 4. 27}$$

$$\frac{P^*}{P} = \frac{P^*}{P_0}\frac{P_0}{P} = \left(\frac{1 + \frac{\gamma - 1}{2}Ma^2}{1 + \frac{\gamma - 1}{2}}\right)^{\frac{\gamma}{\gamma - 1}} \quad \textbf{Eq 4. 28}$$

$$\frac{\rho^*}{\rho} = \frac{\rho^*}{\rho_0}\frac{\rho_0}{\rho} = \left(\frac{1 + \frac{\gamma - 1}{2}Ma^2}{1 + \frac{\gamma - 1}{2}}\right)^{\frac{1}{\gamma - 1}} \quad \textbf{Eq 4. 29}$$

$$\frac{c^*}{c} = \frac{a^*}{c} = \frac{\sqrt{kRT^*}}{c} = \frac{1}{Ma}\sqrt{\left(\frac{2}{\gamma + 1}\right)\left(1 + \frac{\gamma - 1}{2}Ma^2\right)} \quad \textbf{Eq 4. 30}$$

4.1.6. Velocity changes due to area changes

The equation of continuity and its differential form for a steady 1D flow are:

$$\dot{m} = \rho c A = constant \quad \textbf{Eq 4. 31}$$

$$\frac{d\rho}{\rho} + \frac{dc}{c} + \frac{dA}{A} = 0 \quad \textbf{Eq 4. 32}$$

The momentum equation for a flow without friction can be expressed as:

$$\frac{dP}{d\rho} + cdc = 0 \quad \textbf{Eq 4. 33}$$

Using *Eq 4. 9*, *Eq 4. 28* and *Eq 4. 29*, the next relation between velocity change and area change can be obtained:

$$\frac{dc}{c} = \left(\frac{1}{Ma^2 - 1}\right)\frac{dA}{A} = -\frac{dP}{\rho c^2} \qquad \textbf{Eq 4. 34}$$

The latter relation is very important and its analysis provides a lot of information about the behavior of compressible flow when area changes. This behavior depends on whether flow is subsonic, supersonic or sonic:

- *Subsonic Flow: Ma<1.* In this case $Ma^2 - 1 < 1$, so dP and dA must have the same sign, and dc will have different sign (c, ρ and A are positive quantities). Thus, when the area of the duct is increased, the pressure also increases and the velocity of the flow decreases. However, when the area is decreased, P is decreased and the velocity increases. The behavior of a subsonic flow is the same behavior that can be seen in an incompressible flow.
- *Supersonic flow: Ma>1.* In this case, $Ma^2 - 1 > 1$, so the behaviour of the flow will be the opposite. dP and dA must have different sign, and dc will have the same sign as dA. Thus, in a supersonic flow, when area increases the pressure decreases and the velocity increases, and when area decreases, pressure increases and the velocity decreases.
- *Sonic flow: Ma=1.* In a sonic flow, $Ma^2 - 1 = 0$. In this case, if $dA \neq 0$, then $dc = \infty$. Since an infinite acceleration is physically impossible, dA must be 0 to ensure a finite acceleration, so A is a maximum (bulge) or a minimum (throat). However, the transition from subsonic flow to supersonic flow cannot take place in a bulge section, as can be deduced from Eq. 4.30 and can be seen in Fig. 4. 1. In a bulge section, the Mach number tends to move away from the sonic condition. Thus, the only way a subsonic flow can be accelerated to a supersonic flow by means of a change of area is by flowing through a throat section.

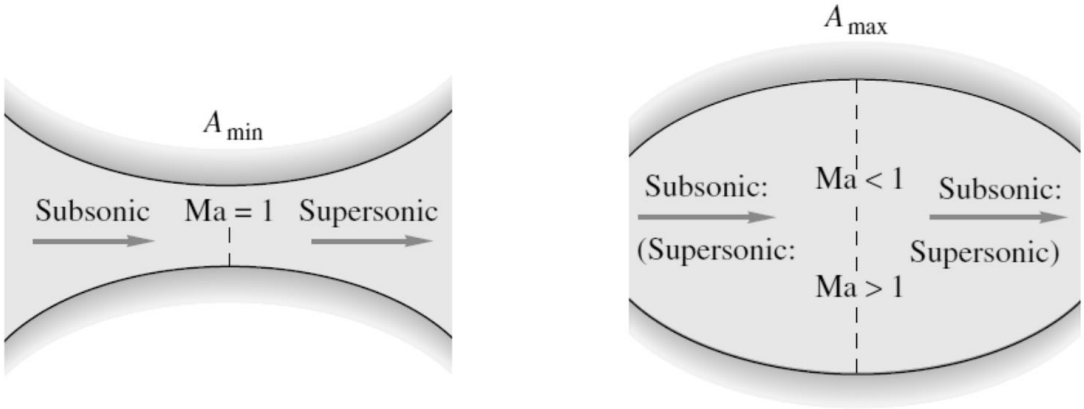

Fig. 4. 1- Flow through a throat section and a bulge section. (White 1999)

In order to give a further explanation of this last point, *Eq 4. 31* will be converted to an algebraic expression involving only area and Mach number. *Eq 4. 31* can be expressed as:

$$\frac{A}{A^*} = \frac{\rho^*}{\rho}\frac{c^*}{c} \qquad \textbf{Eq 4. 35}$$

Combining *Eq 4. 29*, *Eq 4. 30* and *Eq 4. 35*:

$$\frac{A}{A^*} = \frac{1}{Ma}\left(\frac{1+\frac{\gamma-1}{2}Ma^2}{1+\frac{\gamma-1}{2}}\right)^{\frac{1}{2}\left(\frac{\gamma+1}{\gamma-1}\right)} \qquad \textbf{Eq 4. 36}$$

In this last relation, the sonic condition can only be achieved when A=A*, and A* is the minimum area that can be obtained. *Eq 4. 36* is plotted, assuming air (γ=1.4), in *Fig. 4. 2*. A more general way to express *Eq 4. 36* would be:

$$\frac{A_1}{A_2} = \frac{Ma_2}{Ma_1}\left(\frac{1+\frac{\gamma-1}{2}Ma_1^2}{1+\frac{\gamma-1}{2}Ma_2^2}\right)^{\frac{1}{2}\left(\frac{\gamma+1}{\gamma-1}\right)} \qquad \textbf{Eq 4. 37}$$

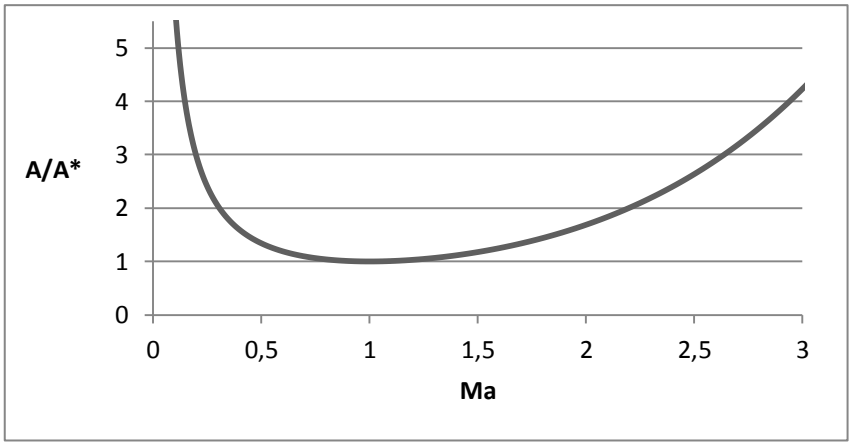

Fig. 4. 2- Area ratio versus Mach number for air.

4.1.7. Choking phenomena

From *Eq 4. 35*, it can be deduced that the ratio A/A* equals the ratio of sonic mass flow per unit area divided by the mass flow per unit area. This ratio will have a minimum (*Fig. 4. 2*) for Ma=1. Thus, the mass flow through a duct will reach its maximum, for a certain stagnation conditions, when its throat is under sonic conditions. When the throat of a duct reaches sonic condition, the throat is said to be choked and the mass flow through the duct cannot be increased without changing the stagnation properties of the flow.

The maximum, or choked, mass flow can be calculated using *Eq 4. 24*, *Eq 4. 25* and *Eq 4. 26*:

$$\dot{m}_{max} = \dot{m}^* = \rho^* \cdot c^* \cdot A^* = \frac{A^* \cdot P_0}{\sqrt{T_0}} \cdot \sqrt{\frac{\gamma}{R} \cdot \left(\frac{2}{\gamma+1}\right)^{\frac{\gamma+1}{\gamma-1}}} \qquad \textbf{Eq 4. 38}$$

Eq 4. 38 gives the maximum mass flow which occurs at the choking condition for a given value of stagnation pressure and temperature. It can be modified to obtain the mass flow at any section where local area and pressure are known (White 1999):

$$\Psi = \frac{\dot{m}\sqrt{RT_0}}{AP_0} \qquad \textbf{Eq 4. 39}$$

Where Ψ is the mass flow function:

$$\Psi = \sqrt{\frac{2\gamma}{\gamma-1}\left(\frac{P}{P_0}\right)^{\frac{2}{\gamma}}\left[1-\left(\frac{P}{P_0}\right)^{\frac{\gamma-1}{\gamma}}\right]} \qquad \textbf{Eq 4. 40}$$

4.1.8. Normal shock waves

A shock wave takes place when a wave moves faster than the speed of sound of the fluid, and thus it can only appear when the upstream flow is supersonic. A shock wave is followed by an abrupt change in the thermodynamic properties of the flow. Shock waves are very common in supersonic and external flows.

A normal shock wave takes place in a plane normal to the direction of the flow, and is an irreversible process that produces an almost discontinuous change in flow properties.

The shock wave in Fig. 4. 3 is a strong fixed pressure wave. This wave is very thin, so it can be assumed that A_1=A_2. Applying continuity, momentum and energy equations:

$$\rho_1 c_1 A_1 = \rho_2 c_2 A_2 \rightarrow \rho_1 c_1 = \rho_2 c_2 \qquad \textbf{Eq 4. 41}$$

$$P_1 - P_2 = \rho_2 c_2^2 - \rho_1 c_1^2 = P_2 \gamma M a_2^2 - P_1 \gamma M a_1^2 \qquad \textbf{Eq 4. 42}$$

$$h_{01} = h_1 + \frac{1}{2} {c_1}^2 = h_2 + \frac{1}{2} c_2^2 = h_{02} \qquad \textbf{Eq 4. 43}$$

These latter equations can be combined to obtain the Rankine-Hugoniot relation:

$$h_2 - h_1 = \frac{1}{2}(P_2 - P_1)\left(\frac{1}{\rho_2} - \frac{1}{\rho_1}\right) \qquad \textbf{Eq 4. 44}$$

Introducing the next perfect gas relation:

$$h = C_p T = \frac{\gamma P}{\rho(\gamma - 1)} \qquad \textbf{Eq 4. 45}$$

$$\frac{\rho_2}{\rho_1} = \frac{1 + \frac{P_2}{P_1}\left(\frac{\gamma+1}{\gamma-1}\right)}{\frac{\gamma+1}{\gamma-1} + \frac{P_2}{P_1}} \qquad \textbf{Eq 4. 46}$$

The system composed by *Eq 4. 41*, *Eq 4. 42* and *Eq 4. 43* has two possible solutions due to the square of velocity: $\frac{P_2}{P_1} < 1$ and $\frac{P_2}{P_1} > 1$. The correct solution is

obtained from the second law of thermodynamics, as $s_2 \geq s_1$. The change in entropy can be computed from the next perfect gas relation:

$$\frac{s_2 - s_1}{C_v} = \ln\left(\frac{P_2}{P_1}\left(\frac{\rho_1}{\rho_2}\right)^{\gamma}\right) \qquad \textbf{Eq 4. 47}$$

If $\frac{P_2}{P_1} < 1$, then $\frac{\rho_1}{\rho_2} < 1$ and $s_2 < s_1$, which violates the second law. So, a normal shock wave can only appear when the pressure increases across the shock. Thus, normal shock waves produce an expansion and decrease Mach number.

Adding the ideal gas law to the equation of continuity, and taking into account that the stagnation temperature does not change, the next relation is obtained:

$$Ma_2^2 = \frac{(\gamma-1)Ma_1^2 + 2}{2\gamma Ma_1^2 - (\gamma-1)} \qquad \textbf{Eq 4. 48}$$

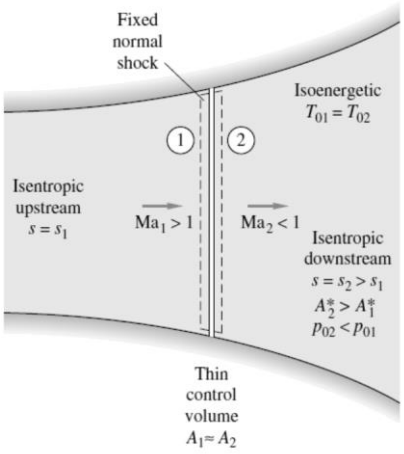

Fig. 4. 3- A fixed normal shock wave. (White 1999)

As the flow upstream is supersonic (Ma_1>1), Ma_2 must be subsonic to satisfy *Eq 4. 48*. Thus, normal shock waves decelerate a flow from supersonic to subsonic conditions.

Additional relations can be obtained through a further manipulation of *Eq 4. 41*, *Eq 4. 42* and *Eq 4. 43* (White 1999):

$$\frac{\rho_2}{\rho_1} = \frac{(\gamma+1)Ma_1^2}{(\gamma-1)Ma_1^2 + 2} = \frac{c_1}{c_2} \qquad \textbf{Eq 4. 49}$$

$$\frac{T_2}{T_1} = [(\gamma-1)Ma_1^2 + 2]\frac{2\gamma Ma_1^2 - (\gamma-1)}{(\gamma-1)^2 Ma_1^2} \qquad \textbf{Eq 4. 50}$$

4.1.9. Oblique shock waves

Shock waves are not always normal to the direction of the flow. They can also appear at an oblique angle to the oncoming stream, deflecting it through an angle θ. An example of that would be a supersonic flow over a concave corner, as seen in Fig. 4. 5. At point A, the surface is deflected upwards and so are the flow streamlines. This change in flow direction takes places across a shock wave which is oblique to the free-stream direction. The flow streamlines experience a deflection angle θ at the shock, and the pressure temperature and density increase, while Mach number decreases.

Fig. 4. 4 shows an oblique shock. The shock angle is β, and the flow obtained downstream is a function of β and the upstream flow conditions.

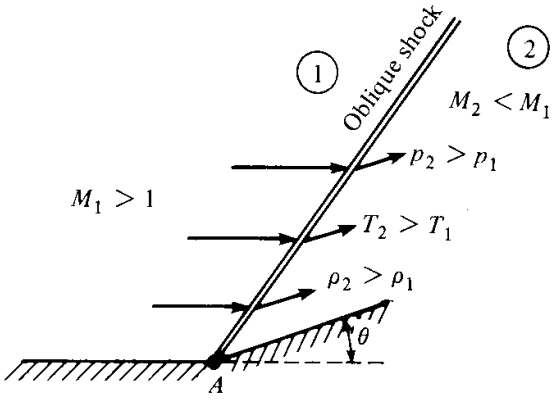

Fig. 4. 5- Supersonic flow over a concave corner. (Anderson 2004)

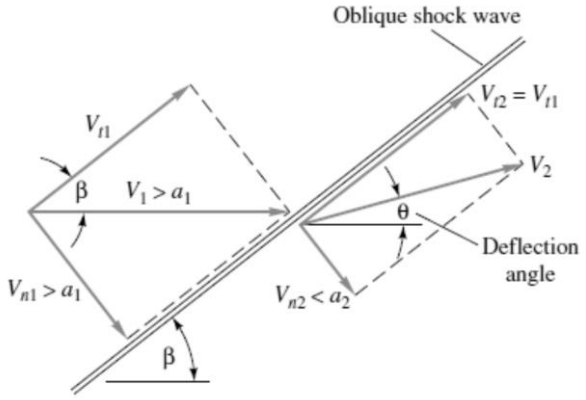

Fig. 4. 4- Oblique Shock analysis. (White 1999)

Continuity, momentum and energy equations can be expressed in terms of tangential and normal velocities:

$$\gamma_1 c_{n1} = \gamma_2 c_{n2} \qquad \textbf{Eq 4. 51}$$

$$P_1 - P_2 = \rho_2 c_{n2}^2 - \rho_1 c_{n1}^2 \qquad \textbf{Eq 4. 52}$$

$$0 = \rho_1 c_{n1}(c_{t2} - c_{t1}) \rightarrow c_{t2} = c_{t1} \qquad \textbf{Eq 4. 53}$$

$$h_1 + \frac{1}{2}c_{n1}^2 = h_2 + \frac{1}{2}c_{n2}^2 \qquad \textbf{Eq 4. 54}$$

These latter equations are the same as those obtained for normal shocks, but replacing velocity with its normal component. Thus, oblique shocks can be analyzed using normal shocks equations with the normal component of velocity and Mach number:

$$Ma_{n1} = Ma_1 \cdot \sin(\beta) \qquad \textbf{Eq 4. 55}$$

$$Ma_{n2} = Ma_2 \cdot \sin(\beta - \theta) \qquad \textbf{Eq 4. 56}$$

$$Ma_{n2}^2 = \frac{(\gamma - 1)Ma_{n1}^2 + 2}{2\gamma Ma_{n1}^2 - (\gamma - 1)} \qquad \textbf{Eq 4. 57}$$

$$\frac{\tan(\beta)}{\tan(\beta - \theta)} = \frac{c_{n1}}{c_{n2}} = \frac{\rho_2}{\rho_1} = \frac{(\gamma + 1)Ma_1^2}{(\gamma - 1)Ma_1^2 + 2} \qquad \textbf{Eq 4. 58}$$

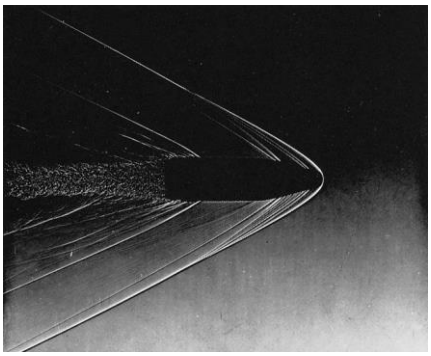

Fig. 4. 6- Supersonic wave pattern emanating from a projectile moving at Ma=2. Heavy lines are oblique-shock waves and light lines are Mach waves. (White 1999)

In an oblique shock wave, the normal component of Mach number downstream must be subsonic, but, as the tangential component does not change, the total Mach number downstream can be either subsonic, sonic or supersonic. From *Eq 4. 58*:

$$\tan(\theta) = \frac{2\cot(\beta)(Ma_1^2 \sin^2(\beta) - 1)}{Ma_1^2[\gamma + \cos(2\beta)] + 2} \qquad \textbf{Eq 4. 59}$$

This equation is plotted in Fig. 4. 7 for different values of Mach number. For every value of $Ma_1>1$ the value of θ ranges between 0 and θ_{max}, while β ranges between β_{min} and 90º. Linear oblique shocks with other values of θ or β cannot exist. If the geometry of the body imposes a different value of these angles, then a detached curve shock wave forms in front of the body (Fig. 4. 8). Detached shock waves are complex to analyze, and experimentations and computational methods are usually needed. Fig. 4. 7 also shows that there are two possible solutions for deflections $\theta<\theta_{max}$: a weak shock (small β) and a strong shock (large β). For strong shocks, flow downstream is always subsonic, while, for weak shocks, flow downstream can be either supersonic or subsonic.

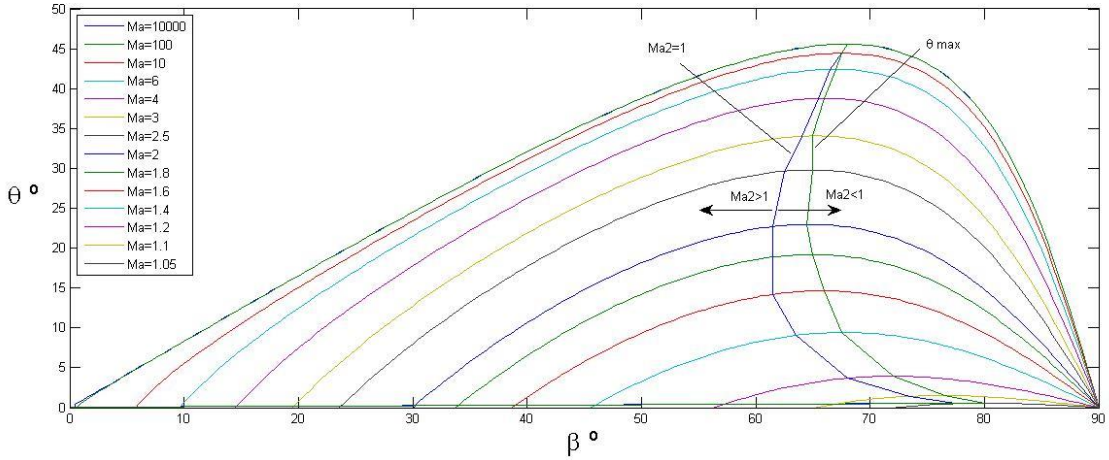

Fig. 4. 7- Oblique-shock deflection versus wave angle for different Mach numbers.

For every value of Ma_1 there are two values of β for which the flow does not change its direction: β=90º, which corresponds with a normal shock wave, and $\beta= \beta_{min}$ (θ=0). The latter value of β corresponds to the weakest oblique shock wave that can appear for a given value of Ma_1, which is called Mach wave. Mach

waves can be considered isentropic as the effects of the shock are really weak. The shock angle for a Mach wave can be obtained from Eq 4. 59:

$$\beta_{\text{Mach}} = \sin^{-1}\frac{1}{Ma_1} \qquad \textbf{Eq 4. 60}$$

When an oblique shock wave approximates a solid wall, the deflection angle due to the oblique shock wave must be compensated in order to obtain a flux parallel to the wall. Thus, the shock wave must be reflected downstream as shown in Fig. 4. 9. This reflected shock is weaker, as $Ma_1 > Ma_2$, and its shock angle is different than β_1.

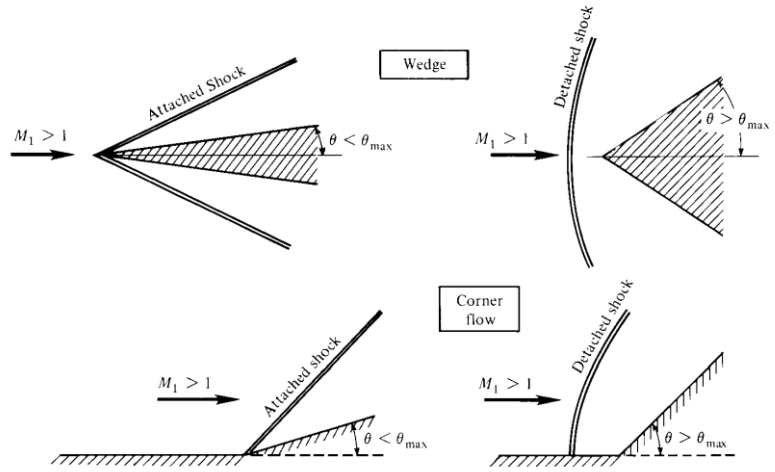

Fig. 4. 8- Attached and detached shocks. (White 1999)

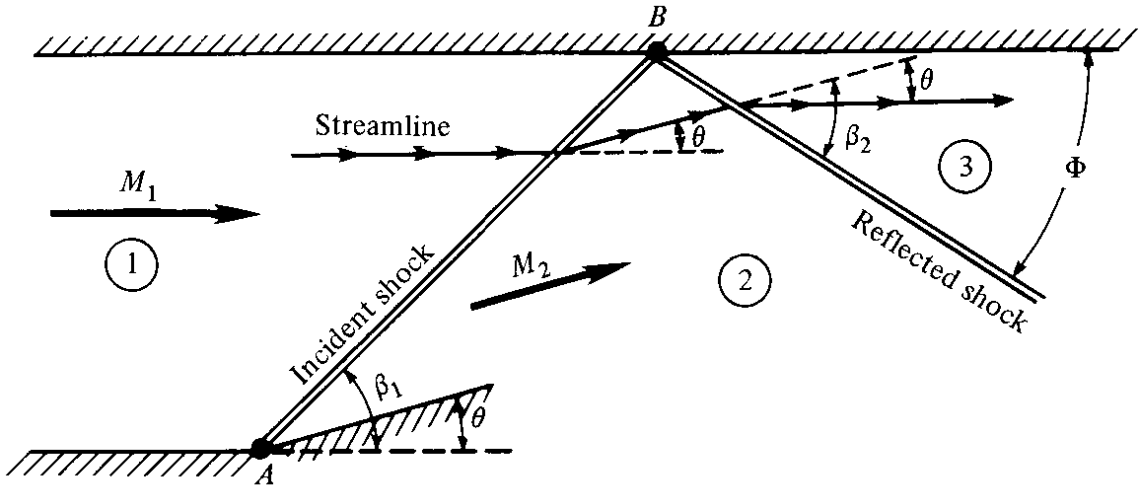

Fig. 4. 9- Shock reflection from a solid boundary. (Anderson 2004)

4.1.10. Expansion waves

Oblique shock waves appear when supersonic flow is "turned into itself", thus they are compression waves. When supersonic flow is "turned away from itself", it expands through an expansion wave (Anderson 2004). An example of an expansion wave can be seen in Fig. 4. 10, where the surface is deflected downward through an angle θ, changing the direction of the flow across an

expansion wave centered at point A. Property changes of the flow are smooth and continuous, and local flow deflections are infinitesimal. Thus, the flow is nearly incompressible and the expansion wave is composed by a fan of centered Mach waves emanating from point A. Across the expansion wave, the Mach number increases, the pressure, temperature and density decrease and the flow streamlines are curved until they are parallel to the wall behind A.

Expansion waves can be handled using the Prandtl-Meyer expansion wave theory (Anderson 2004).

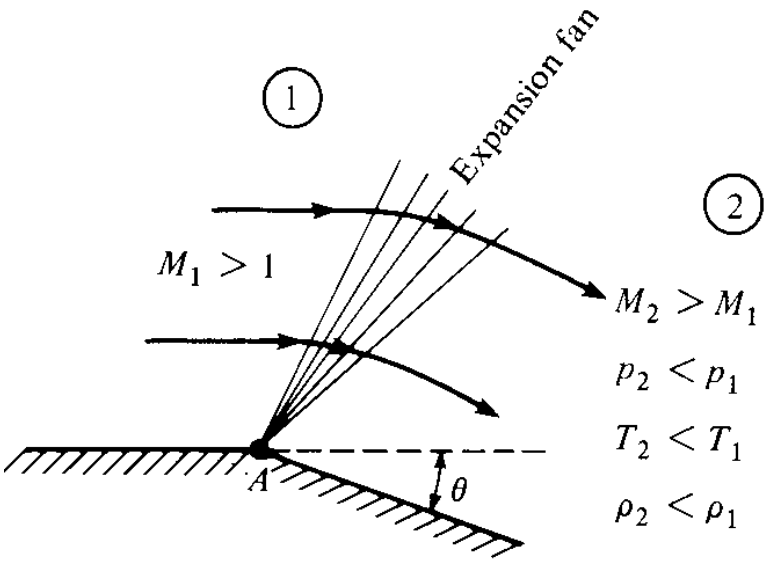

Fig. 4. 10- Supersonic flow over a convex corner. (Anderson 2004)

4.1.11. Nozzles

The converging nozzle in Fig. 4. 11 is considered. Pressure upstream is constant and in stagnation conditions (P_0 and T_0). A flow through the nozzle is induced by lowering the downstream back pressure P_b below to P_0, resulting in the sequence of states A to E. If $P_b=P_0$, then the pressure is constant throughout the nozzle and the mass flow is zero.

For curves A and B, P_b is not low enough to induce sonic flow at the throat. The flow is subsonic throughout the nozzle, so the throat will not be choked and the mass flow will be lower than the maximum mass flow predicted by *Eq 4. 38*.

When the back pressure is reduced to its critical value (curve C), the fluid exits the throat at the speed of sound (M=1). The flow is choked at the throat of the nozzle and the mass flow reaches its maximum value (*Eq 4. 38*).

If the back pressure is reduced further (Curves D and E), it does not result in changes of the pressure, velocity and temperature along the nozzle. Since the throat is choked, the information of the flow conditions downstream the nozzle cannot reach the points upstream the throat of the nozzle. The flow outside the nozzle expands supersonically from P* to P_b. This expansion takes places through a complex succession of expansion waves and oblique shock waves.

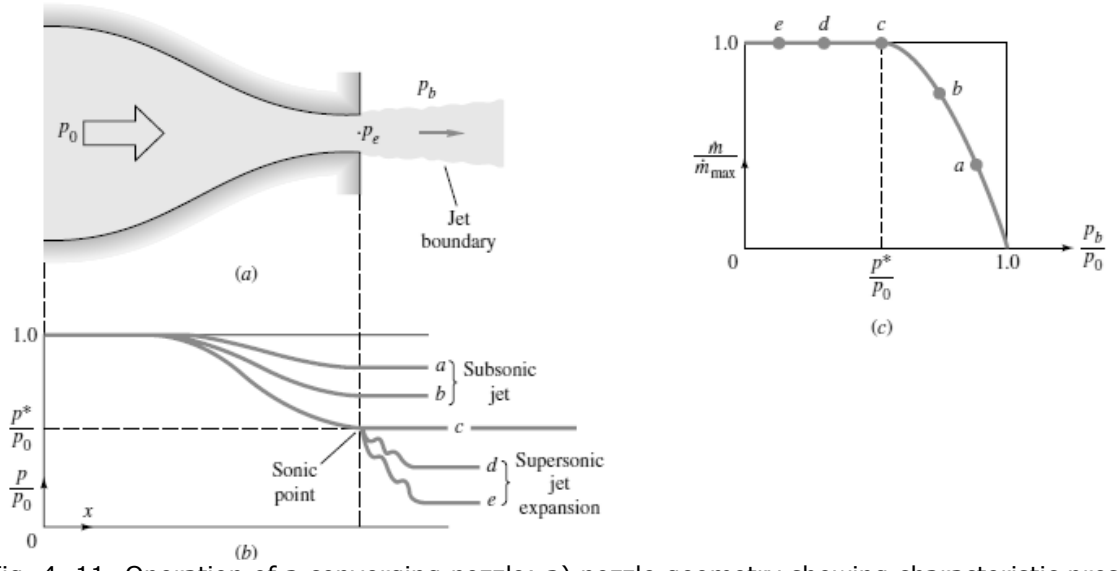

Fig. 4. 11- Operation of a converging nozzle: a) nozzle geometry showing characteristic pressures; b) Pressure distribution caused by various back pressures; c) Mass flow versus back pressure. (White 1999)

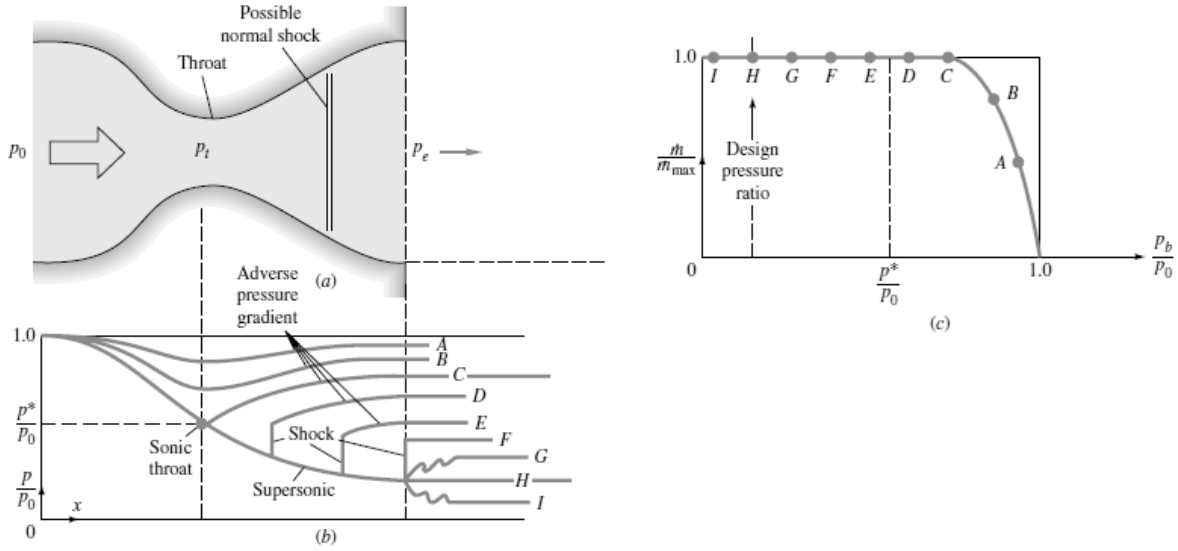

Fig. 4. 12- Operation of a converging diverging Nozzle, (3); a) Converging-Diverging Nozzle; b) Pressure distribution caused by various back pressures; c)mass flow versus back pressure. (White 1999)

If a diverging section is added to the nozzle, then the nozzle is a converging-diverging nozzle. The converging-diverging nozzle in Fig. 4. 12 is now analyzed. Pressure upstream is assumed to be constant and in stagnation conditions (P_0 and T_0). A flow through the nozzle is induced by lowering the downstream back pressure P_b below to P_0, resulting in the sequence of states A to I.

For curves A and B, P_b is not low enough to induce sonic flow at the throat. The flow is subsonic throughout the nozzle and the mass flow can be calculated using the mass-flow function (*Eq 4. 39*).

As P_b is reduced further, the mass flow will be increased until the throat becomes sonic (curve C). Then, critical conditions are reached at the throat. The flow is

said to be choked and the mass flow rate reaches its maximum possible value for given nozzle and stagnation conditions. This maximum mass flow rate can be calculated using *Eq 4. 38*.

Thus, the maximum flow through a nozzle only depends on the ratio $P_0/\sqrt{T_0}$. When the flow is choked, the throat cannot receive information about downstream conditions, so the pressure, temperature and velocity conditions along the converging section are the same in curves C, D, E, F, G, H and I.

For M=1 at the throat, the diverging section accelerates the flow to supersonic speed as the pressure is decreased from P* to P_b. For curve H, the nozzle is operating at the design conditions, and the flow is isentropic through the nozzle.

For curves D to F, the throat remains choked at sonic value and back pressure is reached by placing a normal shock wave at the right place in the diverging section to increase the pressure of the flow to P_b. As the backpressure is decreased, the normal shock wave moves from the throat to the outlet of the nozzle. For curve F, the normal shock is placed in the nozzle exit. If P_b is decreased further, then there is no normal shock wave and the flow is compressed to the back pressure through a succession of oblique-shock waves (curve G). Curve H will be obtained when P_b is the design pressure. In this case, the flow can be considered isentropic inside the nozzle, and there are no shock waves. If P_b is lower than the design pressure, then curve I is obtained and the flow must expand outside the nozzle through a complex succession of expansion and oblique shock waves.

4.2. Ejectors

Ejectors are devices used to induce a secondary fluid by momentum and energy transfer from a high velocity primary jet (Liao and Best 2010). They are used for a wide range of applications, especially in industrial refrigeration, vacuum generation and recirculation of gases. Ejectors can be used either for compressible or incompressible flows (in this case they are usually called jet pumps). However, this work is focused on the use of ejectors to recirculate gases, so their incompressible flow applications are not going to be treated here.

The geometry of ejectors is composed by 4 main sections (Fig. 4. 13 and Fig. 4. 14): primary nozzle, suction chamber, mixing chamber and diffuser. The primary nozzle can either be a convergent nozzle or a convergent-divergent nozzle. The primary or motive stream, which is a high-pressure flow, enters to the nozzle and accelerates to subsonic speed (subcritical mode) or to sonic speed (critical mode). If the nozzle is a convergent nozzle and the primary pressure is high enough, the flow reaches the sonic condition at the throat and expands outside the nozzle until its pressure reaches the pressure of the secondary stream. If the nozzle is convergent-divergent, its throat will be choked and the flow will reach supersonic condition in its diverging section. If the pressure is not high enough, a normal shock wave will appear at the diverging section of the nozzle.

The suction section is a chamber where the secondary flow can reach a condition near stagnation. The secondary stream enters through the suction inlet and it decelerates and increases its pressure in the suction chamber. The secondary flow is accelerated to the mixing chamber due to a mix of the low pressure

reached by the main stream outside the nozzle and shear stresses in the mixing between both flows.

The mixing section is where both flows mix. The mixing chamber is usually a constant area section, but can have a converging section at the inlet. The mixing between both flows is very complex and hard to analyze. Both flows do not mix until they reach a point inside the constant-area section, and the expansion of the main stream outside the nozzle reduces the area of the secondary stream (Fig. 4. 14). When the main pressure is high enough, a secondary throat appears and secondary flow is choked before the mixing.

Ejectors usually have a diffuser at the outlet to bring the flow back to stagnation and recover pressure. The constant-area section must be long enough to allow the mixing of both flows and to reduce the velocity to a subsonic condition. If supersonic flow reaches the diffuser, a normal shock wave will appear reducing the performance and the pressure obtained at the outlet. However, if the constant-area section is too long the performance of the ejector will decrease due to friction in the mixing chamber.

The analysis of ejectors is complex, especially due to the mixing of both flows in the mixing chamber which have not been completely explained yet. The behavior of the flow in the nozzle and the diffuser can be explained using 1-D flows analysis (or quasi 1D flow), as has been seen in previous sections. However, 1D models usually fail when evaluating the mixing process and CFD is needed to analyze the behavior of both flows inside the mixing chamber. The modeling of ejectors will be treated in the next chapter.

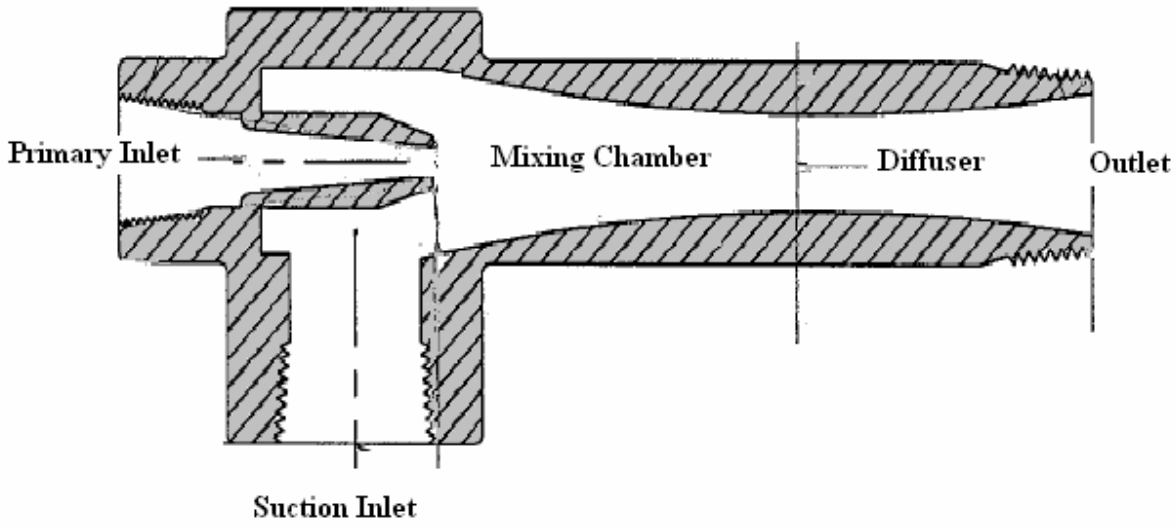

Fig. 4. 13- Geometry of an ejector. (Liao 2008)

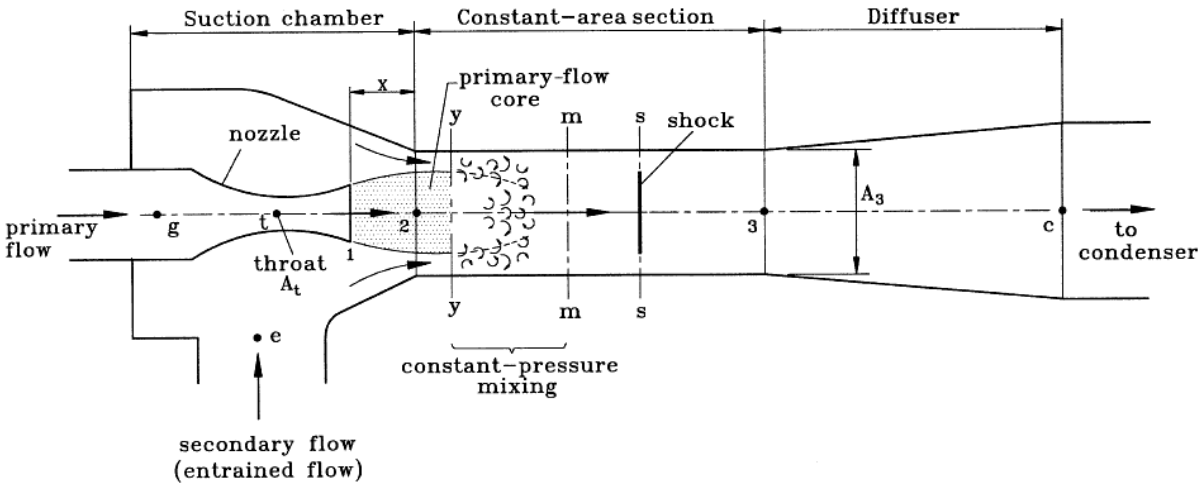

Fig. 4. 14- Geometry of a convergent-divergent nozzle ejector. (B. Huang 1999)

4.2.1. Geometrical parameters of an ejector

The geometry of an ejector depends on several geometrical parameters. The two most important geometrical parameters are the **throat area** and the **area of the mixing chamber**. These areas have a great effect upon the mass flows and temperatures and pressures obtained inside the ejector. The area of the throat strongly affects the mass flow of the primary stream, especially when it is choked. When the primary stream reaches supersonic conditions, no information can travel upstream the nozzle and the mass flow will only depend on the stagnation values of pressure and temperature of the primary flow and the area of the throat (*Eq 4. 38*). The secondary mass flow (or recirculation mass flow) will depend on the primary mass flow and its conditions outside the nozzle (especially its pressure and Mach number) and the area of the mixing chamber. When the primary stagnation pressure is high enough, the mixing chamber is choked and the mass flow depends on the stagnation properties of both flows and the area of the mixing chamber.

While designing and ejector it is important the proper **design of the nozzle**, which can have a convergent and a divergent part or just a convergent section. For the recirculation of hydrogen in a PEM fuel cell is more desirable to have just the convergent section in order to decrease condensation of water vapor inside the ejector due to the low temperature of the primary and secondary streams in the PEM fuel cell system. Since the flow reaches supersonic conditions, the temperatures obtained inside the ejector can be under 0 ºC, and will be lower if the nozzle has a divergent section than if it only has a convergent section.

Other important geometrical parameters are the constant-area section length, the distance between the outlet of the nozzle and the inlet of the mixing chamber, the length and angle of the diffuser, the angle of the converging part of the mixing chamber and the angle of the diffuser. Due to the complex nature of ejectors, there is no fixed optimum value for these parameters that can meet all the possible operating conditions. However, there are some ranges of values which are known to usually give higher performance in terms of recirculation.

The **length of the constant-area section** affects the pressure drop inside the mixing chamber and the mixing process. It is important to have enough length to

allow the mixing to take place before the diffuser, and also to reduce the Mach number from supersonic conditions to subsonic conditions. As the physics of the ejector are not yet well known, the optimal constant-area section length given by different authors differ. They agree that the optimal value should be decided depending on the area of the mixing chamber, and that the ratio between the length of the constant area section and the area of the diameter of the mixing chamber should be between 3 and 14. Zhu et al. recommend this length to be 3 or 5 times the diameter of the mixing chamber for an ejector for an anodic recirculation SOFC system (Zhu et al. 2007) and 5 to 8 when the ratio of pressures is high (Zhu and Jiang 2011). Marsano et al. recommend this ratio to be 10 (Marsano, Magistri, and Massardo 2004). Afshari et al. studied this ratio for a convergent nozzle ejector used in a PEM fuel cell system and found this value to be optimum when the length of the constant-area section is 6 times the diameter of this section (Maghsoodi, Afshari, and Ahmadikia 2014).

The distance between the nozzle and the inlet of the mixing chamber, or **nozzle position**, affects the secondary mass flow and the mixing process. When the nozzle is moved away from the mixing section, the average speed of the secondary flow is increased due to a relatively longer time period for the secondary flow to be accelerated due to the primary flow in the convergent section of the mixing chamber (Maghsoodi, Afshari, and Ahmadikia 2014). However, as the distance between the nozzle and the mixing chamber is increased, the kinetic energy and friction losses during the turbulent flow in the suction chamber and the mixing chamber are also increased. So, is necessary to know the optimum value of this distance. This value has been studied by different authors, and different results have been obtained. Maghsoodi et al. studied this value for a convergent nozzle ejector designed to recirculate hydrogen in a PEM fuel cell system, and found that the optimum value was 0.52 times the diameter of the constant-area section of the mixing chamber (Maghsoodi, Afshari, and Ahmadikia 2014). Zhu et al. studied this parameter, and found that the optimum parameter was larger than 1.7 times the diameter of the mixing chamber, and that it changed with the operation conditions (Zhu et al. 2009).

The **converging angle of the mixing section** can affect the performance of the ejector. Zhu et al. studied how it affected the performance of the ejector, and concluded that the optimum value varied between 1º and 3º depending on the pressure (Zhu et al. 2009). However, values much higher than 3º gave also an acceptable performance without depending on the pressure.

The **angle of the diffuser** is important in the performance of the ejector, and can affect the amount of flow recirculated by the ejector. Maghsoodi et al. studied this value for a convergent nozzle ejector designed to recirculate hydrogen in a PEM fuel cell system and concluded that the optimum angle varied from 2º to 8º degrees, depending on geometric parameters and the pressure (Maghsoodi, Afshari, and Ahmadikia 2014). However, this optimum value changes a lot with pressure, and Maghsoodi et al. did not studied all the possible operational conditions and geometries, so this parameter will have to be studied further.

4.2.2. Flow behavior within the ejector

An ejector can work in three different operational modes: back flow, subcritical flow and critical flow (Fig. 4. 15). The back flow mode takes place when the primary pressure is not high enough to prompt recirculation. In an ejector working in a PEM fuel cell, this can happen during start up and load changes. Subcritical mode takes place when the primary pressure is high enough to produce entrainment of the secondary flow, and critical mode is reached when the secondary stream is choked in the mixing chamber. Stoichiometry increases in subcritical mode with pressure until critical mode is reached. Then, stoichiometry begins to decrease as the primary pressure is increased. Thus, the maximum entrainment ratio and stoichiometry will be obtained just at the beginning of the critical mode. The throat of the nozzle gets choked in a point of the subcritical mode. For larger primary stagnation pressures, the mass flow will increase linearly and will only depend on the stagnation values of pressure and temperature, and the area of the throat (*Eq 4. 38*).

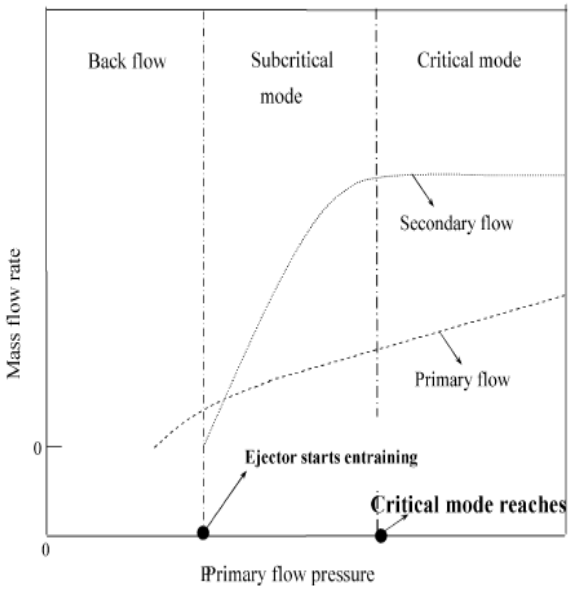

Fig. 4. 15- Operational modes of an ejector.(Zhu and Li 2009)

The mixing process is complex and does not begin just outside the outlet of the nozzle. When the main stream gets outside the nozzle, it expands and the mixing does not start until both streams reach a point downstream the nozzle. The entrainment of the secondary stream takes place due to suction and the shear action at the boundary between both flows.

If the nozzle is choked and the inlet pressure of the primary stream is high enough to reach supersonic conditions outside the nozzle, then the primary flow will expand outside the nozzle to reach the pressure of the secondary stream. Just after the nozzle, a succession of expansion waves will expand the flow and reduce its pressure (Fig. 4. 16). This expansion wave can be reflected at the jet boundary as compression or oblique shock waves, increasing the pressure of the flow. This wave reflection pattern changes depending on the pressure conditions, and the area of the primary jet will change with the amount of secondary and primary flows.

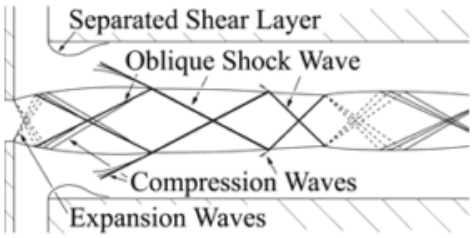

Fig. 4. 16- Flow pattern in the mixing chamber of a rectangular ejector (see Fig. 4. 17). (Koita and Iwamoto 2009)

In order to analyze the mixing and this diamond wave pattern, several authors have visualized the internal flow of the ejector using shadowgraph and Schlieren methods. Koita et al. used these techniques to visualize the flow pattern inside a rectangular model of an ejector (Fig. 4. 17), either with and without secondary flow. When there was secondary flow, the results obtained for different ratios of pressure showed the pattern explained before (Fig. 4. 18). As the primary pressure was increased, the succession of expansion and compression waves was larger and more waves appeared (Koita and Iwamoto 2009).

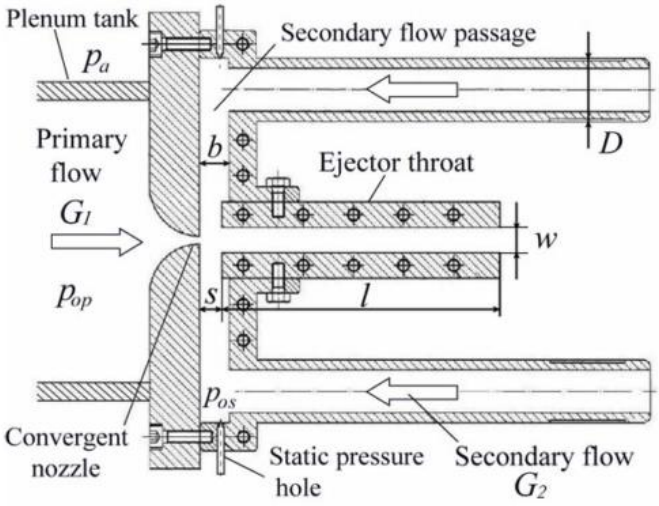

Fig. 4. 17- Rectangular ejector used by Koita el al. (Koita and Iwamoto 2009)

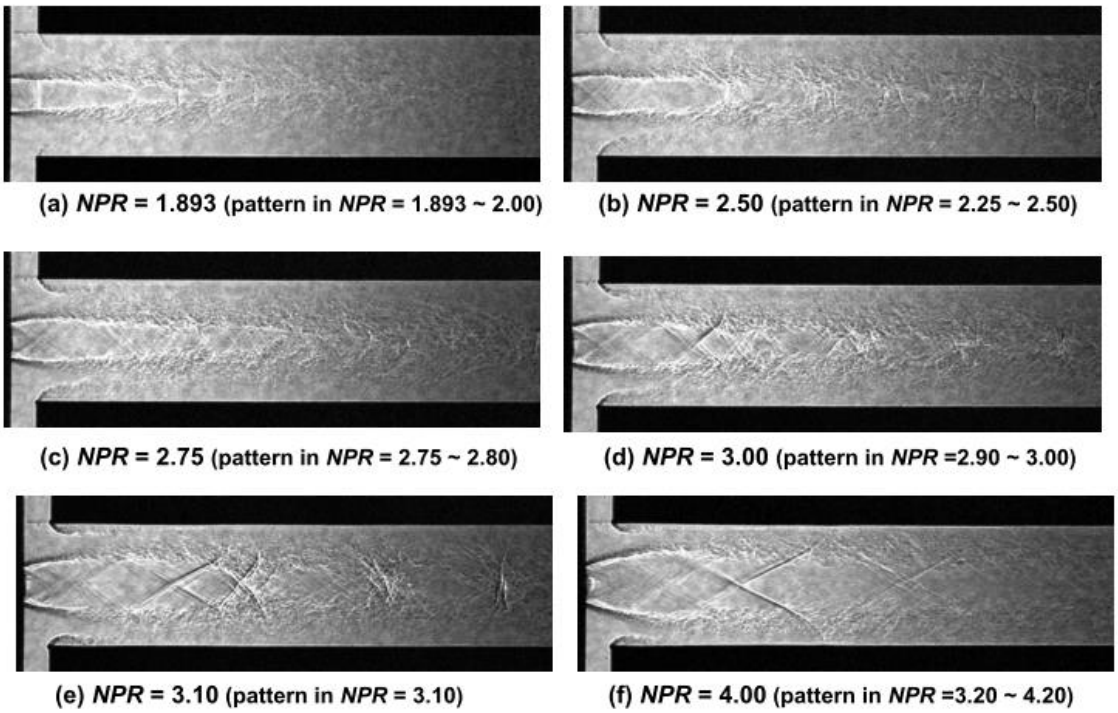

Fig. 4. 18- Shadowgraph pictures for different NPR (nozzle pressure ratio, P_{p0}/P_b) with entrainment flow. (Koita and Iwamoto 2009)

CHAPTER 5: EJECTOR MODELLING

In this section, different approaches are introduced to obtain a mathematical model of the ejector. 1D mathematical models are briefly introduced, and its advantages and disadvantages are commented.

1D mathematical models cannot take into account some of the characteristics of the geometry such as the length of the different sections or their angles. In order to obtain better results, the ejector was modeled using CFD. The physics package "High-Mach number flow" of the software COMSOL Multiphysics was used to model the ejector. In this chapter, the equations, boundary conditions, geometry, mesh and solver used in the simulation are explained. Moreover, an introduction to the Favre-averaged Navier-Stokes equations and the k-ε model can be found here.

5.1. 1D Mathematical Models

The first comprehensive theoretical and experimental analysis of the ejector problem was published by Keenan and Neumann (Keenan and Neumann 1942). They used 1D continuity, momentum and energy equations to predict the performance of the ejector. However, some experimental coefficients were needed to obtain a relatively accurate solution for the momentum equation during the mixing.

In order to solve this problem, Keenan et al. (Keenan, Neumann, and Lustwerk 1950) developed two theoretical models: the constant-pressure and the constant area mixing models, which became the basis of ejector design and performance analysis (Liao 2008). The first one considers that dP=0 during the mixing, while the second one considers that the mixing takes place inside a duct with constant

area (S. He, Li, and Wang 2009). Keenan et al. stated that a constant-pressure mixing gives better performance than a constant-area mixing. However, constant-area mixing ejectors have been widely used since the constant-area mixing model offers better agreement with experimental results than the constant-pressure mixing model.

The models developed by Keenan et al. could not give detailed information about several phenomena occurring inside the ejector, and they were therefore improved and modified by several authors (S. He, Li, and Wang 2009). Munday and Bagster (Munday and Bagster 1977) developed the constant-pressure mixing model and assumed that the main flow does not mix with the secondary flow just after discharging from the nozzle exit. Instead, they assumed that the primary flow expands outside the nozzle until the secondary flow is choked, forming an hypothetical throat after which the mixing begins.

Eames et al. (Eames, Aphornratana, and Haider 1995) modified the constant-pressure mixing model to take into account the irreversibility due to friction in the primary nozzle, mixing chamber and diffuser. However, the choking of the secondary flow was not considered.

The model by Munday et al. was further developed by Huang et al. (B. J. Huang and Chang 1999). They developed a double-choking model which assumed both mixing models: they considered that a constant-pressure mixing takes places inside a constant-area section. They also tested eleven different ejectors to validate the theoretical analysis and obtain the coefficients of efficiency.

Liao developed a general model which solved the momentum equation in the mixing chamber without using the constant-area or constant-pressure mixing models (Liao 2008). The constant-area and constant-pressure models can be derived from this general model, so that the relationship between both models can be studied further using Liao's model.

Another interesting model was developed by Zhu et al. (Zhu and Li 2009). This model was developed assuming an ejector with a convergent nozzle used to recirculate hydrogen in a PEM fuel cell system. This model is a semi-empirical model, as it uses a coefficient found empirically, and it can be considered as a quasi-2D model as it takes into account the radial distribution of the velocity inside the mixing chamber.

More 1D models have been published by other authors. A brief summary of these models was published by He et al. (S. He, Li, and Wang 2009). 1D models are widely used due their simplicity and their easy implementation. They need very low computational resources and can be solved without using a computer. However, they do not take into account some of the phenomena occurring inside the ejector such as oblique-shock waves, expansion waves, the mixing layer and the effects due to turbulence or related to 3D flows. Furthermore, these methods tend to take into account just two geometrical parameters, the area of the nozzle throat and the mixing chamber. Other important geometric parameters, such as the length of the mixing chamber, the angle of the different sections, and the shape of the suction chamber, are not taken into account and their effect cannot be evaluated using these methods. In order to obtain more information about the ejector, and more accurate results, it is necessary to use CFD models.

5.2. Introduction to the CFD model

A turbulence model is useful to simulate the behavior of the flow within the ejector. This way, the amount of computational resources is reduced and steady simulations can be obtained. Turbulence models are used to approximate the Reynolds-averaged Navier-Stokes equations, or, in the case of density fluctuations, the Favre-averaged Naver-Stokes equations, without the need to compute the high number of extra variables that appear in these equations. Reynolds-averaged and Favre-averaged Navier-Stokes equations are an economic approximation of the Navier-Stokes equations in which the variables are composed of an average part and a fluctuation part. This separation of variables is used to avoid the need to calculate the wide range of scales that appear in a turbulent flow.

The turbulence model that will be used here is the k-ε model. This model is the most widely used and validated turbulence model. Its features are well known and it has achieved good success in calculating a wide variety of flows. Even though more accurate models have appeared recently, the good balance between accuracy and the need of computational resources make the k-ε an attractive turbulence model (Bartosiewicz et al. 2003).

5.2.1. Reynolds-averaged and Favre-averaged Navier-Stokes equations

The behavior of a compressible flow can be explained using the compressible Navier-Stokes equations for a newtonian fluid (Versteeg and Malalasekera 2007):

- Continuity equation:

$$\frac{\partial \rho}{\partial t} + div(\rho \boldsymbol{c}) = 0 \qquad \textbf{Eq 5.1 a}$$

- x-momentum:

$$\frac{\partial(\rho u)}{\partial t} + div(\rho u \boldsymbol{c}) = -\frac{\partial P}{\partial x} + div[\mu\ grad(u)] + S_{Mx} \qquad \textbf{Eq 5.1 b}$$

- y-momentum:

$$\frac{\partial(\rho v)}{\partial t} + div(\rho v \boldsymbol{c}) = -\frac{\partial P}{\partial y} + div[\mu\ grad(v)] + S_{My} \qquad \textbf{Eq 5.1 c}$$

- z-momentum:

$$\frac{\partial(\rho w)}{\partial t} + div(\rho w \boldsymbol{c}) = -\frac{\partial P}{\partial y} + div[\mu\ grad(w)] + S_{Mz} \qquad \textbf{Eq 5.1 d}$$

- Energy:

$$\frac{\partial(\rho u_i)}{\partial t} + div(\rho u_i \boldsymbol{c}) = -P div(\boldsymbol{c}) + div[k_t\ grad(T)] + \Phi + S_i \qquad \textbf{Eq 5.1 e}$$

- Equations of state (perfect gas):

$$P = \rho R T \qquad \textbf{Eq 5.1 f}$$

$$u_i = c_v T \qquad \textbf{Eq 5. 1 g}$$

The term S_M is a momentum source, while S_i represents an energy source:

$$\mathbf{S_M} = \boldsymbol{S_{MB}} + S_{Mv} = S_{MB} + \left[\frac{\partial}{\partial x}\left(\mu\frac{\partial u}{\partial x}\right) + \frac{\partial}{\partial y}\left(\mu\frac{\partial v}{\partial x}\right) + \frac{\partial}{\partial z}\left(\mu\frac{\partial w}{\partial x}\right) + \frac{\partial}{\partial x}\left(\lambda\, div\underline{c}\right)\right] \quad \textbf{Eq 5. 2}$$

$$\mathrm{S_i} = S_E - \boldsymbol{c}\cdot\boldsymbol{S_M} \quad \textbf{Eq 5. 3}$$

The term S_{MB} is a source of momentum due to body forces only. For example, gravity could be modeled as $S_{MBx} = 0, S_{MBz} = 0$ and $S_{MBy} = -\rho g$. S_E is used to represent different sources of energy.

The term Φ is a dissipation function that describes the effects due to viscous stresses in the energy equation. It is equal to (Versteeg and Malalasekera 2007):

$$\Phi = \mu\left\{2\left[\left(\frac{\partial u}{\partial x}\right)^2 + \left(\frac{\partial v}{\partial y}\right)^2 + \left(\frac{\partial w}{\partial z}\right)^2\right] + \left(\frac{\partial u}{\partial y} + \frac{\partial v}{\partial x}\right)^2 + \left(\frac{\partial v}{\partial z} + \frac{\partial w}{\partial y}\right)^2 + \left(\frac{\partial u}{\partial z} + \frac{\partial w}{\partial x}\right)^2\right\} + \lambda(div\boldsymbol{c}) \quad \textbf{Eq 5. 4}$$

Flows in the laminar range are completely described by Navier-Stokes (NS) equations. NS equations can also be used for turbulent flow simulation, although this would require a large number of elements in order to capture the wide range of scales in the flow. The classification of a flow as turbulent or laminar is based on the Reynolds number. This number gives a measure of the relative importance of inertia forces, which are related to convective effects, and viscous forces:

$$\mathrm{Re} = \frac{\rho c L_c}{\mu} \quad \textbf{Eq 5. 5}$$

Where L_c is a characteristic length. At values bellow critical Reynolds number the flow is said to be laminar as it is smooth and composed by adjacent layers of fluid that slide past each other in an orderly fashion (Versteeg and Malalasekera 2007). If the boundary conditions of a laminar flow are steady, then the flow is steady too. When the Reynolds number is over its critical value, it is said to be turbulent and its character changes drastically. A turbulent flow is unsteady even if its imposed boundary conditions do not change with time. The flow properties of a turbulent flow vary in a random and chaotic way (Fig. 5. 1). The flow now has a wide range of scales, increasing dramatically the computational costs of the simulation of such flows.

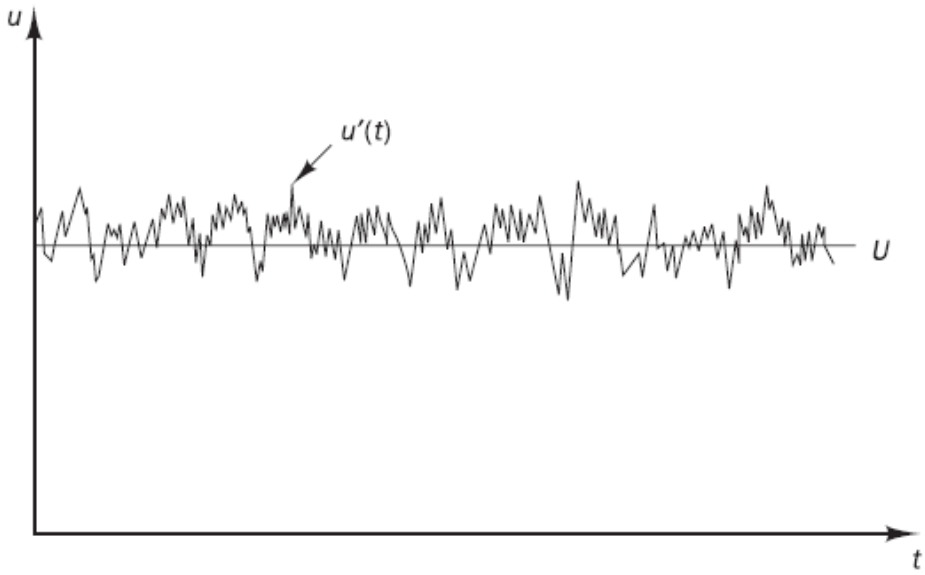

Fig. 5. 1- Typical point velocity measurement in turbulent flow (Versteeg and Malalasekera 2007).

An economical way to handle turbulent flows is using a Reynolds decomposition (Reynolds-averaged turbulent flow). The Reynolds-averaged representation of turbulent flows divides flow properties (for example, c) into a steady mean value ($\overline{c}$) with a fluctuating component ($c'(t)$):

$$c(t) = \overline{c} + c'(t) \qquad \textbf{Eq 5. 6}$$

The time average of the fluctuation c' is considered, by definition, 0. Decomposition of the flow field into an averaged part and a fluctuating part and a further manipulation of the NS equations give the famous Reynolds-averaged Navier-Stokes (RANS) equations. For compressible turbulent flow, in which the variation of mean density is non-negligible, it is recommendable to use a density-based average, known as the Favre average:

$$\tilde{c} = \frac{\int_{t_0}^{t_0+\Delta t} \rho(t)c(t)dt}{\int_{t_0}^{t_0+\Delta t} \rho(t)dt} = \frac{\overline{\rho c}}{\overline{\rho}} \qquad \textbf{Eq 5. 7}$$

In the Favre average decomposition, the variables are also decomposed into a mean mass-averaged component $\tilde{c}$ and a fluctuating component c':

$$c(t) = \tilde{c} + c'(t) \qquad \textbf{Eq 5. 8}$$

Using the Favre average decomposition, the Favre-averaged Navier-Stokes equations can be obtained (Versteeg and Malalasekera 2007):

- Continuity:

$$\frac{\partial \overline{\rho}}{\partial t} + div(\overline{\rho}\tilde{\boldsymbol{c}}) = 0 \qquad \textbf{Eq 5. 9 a}$$

- Reynolds equations:

$$\frac{\partial(\overline{\rho}\tilde{u})}{\partial t}+div(\overline{\rho}\tilde{u}\tilde{\boldsymbol{c}})=-\frac{\partial\overline{P}}{\partial x}+div[\mu\ grad(\tilde{u})]+\left[-\frac{\partial\left(\overline{\overline{\rho}u'^2}\right)}{\partial x}-\frac{\partial\left(\overline{\overline{\rho}u'v'}\right)}{\partial y}-\frac{\partial\left(\overline{\overline{\rho}u'w'}\right)}{\partial z}\right]+S_{Mx} \qquad \textbf{Eq 5. 9 b}$$

$$\frac{\partial(\overline{\rho}\tilde{v})}{\partial t}+div(\overline{\rho}\tilde{v}\tilde{\boldsymbol{c}})=-\frac{\partial\overline{P}}{\partial y}+div[\mu\ grad(\tilde{v})]+\left[-\frac{\partial\left(\overline{\overline{\rho}u'v'}\right)}{\partial x}-\frac{\partial\left(\overline{\overline{\rho}v'^2}\right)}{\partial y}-\frac{\partial\left(\overline{\overline{\rho}v'w'}\right)}{\partial z}\right]+S_{My} \qquad \textbf{Eq 5. 9 c}$$

$$\frac{\partial(\overline{\rho}\tilde{w})}{\partial t}+div(\overline{\rho}\tilde{w}\tilde{\boldsymbol{c}})=-\frac{\partial\overline{P}}{\partial z}+div[\mu\ grad(\tilde{w})]+\left[-\frac{\partial\left(\overline{\overline{\rho}v'w'}\right)}{\partial x}-\frac{\partial\left(\overline{\overline{\rho}w'^2}\right)}{\partial z}-\frac{\partial\left(\overline{\overline{\rho}u'w'}\right)}{\partial y}\right]+S_{Mz} \qquad \textbf{Eq 5. 9 d}$$

- Scalar transport equation:

$$\frac{\partial(\overline{\rho}\tilde{\phi})}{\partial t}+div(\overline{\rho}\tilde{\phi}\tilde{c})=div(\Gamma_{\phi}grad(\tilde{\phi}))+\left[-\frac{\partial\left(\overline{\overline{\rho}u'\phi'}\right)}{\partial x}-\frac{\partial\left(\overline{\overline{\rho}v'\phi'}\right)}{\partial y}-\frac{\partial\left(\overline{\overline{\rho}w'\phi'}\right)}{\partial z}\right]+\boldsymbol{S_{\phi}} \qquad \textbf{Eq 5. 9 e}$$

Where Γ_{ϕ} is the diffusivity of ϕ. The latter equation is a transport equation for an arbitrary scalar quantity ϕ, which could be, for example, the temperature.

It is important to note that the process of time and mass averaging has introduced new terms. Six new turbulent stresses have appeared: three normal stresses and three shear stresses. These stresses are called Reynolds stresses:

$$\tau_{xx}=-\rho\overline{u'^2} \qquad \tau_{yy}=-\rho\overline{v'^2} \qquad \tau_{zz}=-\rho\overline{w'^2} \qquad \textbf{Eq 5. 10 a}$$

$$\tau_{xy}=-\rho\overline{u'v'} \qquad \tau_{xz}=-\rho\overline{u'w'} \qquad \tau_{yz}=-\rho\overline{v'w'} \qquad \textbf{Eq 5. 10 b}$$

In order to be able to compute turbulent flows using the Reynols-averaged NS equations, or the Favre-averaged NS equations, these extra unknowns must be predicted using turbulence models.

Boussinesq proposed that the Reynolds stresses might be proportional to mean rates of deformation (Comsol: The CFD module user's guide, 2012):

$$\tau_{ij}=-\rho\overline{c_i'c_j'}=\mu_t\left(\frac{\partial\widetilde{c_i}}{\partial x_j}+\frac{\partial\widetilde{c_j}}{x_i}\right)-\frac{2}{3}\left(\mu_t\frac{\partial\widetilde{u_k}}{\partial x_k}+\overline{\rho}k\right)\delta_{ij} \qquad \textbf{Eq 5. 11}$$

Where δ_{ij} is the Kronecker delta, μ_t is the turbulent viscosity or eddy viscosity and k is the turbulent kinetic energy per unit mass. Eq 5. 11 is expressed using suffix notation.

Eq 5. 11 assumes that the three normal Reynolds stresses are equal. However, this isotropic assumption has been demonstrated to be inaccurate for some flows (Versteeg and Malalasekera 2007).

The turbulent kinetic energy can be interpreted as the mean kinetic energy per unit mass contained in the velocity fluctuations:

$$k=\frac{1}{2}\left(\overline{u'^2}+\overline{v'^2}+\overline{w'^2}\right) \qquad \textbf{Eq 5. 12}$$

Turbulent transport of heat, mass and other scalar properties can be modeled in a similar way by assuming it to be proportional to the gradient of the mean value of the transported quantity:

$$-\rho\overline{u_i'\phi'} = \Gamma_t \qquad \textbf{Eq 5. 13}$$

Where Γ_t is the turbulent diffusivity. The value of the turbulent diffusivity is expected to be close to the value of turbulent viscosity, since the turbulent transport of momentum, heat and mass are due to the same mechanism. The turbulent Prandtl/Schmidt number is used to evaluate this similarity:

$$\sigma_t = \frac{\mu_t}{\Gamma_t} \qquad \textbf{Eq 5. 14}$$

5.2.2. The standard k-ε turbulence model

The k-ε model is one of the most used turbulence models. This model introduces two additional transport equations and two dependent variables to model the extra terms that appear on the Reynolds-averaged and Favre-averaged NS equations: the turbulent kinetic energy, k (Eq 5. 12), and the turbulent dissipation rate, ε.

The rate of dissipation of turbulent kinetic energy per unit mass can be expressed as (Versteeg and Malalasekera 2007):

$$\varepsilon = 2\frac{\mu}{\rho}\overline{S_{ij}' \cdot S_{ij}'} \qquad \textbf{Eq 5. 15}$$

Where S_{ij}' expresses the fluctuation of the different components of the rate deformation tensor.

In the k-ε model, the turbulent viscosity is modeled as (Comsol: The CFD module user's guide, 2012):

$$\mu_t = \rho C_\mu \frac{k^2}{\varepsilon} \qquad \textbf{Eq 5. 16}$$

Where C_μ is a constant.

After a long manipulation of NS and Reynolds-averaged NS equations, the governing equation for turbulent kinetic energy, k, can be obtained:

$$\frac{\partial(\rho k)}{\partial t} + div(\rho k \boldsymbol{c}) = div\left[\frac{\mu_t}{\sigma_k} grad(k)\right] + 2\mu_t S_{ij} \cdot S_{ij} - \rho\varepsilon \qquad \textbf{Eq 5. 17}$$

Similarly, a transport equation for ε could be developed. However, this equation would contain many unknowns and immeasurable terms (Versteeg and Malalasekera 2007). Thus, the transport equation for ε that is used in the k- ε model must be modified including some constants:

$$\frac{\partial(\rho\varepsilon)}{\partial t} + div(\rho\varepsilon \boldsymbol{c}) = div\left[\frac{\mu_t}{\sigma_\varepsilon} grad(\varepsilon)\right] + C_{1\varepsilon}\frac{\varepsilon}{k} 2\mu_t S_{ij} \cdot S_{ij} - C_{2\varepsilon}\rho\frac{\varepsilon^2}{k} \qquad \textbf{Eq 5. 18}$$

Eq 5. 16, Eq 5. 17 and Eq 5. 18 contain five constants. The values of these constants have been determined from experimental data (Comsol: The CFD module user's guide, 2012):

$$C_\mu = 0.09 \quad C_{\varepsilon 1} = 1.44 \quad C_{\varepsilon 2} = 1.92 \quad \sigma_k = 1.00 \quad \sigma_\varepsilon = 1.30$$

5.2.3. Wall functions

In turbulent flows the flow behavior and turbulence structure near a solid boundary are very different from the free turbulent flow. Since the k- ε model is designed to be used at high Reynolds numbers, the assumptions used to derive this model are not valid close to the walls. It is possible to modify the model so that it describes the flow in wall regions (then the model is called "Low Reynolds number k-ε model"). However, this option requires a very fine mesh in the region near the wall, the resulting equation set is numerically stiff and it is harder to achieve convergence.

At high Reynolds number this can be avoided by using analytical expressions to describe the flow near the walls. These expressions are known as wall functions.

Close to the wall the flow is influenced by viscous effects and the mean flow velocity only depends on the distance from the wall (δ_w), fluid density and viscosity and the wall shear stress (τ_w). Dimensional analysis shows that (Versteeg and Malalasekera 2007):

$$\frac{\mathrm{c}}{\mathrm{c}_\tau} = c^+ = f\left(\frac{\rho c_\tau \delta_w}{\mu}\right) = f(\delta_w^+) \qquad \textbf{Eq 5. 19}$$

Where c^+ and δ_w^+ are dimensionless parameters and c_τ is the friction velocity:

$$\mathrm{c}_\tau = \sqrt{\frac{\tau_w}{\rho}} \qquad \textbf{Eq 5. 20}$$

The boundary layer can be divided in the inner region, where viscous effects are important, and the outer region, where the flow is dominated by the inertia forces.

The zone of the inner region which is closest to the wall is called the viscous sub-layer. In this region, the flow is dominated by viscous effects. The viscous sub-layer is extremely thin ($\delta_w^+ < 5$), and it may be assumed that the shear stress is almost constant and equal to the wall shear stress:

$$\tau = \mu \frac{\partial \mathrm{c}}{\partial \delta_w} = \tau_w \qquad \textbf{Eq 5. 21}$$

After the application of the boundary condition c(δ_w=0)=0:

$$\mathrm{c} = \frac{\tau_w \delta_w}{\mu} \rightarrow c^+ = \delta_w^+ \qquad \textbf{Eq 5. 22}$$

Outside the viscous sublayer there is a region where viscous and turbulent effects are both important. In this region a functional relationship, called the log-law, can be used to relate c^+ and δ_w^+:

$$c^+ = \frac{1}{k_v}\ln(\delta_w^+) + B \qquad \textbf{Eq 5. 23}$$

Where k_v=0.41 is the Von Karman constant and B is an additive constant which in COMSOL Multiphysics' module High Mach Number Flow is, by default, 5.2. In the log-law layer the rate of turbulence kinetic energy production can be assumed to be equal to the rate of its dissipation. Using this assumption and Eq 5. 16:

$$\mathrm{k} = \frac{\mathrm{c}_\tau^2}{\sqrt{c_\mu}} \qquad \textbf{Eq 5. 24}$$

$$\varepsilon = \frac{\mathrm{c}_\tau^3}{k_v \delta_w} = \frac{\left(C_\mu\right)^{\frac{3}{4}} k^{\frac{3}{2}}}{k_v \delta_w} \qquad \textbf{Eq 5. 25}$$

5.3. COMSOL model

In order to simulate the steady behavior of an ejector under different conditions through CFD, the software COMSOL Multiphysics will be used as the pre and post-processors and the solver. COMSOL Multiphysics includes several CFD modules with different physics, and one of them is the module of physics called "High-Mach number flow". This module includes a coupling between other COMSOL modules and is designed to solve flows where Ma>0.3. This module has three interfaces: Laminar flow, k-ε turbulence model and Spallart-Allmaras turbulence model. The Laminar flow interface solves the equations of Navier-Stokes for a compressible fluid that acts as a perfect gas. The other two interfaces solve the problem using two different turbulence models, the k- ε and the Spallart-Allmaras model.

The model proposed in this work solves the problem of the ejector using an axisymmetric 2D geometry. As the density of the fluid is variable along the ejector, the Favre averaged Navier-Stokes equations are used. The Navier-Stokes equations are approximated using the standard k-ε turbulence model and assuming that the fluid follows the ideal gas law. Wall functions are used in order to approximate the behavior of the flow near the walls without adding the need of more computational resources.

In this section, the governing equations, boundary conditions, geometry, mesh and solver used in the model are explained. A tutorial of how to implement the model can be found in Appendix A, where the implementation of the model in COMSOL Multiphysics is explained step by step and used to solve the example introduced in section 5.3.7.

5.3.1. Governing equations

The problem is governed by the Favre-averaged Navier-Stokes equations, so that the velocity obtained is the average velocity. The k- ε turbulence model is used to approximate the Reynolds stresses. The thermodynamics and transport properties for the gas (hydrogen) are held constant (Bartosiewicz et al. 2003). The fluid is treated as a perfect gas. The governing equations are (Comsol: The CFD module user's guide, 2012):

$$\nabla \cdot (\rho \boldsymbol{c}) = 0 \qquad \textbf{Eq 5.26 a}$$

$$\rho(\boldsymbol{c} \cdot \nabla)\mathbf{c} = \nabla \cdot \left[-p\boldsymbol{I} + (\mu + \mu_t)(\nabla \boldsymbol{c} + (\nabla \boldsymbol{c})^T) - \frac{2}{3}(\mu + \mu_t)(\nabla \cdot \boldsymbol{c})\boldsymbol{I} - \frac{2}{3}k\boldsymbol{I}\right] + S_M \qquad \textbf{Eq 5.26 b}$$

$$\rho C_p \boldsymbol{c} \cdot \nabla T = \nabla \cdot (k_t \nabla T) + \dot{Q} + \mu\left[\nabla \boldsymbol{c} + (\nabla \boldsymbol{c})^T - \frac{2}{3}(\nabla \cdot \boldsymbol{c})\boldsymbol{I}\right] : \boldsymbol{c} + \frac{T}{\rho}\left(\frac{\partial \rho}{\partial T}\right)\Big|_P \left(\frac{\partial P}{\partial t} + \boldsymbol{c} \cdot P\right) \qquad \textbf{Eq 5.26 c}$$

$$\rho(\boldsymbol{c} \cdot \nabla)k = \nabla \cdot \left[\left(\mu + \frac{\mu_t}{\sigma_k}\right)\nabla k\right] + \mu_t\left[\nabla \boldsymbol{c} + (\nabla \boldsymbol{c})^T - \frac{2}{3}(\nabla \cdot \boldsymbol{c})^2\right] - \frac{2}{3}\rho k \nabla \cdot \boldsymbol{c} - \rho\varepsilon \qquad \textbf{Eq 5.26 d}$$

$$\rho(\boldsymbol{c} \cdot \nabla)\varepsilon = \nabla \cdot \left[\left(\mu + \frac{\mu_t}{\sigma_\varepsilon}\right)\nabla \varepsilon\right] + C_{1\varepsilon}\frac{\varepsilon}{k}\left\{\mu_t\left[\nabla \boldsymbol{c} + (\nabla \boldsymbol{c})^T - \frac{2}{3}(\nabla \cdot \boldsymbol{c})^2\right] - \frac{2}{3}\rho k \nabla \cdot \boldsymbol{c}\right\} - C_{2\varepsilon}\rho\frac{\varepsilon^2}{k} \qquad \textbf{Eq 5.26 e}$$

$$\rho = \frac{P}{RT} \qquad \textbf{Eq 5.26 f}$$

$$C_p = \frac{\gamma R}{\gamma - 1} \qquad \textbf{Eq 5.26 g}$$

$$\mu_t = \rho C_\mu \frac{k^2}{\varepsilon} \qquad \textbf{Eq 5. 26 h}$$

Since this is a highly convective problem, the governing equations are not stable and it is harder to achieve convergence than for conduction-dominated problems because the numerical solutions of the transport equations can exhibit oscillations and instabilities. In order to ensure the convergence of the model and restore numerical stability it is necessary to use different stabilization methods.

Two different stabilization methods are used: Consistent and inconsistent methods. Their common feature is that both of them add terms to the transport equation, introducing numerical diffusion that stabilizes the solution.

Consistent stabilization methods do not perturb the original transport equation. They add numerical diffusion in such a way that if the solution obtained is an exact solution of the problem, then it is also a solution of the problem with numerical diffusion. In other words, a consistent stabilization method gives less numerical diffusion the closer the numerical solution comes to the exact solution (Comsol Multiphysics Reference Guide, 2012).

An inconsistent stabilization method can perturb the original transport equation. They add a certain amount of numerical diffusion independently of how close the numerical solution is to the exact solution. Thus, inconsistent stabilization should be used carefully or even avoided.

In this problem both stabilization methods are used. Consistent stabilization is introduced by adding streamline diffusion and crosswind diffusion with a tuning parameter $C_k = 1$ for the flow, heat transfer and turbulence equations. Inconsistent stabilization is used adding isotropic diffusion in order to obtain the initial solution from which to begin to solve the problem. First, the problem is solved with a tuning parameter $\delta_{id} = 0.25$. Then, the solution obtained is used as the initial solution to solve the problem again using $\delta_{id} = 0.225$. This is repeated until $\delta_{id} = 0$ and the final solution is reached. This process is called a continuation study.

It is not the aim of this work to explain stabilization methods. More information can be found in more specialized bibliography (Zienkiewicz, Taylor, and Nithiarasu 2005) (John and Knobloch 2007).

If it is desired to know how the ejector behaves for different values of the stagnation pressure at the inlet, then a good strategy is to solve the problem for the lowest value of primary pressure using inconsistent stabilization and then reduce inconsistent stabilization until $\delta_{id} = 0$. Then, a continuation study is carried out by increasing the stagnation pressure at the inlet. This way, the time needed to obtain the simulation of the whole range of pressures is lowered because the continuation studio used to obtain the first solution by decreasing δ_{id} just needs to be carried out for the first value of pressure.

5.3.2. Geometry

The geometry used is an axisymmetric 2D geometry like the one shown in Fig. 5. 2 a. Results for a 3D geometry can be approximated through the revolution of this 2D geometry.

Since the k- ε is not suitable for complex geometries with curved boundaries, the vertexes are not rounded. However, in the real geometry of the ejector the corners are rounded or chamfered.

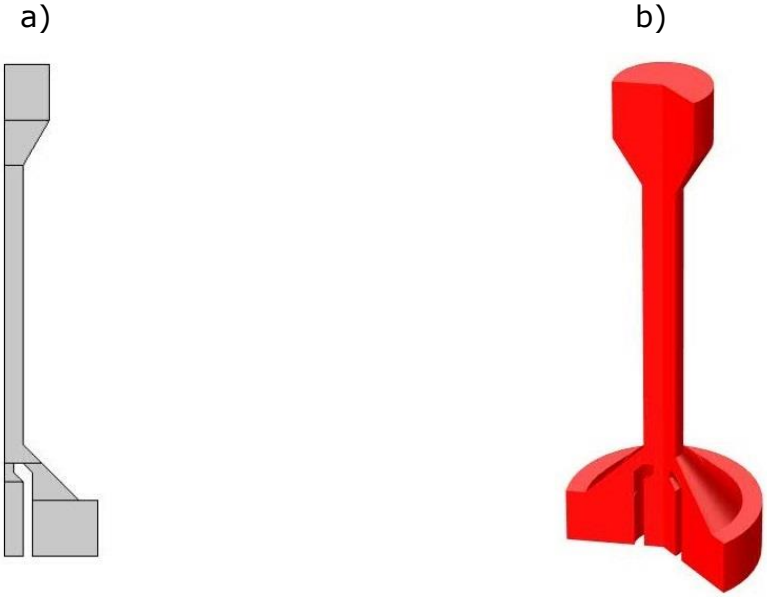

Fig. 5. 2- Geometry of the model. a) 2D geometry for axisymmetric calculus. b) 3D geometry obtained from the revolution of the 2D geometry.

5.3.3. Boundary conditions and initial values

There are five different boundaries: The walls, the primary and secondary inlets, the outlet and the axisymmetric axis.

The flow near the walls is approximated by wall functions. The boundary conditions for the velocity is a homogeneous Dirichlet condition (Eq 5.27 a) and a shear stress condition (Eq 5.27 b). The turbulent kinetic energy is subjected to a homogeneous Neumann condition (Eq 5.27 c) and the boundary conditions for ε (Eq 5.27 d) are based on Eq 5. 25. The walls are assumed to be thermally insulated (Eq 5. 27 e).

$$\mathbf{c} \cdot \mathbf{n} = 0 \qquad \textbf{Eq 5.27 a}$$

$$\boldsymbol{n} \cdot \mu[\nabla \boldsymbol{c} + (\nabla \boldsymbol{c})^T] - \{\boldsymbol{n} \cdot \mu[\nabla \boldsymbol{c} + (\nabla \boldsymbol{c})^T] \cdot \boldsymbol{n}\}\boldsymbol{n} = -\frac{\rho c_\tau \boldsymbol{c}}{|\boldsymbol{c}|} \cdot max\left(\left(C_\mu\right)^{\frac{1}{4}}\sqrt{k}, c\_\tau\right) \qquad \textbf{Eq 5.27 b}$$

$$\mathbf{n} \cdot \nabla \mathrm{k} = 0 \qquad \textbf{Eq 5.27 c}$$

$$\varepsilon = \frac{\left(C_\mu\right)^{\frac{3}{4}} k^{\frac{3}{2}}}{k_v \delta_w} \qquad \textbf{Eq 5.27 d}$$

$$-\mathbf{n} \cdot (\mathrm{k_t} \nabla \mathrm{T}) = 0 \qquad \textbf{Eq 5. 27 e}$$

The wall functions in COMSOL Multiphysics are such that the computational domain is assumed to be located a distance δ_w from the wall (Comsol: The CFD module user's guide, 2012). δ_w is automatically computed so that δ_w^+ is equal to 11.06:

$$\delta_w^+ = \frac{\rho \delta_w \left(C_\mu\right)^{\frac{1}{4}} \sqrt{k}}{\mu} \qquad \textbf{Eq 5. 28}$$

δ_w must be limited from below so that it never becomes smaller than half the height of the boundary mesh cell. Thus, δ_w^+ can become larger than 11.06 if the mesh is coarse. This can be used as an indicator to know if the mesh is too coarse.

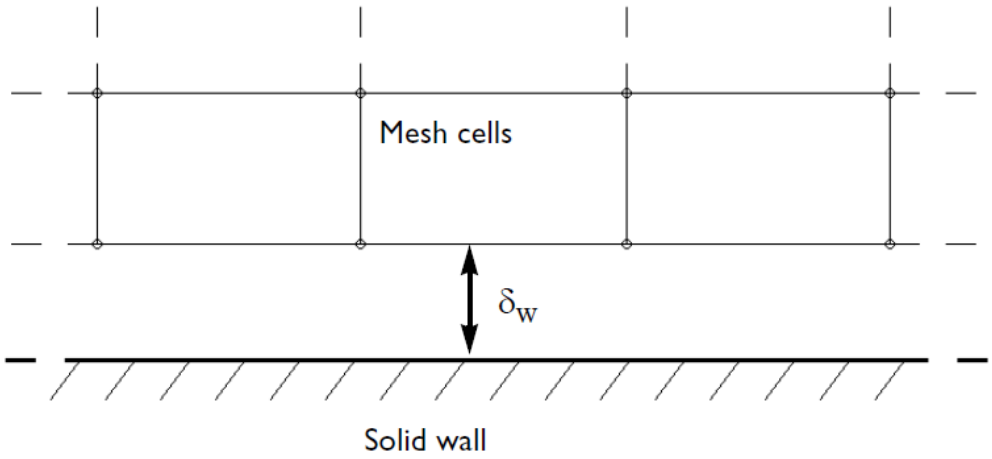

Fig. 5. 3- Wall distance. (Comsol: The CFD module user's guide, 2012)

The inlets are described using a plane wave analysis of the inviscid part of the flow (Comsol: The CFD module user's guide, 2012). The full flow condition at the inlet is specified by the stagnation values of the pressure (P_{p0} and P_{s0}) and temperature (T_{p0} and T_{s0}) of the flow, which are measured at Ma=0, and the values of k and ε. Since there is no information about the values of k and ε at the inlet, an approximation for the inlet distribution of these variables can be obtained from the turbulence intensity I_T and the turbulence length scale L_T:

$$\mathrm{k} = \frac{3}{2}(|\boldsymbol{c}|I_T)^2 \qquad \textbf{Eq 5. 29}$$

$$\varepsilon = \frac{(C_\mu)^{\frac{3}{4}} k^{\frac{3}{2}}}{L_T} \qquad \textbf{Eq 5. 30}$$

The turbulence intensity for fully turbulent flows has a value between 5% and 10 %. For low turbulence intensity flows, I_T has a value of 0.1%. The default value used in COMSOL is 5%.

The turbulence length scale can be approximated empirically. For flow in pipes it can be assumed to be 0.07 times the radius of the pipe.

The flow at the outlet is assumed to be subsonic. The back pressure (P_b) is specified. k and ε are subjected to a homogenous Neumann condition and the outlet is assumed to be thermally insulated:

$$\mathbf{n}\cdot\nabla\mathrm{k} = 0 \quad \mathbf{n}\cdot\nabla\varepsilon = 0 \quad -\mathbf{n}\cdot(\mathrm{k_t}\nabla\mathrm{T}) = 0 \qquad \textbf{Eq 5. 31}$$

In order to be able to solve the non-linear system, initial values must be added as an initial guess for the nonlinear solver. The initial value for the velocity is 0 for both the radial and axial directions. The initial pressure is set as the secondary stagnation pressure, and the initial temperature is set as the primary stagnation temperature. The initial values for k and ε depen on the mixing length limit $l_{\lim mix}$, which is automatically computed by COMSOL Multiphysics:

$$\mathrm{k_{init}} = \left(\frac{10\mu}{\rho(\,0.1 l_{\lim mix})}\right)^2 \qquad \textbf{Eq 5. 32}$$

$$\varepsilon = \frac{\mathrm{C_\mu} k_{init}^{\frac{3}{2}}}{0.1 l_{\lim mix}} \qquad \textbf{Eq 5. 33}$$

5.3.4. Solver

Since the equations of this problem are highly nonlinear, they must be solved using an iterative procedure. The variables will be solved using a segregated solver with a maximum of 500 iterations. The variables are segregated in two different groups:

- Group 1: $\mathbf{c}$, p, T and $\mathrm{T_{wall}}$ $(Temperature\ of\ the\ Wall)$.
- Group 2: ε and k.

Group 1 will be solved using one iteration per every iteration of the segregated solver, using a constant damping factor of 0.5 and the solver Pardiso. The

second group will be solved using four iterations per every iteration of the segregated solver, using a constant damping factor of 0.3 and the solver Pardiso. The relative tolerance for which the solver ends is 10^{-3}.

5.3.5. Mesh

Different meshes have been studied in order to find a mesh that can provide accurate results without requiring an excessively high amount of computational resources. This study has been done using the geometry of the ejector used in the experimental validation (Section 6.2). The distance between the nozzle and the inlet of the constant-area section of the mixing chamber is 1.5 mm.

A mesh that would be able to provide good results without the need of very high computational resources would be a structured mesh with quadrilateral elements oriented in the direction of the flow. This mesh can be used to model, for example, a nozzle (Section 5.3.8). However, the geometry of the ejector is more complex and the presence of the boundary layer elements distorts the mesh and makes it hard to obtain a structured mesh. Thus, an unstructured mesh must be used.

The mesh used can be composed by triangular or quadrilateral elements. However, COMSOL Multiphysics works better with triangular elements and can refine them, while it cannot refine quadrilateral elements. Thus, the mesh will consist of triangular elements. The mesh used consists of two different regions: The inner mesh and the boundary layer mesh. Since boundary layers in COMSOL Multiphysics are created by default using quadrilateral elements, the boundary layer mesh will consist of these elements. After obtaining the mesh it can be useful to use the COMSOL's Refine Mesh tool to refine the zones where shock waves appear. In the case of the ejector, this zone is composed of the outlet of the nozzle and the inlet of the mixing chamber.

Five different meshes have been studied: Normal, finer, fine, extra fine and extremely fine. These meshes are the ones created per default by COMSOL for the physics used, but refining the zones where shock waves appear.

The results obtained for the secondary mass flow for every mesh have been compared in order to select the most appropriate mesh for the simulation. Two studios have been carried out: The initialization studio, in which the tuning parameter for the inconsistent stabilization is decreased until it reaches 0, and a second studio in which the primary stagnation pressure has been increased from 1.5 bar_{abs} to 4 bar_{abs} using steps of 0.25 bar. In order to find the convergence of the simulation, the relative error has been computed respect to the extremely fine mesh. The results obtained are shown in Fig. 5. 4 and Fig. 5. 5. The time of the simulation is the time needed to compute the whole range of primary pressure and the continuation studio done to decrease the inconsistent stabilization tuning parameter.

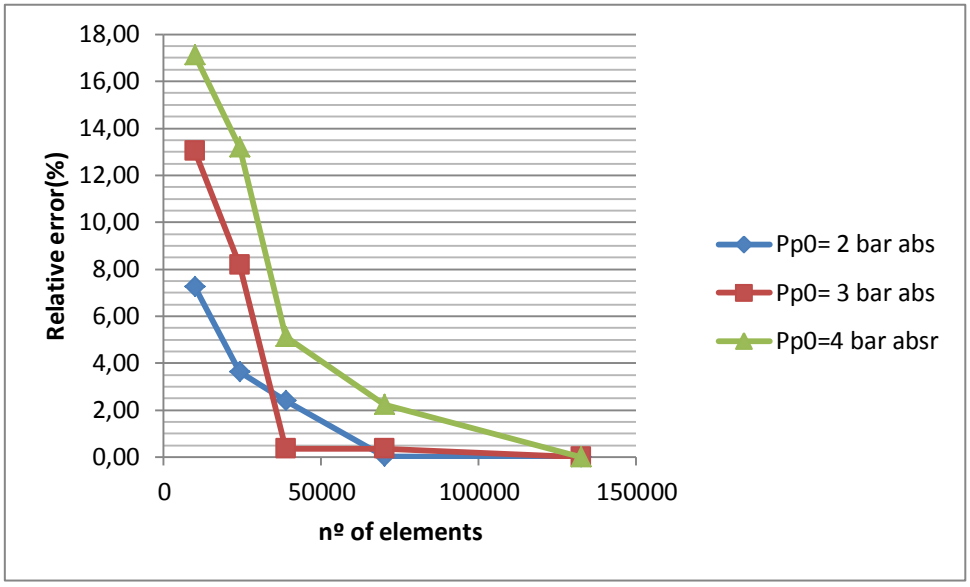

Fig. 5. 4- Relative error respect to the finest mesh vs number of elements of the mesh.

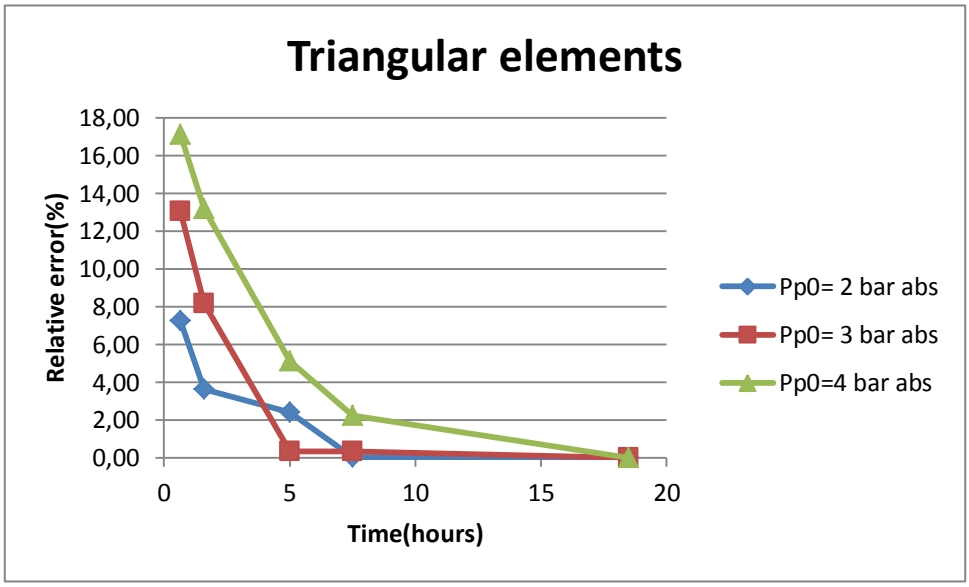

Fig. 5. 5- Relative error respect to the finest mesh vs time.

As it can be seen, for low values of pressure the error is low for relatively coarse meshes. However, the problem does not converge for Pp0=4 bar abs, so that finer meshes would be needed. Since the simulation of the whole ranges of pressures takes more than 15 hours with the extremely finer mesh, it is not possible to refine the mesh further since a lot of simulations will have to be done and time is an important issue. However, in some simulations it will be needed to work with higher pressures, so the error can be larger than the one obtained in this studio.

Since the simulations are computed in a cluster where up to eight simulations can be carried out in parallel, it is not a bad option to use the extra fine mesh, which is composed of 70072 elements, because 8 simulations that include the whole range of primary pressures can be computed with a low error in 7 hours.

Thus, the chosen mesh will be the extra fine mesh. This mesh is shown in Fig. 5. 6. The implementation of this mesh is explained in Appendix A.

This mesh can see too fine, but it must be taken into account the appearance of shock diamond wave patterns (for example, see Fig. 5. 11 in section 5.3.7) and the abrupt changes of the variables of the problem inside the ejector.

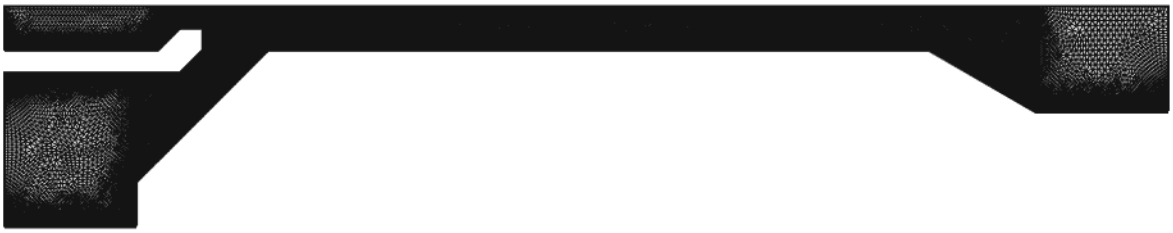

Fig. 5. 6- Chosen mesh.

5.3.6. Cluster computation

The simulations have been computed on a remote cluster provided by the fluid mechanics department of the EUETIB. The cluster has 32 cpu and 64 Gb of RAM. The simulations must be uploaded to the cluster using a software like WinSCP and knowing the IP, user and password of the cluster. Then, a software like Putty can be used to communicate with the cluster and execute the simulations, stop them or see which processes are currently running on the cluster. 4 cpu have been used for every simulation.

5.3.7. Example

In order to give an example of the simulation of an ejector, the model is used to solve the problem of an ejector with the geometry and mesh shown in Fig. 5. 6 and assuming that $P_b=P_{s0}=1.2$ bar_{abs}. This geometry corresponds with the geometry of the ejector used in Chapter 6 to validate the model, but with a nozzle position equal to 1.5 mm. The gas is air and both the primary and secondary stagnation temperatures are set to 298 K. The problem will be solved for a range of primary stagnation pressures between 1.75 and 4.5 bar_{abs} with an increase of 0.25 bar between every value of P_{p0} solved. The implementation of this simulation in COMSOL is explained step by step in Appendix A.

As explained before, the simulation consists of two different studios: An initialization study where the problem is solved for $P_{p0}=1.75$ bar_{abs} with a certain amount of isotropic diffusion which is reduced iteratively, and then a second study in which there is no isotropic diffusion and the problem is solved for every desired value of P_{p0} using the results of the previous value of P_{p0} as the initial values of the problem.

This work is focused on the mass flows produced by the ejector, so this information is the most important in every simulation. Moreover, the variation of the primary, secondary and mixed mass flows with the primary stagnation

pressure give a lot of information about the flow within the ejector. The mass flow that crosses a boundary can be obtained using:

$$\dot{m} = \int_L 2\pi r \rho c_n \, dr \qquad \textbf{Eq 5. 34}$$

Where c_n is the component of the velocity normal to the boundary and L is its length. The primary, secondary and mixed mass flows can be obtained applying Eq 5. 34 to the primary and secondary inlets and the outlet. The different mass flows obtained for the different values of P_{p0} studied are shown in Fig. 5. 7.

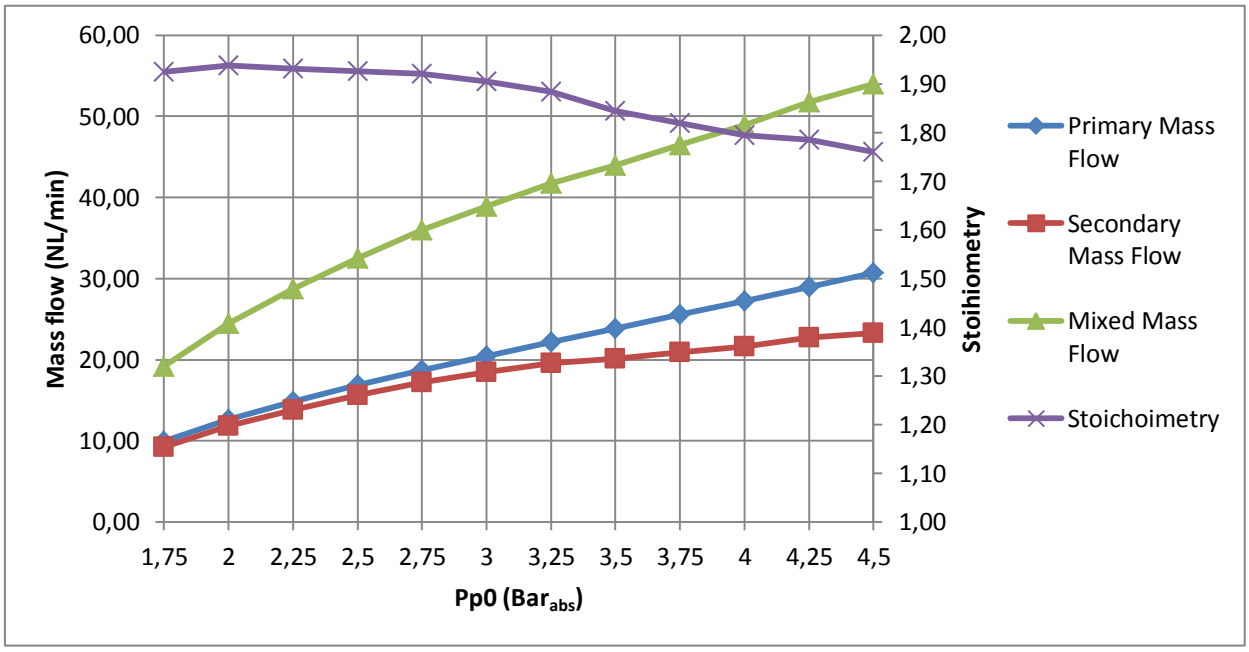

Fig. 5. 7- Mass flows obtained for the different values of P_{p0} analyzed.

Since the secondary flow increases with pressure, the ejector is working in the subcritical mode. For P_{p0}=1.75 bar_{abs}, the primary mass flow function is not a line, so the throat is not choked yet and the flow should be subsonic throughout the ejector. The throat should begin to be choked for P_{p0}=2.25 bar_{abs} since the primary mass flow function is a line for higher values of P_{p0}. However, for this pressure the secondary flow is not yet choked since the mixed mass flow function is not a line. A secondary throat should appear for P_{p0}=3.25 bar_{abs}. For this value of pressure, both primary and secondary flows are choked in the mixing chamber. For higher values of pressure, the change of primary and mixed mass flows is linear and the secondary flow increases slowly as the ejector is getting close to its critical mode (Fig. 4. 15). From this point on, the flow inside the mixing chamber should follow a shock diamond wave pattern (Section 4.2.2).

The obtained values of pressure, temperature and Mach number for P_{p0}=1.75 bar_{abs}, 2.25, 3.25 and 4.5 bar abs are shown in Fig. 5. 8, Fig. 5. 9, Fig. 5. 10 and Fig. 5. 11. As can be seen, the behavior of the flow inside the ejector is the one predicted above using the information in Fig. 5. 7.

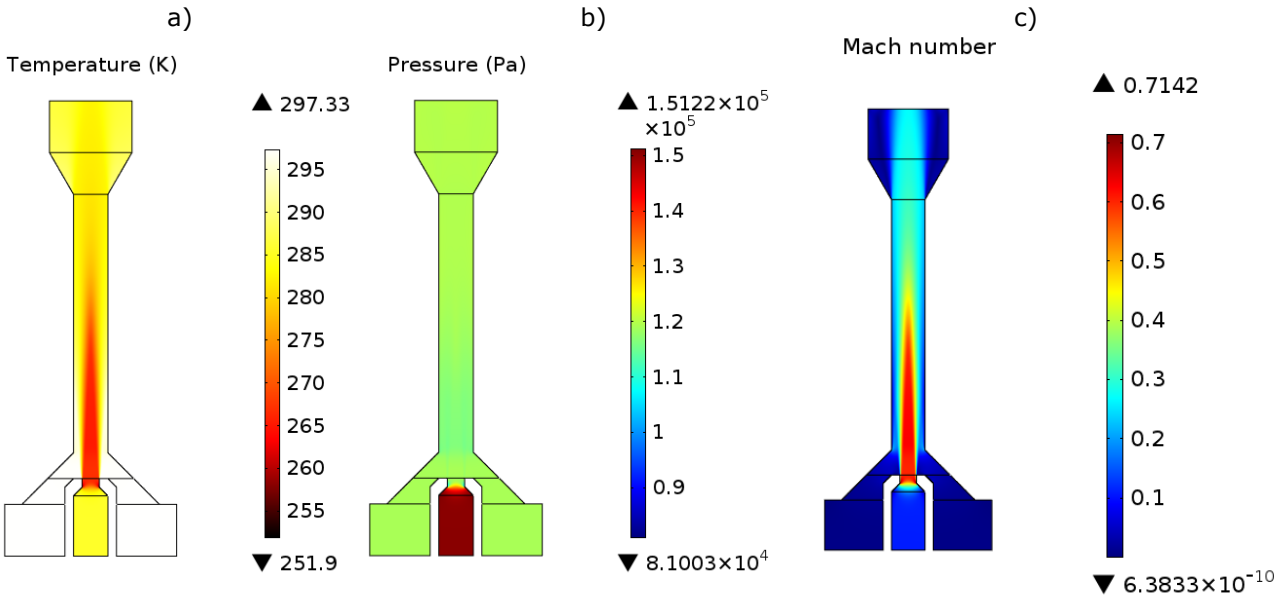

Fig. 5. 8- Results for P_{p0}=1.75 bar_{abs}. a) Temperature. b) Pressure. c) Mach Number.

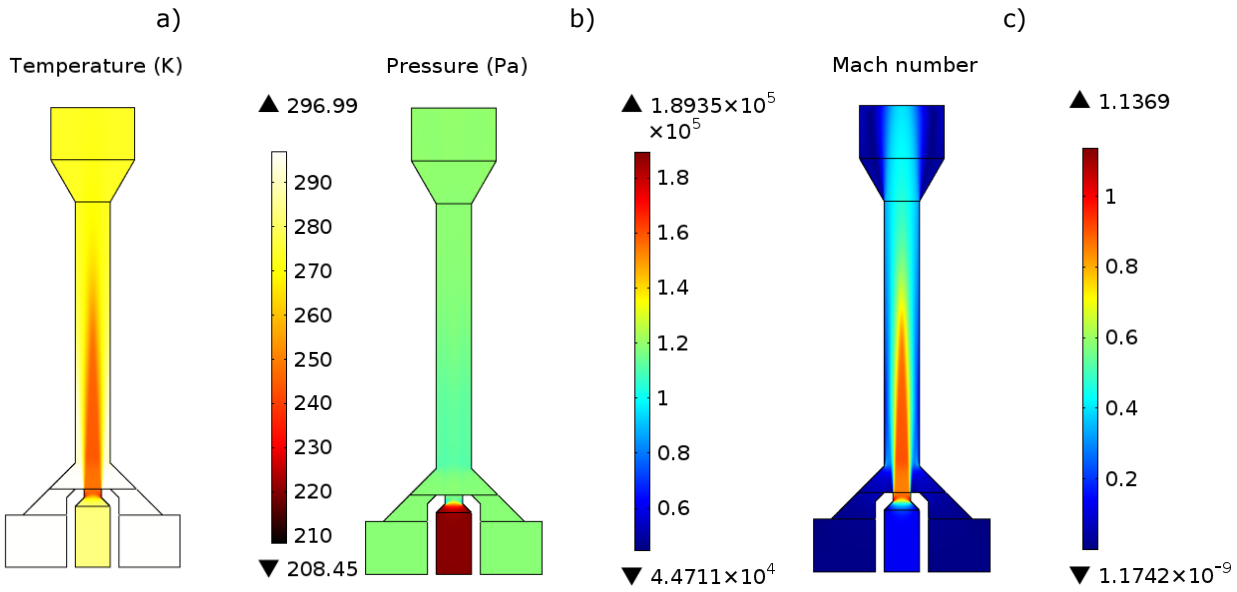

Fig. 5. 9- Results for P_{p0}=2.25 bar_{abs}. a) Temperature. b) Pressure. c) Mach Number.

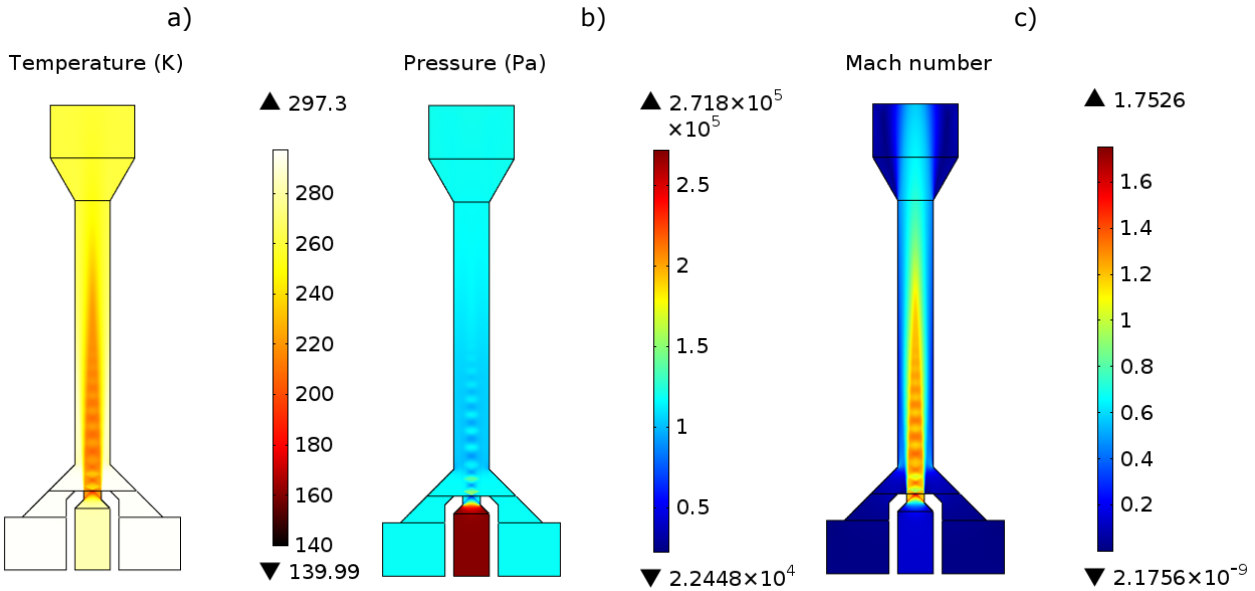

Fig. 5. 10- Results for P_{p0}=3.25 bar_{abs}. a) Temperature. b) Pressure. c) Mach Number.

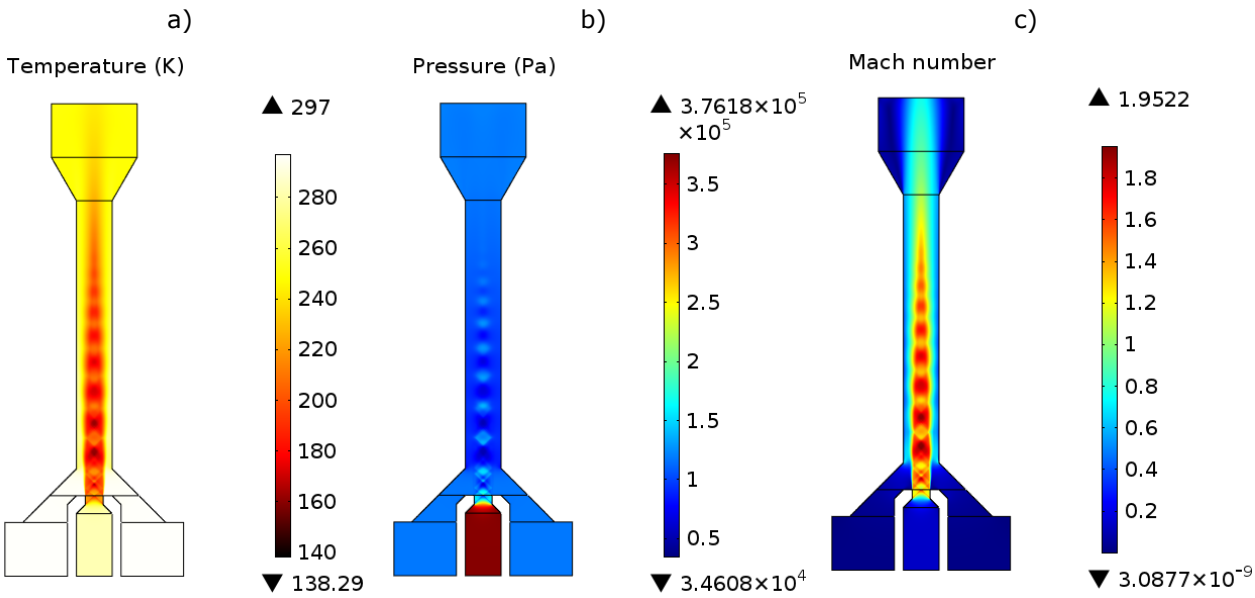

Fig. 5. 11- Results for P_{p0}=4.5 bar_{abs}. a) Temperature. b) Pressure. c) Mach Number.

5.3.8. Modeling an experimental nozzle

In order to validate the model it was used to simulate an experimental convergent-divergent nozzle. This nozzle is used by the Department of Fluid Mechanics of the EUETIB to teach about the features of supersonic flow and how nozzles work.

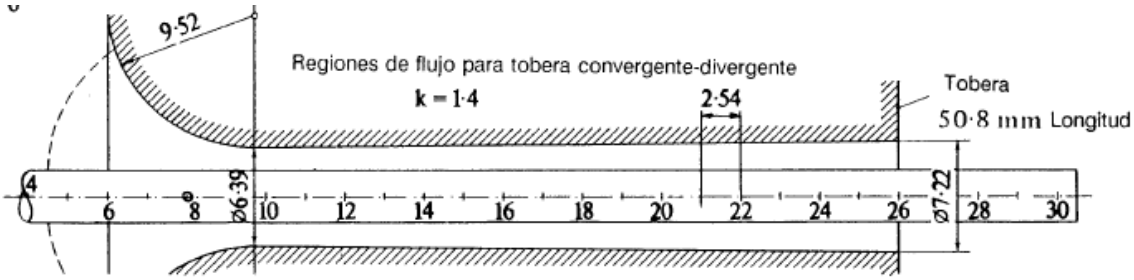

Fig. 5. 12- Geometry of the experimental convergent-divergent nozzle. (EUETIB, Manual de Prácticas de Ingeniería de Fluidos: Flujo Compresible en Toberas, 2010)

The geometry of the nozzle is shown in Fig. 5. 12. This nozzle is studied experimentally in the experimental set-up shown in Fig. 5. 14 and Fig. 5. 13. This experimental set-up can be used to study convergent and convergent-divergent nozzles using air. At point 1 there is a compressor which supplies compressed air to the tank in point 2. There is a valve between 2 and 3 that is used to regulate stagnation pressure at the inlet of the nozzle and mass flow through the nozzle. Point 3 is the central body of the experimental set-up. The body is composed by the nozzle, two manometers and a thermometer. The first manometer is used to measure the stagnation pressure of the air and the thermometer measures the temperature of air at the inlet of the nozzle. The second manometer is coupled to an axial pressure meter that can move along the nozzle and it is used to measure the pressure at different points of the nozzle. The valve situated after the body allows the regulation of the back pressure. After this valve there is a thermometer that measures the temperature of the air leaving the nozzle. At point 4, air passes through an orifice plate and a manometer which are used to measure the mass flow and back pressure.

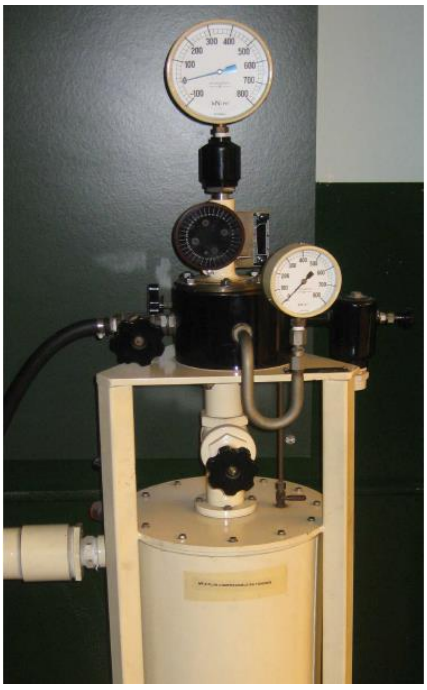

Fig. 5. 14- Experimental set-up. (EUETIB, Manual de Prácticas de Ingeniería de Fluidos: Flujo Compresible en Toberas, 2010)

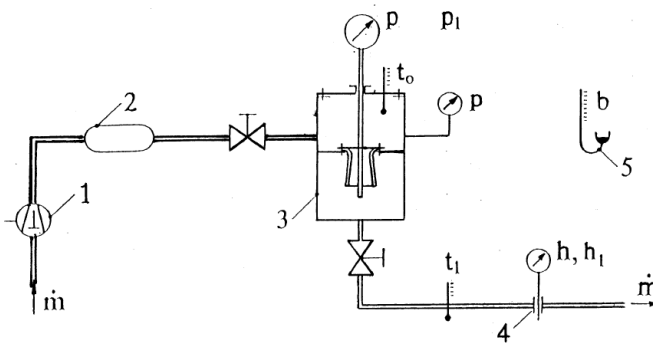

Fig. 5. 13- Layout of the experimental set-up. (EUETIB, Manual de Prácticas de Ingeniería de Fluidos: Flujo Compresible en Toberas, 2010)

Two different series of pressures were studied: One with a stagnation pressure of 3.8 bar_{abs} and another with a stagnation pressure of 6 bar_{abs}. For every series, three different back pressures were studied: One in which the nozzle was fully subsonic, another where the throat was choked and there was a shock wave inside the diverging section of the nozzle and another in which the nozzle worked under design conditions.

The experimental results obtained are shown in Fig. 5. 15 and Fig. 5. 16. z is the axial position of the pressure sensor inside the nozzle.

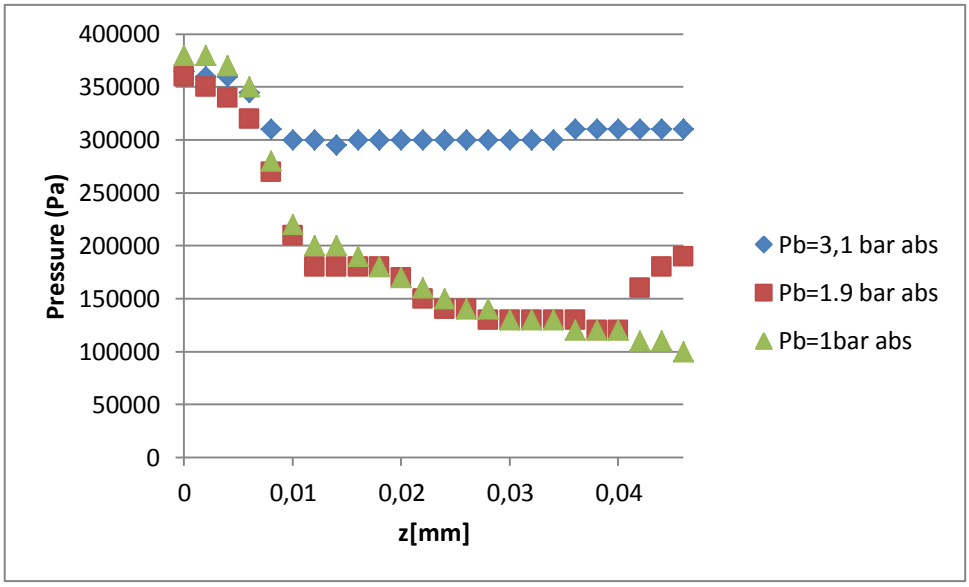

Fig. 5. 15- Pressure along the axis of the nozzle for a stagnation pressure of 3.8 bar_{abs} and three different back pressures.

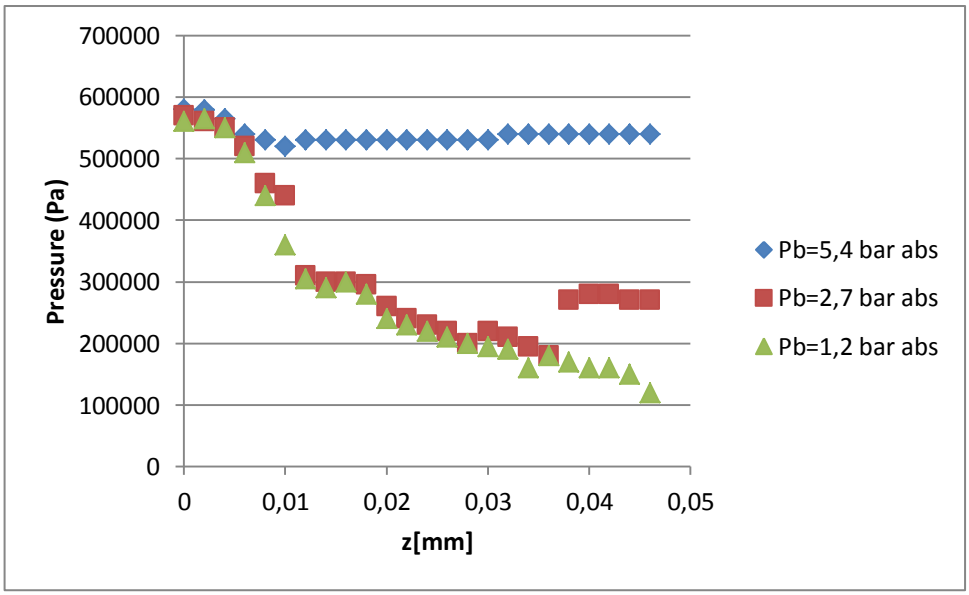

Fig. 5. 16- Pressure along the axis of the nozzle for a stagnation pressure of 6 bar_{abs} and three different back pressures.

The first attempt to model the nozzle was using its exact geometry but simplifying it to a 2D axisymmetric geometry (Fig. 5. 17 a). However, the k-ε model is not able to work with highly rounded geometries, so that it was impossible to achieve convergence without adding too much isotropic diffusion or

without working with a worse tolerance. Both affected the results obtained so that they did not match reality.

The second attempt made to model the nozzle was to approximate the nozzle using two lines and three points: the diameter of the inlet, the diameter of the throat and the diameter at the outlet (Fig. 5. 17 b). However, the results obtained could not be compared with reality since the high angle of the converging section of the nozzle produced the appearance of strong oblique shock waves (Fig. 5. 18).

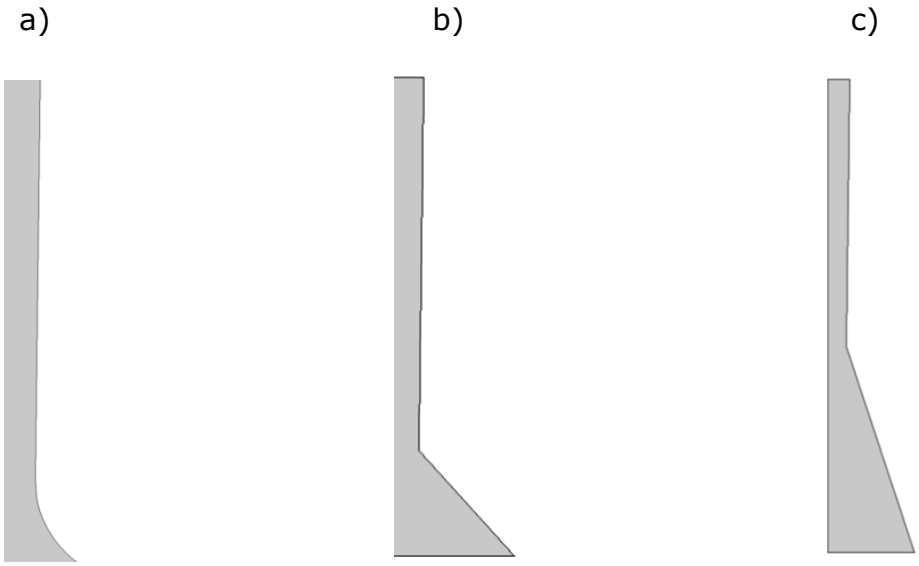

Fig. 5. 17- Geometries used in the simulation. a) First attempt (Real geometry). b)Second attempt. c)Third attempt.

The third attempt made to model the nozzle consisted of increasing the length of the converging section from 11 mm to 30 mm, reducing its angle (Fig. 5. 17 c). In this way, the oblique shock waves that appeared in the solution were weaker and had a lower effect over the solution.

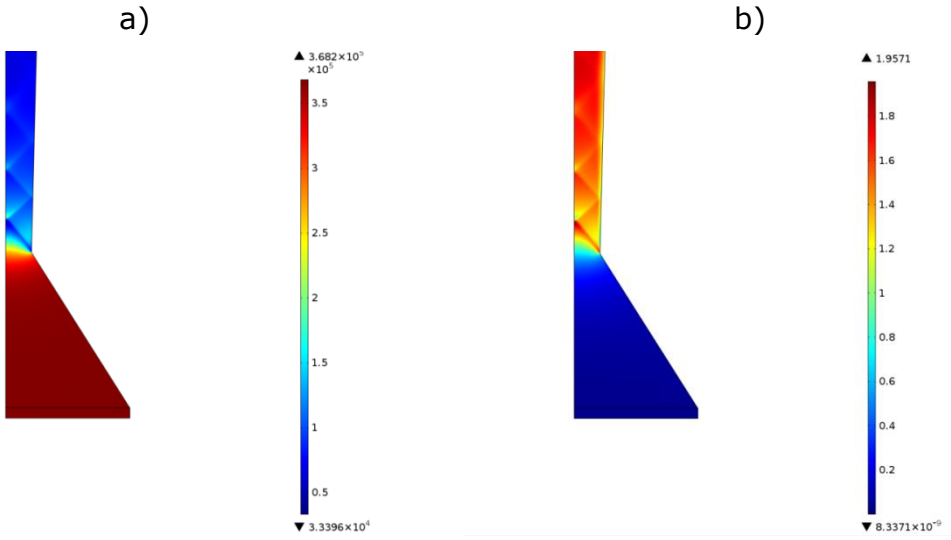

Fig. 5. 18- Results obtained with the second geometry (P_0=3.8 bar abs, P_b=1 bar abs). There are strong oblique shock waves that perturb the solution. a)Pressure (Pa). b) Mach number.

The mesh used to compute the third geometry is a structured mesh with quadrilateral elements. The number of divisions in the radial direction is 25, while in the axial direction there are 40 divisions in the convergent section and 90 in the divergent section. The boundary layer is also composed by quadrilateral elements. The mesh used is shown in Fig. 5. 19.

Fig. 5. 19- Mesh.

The obtained values of pressure along the axis were compared with the experimental results, taking into account that the convergent section used in the simulation has a larger length than the real one (Fig. 5. 20, Fig. 5. 21, Fig. 5. 22, Fig. 5. 23, Fig. 5. 24 and Fig. 5. 25).In the figures, the lines show the distribution of pressure obtained with the model, and asterisks are the results measured experimentally.

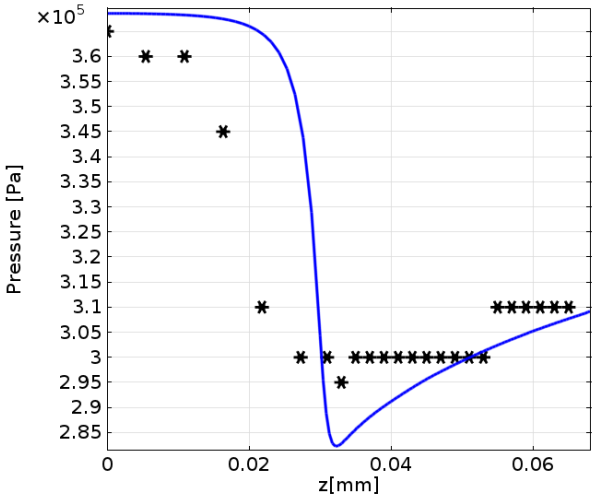

Fig. 5. 20- P_p=3.8 bar abs, P_b=3.1 bar abs.

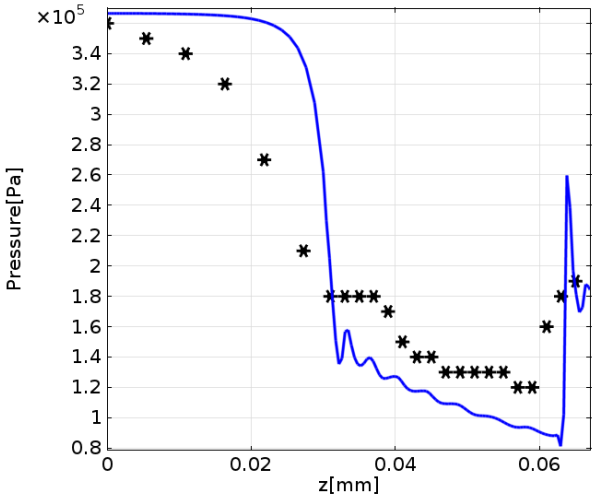

Fig. 5. 21- P_p=3.8 bar abs, P_b=1.9 bar abs.

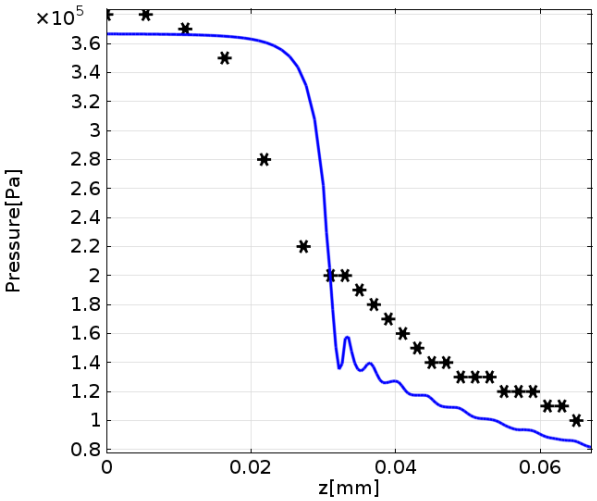

Fig. 5. 22- P_p=3.8 bar abs, P_b=1 bar abs.

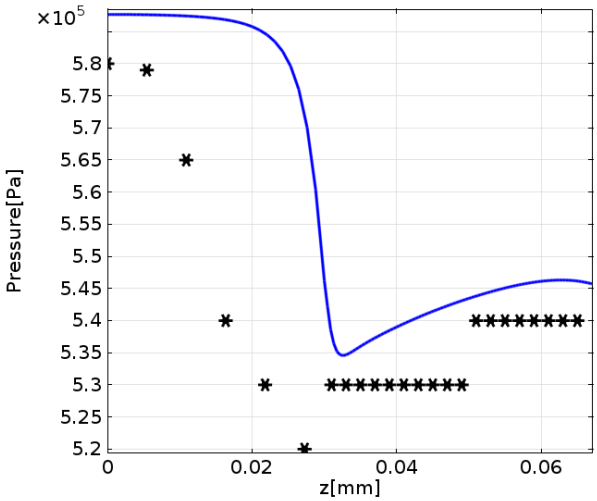

Fig. 5. 23- P_p=6 bar abs, P_b=5.4 bar abs.

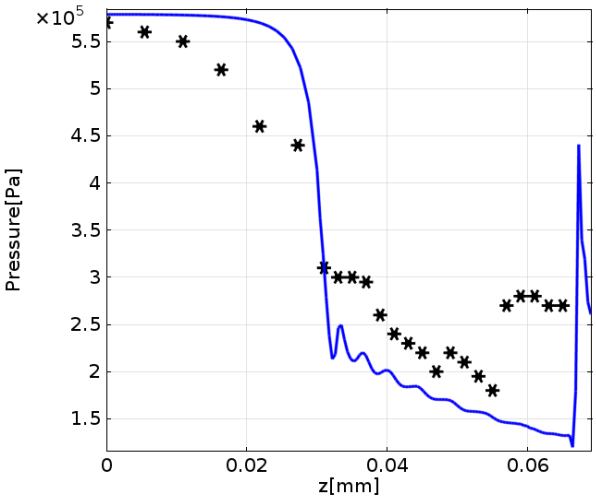

Fig. 5. 24- P_p=6 bar abs, P_b=2.7 bar abs.

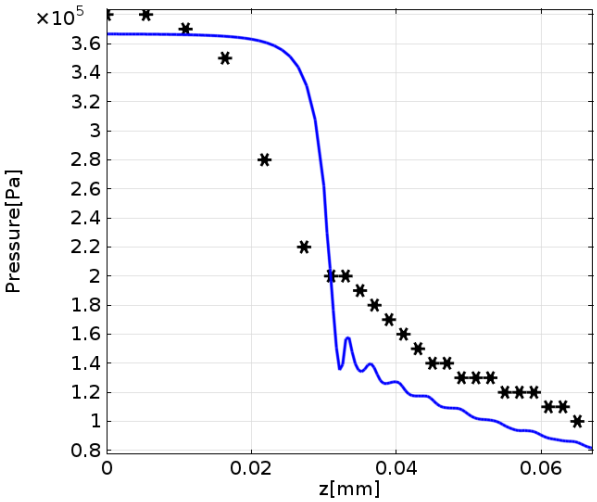

Fig. 5. 25- P_p=6 bar abs, P_b=1.2 bar abs.

The results obtained show that, in the diverging section, the model works quite well for subsonic flow (Fig. 5. 20 and Fig. 5. 23) and for supersonic flow under the design conditions of the nozzle (Fig. 5. 22 and Fig. 5. 25). It has also demonstrated its ability to detect the presence of shock waves (Fig. 5. 26), however, it has problems to find the exact position where the wave takes place (Fig. 5. 21 and Fig. 5. 24). In the converging section there are small differences between the simulation and the experimental data since the geometry simulated is not the same as the real geometry.

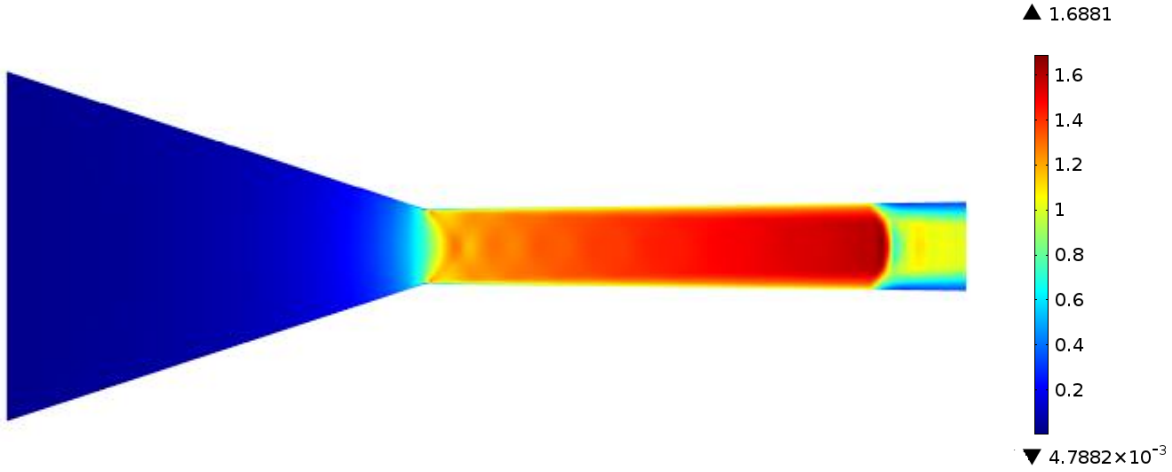

Fig. 5. 26- Mach number for P_p=3.8 bar_{abs} and P_b=1.9 bar_{abs}. A shock wave appears near the outlet of the nozzle.

CHAPTER 6: EXPERIMENTAL VALIDATION OF THE CFD MODEL

In Chapter 5 the CFD model has been tested by modeling an experimental convergent-divergent nozzle.

The CFD model was also validated experimentally at IRII Fuel Cells laboratory in order to demonstrate that it is able to predict the mass flows and stoichiometry produced by the ejector under different pressure conditions. This experimental validation was carried out manufacturing an ejector and experimenting it with air. The geometry of the ejector used in the validation was designed and fabricated taking into account that another ejector will have to be manufactured to be used in Test Station 4. In order to avoid the manufacturing of another whole ejector, the mixing chamber and the nozzle of the ejector can be changed by only manufacturing two small pieces. Thus, some of the pieces of the experimental ejector can be used in the final ejector.

6.1. Layout of the experimental set-up

A scheme of the experimental set-up used to validate the model is shown in Fig. 6. 4.The different elements used are summarized in Table 6.1.

The objective of this validation was to compare the mass flows predicted by the CFD model with the mass flows obtained for a certain pressure conditions. The primary mass flow can be controlled using either a mass flow controller or a

pressure regulator, while the amount of recirculation that can achieve the ejector is measured by placing a mass flow meter at the outlet, thus obtaining the sum of the primary and secondary mass flows. Since mass flow meters are used, the gas has to be synthetic air to avoid the presence of humidity and impurities.

The experimental set up can be used in two different modes: The normal mode and the recirculation mode. In the normal mode, valves V4 and V5 are closed, and the primary and secondary inlets of the ejector are connected to the synthetic air bottle. Both lines have a flow valve (V1 and V2) and a pressure regulator (PR1 and PR2) at the inlet which are used to regulate the primary and secondary stagnation pressures. The primary line is also composed of a mass flow controller (MFC1) to control the primary mass flow, a pressure transmitter (P1) and a thermocouple (T1), all of them situated just before the primary inlet of the ejector. The mass flow controller can be used either as a controller or just as a flow meter. A filter (F1) is placed before the mass flow controller, and a check valve (CV1) after it. The secondary line has two sensors: a pressure transmitter (P2) and a thermocouple (T2). The outlet line (after the ejector) is composed of a pressure transmitter (P3), a mass flow meter (MFS1), a filter (F2), a check valve (CV2) and a flow valve (V3) which is used to control the back pressure. After passing through valve V3, the flow is exhausted to the atmosphere.

In the recirculation mode, valves V4 and V5 are open and V2 and V3 are closed. In this mode only the primary stagnation pressure is controlled, either by MFC1 or PR1, while the flow measured by MFS1 is only the secondary flow produced by the ejector. The back pressure is controlled using valve V5. A check valve (CV3) is placed at the outlet to avoid the presence of humidity in the mass flow meter MFS1.

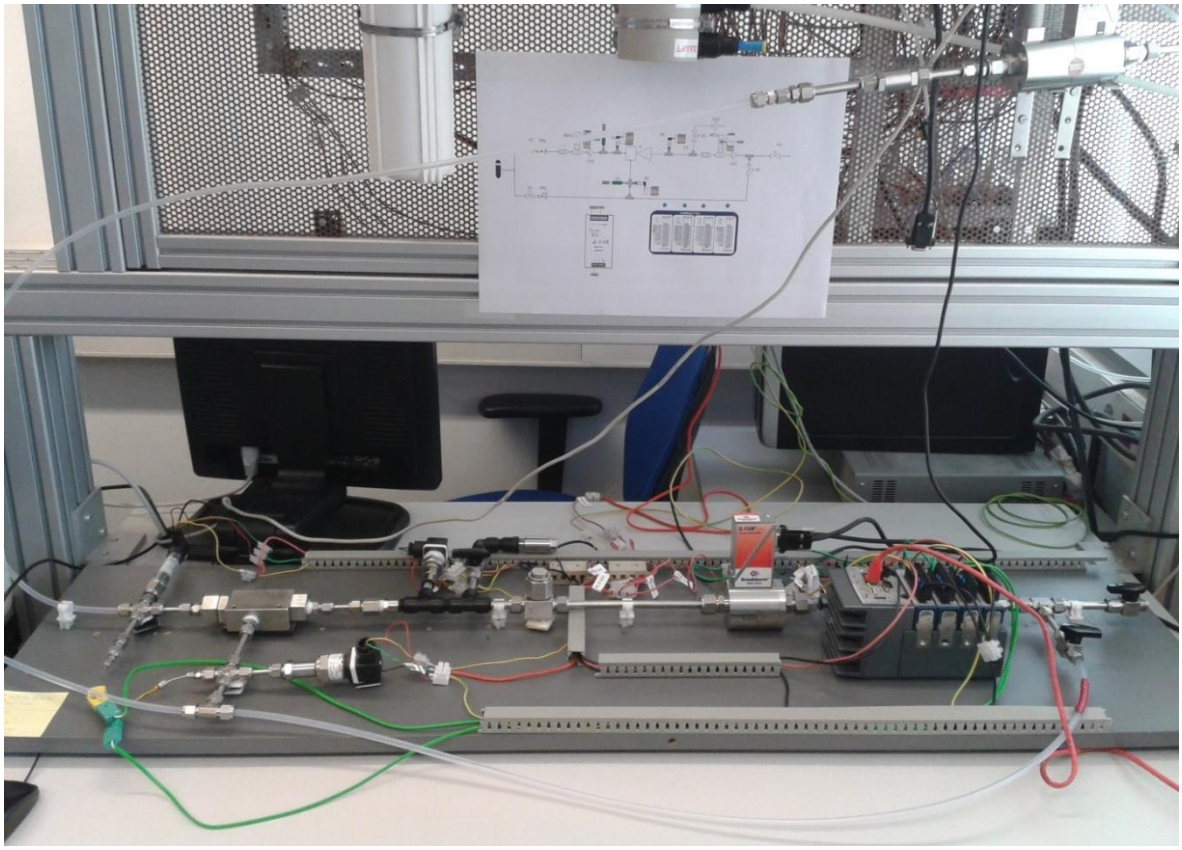

Fig. 6. 1- Picture of the assembly of the experimental validation.

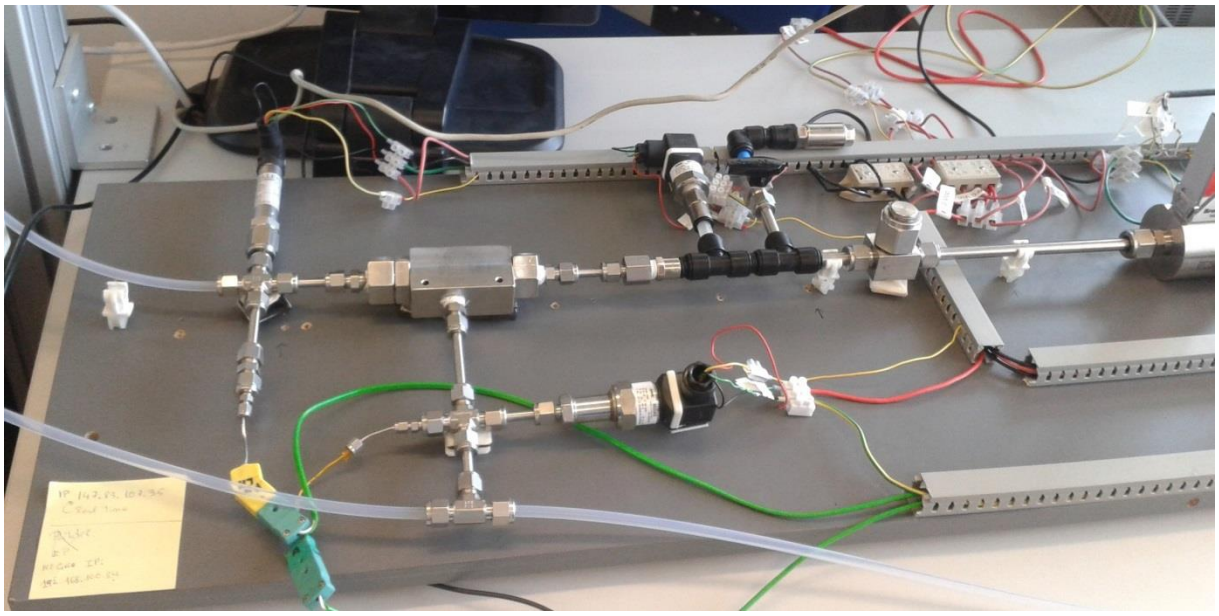

Fig. 6. 2- Picture of the experimental set-up.

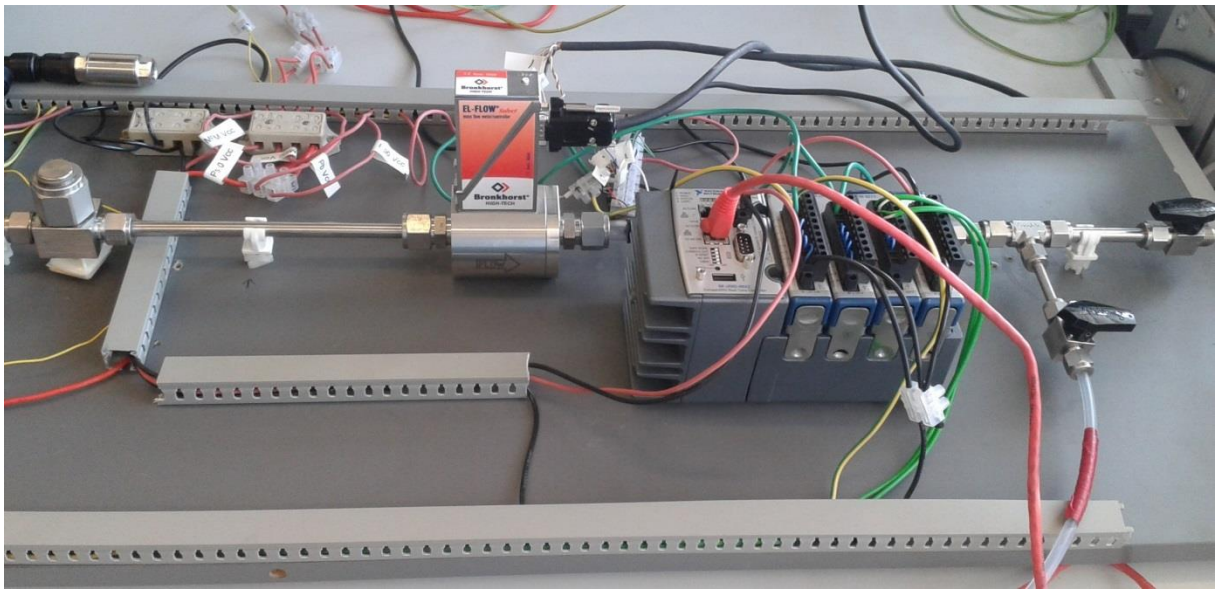

Fig. 6. 3- Picture of the experimental set-up.

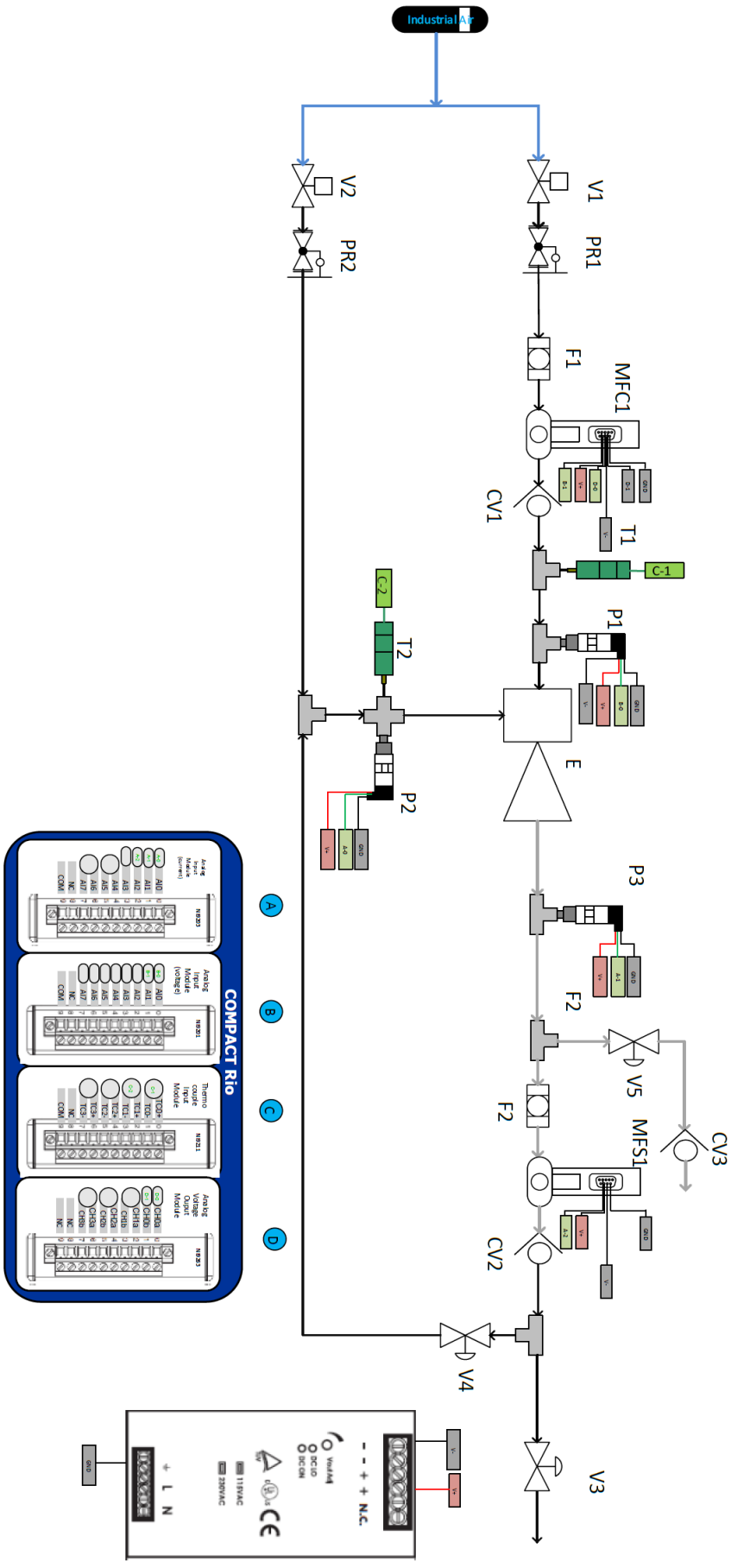

Fig. 6. 4- Layout of the experimental set-up.

Table 6. 1- Elements used in the experimental validation.

Nº	Code	Element	Specifications
2	V1, V2	2 Way Flow valve 	Hy-Lok Ball Valves 110 serie BVH-10M-S316
3	V3, V4,V5	2 Way Flow valve 	Swagelok Ball Valve SS-42S4
2	PR1,PR2	Pressure regulator 	Pressure regulator used to reduce pressure. The maximum pressure that can be obtained is 7 bar.
1	F1	Filter 	Swagelok in-line filter SS-6F-MM
1	F2	Filter 	Swagelok tee-type filter SS-10TF-MM-140 End Connections: 10 mm Nominal pore size: 140 µm
1	CV1	Check valve 	Swagelok check valve SS-6C-1/3

2	CV2,CV3	Check valve 	Legris check valve 4890 13 13 Maximum pressure: 40 bar
1	MFC1	Mass Flow Controller 1 	Bronkhorst High-Tech Mass Flow Controller Model: F-202AV-AAD-55-V Range: 0.8-150 Nl/min (Air) Analog output: 0-5 V_{DC} Digital communication: Standard RS232 Supply: 15 V_{DC} (290 mA) or 24V_{DC} (200 mA)
1	MFS1	Mass Flow Meter 1 	Bronkhorst High-Tech Mass Flow Meter Model: F-112Ac—M10-AGD-55-V Range: 0.8-100 Nl/min (Air) Analog output: 4-20 mA Digital communication: Standard RS232 Supply: 15 V_{DC} (95 mA) or 24V_{DC} (65 mA)
1	P1	Pressure sensor 1 	Keller pressure transmitter: PR-21S/6bar Range: 0-6 bar Output: 0-10V_{DC} Supply: 13-28V_{DC}
2	P2,P3	Pressure sensors 2 and 3 	Jumo Midas pressure transmitter: 401001/000-456-405-502-20-601-61/000 Range: 0-2.5 bar Output: 4..20 mA Connection: G 1/4

2	T1,T2	Thermocouple 	RS thermocouple type K 363-0250
1	E	Ejector 	Experimental ejector (see Section 6.2.2 and drawings 1-6)

6.2. Geometry of the experimental ejector

Different geometries were simulated using COMSOL in order to select the geometry of the experimental ejector. The geometry of the ejector was selected taking into account two different factors: the range of mass flows that can be measured in the Fuel Cell laboratory and the impediments due to the manufacturing of the ejector.

A first initial solution, which used the optimum geometrical parameters proposed in the literature (Section 4.2.1), was proposed. However, some of its features made its manufacturing process hard and expensive, and therefore the chosen geometry differed from the initially proposed geometry.

6.2.1. Initial solution

The design of the ejector was done taking into account the optimum geometrical relations found in the literature and the impediments imposed by the manufacturing of the pieces. Moreover, it was desirable to have the possibility to change the position of the nozzle in order to test experimentally which is the optimum nozzle position.

The first proposed solution was composed by 3 Swagelok SS-400-1-4 connectors and 4 manufactured pieces: The nozzle, the "outlet" piece (composed by the mixing chamber and the diffuser), the body of the ejector and a hexagonal nut used to change the distance between the nozzle and the mixing chamber (Fig. 6. 5). The stagnation of the ejector is obtained thanks to the NPT threads of the connectors and two o-ring placed at the outlet and nozzle pieces.

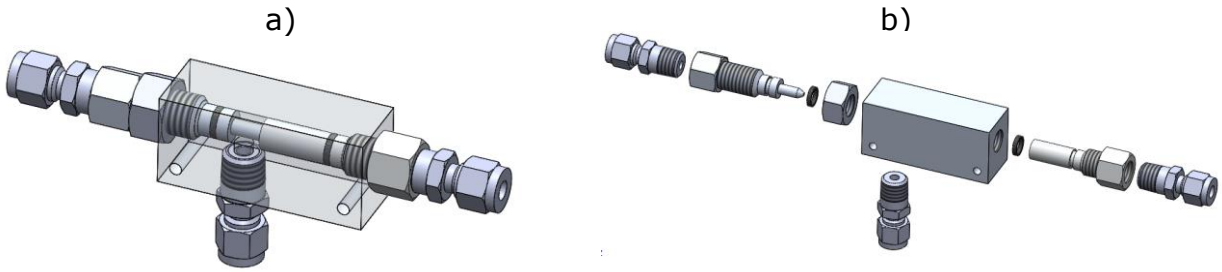

Fig. 6. 5- Initial solution. a)Ejector assembled. b)Exploded view.

A sectional view of the ejector is shown in Fig. 6. 6.

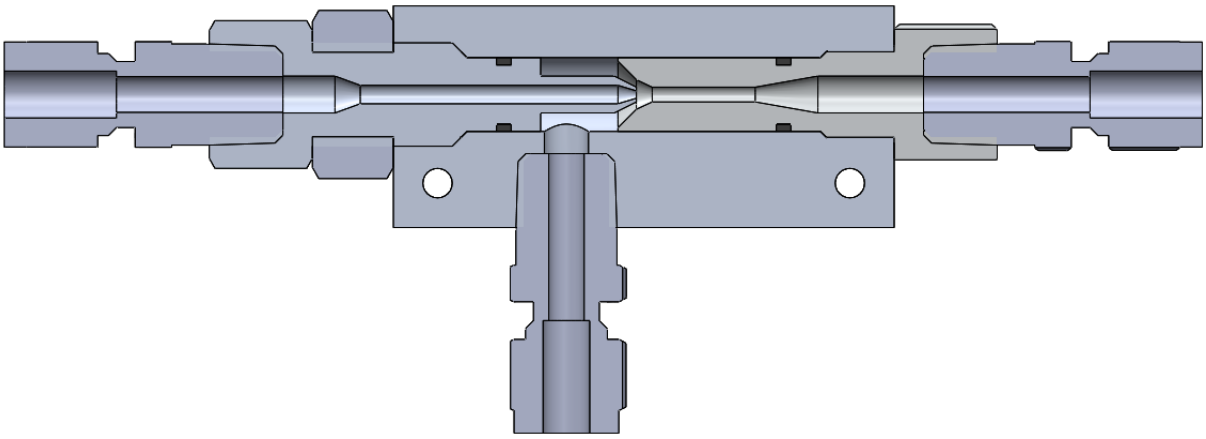

Fig. 6. 6- Sectional view of the initial solution.

The body (Fig. 6. 7 e) has three holes which are connected to the nozzle (Fig. 6. 7 a), the outlet piece (Fig. 6. 7 b) and a connector (Fig. 6. 7 d) using different threads. The other two connectors are connected to the nozzle and the outlet pieces. The thread of the connectors is a NPT ¼'' thread, which is a conical thread used to avoid gas leakage in gas installations. The thread that connects the body with the outlet and nozzle pieces is an M18 thread. An M18 hexagonal nut (Fig. 6. 7 c) is used to change and measure the distance between the nozzle and the mixing chamber. The nozzle and outlet pieces have a groove to insert the o-rings (Fig. 6. 7 f) used to ensure the stagnation of the ejector.

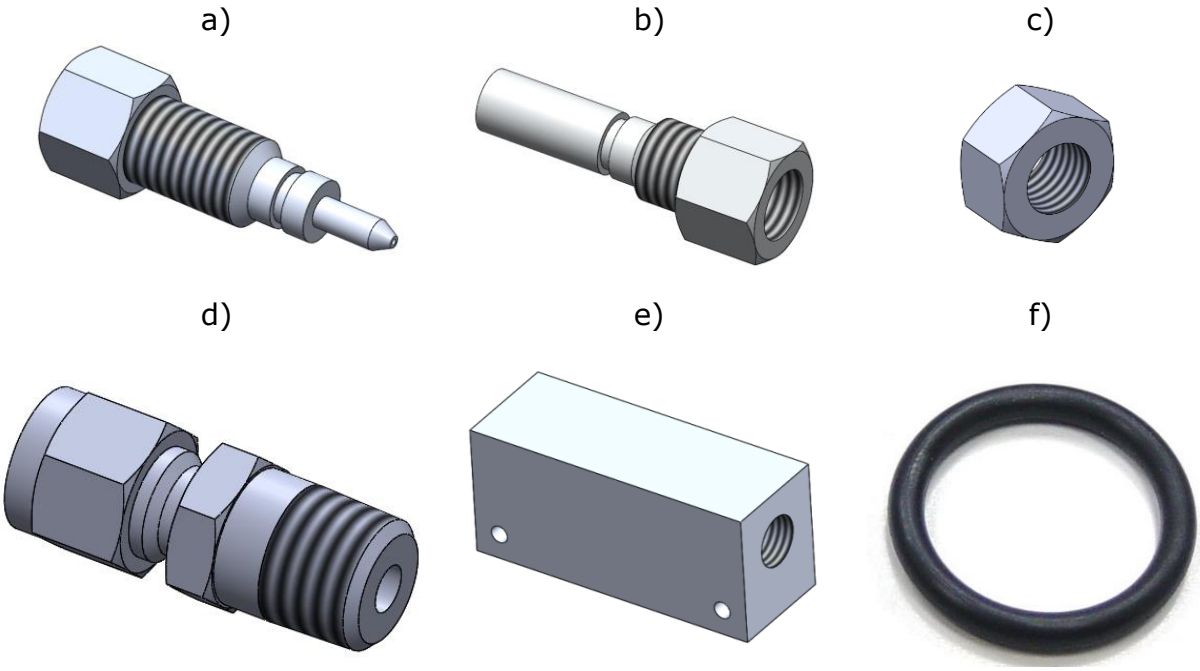

Fig. 6. 7- Parts of the initial ejector. a) Nozzle b)Outlet c)Hexagonal nut d) Connector e) Body f) O-ring

The most important geometrical parameters are shown in Fig. 6. 8.

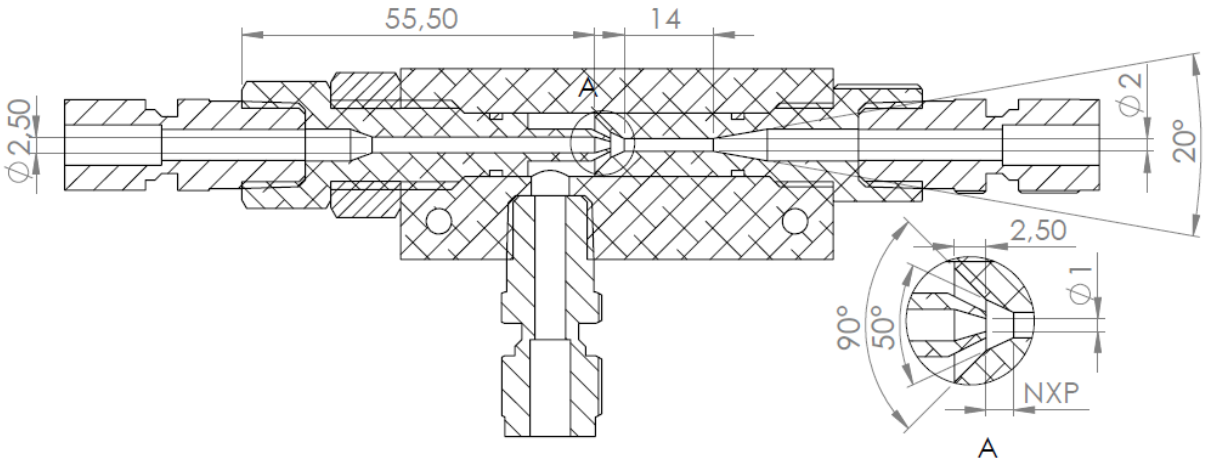

Fig. 6. 8- Sectional view of the initial ejector with some of its dimensions.

The initial solution was simulated using COMSOL Multiphysics. Since the outlet of the ejector is connected to the atmosphere, the back pressure and the stagnation pressure of the secondary stream were assumed to be 1 bar_{abs}. The stagnation pressure of the primary flow was increased from 1.5 bar_{abs} to obtain different primary mass flows. An axisymmetric geometry was used (Fig. 6. 9). Primary and secondary stagnation temperatures were set to 298 K.

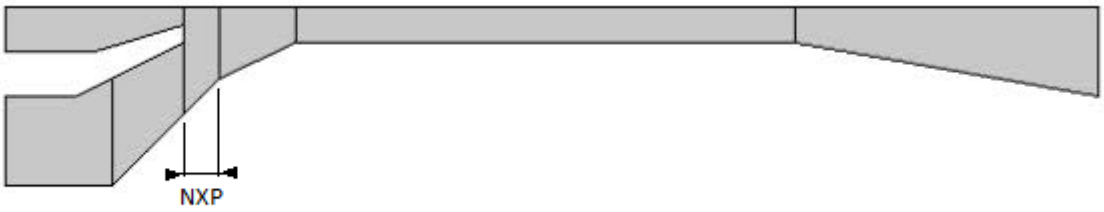

Fig. 6. 9- Geometry used in the CFD simulations of the initial ejector.

The nozzle position (NXP) used in the simulation was 1 mm. The mass flows obtained with the model are shown in Fig. 6. 10.

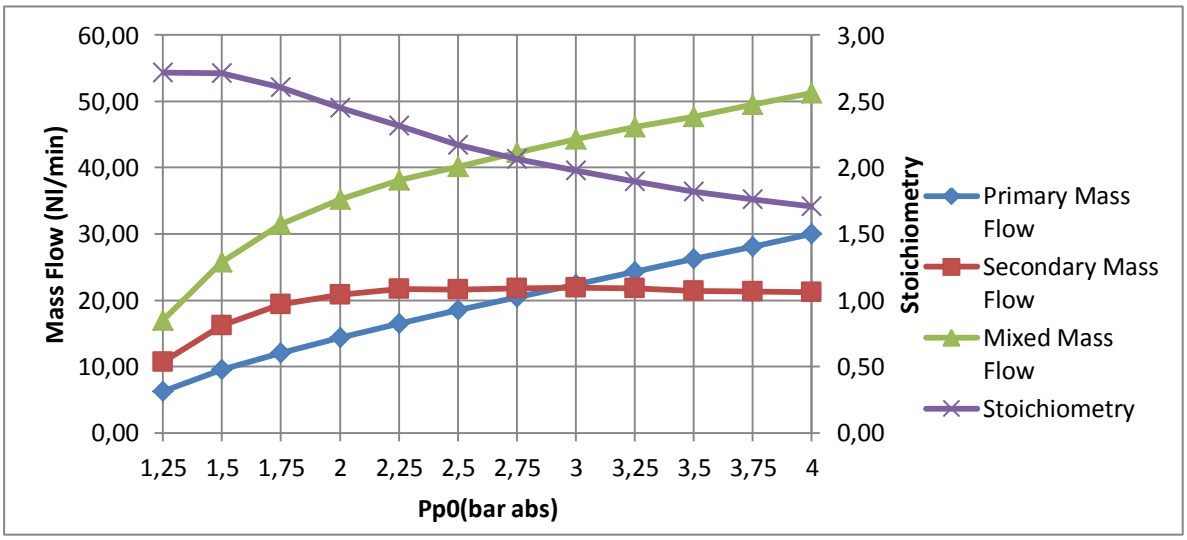

Fig. 6. 10- Mass flows obtained with COMSOL for the initial ejector (P_{s0}=P_b=1 bar_{abs} and T_{s0}=T_{p0}=298 K).

The results obtained from the simulation show that the mass flows obtained with this geometry can be measured with the mass flow meters used. However, some changes are needed in order to reduce the complexity, costs and time of the manufacturing process:

- Since the holes will be obtained through drilling, it is hard to obtain small angles without breaking the drill. Moreover, it is recommendable to use the angle of commercial drills in order to avoid the manufacturing of a drill to be used only for the fabrication of the ejector. Thus, the angles used had to be changed.
- It is recommendable that the length of a hole does not exceed 10 times its diameter. If this length is larger, then it is harder to remove the cheap and the drill will be under higher stress and will break easily. This makes hard to manufacture the nozzle piece, since a drilling length of 55.5 mm is needed to drill a hole with a diameter of 2.5 mm. This can be solved if this piece is separated into 2 different pieces, the nozzle support and the nozzle itself (See the chosen geometry below). This solution also has another advantage: It makes it easier to change the nozzle since the nozzle support does not need to be machined again.
- It is recommendable to change the position of the o-rings in order to ensure stagnation and to avoid the movement of the o-ring.
- The tip of the nozzle should be changed to improve its strength.

6.2.2. Chosen geometry

The final ejector for the experimental validation was designed using the CAD software SolidWorks and manufactured in the Laboratory of Mechanical Engineering of the ETSEIB ("Escola Tècnica Superior d'Enginyeria Industrial de Barcelona"). This ejector is composed of 5 different manufactured pieces, 3 o-rings to seal and 3 connectors (Fig. 6. 11 and Fig. 6. 12). A summary of the parts can be found in Table 6. 2. The technical drawings of the pieces and the assembly of this experimental ejector can be found in the document "Technical drawings" (Drawings 1-6).

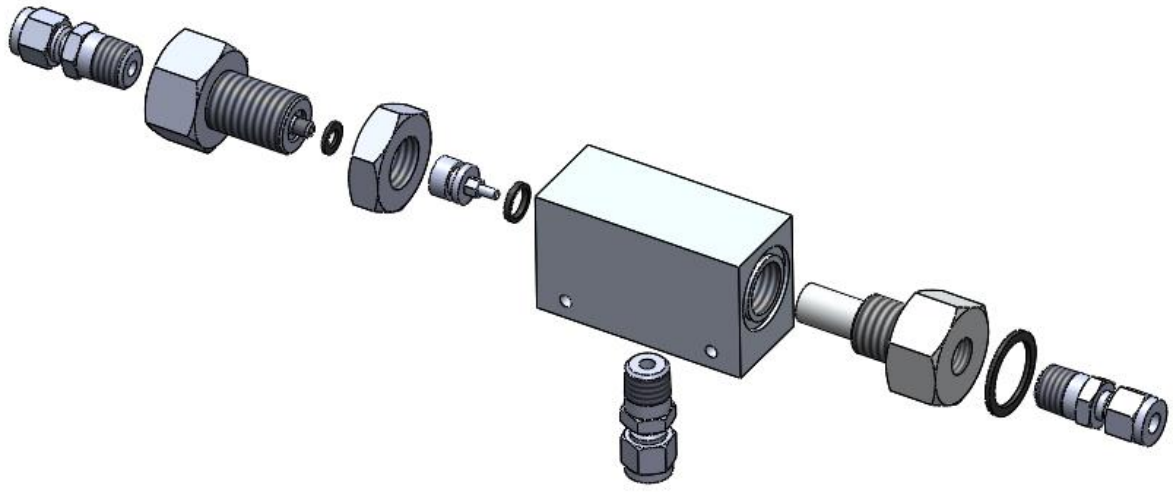

Fig. 6. 11- Solid Works exploded view of the chosen geometry for the experimental ejector.

The nozzle is divided into two different pieces: The nozzle itself and the nozzle support. Both pieces are connected using an M5 thread. This division was done in order to avoid the drilling of a long hole and to be able to change the nozzle without having to manufacture the whole piece again. The nozzle support and the body are connected using an M18 thread, and the nozzle support is connected to the connector using a ¼'' NPT thread. A hexagonal nut with an M18 thread is used to change the distance between the inlet of the mixing chamber and the nozzle.

Fig. 6. 12- Pieces of the experimental ejector.

The mixing chamber and the diffuser were fabricated together as a whole piece called "outlet". This piece is connected to the connector using a ¼'' NPT thread, and a M18 thread is used to connect the outlet to the body.

The connectors used were fabricated by Swagelok, model SS-400-1-4. The o-rings were manufactured by Epidor.

A sectional view of the ejector is shown in Fig. 6. 13 and Fig. 6. 14.

Table 6. 2- Parts of the experimental ejector

Name	**Picture**	**Specifications**
Body		Material: SS316
Nozzle support		Material: SS316

Nozzle		Material: SS316
Outlet		Material: SS316
Hexagonal nut	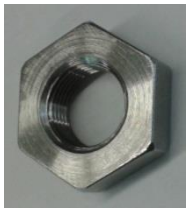	Material: SS316
3 Connectors		Swagelok SS-400-1-4 2 threads: NPT ¼'' BSP ¼''
O-ring 1		Epidor OR 400.762 Material: NBR70 Diameter: 8.73 mm Thickness: 1.78 mm
O-ring 2		Epidor OR 639.922 Material: NBR70 Diameter: 7 mm Thickness: 1.5 mm
O-ring 3		Epidor OR 395.872 Material: NBR70 Diameter: 22.5 mm Thickness: 2 mm

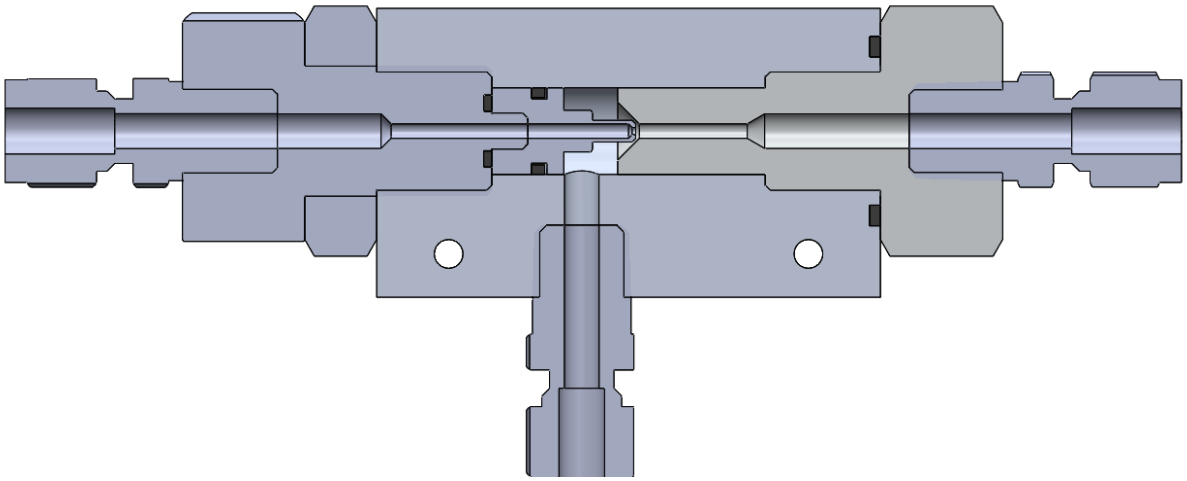

Fig. 6. 13- Sectional view of the ejector.

The dimensions of some of the most important geometric parameters of the ejector can be found in Fig. 6. 14.

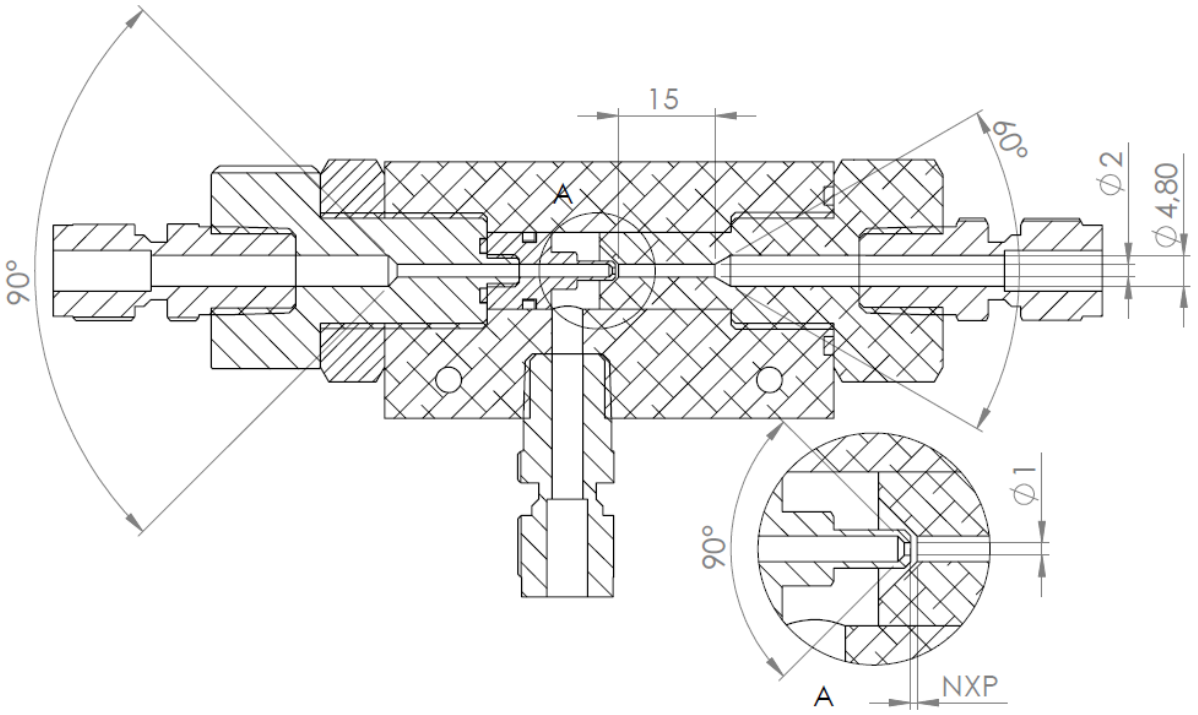

Fig. 6. 14- Sectional view of the ejector with some of its dimensions.

The chosen geometry was also studied using COMSOL Multiphysics. The nozzle position (NXP) used in the analysis was 1 mm, $P_{s0}=P_b=1$ bar_{abs} and $T_{s0}=T_{p0}=298$ K. The results obtained are depicted in Fig. 6. 15.

These results show that the mass flows obtained are within the range of mass flows that can be measured (0.8-100 Nl/min for the mixed flow and 0.8-150 Nl/min for the primary mass flow, see Table 6. 1). It is also clear that the changes introduced with respect to the initial geometry have decreased the ability of the ejector to recirculate air and the stoichiometry obtained is lower. This is due to the fact that some of the geometrical parameters used are not the optimal ones.

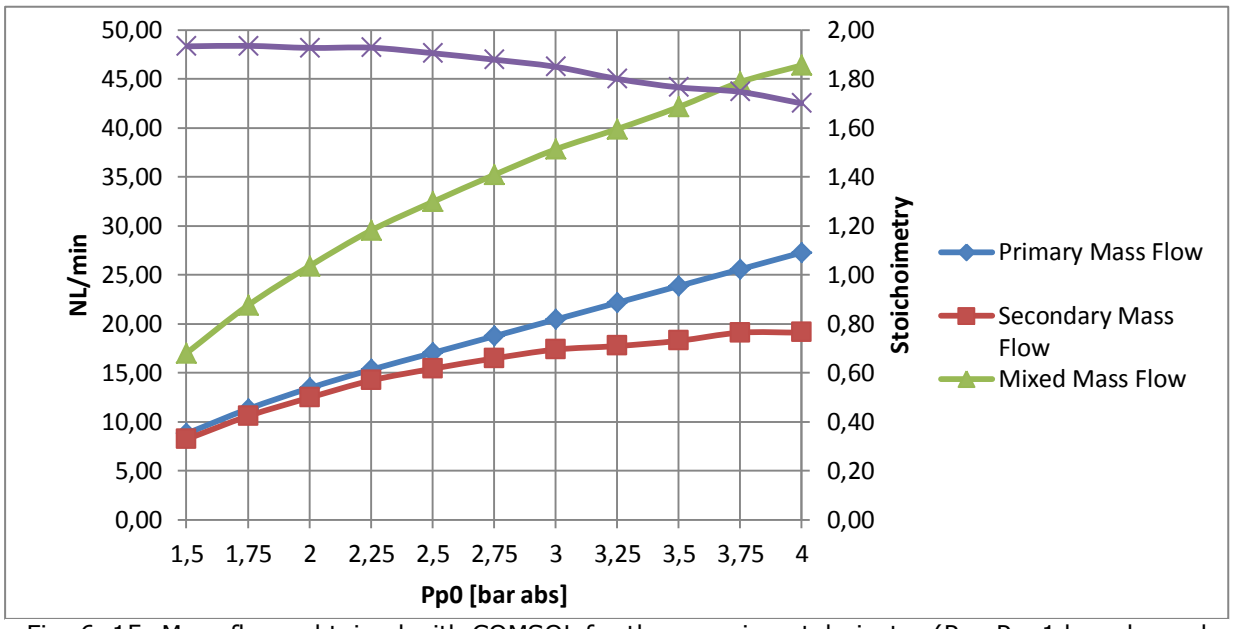

Fig. 6. 15- Mass flows obtained with COMSOL for the experimental ejector (P_{s0}=P_b=1 bar abs and T_{s0}=T_{p0}=298 K).

The distributions of temperature, pressure and Mach number obtained for P_{p0}=4 bar_{abs} are shown in Fig. 6. 16. The minimum temperatures obtained are very low (140 K), which could be a problem due to the contraction of the steel in the mixing chamber. However, these low temperatures are very punctual and appear at the middle of the mixing chamber. The temperature near the walls is much higher, so there should be no problem due to this low temperature.

This low temperature could be a problem if there was humidity in the air. Thus, it can be problematic for the implementation of the ejector in the Station TS4 since the hydrogen that is recirculated is mixed with water from the PEM fuel cell.

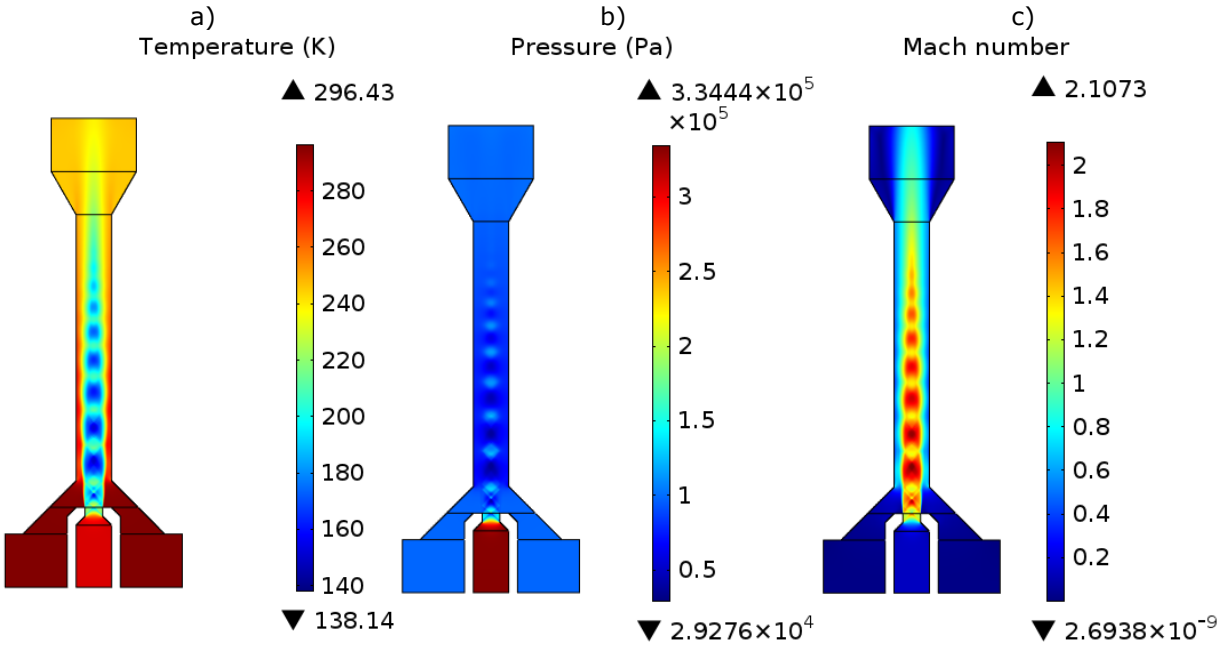

Fig. 6. 16- Results for P_{p0}=4 bar abs. a) Temperature. b) Pressure. c) Mach Number.

6.3. Data acquisition and control

The experimental set-up is composed of several sensors and controllers which work with electrical analogic signals. The control and data acquisition is programmed in LabVIEW and its logical hierarchy is similar to the one used in Station TS4 (Section 3.2). The communication with the analogical signal is achieved using 4 I/O modules which transform the electrical signals into binary data and vice versa. These modules are connected to the NI CompactRIO 9022, which acts as the RTOS and have the FPGA inside it (FPGA 9113). The NI cRIO is connected to the Host Computer using a Local Area Network (LAN) connection. The I/O modules used are:

- NI9203: 8 Channel, ±20mA, 16 Bit Analog Input Module. 3 channels are used:
  - Output of sensors P2 and P3.
  - Output of mass flow meter MFS1.
- NI9201: 8 Channel, 12 Bit Analog Input Module (±10V). 2 channels are used:
  - Output of sensor P1.
  - Output of mass flow controller MFC1.
- NI9211: 4 Channel, Thermocouple Input Module. 2 channels are used:
  - Output of thermocouples T1 and T2.
- N I9263: 4 Channel, ±10V, 16 Bit Analog Voltage Output Module. 1 channel is used:
  - Voltage input for mass flow controller MFC1.

The power supply used was manufactured by Carlo Gavazzi, model SPD24120, and can supply 120W with a voltage of 24 V_{DC}.

The LabVIEW program is composed by three different codes: The FPGA, the RTOS and the Host. These programs can be found in Appendix B.

6.3.1. FPGA program

The FPGA code is developed in the Host computer and deployed in the FPGA inside the NI CompactRIO. This code reads and stores the analogical data from modules NI9201, NI9203 and NI911 and sends the voltage set point to the Mass Flow Controller MFC1 in a 16 bit analog format.

6.3.2. RTOS program

The RTOS code is developed in the Host computer and deployed in the NI CompactRIO. This code has several functions. First, it runs the FPGA and stops it either when there is some emergency or at the end. Second, it creates a ".tdms" file and defines its path. Third, it converts the analogical data read by the I/O to engineering values (temperatures in ºC, pressures in bar and mass flows in Nl/min) and stores this converted data in the ".tdms" file and as global variables that can be read by the host program. This program also has a timer to save the moment at which every value of the data was stored. The time is saved in seconds and a constant must be added in order to read the time correctly using

other software different than LabVIEW. The RTOS code also reads the set point of the mass flow controller, which is defined as a global variable in the host program, and converts it to 16 bit analogical data that can be sent to the FPGA and module NI9263. Another function of this code is to send to the FPGA the rate at which the acquisition loop must be done.

The last function of this code is the management of the errors that can appear. It reads the errors in the FPGA and the ".tdms" file and stores them as a global variable that will be read by the Host program.

6.3.3. Host program

This code is developed and deployed in the Host computer. It is the program that interacts with the user. It reads the data stored by the RTOS as global variables and shows it to the user using plots and indicators. It also displays the errors that appear and gives the user the option to stop the program.

The path of the RTOS is defined at the beginning of the code and used to run the code in the RTOS.

6.3.4. Mass flow meter/controller

The control of the primary mass flow can be done either by the mass flow controller MFC1 or through regulation of the inlet pressure using the pressure regulator PR1. This second option requires that MFC1 acts as a mass flow meter instead of a mass flow controller. This way, the valve inside MFC1 will be fully open. If MFC1 acted as a mass flow controller, its valve would depend on the voltage set point.

The mass flow controller can be switched to a mass flow meter using the software FlowDDE to communicate with the device through a RS232 connector, and the software FlowView to change the control mode.

6.4. Results

The results obtained in the experimental validation are explained here. Both the normal and the recirculation mode of the experimental set-up were tested.

Before the first session with the experimental set-up, a test was performed to check how much pressure was lost due to leakage. The outlet valves were closed and then the gas was introduced in the system until it reached 3.5 bar_{abs}, which is the maximum pressure that can be measured by sensors P2 and P3. The pressure dropped at an average rate of 0.01 bars per minute. This is an acceptable leakage since this is not a fix station, the gas used is not dangerous and this drop has a low impact over the results of the experimental validation. This test should be repeated every time in which some change is made to the experimental set-up.

6.4.1. Primary mass flow

The first experimentation was done in the normal mode but keeping the secondary inlet (valve V2) closed. This way, there was flow only in the primary line and the ability of COMSOL to predict the primary mass flow could be tested.

This test was done with MFC1 acting as a mass flow meter (keeping the valve fully open) and controlling the primary stagnation pressure with PR1. The primary pressure was kept to P_{p0}=3.5 bar_{abs}, and the back pressure was reduced from 3.5 bar_{abs} to 1.2 bar_{abs}. The back pressure could not be reduced further due to the presence of the check valves, which produce a strong drop of pressure.

The experimental and COMSOL results are shown in Fig. 6. 17. They are also compared with the values of the mass flow predicted by the 1D theory (*Eq 4. 38* and *Eq 4. 39*). The results obtained show that, for the supersonic region, the COMSOL model has a better agreement with the experimental results than the 1D theory. Moreover, the small error obtained with the model can be due to the actual dimension of the diameter of the throat, which can be a little larger than expected due to the geometrical tolerances used. However, in the subsonic region, COMSOL and 1D models show a similar agreement with the experimental results.

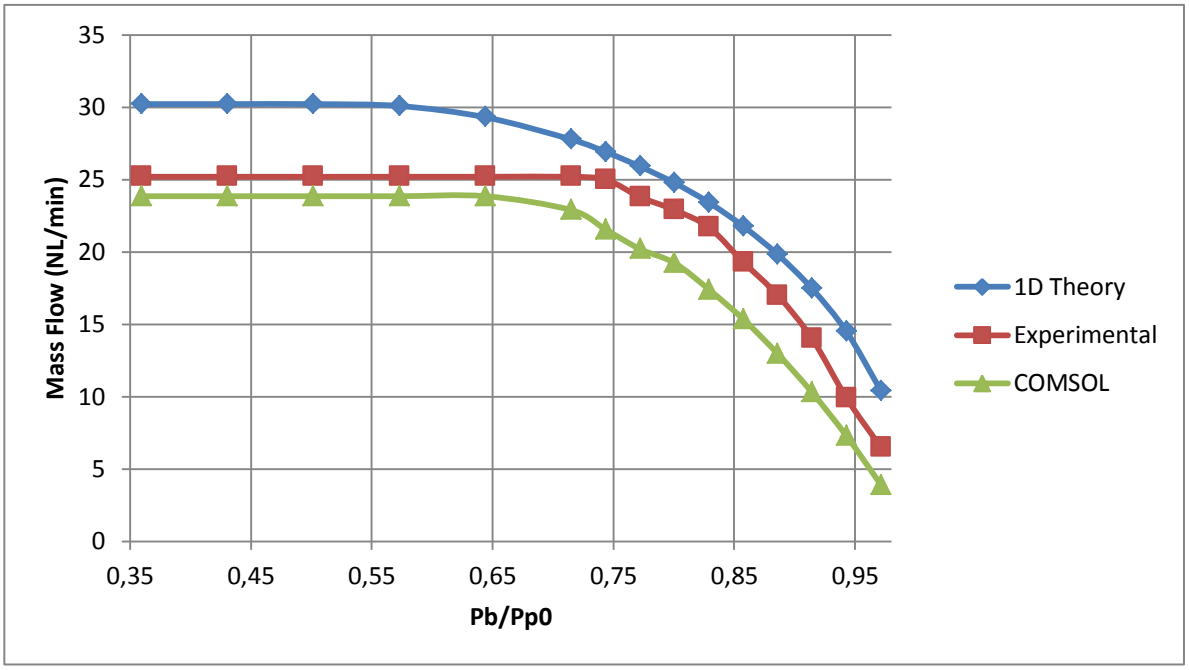

Fig. 6. 17- Primary mass flow without recirculation. The experimental results are compared with 1D predictions and COMSOL results.

6.4.2. Normal mode

The ejector was tested for different pressure conditions and nozzle positions using the normal mode of the experimental setup. In all the experiments done, the secondary pressure was controlled to be equal to the back pressure. The Nozzle positions studied with P_b=P_{s0}=1.2 bar_{abs} were 1.5 mm, 2.5 mm and 3.5 mm. NXP=1.5 mm was also used to work with P_b=P_{s0}=1.5 bar_{abs}. The results obtained are depicted in Fig. 6. 18, Fig. 6. 19, Fig. 6. 20 and Fig. 6. 21.

As can be seen, for $P_b=P_{s0}=1.2$ bar_{abs} both mixed and primary mass flows obtained with COMSOL have a very good agreement with their experimental values. However, the experimental Stoichiometry differs a bit from the one predicted by COMSOL's model, especially for low values of P_{p0}.

For $P_b=P_{s0}=1.5$ bar, the primary mass flow obtained with COMSOL has a very good agreement with the experimental values. However, the error obtained for the mixed mass flow is a bit larger for all the values of P_{p0} studied. For low values of P_{p0}, the experimental stoichiometry differs a bit from the one predicted by the CFD model.

All these results lead to the conclusion that this model is able to predict with high accuracy the mass flows obtained within an ejector where $P_b=P_{s0}$.

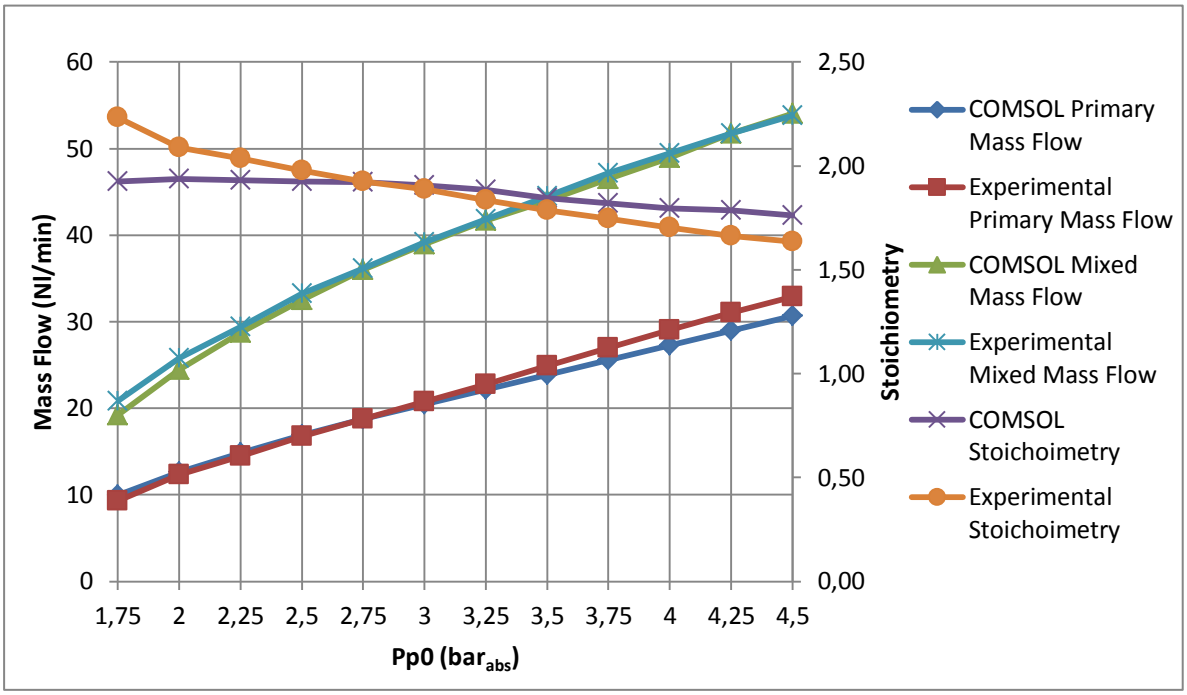

Fig. 6. 18- Comparison of the mass flows and stoichiometry obtained experimentally and with COMSOL (Normal Mode and $P_b=P_{s0}=1.2$ bar_{abs}, NXP=1.5 mm).

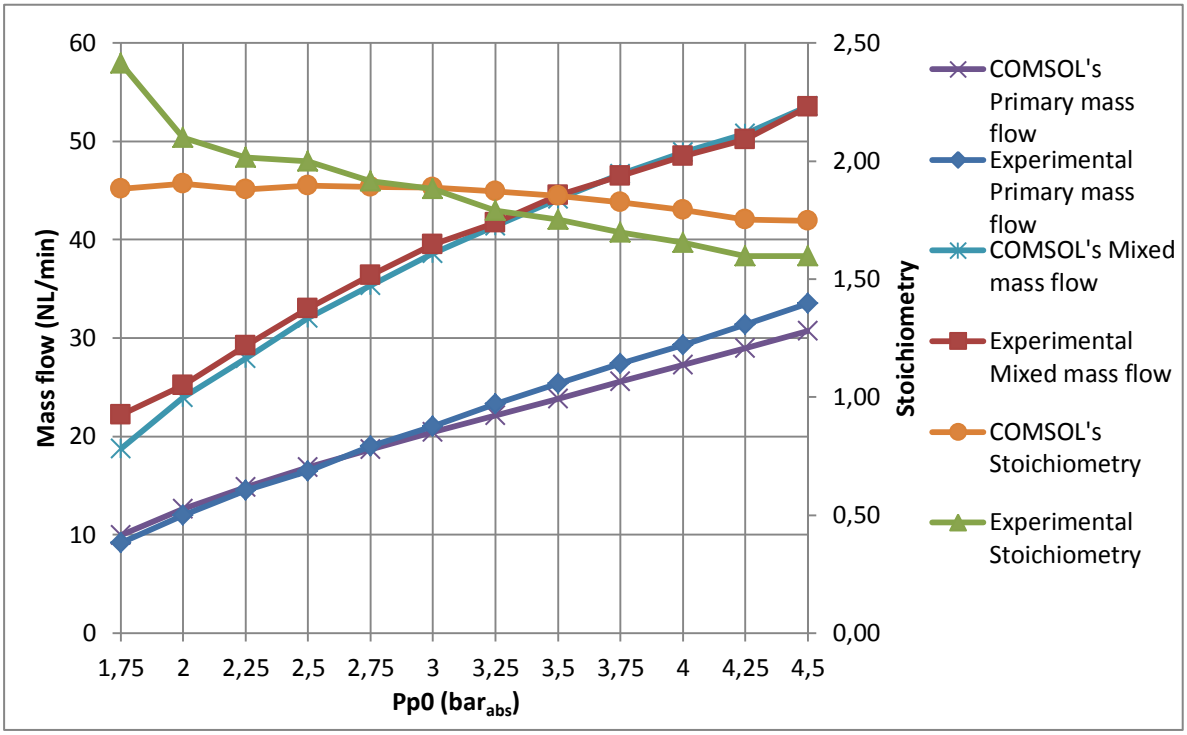

Fig. 6. 19- Comparison of the mass flows and stoichiometry obtained experimentally and with COMSOL (Normal Mode and P_b=P_{s0}=1.2 bar_{abs}, NXP=2.5 mm).

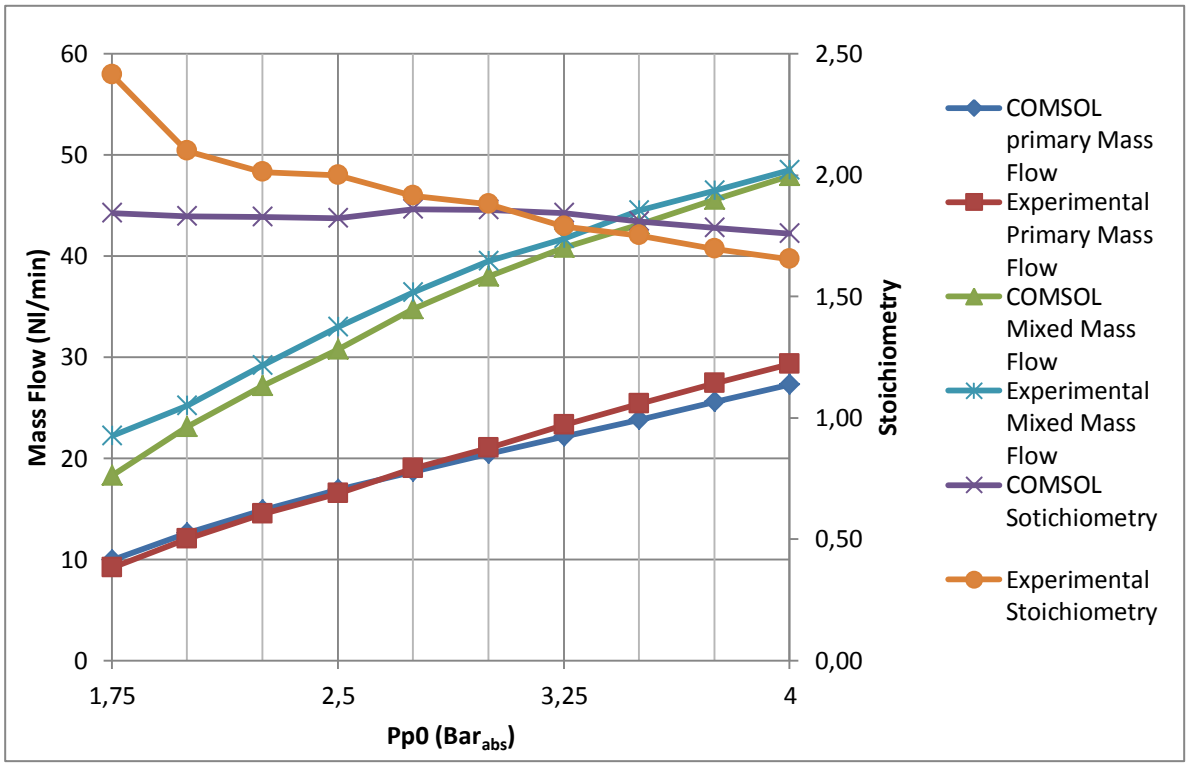

Fig. 6. 20- Comparison of the mass flows and stoichiometry obtained experimentally and with COMSOL (Normal Mode and P_b=P_{s0}=1.2 bar_{abs}, NXP=3.5 mm).

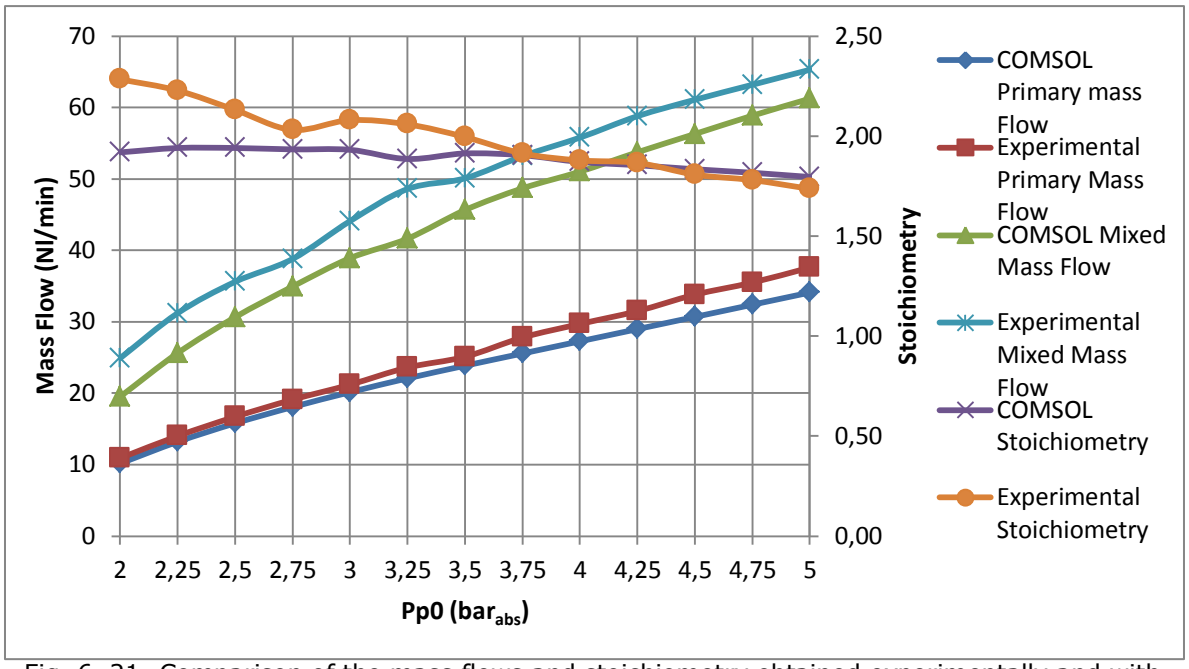

Fig. 6. 21- Comparison of the mass flows and stoichiometry obtained experimentally and with COMSOL (Normal Mode and P_b=P_{s0}=1.5 bar_{abs}, NXP=1.5 mm).

6.4.3. Recirculation mode

The ejector was also tested using the recirculation mode of the experimental setup with NXP=1.5 mm. It was tested for two different back pressures, P_b=1.2 bar_{abs} and P_b=1.5 bar_{abs}. For both values of pressure the pressure drop in the recirculation line was near to 0.2 bar, so the simulations with COMSOL Multiphysics were done with P_{s0}=1 bar_{abs} and P_{s0}=1.3 bar_{abs}, respectively. The mass flows and stoichiometry obtained experimentally and predicted by COMSOL's model are shown in Fig. 6. 22 and Fig. 6. 23.

The results obtained for the primary mass flow show a good agreement between experiments and COMSOL. The secondary mass flow obtained with the model shows a larger error, especially for small values of the primary pressure. This produces a certain error in the stoichiometry predicted by the CFD model.

However, it can be concluded that the model can be used to approximate the mass flows obtained in an ejector when there is a pressure drop between back pressure and secondary pressure.

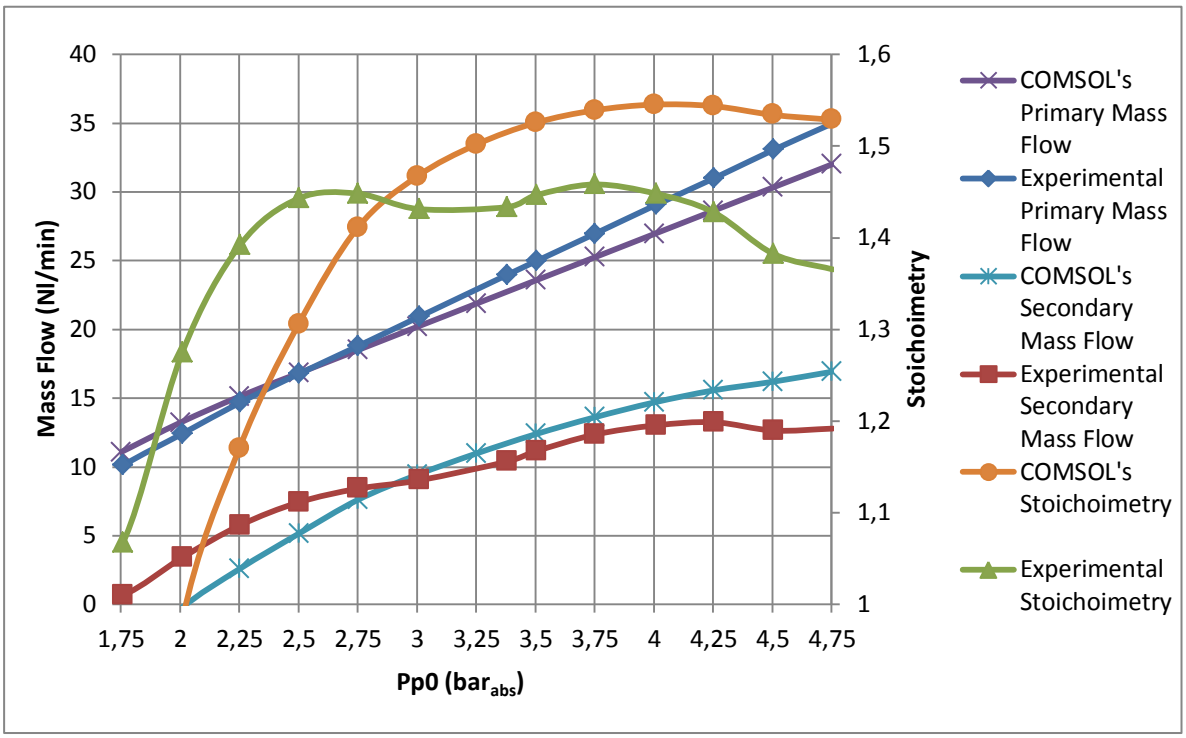

Fig. 6. 22- Comparison of the mass flows and stoichiometry obtained experimentally and with COMSOL (Recirculation Mode and P_b=1.2 bar_{abs}, NXP=1.5 mm).

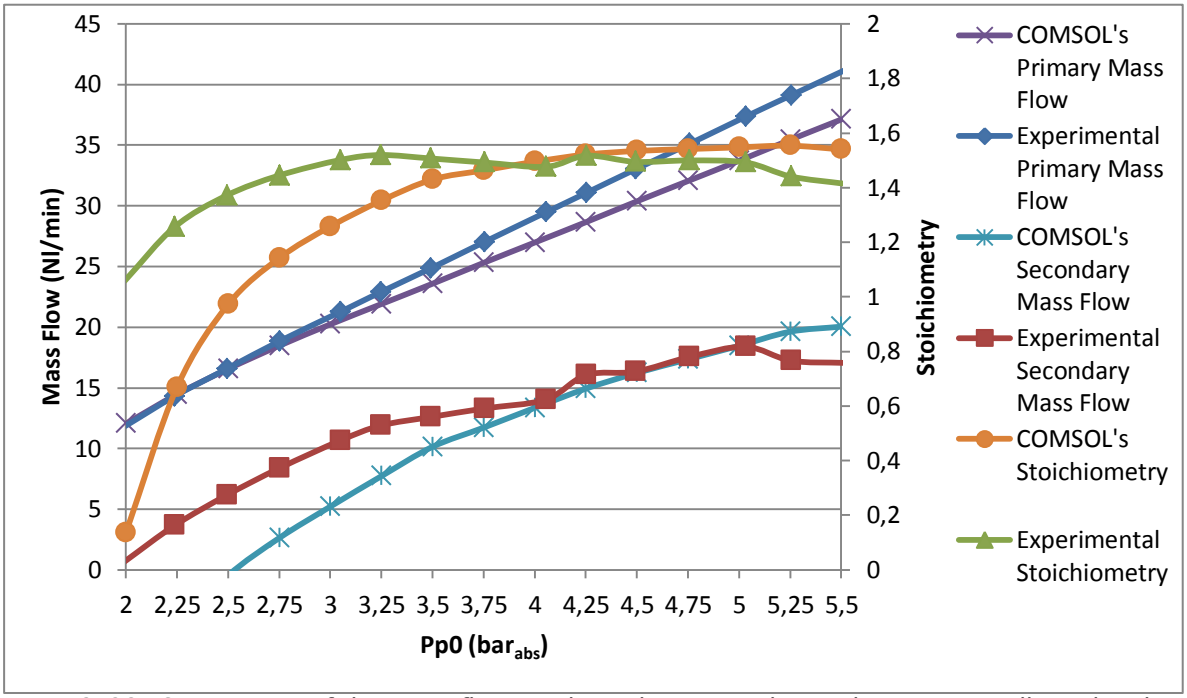

Fig. 6. 23- Comparison of the mass flows and stoichiometry obtained experimentally and with COMSOL (Recirculation Mode and P_b=1.5 bar_{abs}, NXP=1.5 mm).

CHAPTER 7: GEOMETRY OF THE EJECTOR FOR TS4

In order to design the ejector used in Test Station 4, the optimal geometrical parameters for the ejector had to be found. The study of these optimal geometrical parameters was done using the CFD model. Then, the chosen geometry was designed using SolidWorks and fabricated in the Laboratory of Mechanical Engineering of the ETSEIB.

7.1. Parametrical studies to find the optimal geometrical parameters

The ejector implemented in station TS4 will be very similar to the one used to validated the CFD model. Only two pieces have to be manufactured again: The outlet and the nozzle. The changes that must be made to these parts are 4: The diameter of the throat of the nozzle, the diameter of the mixing chamber, the length of the mixing chamber and the nozzle position.

7.1.1. Diameter of the throat

As explained in chapter 4, when the flow conditions in a nozzle reach the supersonic condition the throat becomes choked and mass flow only depends on the diameter of the throat and the stagnation values of pressure and temperature. In order to obtain the optimal value of the diameter of the throat of the nozzle, several different diameters have been studied applying the isentropic

choked mass flow function (*Eq 4. 38*). The values of R and γ used for hydrogen are 4124 J/(kg·K) and 1.4 . The results obtained are depicted in Fig. 7. 1. Since the maximum primary mass flow of the station must be around 20 Nl/min and it is interesting to work with a primary stagnation pressure in the range of 1 to 5 bar_{abs}, the chosen diameter for the throat will be 0.4 mm.

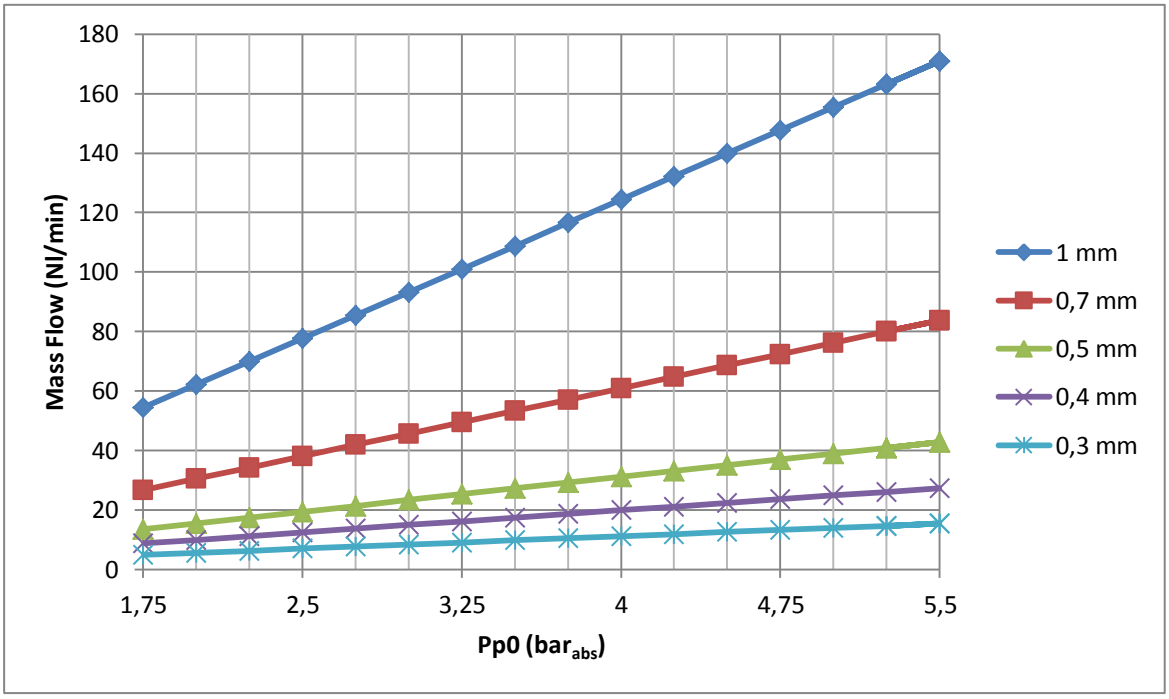

Fig. 7. 1- Primary mass flow for different diameters of the throat using the isentropic 1D theory.

In order to better know the evolution of the primary mass flow with a diameter of 0.4 mm, it was studied using COMSOL's model (Fig. 7. 2).

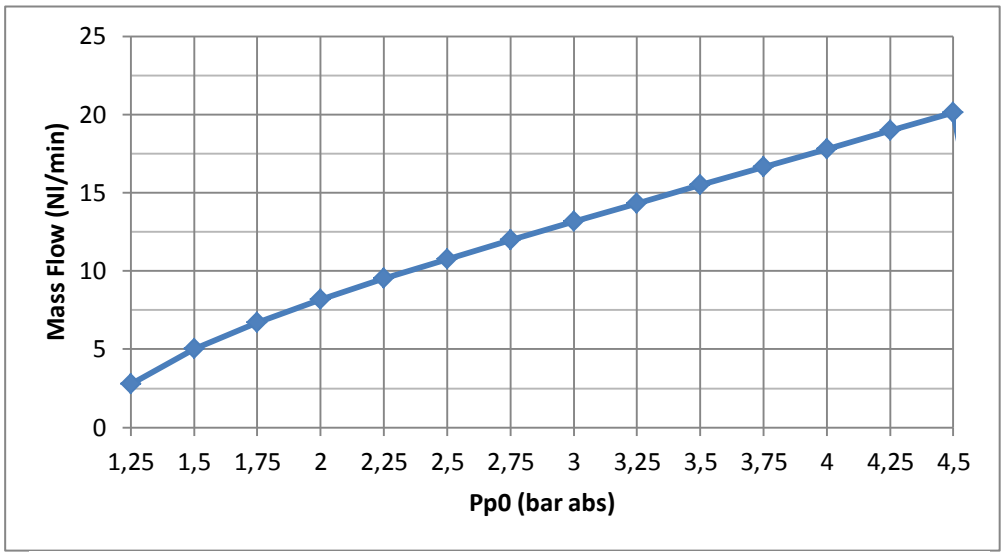

Fig. 7. 2- Primary mass flow for Dt=0.4 mm obtained using COMSOL's model.

7.1.2. Diameter of the mixing chamber

In order to decide the diameter of the mixing chamber, different diameters have been studied using the model. Primary mass flow depends on the diameter of the throat, so the different configurations studied will have the same primary mass flow as in Fig. 7. 2 and their behavior is defined by the stoichiometry obtained. Since the PEM Fuel Cell stack used in the station (UBzM BZ100) works under atmospheric pressure, all diameters will be studied assuming two different cases, $P_b = P_{s0} = 1\ bar_{abs}$ and $P_b = P_{s0} = 1.1\ bar_{abs}$. The temperature of the secondary flow has been set to 50ºC, which is the temperature of hydrogen leaving the stack. The results obtained are shown in Fig. 7. 3 and Fig. 7. 4. It would be interesting to work with the maximum stoichiometry allowed by the stack, which is 2.5. Thus, the diameter of the mixing chamber used will be 1.2 mm.

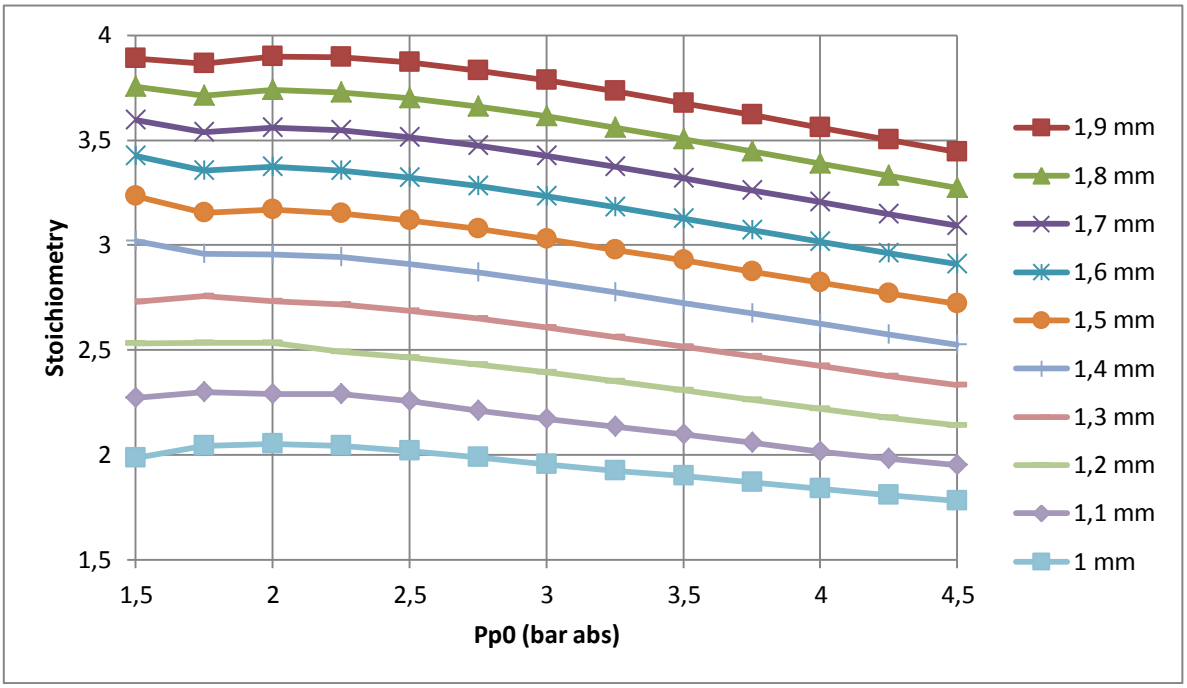

Fig. 7. 3- Stoichiometry obtained for different diameters of the mixing chamber when Pb=Ps0=1 bar_{abs}.

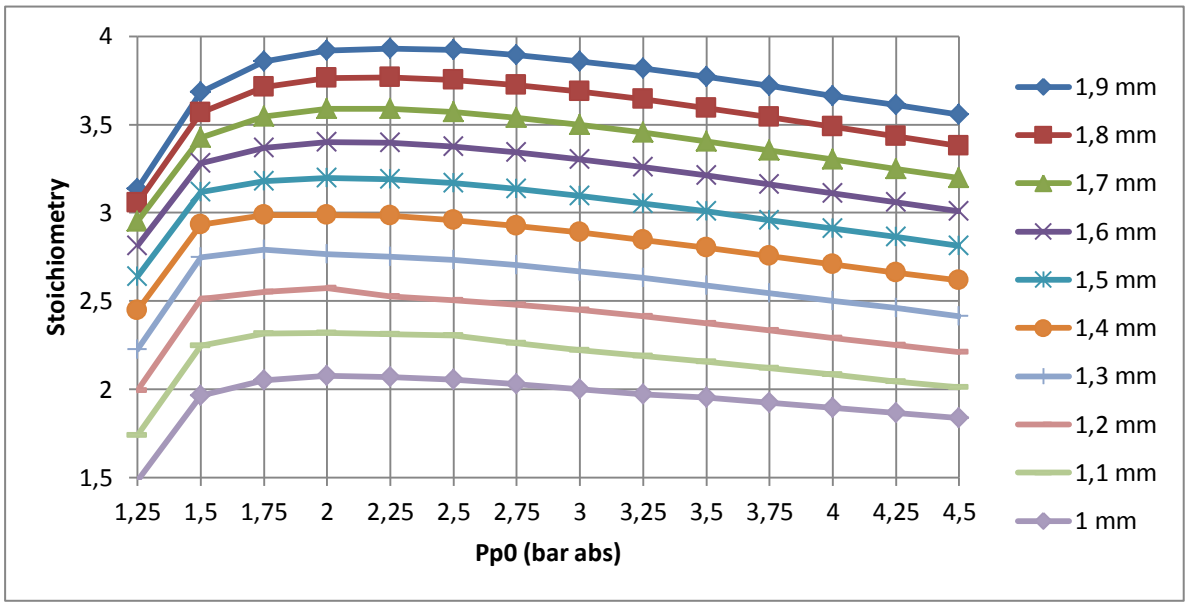

Fig. 7. 4- Stoichiometry obtained for different diameters of the mixing chamber when Pb=Ps0=1.1 bar_{abs}.

7.1.3. Length of the mixing chamber

The selection of the diameter of the mixing chamber has been done assuming that there is no loss of pressure in the recirculation. However, in the real station there will be a drop of pressure between the outlet of the ejector and the inlet of the recirculation flow. In order to reduce the effect that this drop of pressure could have over the stoichiometry obtained it will be necessary to use the optimum values of the length of the mixing chamber and the nozzle position (section 7.1.4). Due to the manufacturing of the different pieces and the maximum length of the holes obtained through drilling, the length of the mixing chamber that can be manufactured must be between 4 and 7 times the diameter of the mixing chamber. However, values outside this range have also been studied in order to have a better idea of the effect that this parameter has over the stoichiometry. The stoichiometry obtained for the different lengths of the mixing chamber that have been studied is shown in Fig. 7. 5. The chosen length of the mixing chamber will be equal to 4 times the diameter of the mixing chamber.

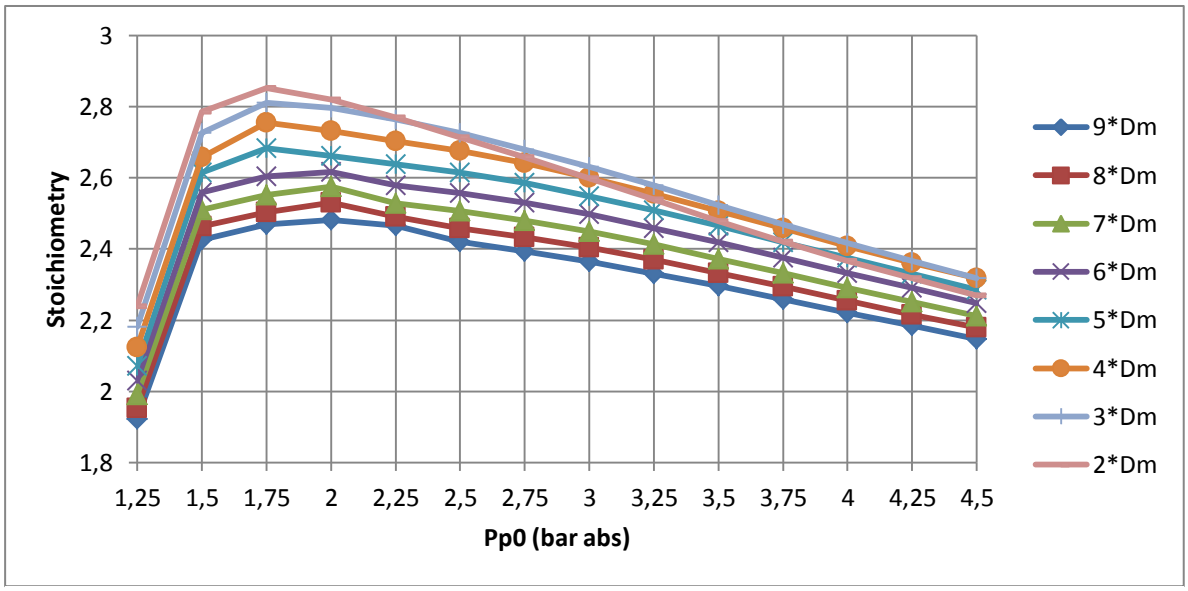

Fig. 7. 5- Stoichoimetry obtained for different lengths of the mixing chamber when Pb=Ps0=1.1 bar abs.

7.1.4. Nozzle position

The only remaining geometrical parameter is the nozzle position, which is the distance between the outlet of the nozzle and the inlet of the constant-area section of the mixing chamber. Different nozzle positions were studied using COMSOL's model in order to find the optimum value. The results obtained are depicted in Fig. 7. 6. The selected nozzle position was 1.5 mm since it is the nozzle position that produces the highest stoichiometry for the widest range of primary pressure.

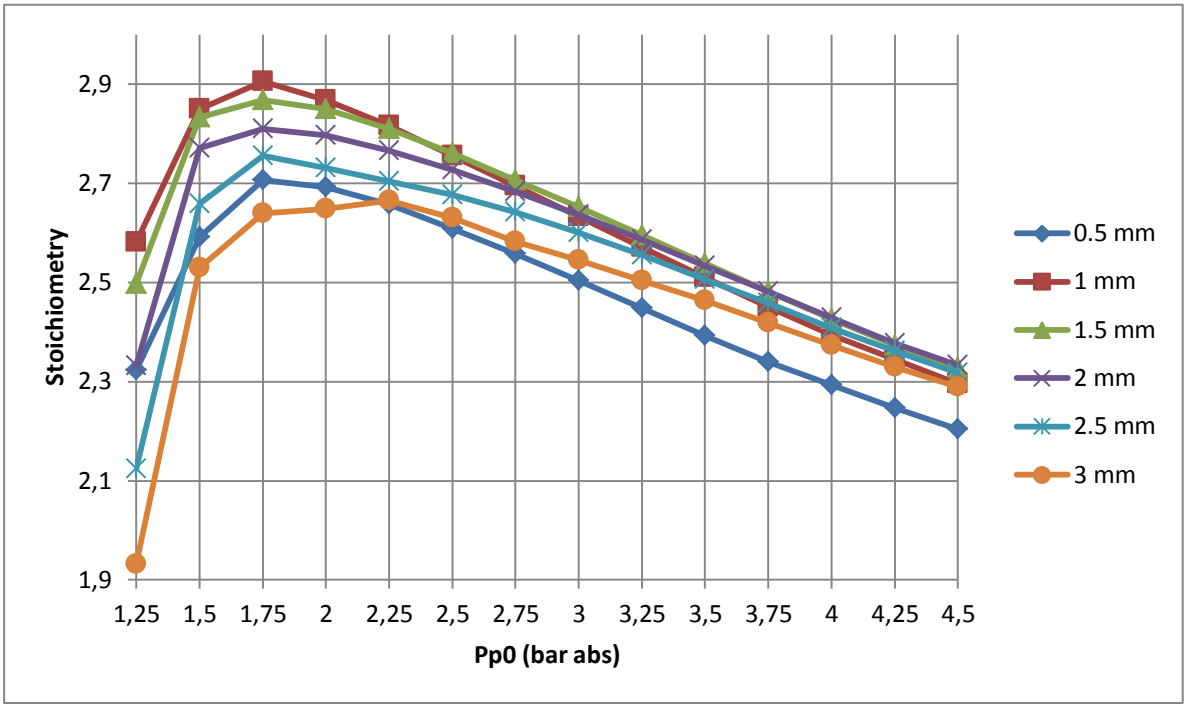

Fig. 7. 6- Stoichiometry obtained for different nozzle positions.

7.1.5. Pressure drop

The study of how the different geometrical parameters affect the mass flows obtained has been carried out without taking into account the drop of pressure in the fuel cell. In the actual case, this drop of pressure will range between 0 bar, for very low values of P_{p0}, and 0.1 bar, for high values of P_{p0}. The worst (ΔP=0.1 bar) and most favorable (ΔP=0 bar) cases have been studied (Fig. 7. 7 and Fig. 7. 8). The behavior of the ejector will be between these both cases. For low values of primary pressure, the stoichiometry obtained will be similar to the one shown in Fig. 7. 8 which, for low values of P_{p0}, is over 2.5, the maximum value recommended by the manufacturer. However, in the real case there will always appear a small drop of pressure in the fuel cell which will ensure that the stoichiometry is not over 2.5. For higher values of pressure, the stoichiometry will decrease until it reaches a minimum of 2 (Fig. 7. 7).

Thus, it can be concluded that this geometrical parameters ensure the optimum work of the ejector for test station 4. It is mandatory to avoid working for prolonged periods of time with low values of primary pressure, or primary mass flow, because the low values of recirculation obtained when the flow in the nozzle is subsonic can have a negative impact over the fuel cell stack.

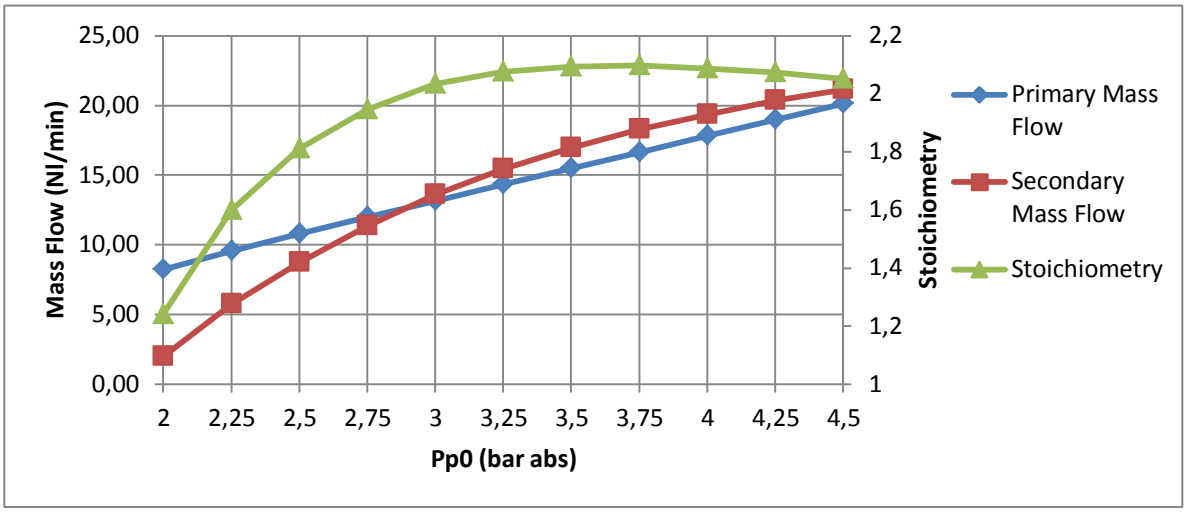

Fig. 7. 7- Stoichiometry, primary and secondary mass flows with the chosen geometrical parameters and a drop of pressure of 0.1 bar_{abs}.

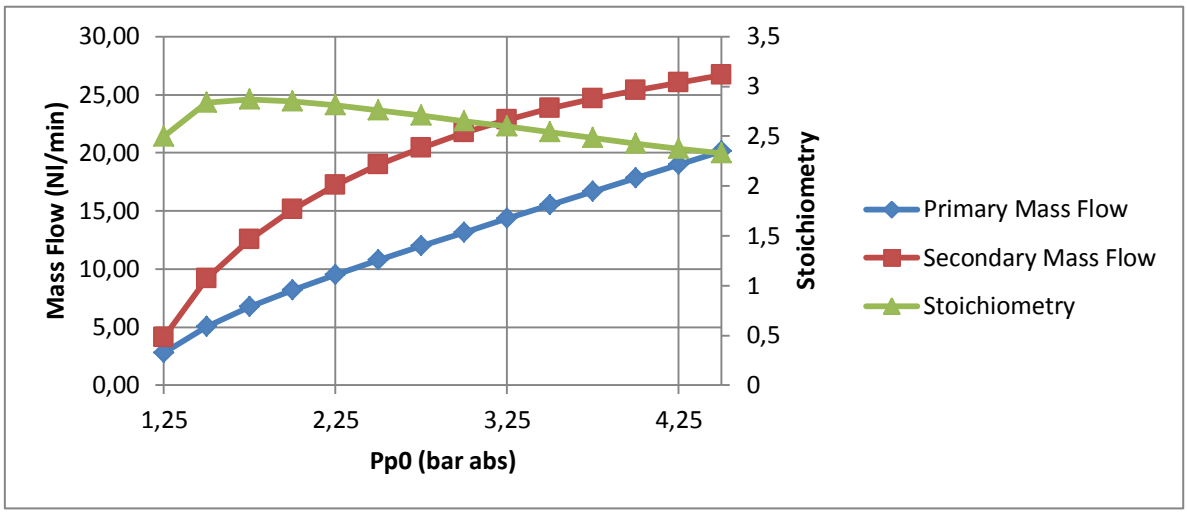

Fig. 7. 8- Stoichiometry, primary and secondary mass flows with the chosen geometrical parameters and $P_b=P_{s0}$.

7.2. Final Geometry

The ejector designed for TS4 is very similar to the ejector used in the experimental validation but changing the outlet and nozzle pieces. The most important geometrical parameters of the final design of the ejector can be found in Fig. 7. 9. The technical drawings of this final ejector can be found in the document "Technical Drawings".

The changes in the outlet piece include the diameter and length of the mixing chamber, the total length of the piece, which has been changed to set the nozzle position to 1.5 mm without the need to manufacture a new Hexagonal Nut, and the design of the NPT thread. It is recommendable to manufacture a hole with a diameter of 11 mm and a length of 17.5 mm before manufacturing a ¼" NPT thread, so this hole has been added to the design of the piece.

The changes in the nozzle piece include the diameter of the throat and the dimension of the hexagonal head, which has been enlarged from 5mm to 6 mm

because in the Fuel Cell Control Laboratory there are more 6 mm spanners than 5 mm spanners.

A sectional view of the designed ejector is shown in Fig. 7. 10.

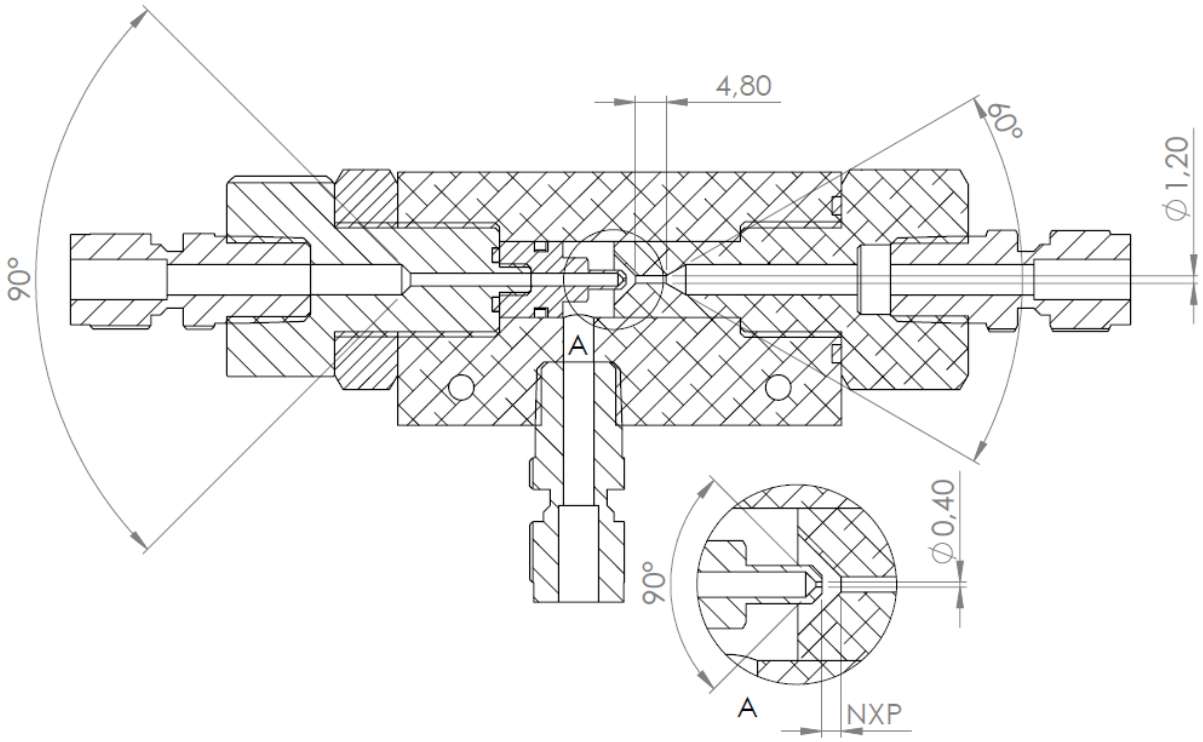

Fig. 7. 9- Sectional view of the ejector designed for TS4 with some of it dimensions.

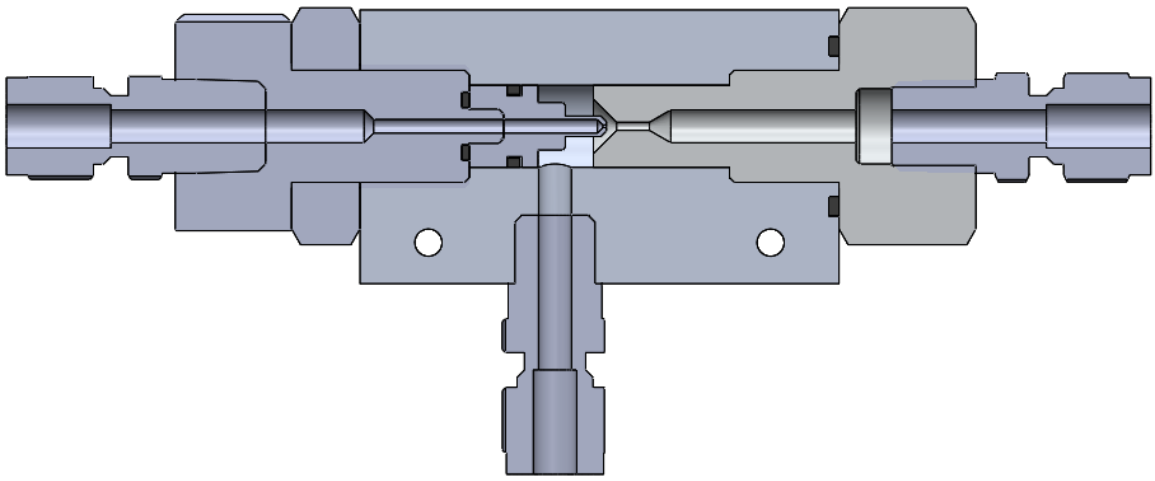

Fig. 7. 10- Sectional view of the designed ejector.

Both parts were manufactured in the Laboratory of Mechanical Engineering of the ETSEIB. They are shown in Fig. 7. 11 and Fig. 7. 12.

Fig. 7. 13, Fig. 7. 14 and Fig. 7. 15 are pictures of the group of pieces that are part of the ejector for Test Station 4.

Fig. 7. 11- Outlet 2.

Fig. 7. 12- Nozzle 2

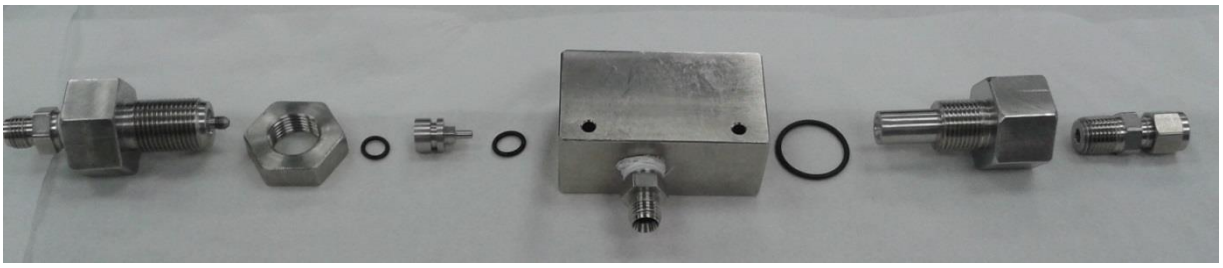

Fig. 7. 13- Parts of the Ejector for TS4.

Fig. 7. 14- Parts of the Ejector for TS4.

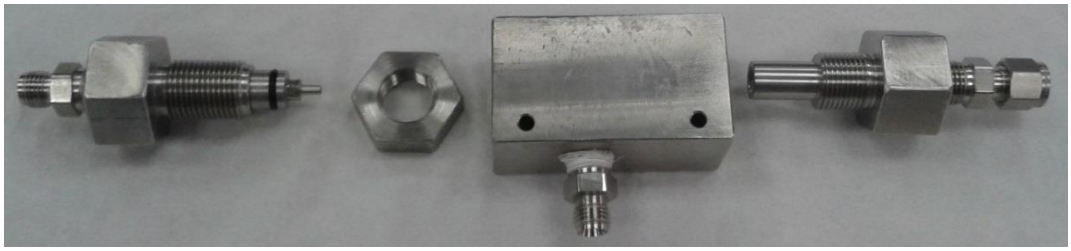

Fig. 7. 15- Parts of the Ejector for TS4.

CHAPTER 8: CONCLUSIONS

8.1. Conclusions

An ejector for Test Station 4 has been designed and manufactured. It has been designed to obtain a primary mass flow in the range of 0 to 20 Nl/min for a primary stagnation pressure between 1 and 4.5 bar_{abs}. The secondary mass flow will depend on the drop of pressure inside the fuel cell, but it is expected to obtain a stoichiometry between 2 and 2.5 for the most common operative conditions of the station.

The geometry of this ejector has been obtained using a COMSOL model that includes the Favre-averaged Navier-Stokes equations and a model of turbulence, the standard k-ε. This model includes the necessary boundary and initial conditions, and stabilization and discretization techniques, needed to ensure convergence. The model can capture shock waves and reproduce the diamond sock pattern that appears inside an ejector when it reaches its critical mode.

Once developed, the model was tested in two different ways. First, it was used to reproduce the pressure distribution along the axis of an experimental nozzle to check if it was able to capture shock waves and reproduce the characteristics of compressible flow. Then, an experimental setup was designed to test the model using a real ejector. The aim of this experimental validation was to check if the mass flows predicted by the model matched reality for different pressure conditions. For this experiment, it was necessary to use temperature sensors, pressure sensors and regulators and mass flow meters and controllers. A data acquisition system, which included a NI CompactRIO, 4 different I/O modules and a LabVIEW program, was also implemented. The experimental results obtained show a good agreement between the mass flows predicted by the model and those measured experimentally.

8.2. Future work

This project is the first part of a larger project that seeks to find how the implementation of ejector based hydrogen recirculation systems affects PEM fuel cells and to find the optimal control and data acquisition methods for these systems. The next step should be to implement the ejector in Station TS4 adding an actuator able to regulate the pressure in the fuel cell and a water management system that removes the water at the outlet of the fuel cell.

Since the hydrogen at the outlet of the anode carries water, the recirculation mass flow cannot be measured using the mass flow meters of the Fuel Cell Control Laboratory. An option to solve this issue would be to measure the secondary pressure and temperature that appear when the ejector is working in the station and reproduce these conditions in the experimental set up used for the experimental validation. This would require to use hydrogen and to change the material constants of the mass flow meters which are currently set to air.

There are other lines of research arising from this project that could be pursued:

- The computational model developed is a single phase model that does not take into account the presence of water in the recirculation line. This model could be improved by including this secondary phase and then reproducing the presence of water in an experimental set up able to measure a mass flow that carries water. Several authors have developed computational models that take into account the presence of waters inside ejectors, however, they have been used mainly for other applications rather than hydrogen recirculation (S. He, Li, and Wang 2009).
- The model developed in this work could be used to design ejectors for fuel cells that work under different pressure and temperature conditions. Then, the effect that ejectors have for these conditions could be analyzed.
- The model could also be improved implementing the RNG (renormalization group) k- ε turbulence model. Several authors state that this model is better to capture the distribution of shock waves inside the mixing chamber (Zhu et al. 2009). However, this model is not implemented in the COMSOL module "High-Mach Number Flow". After implementing the model, the agreement between the mass flows predicted by the model and reality should be checked using an experimental set-up like the one that has been used in this work. Another option to evaluate the advantages of the RNG k- ε model compared to the standard k- ε would be to use flow visualization techniques in order to compare the shock structure and the mixing process obtained with reality. Several authors have used different flow visualization techniques to know more about ejectors (Bouhanguel, Desevaux, and Gavignet 2011)(Koita and Iwamoto 2009)(Zare-Behtash, Gongora-Orozco, and Kontis 2009)(Zhu and Jiang 2014). Another turbulence model that could be used to improve the computational model in terms of stream mixing is the Shear-Stress Transport (SST) k- ω model (S. He, Li, and Wang 2009).
- Only a stoichiometry between 2 and 2.5 can be obtained using the ejector developed in this work for the operative conditions of Test Station 4. In order to be able to work with other values of stoichiometry under the same conditions, a variable geometry ejector could be implemented (Pereira et al. 2014)(Sameen, Kumar, and Kim 2005)(Varga et al. 2011).

BIBLIOGRAPHY

Anderson, John David. 2004. *Modern Compressible Flow: With Historical Perspective*. 3rd ed. Boston: Mc-Graw Hill.

Barbir, Frano. 2005. *PEM Fuel Cells: Theory and Practice*. Elsevier Academic Press.

Bartosiewicz, Y, Zine Aidoun, P. Desevaux, and Yves Mercadier. 2003. "Cfd-Experiments Integration in the Evaluation of Six Turbulence Models for Supersonic Ejector Modeling." *Integrating CFD and …* 1 (450).

Bouhanguel, Ala, Philippe Desevaux, and Eric Gavignet. 2011. "Flow Visualization in Supersonic Ejectors Using Laser Tomography Techniques." *International Journal of Refrigeration* 34 (7). Elsevier Ltd and IIR: 1633–40.

Comsol. 2012a. "The CFD Module User's Guide."

Comsol. 2012b. "Comsol Multiphysics Reference Guide."

Eames, I.W., S. Aphornratana, and H.A. Haider. 1995. "A Theoretical and Experimental Study of a Small-Scale Steam Jet Refrigerator." *International Journal of Refrigeration* 18 (378-386).

EUETIB. 2010. "Manual de Prácticas de Ingeniería de Fluidos: Flujo Compresible En Toberas." Departamento de Mecánica de Fluidos.

He, J., S.Y. Choe, and C.O. Hong. 2008. "Analysis and Control of a Hybrid Fuel Delivery System for a Polymer Electrolyte Membrane Fuel Cell." *Journal of Power Sources* 185: 973–84.

He, S., Y. Li, and R. Z. Wang. 2009. "Progress of Mathematical Modeling on Ejectors." *Renewable and Sustainable Energy Reviews* 13: 1760–80.

Huang, B. 1999. "A 1-D Analysis of Ejector Performance." *International Journal of Refrigeration* 22 (May 1998): 354–64.

Huang, B. J., and J. M. Chang. 1999. "Empirical Correlation for Ejector Design." *International Journal of Refrigeration* 22 (May 1998): 379–88.

John, V., and P. Knobloch. 2007. "On Spurious Oscillations at Layers Diminishing (SOLD) Methods Fon Convection-Diffusion Equations: Part I- A Review." *Computational Methods Applied to Mechanical Engineering* 196: 2197–2215.

Keenan, J.H., and E.P. Neumann. 1942. "A Simple Air Ejector." *ASME Journal of Applied Mechanics* 64: 75–82.

Keenan, J.H., E.P. Neumann, and F. Lustwerk. 1950. "An Investigation of Ejector Design by Analysis and Experiment." *ASME Journal of Applied Mechanics* 72: 299–309.

Knights, Shanna D., Kevin M. Colbow, Jean St-Pierre, and David P. Wilkinson. 2004. "Aging Mechanisms and Lifetime of PEFC and DMFC." *Journal of Power Sources* 127: 127–34.

Koita, Taketoshi, and Junjiro Iwamoto. 2009. "A Study on Flow Behavior inside a Simple Model of Ejector." In *10th International Conference on Fluid Control, Measurements and Visualization*, 1–12. Moscow.

Larminie, J., and A. Dicks. 2003. *Fuel Cell Systems Explained*. 2nd ed. John Wiley & Sons.

Liao, Chaqing. 2008. "Gas Ejector Modeling for Design and Analysis," no. December. http://repository.tamu.edu/bitstream/handle/1969.1/ETD-TAMU-3206/LIAO-DISSERTATION.pdf?sequence=1.

Liao, Chaqing, and Frederick R. Best. 2010. "Comprehensive Gas Ejector Model." *Journal of Thermophysics and Heat Transfer* 24 (3): 516–23.

Maghsoodi, A., E. Afshari, and H. Ahmadikia. 2014. "Optimization of Geometric Parameters for Design a High-Performance Ejector in the Proton Exchange Membrane Fuel Cell System Using Artificial Neural Network and Genetic Algorithm." *Applied Thermal Engineering* 71 (1). Elsevier Ltd: 410–18.

Marsano, F., L. Magistri, and a. F. Massardo. 2004. "Ejector Performance Influence on a Solid Oxide Fuel Cell Anodic Recirculation System." *Journal of Power Sources* 129: 216–28.

Migliardini, F., C. Capasso, and P. Corbo. 2014. "Optimization of Hydrogen Feeding Procedure in PEM Fuel Cell Systems for Transportation." *International Journal of Hydrogen Energy* 39. Elsevier Ltd: 21746–52.

Munday, Jt, and Df Bagster. 1977. "A New Ejector Theory Applied to Steam Jet Refrigeration." *Industrial & Engineering Chemistry …* 16: 442–49.

Pereira, Paulo R., Szabolcs Varga, João Soares, Armando C. Oliveira, António M. Lopes, Fernando G. de Almeida, and João F. Carneiro. 2014. "Experimental Results with a Variable Geometry Ejector Using R600a as Working Fluid." *International Journal of Refrigeration* 46: 77–85.

Rojas Fernández, José D. 2011. "Implementation, Modelling and Control of an Experimental PEM Fuel Cell Stack Station." Universitat Politècnica de Catalunya.

Sameen, Jun-hee Lee a, V R Sanal Kumar, and H D Kim. 2005. "Studies on Ejector Systems for Hydrogen Fuel Cell," no. July: 1–8.

Strahl, Stephan. 2010. "Characterization, Development and Experimental Validation of a Dynamic PEM Fuel Cell System Model." Universitat Politècnica de Catalunya.

Varga, Szabolcs, Armando C. Oliveira, Xiaoli Ma, Siddig a. Omer, Wei Zhang, and Saffa B. Riffat. 2011. "Experimental and Numerical Analysis of a Variable Area Ratio Steam Ejector." *International Journal of Refrigeration* 34 (7). Elsevier Ltd and IIR: 1668–75.

Versteeg, H.K., and W. Malalasekera. 2007. *Introduction to Computational Fluid Dynamics*. 2nd ed. Harlow: Person Education Limited.

White, Frank M. 1999. *Fluid Mechanics*. 4th ed. New York: McGraw-Hill.

Zare-Behtash, H., N. Gongora-Orozco, and K. Kontis. 2009. "PSP Visualization Studies on a Convergent Nozzle with an Ejector System." *Journal of Visualization* 12 (2): 157–63.

Zhu, Yinhai, Wenjian Cai, Changyun Wen, and Yanzhong Li. 2007. "Fuel Ejector Design and Simulation Model for Anodic Recirculation SOFC System." *Journal of Power Sources* 173: 437–49.

Zhu, Yinhai, Wenjian Cai, Changyun Wen and Yanzhong Li. 2009. "Numerical Investigation of Geometry Parameters for Design of High Performance Ejectors." *Applied Thermal Engineering* 29 (5-6). Elsevier Ltd: 898–905.

Zhu, Yinhai, and Peixue Jiang. 2011. "Geometry Optimization Study of Ejector in Anode Recirculation Solid Oxygen Fuel Cell System." *Proceedings of the 2011 6th IEEE Conference on Industrial Electronics and Applications, ICIEA 2011*, no. 2: 51–55.

Zhu, Yinhai and Peixue Jiang. 2014. "Experimental and Numerical Investigation of the Effect of Shock Wave Characteristics on the Ejector Performance." *International Journal of Refrigeration* 40. Elsevier Ltd and IIR: 31–42.

Zhu, Yinhai, and Yanzhong Li. 2009. "New Theoretical Model for Convergent Nozzle Ejector in the Proton Exchange Membrane Fuel Cell System." *Journal of Power Sources* 191: 510–19.

Zienkiewicz, O.C., R.L. Taylor, and P Nithiarasu. 2005. *The Finite Element Method for Fluid Dynamics*. Edited by Elsevier. 6th ed.

Escola Universitària d'Enginyeria
Tècnica Industrial de Barcelona
Consorci Escola Industrial de Barcelona
UNIVERSITAT POLITÈCNICA DE CATALUNYA

Volume II
Appendices - Budget

TREBALL DE FI DE GRAU

IMPLEMENTATION AND CHARACTERIZATION OF AN EJECTOR BASED HYDROGEN RECIRCULATION SYSTEM FOR A PEM FUEL CELL

TFG presentat per obtenir el títol de GRAU en
ENGINYERIA MECÀNICA

Per **Xavier Corbella Coll**

Barcelona, 9 de Juny de 2015

Director: Ricardo Torres Cámara
Departament de MF
Universitat Politècnica de Catalunya (UPC)

Codirector: Miguel Allué Fantova
Departament Automatic Control
Institut de Robòtica i Informàtica Industrial (IRI/CSIC)

Escola Universitària d'Enginyeria
Tècnica Industrial de Barcelona
Consorci Escola Industrial de Barcelona
UNIVERSITAT POLITÈCNICA DE CATALUNYA

Appendices

IMPLEMENTATION AND CHARACTERIZATION OF AN EJECTOR BASED HYDROGEN RECIRCULATION SYSTEM FOR A PEM FUEL CELL

TFG presentat per optar al títol de GRAU en
ENGINYERIA MECÀNICA
per **Xavier Corbella Coll**

Barcelona, 9 de Juny de 2015

Director: Ricardo Torres Cámara
Departament de MF
Universitat Politècnica de Catalunya (UPC)

Codirector: Miguel Allué Fantova
Departament Automatic Control
Institut de Robòtica i Informàtica Industrial (IRI/CSIC)

CONTENTS

APPENDIX A: Implementation of the model in COMSOL 3
A.1. Preprocessing 3
A.1.1. Space Dimension, physics and study type. 3
A.1.2. Parameters 3
A.1.3. Geometry 5
A.1.4. Isotropic diffusion 8
A.1.5. Material. 8
A.1.6. Initial Values 8
A.1.7. Boundary Conditions 10
A.1.8. Mesh. 11
A.2. Processing. 11
A.2.1. Study 1 11
A.2.2. Study 2 13
A.2.3. Computation 13
A.3. Postprocessing. 14
A.3.1. Computation of the mass flow 15
APPENDIX B: LabVIEW programs 17
B.1. FPGA 18
B.2. RTOS 19
B.3. HOST 21

APPENDIX A: IMPLEMENTATION OF THE MODEL IN COMSOL

This section explains step by step how to implement the CFD model in COMSOL Multiphysics. The version of the program used is 4.3a, and the physics module is the "Turbulent k-ε High Mach Number Flow".

A.1. Preprocessing

A.1.1. Space Dimension, physics and study type.

The first step when creating a new model in COMSOL is to select the space dimension, the physics and the study type.

In this case, the dimension used is a 2D axisymmetric dimension. The physics selected is the "Turbulent flow, k-ε (hmnf)". The study type used is an Stationary study.

After selecting these items, they will appear in the Model Builder.

A.1.2. Parameters

The next step is to define the parameters (Table A. 1) which will be used in the simulation. These parameters include the geometrical parameters used to create the geometry, the properties of the material used and another inputs relating to the operative conditions, (stagnation pressures and temperatures and the back pressure). Another parameter used is the tuning parameter for inconsistent stabilization. The parameters can be typed or exported from a file.

Parameters are defined in the "Parameters" section under "Global definitions" in the "Model Builder" (Fig. A. 1). In order to see this section, right click on global definitions and select "Parameters".

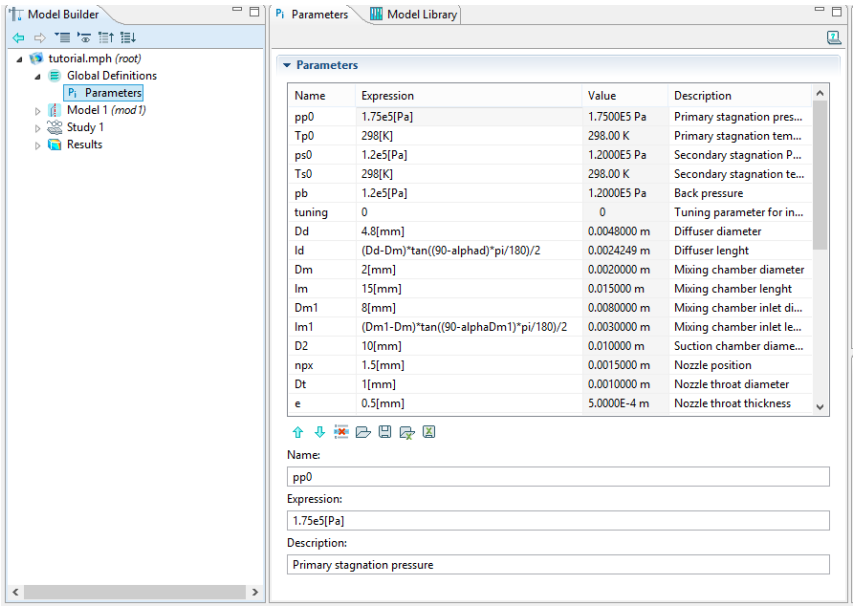

Fig. A. 1- Definition of the Parameters.

The utilization of parameters is useful because it makes easier to make changes to the simulation. For example, in order to do a simulation with a different nozzle position, it can be changed in the parameters section and then COMSOL will automatically change the geometry and the mesh used.

Table A. 1- List of the parameters.

Name	**Expression**	**Description**
pp0	1.75e5[Pa]	Primary stagnation pressure
Tp0	298[K]	Primary stagnation temperature
ps0	1.2e5[Pa]	Secondary stagnation Pressure
Ts0	298[K]	Secondary stagnation temperature
pb	1.2e5[Pa]	Back pressure
tuning	0	Tuning parameter for inconsistent stabilization
Dd	4.8[mm]	Diffuser diameter
ld	(Dd-Dm)*tan((90-alphad)*pi/180)/2	Diffuser lenght
Dm	2[mm]	Mixing chamber diameter
lm	15[mm]	Mixing chamber lenght
Dm1	8[mm]	Mixing chamber inlet diameter
lm1	(Dm1-Dm)*tan((90-alphaDm1)*pi/180)/2	Mixing chamber inlet lenght
D2	10[mm]	Suction chamber diameter
npx	1.5[mm]	Nozzle position
Dt	1[mm]	Nozzle throat diameter
e	0.5[mm]	Nozzle throat thickness
l0	2.5[mm]	Nozzle lenght

D0	2[mm]	Nozzle inlet diameter
l1	3[mm]	lenght of the nozzle outlet change of area
lin	3[mm]	Inlet lenght
D1	5[mm]	Nozzle inlet exterior diameter
alphaDm1	45	Angle of the inlet of the mixing chamber
alphad	30	Angle of the diffuser
alphaN	45	Angle of the nozzle
eh	(D0-Dt)*tan((90-alphaN)*pi/180)/2	Length of the nozzle's tip
lh	0.5[mm]	Thickness
linN	5.5[mm]	Inlet length
Rs	287[J/kg/K]	Specific perfect gas constant
gamma	1.4	Ratio of specific heat
ktherm	0.0241[W/m/K]	Thermal conductivity
mu	1.716e-5[Pa*s]	Dynamic viscosity

A.1.3. Geometry

The creation of the geometry is done in the "geometry" section under "Model 1". The steps to create the geometry are:

- Right click geometry and select "Bézier Polygon". Then, in "Type" select "Solid" and click on the "Add Linear" button. Now, type control points depicted in Table A. 2 for segment 1 and click on the "Add linear button". Create segments 2 to 8 introducing the control points depicted in the table.

Table A. 2-Segments for bézier polygon 1.

Segment nº	**r**	**z**	**Segment nº**	**r**	**z**
1	Dd/2	ld+lm	**5**	D2/2	-lm1
	Dm/2	lm		D2/2	-lm1-lin
2	Dm/2	lm	***6***	D2/2	-lm1-lin
	Dm/2	0		0	-lm1-lin
3	Dm/2	0	**7**	0	-lm1-lin
	Dm1/2	-lm1		0	ld+lm
4	Dm1/2	-lm1	**8**	0	ld+lm
	D2/2	-lm1		Dd/2	ld+lm

- Create a new "Bézier Polygon". It consists of 4 segments:

Table A. 3-Control points for bézier polygon 2.

Segment nº	**r**	**z**	**Segment nº**	**r**	**z**
1	Dd/2	lm+ld	**3**	0	lm+ld+lin
	Dd/2	lm+ld+lin		0	lm+ld
2	Dd/2	lm+ld+lin	**4**	0	lm+ld
	0	lm+ld+lin		Dd/2	lm+ld

- Create a new "Bézier Polygon". It consists of 7 segments:

Table A. 4-Control points for bézier polygon 3.

Segment nº	**r**	**z**	**Segment nº**	**r**	**z**
1	Dt/2	-npx	**5**	D0/2	-npx-eh -linN
	Dt/2+e	-npx		D0/2	-npx-eh –lh
2	Dt/2+e	-npx	**6**	D0/2	-npx-eh –lh
	D0/2+e	-npx-eh		Dt/2	-npx-lh
3	D0/2+e	-npx-eh	**7**	Dt/2	-npx-lh
	D0/2+e	-npx-eh -linN		Dt/2	-npx
4	D0/2+e	-npx-eh -linN			
	D0/2	-npx-eh -linN			

- Right click "Geometry" and select "Boolean Operations->Difference". In "Objects to add" select "b1" (bélzier polygon 1) (Fig. A. 2 a). In "Objects to subtract" select "b3" (Fig. A. 2 b). Click "Build All".

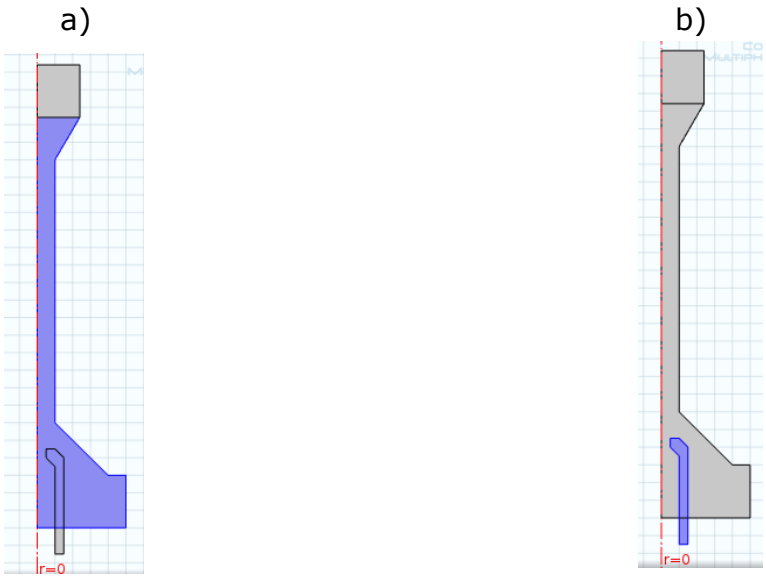

Fig. A. 2- Difference operation. a) Objects to add. b) Objects to substract.

- Now the geometry should look like Fig. A. 3.

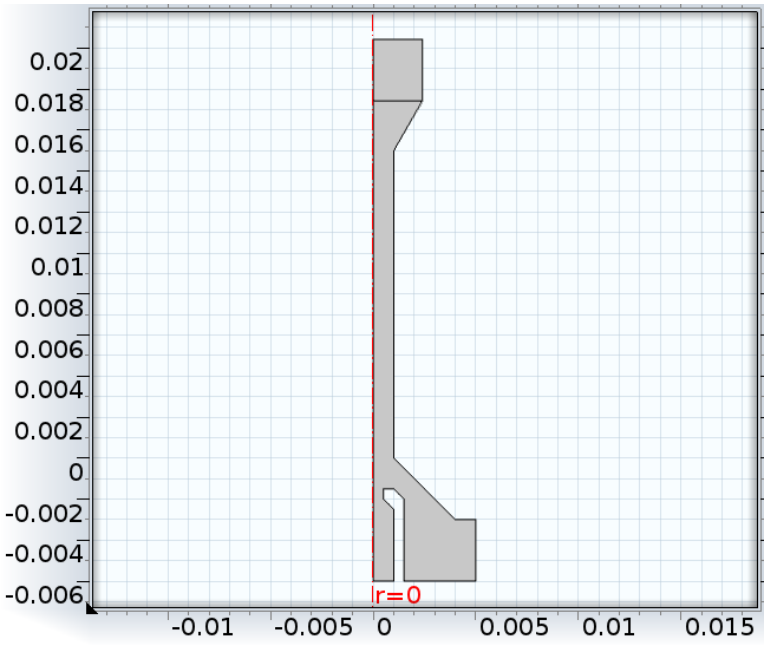

Fig. A. 3- Geometry of the ejector.

The next steps are to create lines to divide the geometry in different domains which will be used in the meshing process:

- Create a new "bézier polygon" set the type to "open curve". It consists of one segment:

Table A. 5-Control points for bézier polygon 4.

r	z
D2/2	-l1
D0/2+e	-l1

- Create a new open curve "bézier polygon". It consists of one segment:

Table A. 6- Control points for bézier polygon 5.

r	z
0	-npx-lh-eh
D0/2	-npx-lh-eh

A.1.4. Isotropic diffusion.

After defining the geometry, the equations of the problem have to be defined. The first step will be adding isotropic diffusion to the problem. Click on the show button (Fig. A. 4) and select "Stabilization". Then, select "High Mach Number Flow" in the model builder and expand the inconsistent stabilization section. Select isotropic diffusion for all the equations and type "tuning" as the "tuning parameter" (Fig. A. 5).

A.1.5. Material.

The gas used will be defined using the parameters defined previously. This way, the properties of the materials can be changed in the "Parameters" section. Select "Fluid 1" in the Model Builder and copy the information depicted in Fig. A. 6.

A.1.6. Initial Values

The initial values are the first guess from which the non-linear solver begins to iterate. They are defined in the "Initial Values 1" section. Type "ps0" as the pressure and "Tp0" as the temperature. The other initial values do not need to be changed.

Fig. A. 4- Show button.

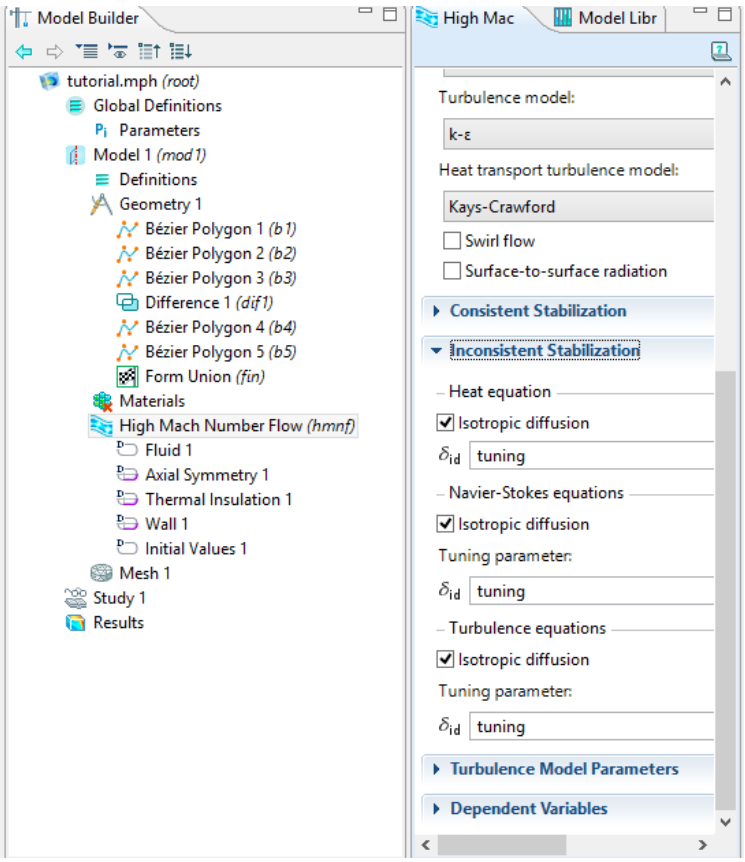

Fig. A. 5- Adding isentropic diffusion.

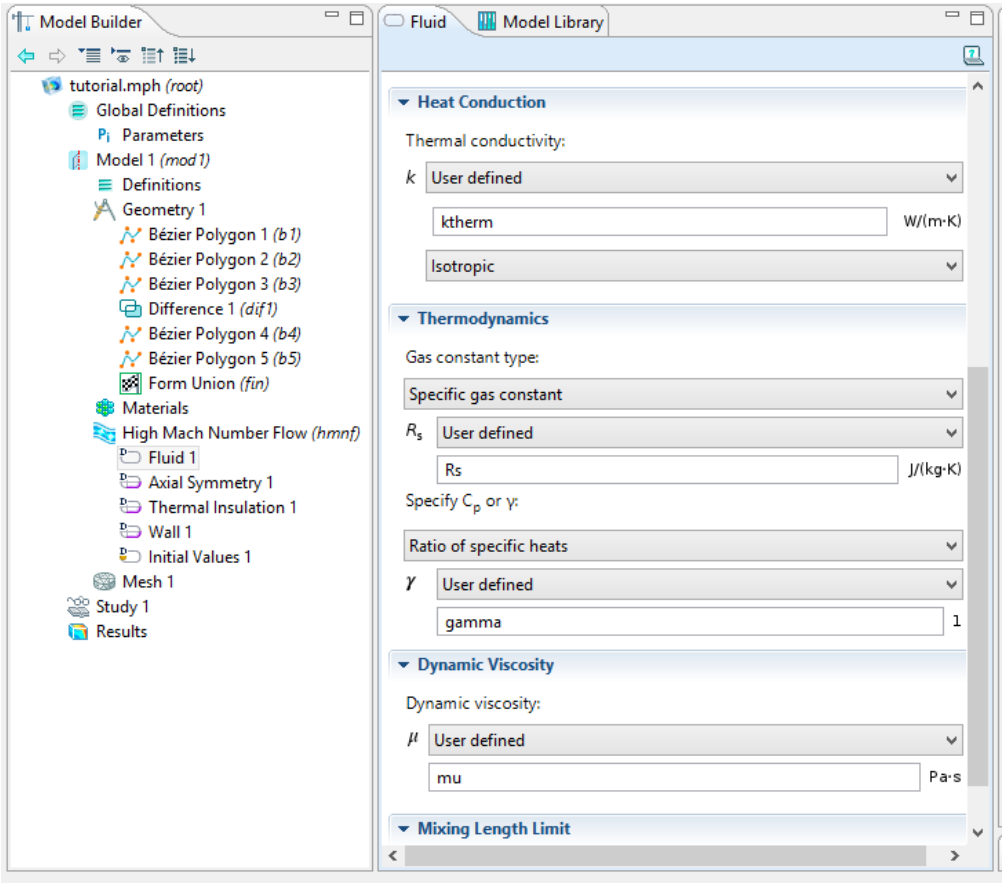

Fig. A. 6- Definition of the properties of the gas.

A.1.7. Boundary Conditions

The boundary conditions that COMSOL defines by default are correct (Wall 1, Axial Symmetry 1 and Thermal Insulation 1). This way, the boundary conditions at the walls are non-slip, thermal insulation and the utilization of wall functions. The other boundary conditions that must be defined are:

- Primary Inlet: First, the inlet of the primary stream is defined. Right click "High Mach Number Flow" and select "Inlet". Set the flow conditions to "Characteristics based" and the input state to "Total". The total pressure, total temperature and Mach number are "pp0", "Tp0" and 0. In the boundary selection select boundary 2 (Fig. A. 7 a).
- Secondary Inlet: Now, the inlet of the secondary stream is defined. Create a new "Inlet" section and set do the same as for the primary inlet. The total pressure, total temperature and Mach number are "ps0","Ts0" and 0. In the boundary selection select boundary 19 (Fig. A. 7 b).
- Outlet: The last boundary condition is the outlet. Right click "High Mach Number Flow" and select "Outlet". Set the flow condition to "subsonic" and, in the "Flow properties" section, set the boundary condition to pressure. Type "pb" as the pressure. Select boundary 7(Fig. A. 7 c).

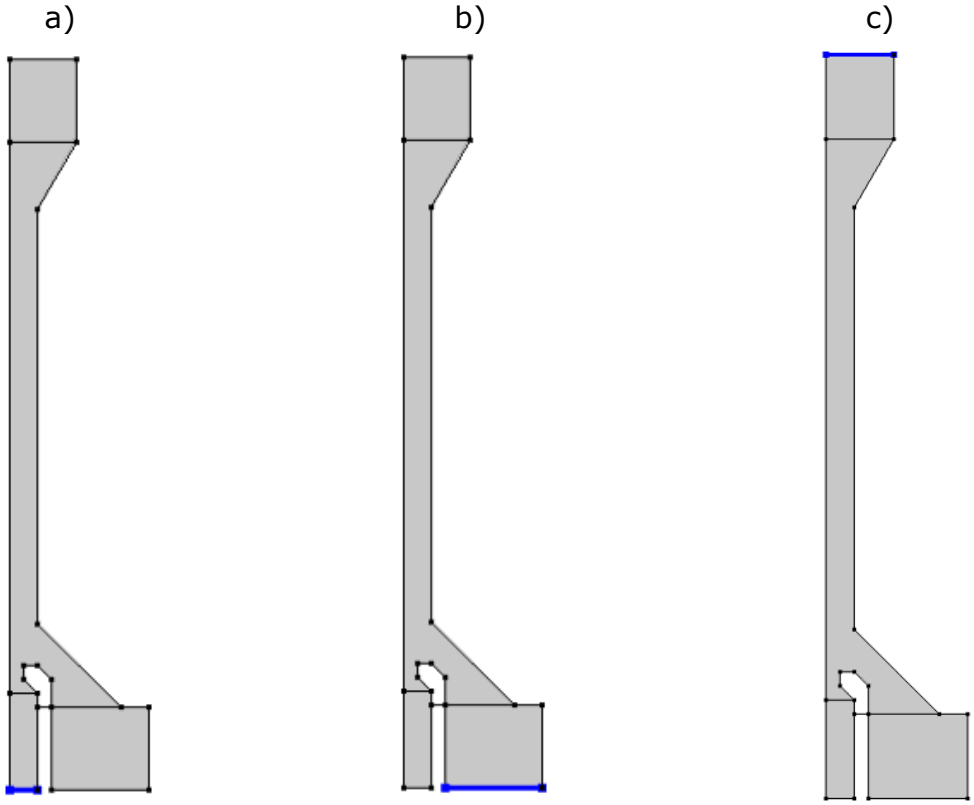

Fig. A. 7- Boundary selection for the primary (a) and secondary (b) inlets and the outlet (c).

A.1.8. Mesh.

In the previous steps the strong form of the problem has been defined. The next step is to discretize the domain. Here are described the steps used to obtained the mesh for the simulations of the project, which is a very fine mesh that requires a high amount of computational resources. However, if a less expensive but less accurate simulation is desired, coarser meshes can be used. The steps to obtain the mesh is:

- Select the "Mesh" section of the Model Builder. Set the "Sequence type to "User-controlled mesh". Now, new sections have appeared in the Model Builder under "Mesh 1".
- Select "Size". Set the "Calibrate for" to "Fluid dynamics" and the predefined mesh to "Finer".
- Select "Size 1". Set the "Calibrate for" to "Fluid dynamics" and the predefined mesh to "Extremely Fine".
- Right click "Mesh 1" and select "Size". Set the "Calibrate for" to "Fluid dynamics" and the predefined mesh to "Extra Fine". In the "Geometry entity selection" select "domain". Select domain 2 (Fig. A. 8).

Fig. A. 8- Domain for Size 2.

- Right click "Mesh 1" and select "More operations->Refine". Expand the "Refine Elements in Box" section and check "Specify bounding box". Set the "Lower bound" to r=0 and z=-npx, and the "Upper bound" to r=D2/2 and z=lin.
- Add a new "Refine" operation. Expand the "Refine Elements in Box" section and check "Specify bounding box". Set the "Lower bound" to r=0 and z=(-npx-lh-eh), and the "Upper bound" to r=D2/2 and z=-npx.
- Click the "Build All" button to mesh the domain.

A.2. Processing.

The process consist of two studies, an initialization study and the continuation study where the problem is solved for different values of the primary pressure.

A.2.1. Study 1

The first study consist of an initialization sweep where the problem is solved using isotropic diffusion and then the isotropic diffusion is reduced iteratively until it is not used.

First, the continuation study will be defined. Click "Step 1: Stationary" under the "Study 1" section. Then, select "Study extensions" and check "Continuation". Add the tuning parameter to the continuation sweep and type "range(0.25,-0.025,0)" in the "Parameter value list" (Fig. A. 9).

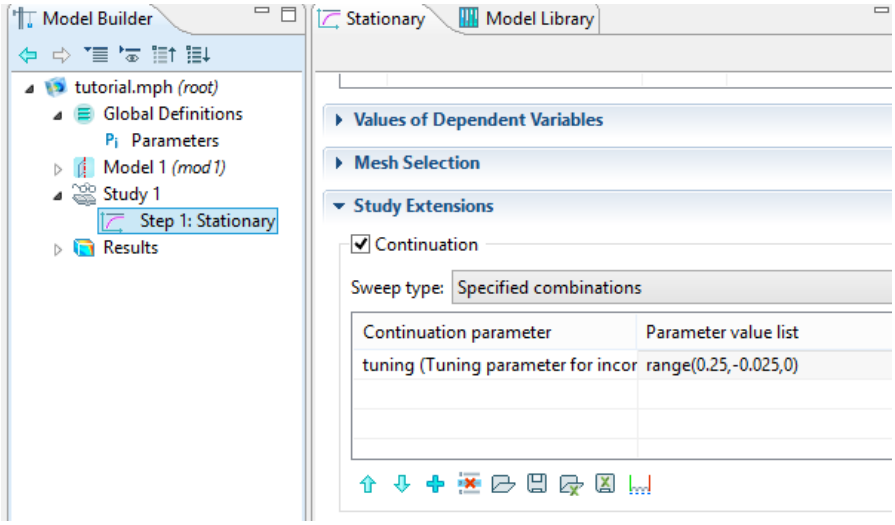

Fig. A. 9- Definition of the continuation sweep for study 1.

This way, the problem will be solved first with a tuning parameter for isotropic diffusion equal to 0.25. Then this solution will be used as the initial solution of a new problem with a tuning parameter of 0.225. Repeating this, the final result is the first value of pressure solved with no isotropic diffusion, which is a useful tool to achieve convergence but can have a negative effect over the solution.

The first parameter of primary pressure solved should be equal or lower than 1.75 bar_{abs} in order to capture the subcritical mode of the ejector and how the ejector works when the flow in the nozzle is subsonic. This first parameter of pressure has been defined in the "Parameters" section as $1.75 \cdot 10^5$ Pa.

Now, the solver used must be defined. Right click "Study 1" and select "Show default solver". This way, COMSOL shows the solver used per default for this problem. The solver can be seen expanding the "Solver 1-> Stationary Solver 1" section. This problem is solved using a segregated solver which solves two different groups of variables different. The maximum number of equations must be changed in order to ensure the obtaining of convergence with the desired relative tolerance (10^{-3}). Select "Segregated 1" and set the maximum number of iterations to 500.

Now "Study 1" could be computed. However, it is more recommendable to define "Study 2" first and compute the whole problem using a "Cluster". If this problem is solved in a personal computer, then it would be useful to use a coarser mesh or it could take several hours to solve the problem and consuming a lot of computational resources.

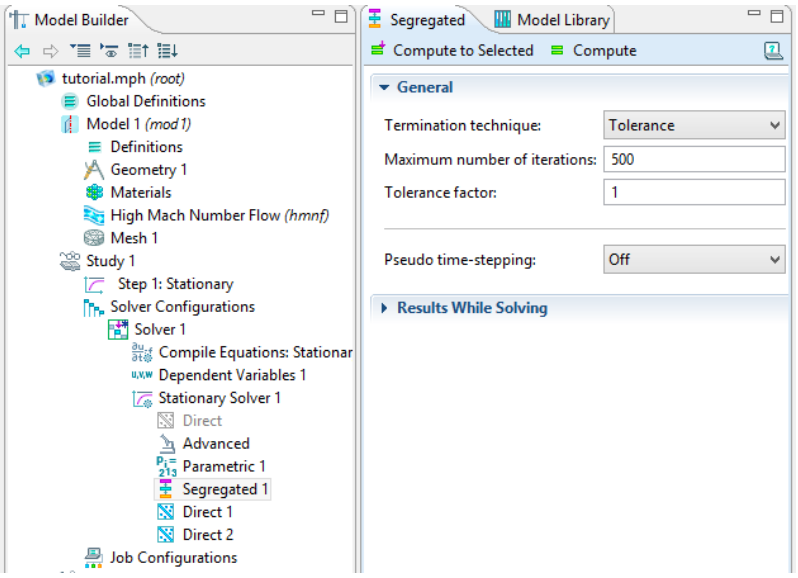

Fig. A. 10- Selection of the maximum number of iterations.

A.2.2. Study 2

This study is the real solution to the problem. It uses the solution obtained in Study 1 to do a continuation sweep in which the problem is solved for all the desired values of the primary pressure.

First, add a new stationary study. Right click the name of the model (in the image below, Fig. A. 11, it is "Tutorial.mph") in the Model Builder and select "Add study". Then, select "Step 1: Stationary Study" under "Study 2" and expand the "Values of Dependent Variables" section. Then, select the last solution of "Study 1" as the initial value of variables solved for (Fig. A. 11).

The next step is to define the continuation sweep done to obtain results with different values of pressure. Add a continuation sweep like in section A.2.1, select "pp0" as the "Continuation parameter" and type "range(1.75e5,0.25e5,4.5e5)". This way, the problem is solved for values of primary pressure between 1.75 bar_{abs} and 4.5 bar_{abs} with an increase of 0.25 bar.

The maximum number of iterations should also be set to 500.

A.2.3. Computation

Now, the problem can be solved. As said before, it is preferably to solve it using a remote cluster since it can take several hours depending on the hardware used. This problem took 10 hours to be solved using an Intel i5 processor with 4 cores.

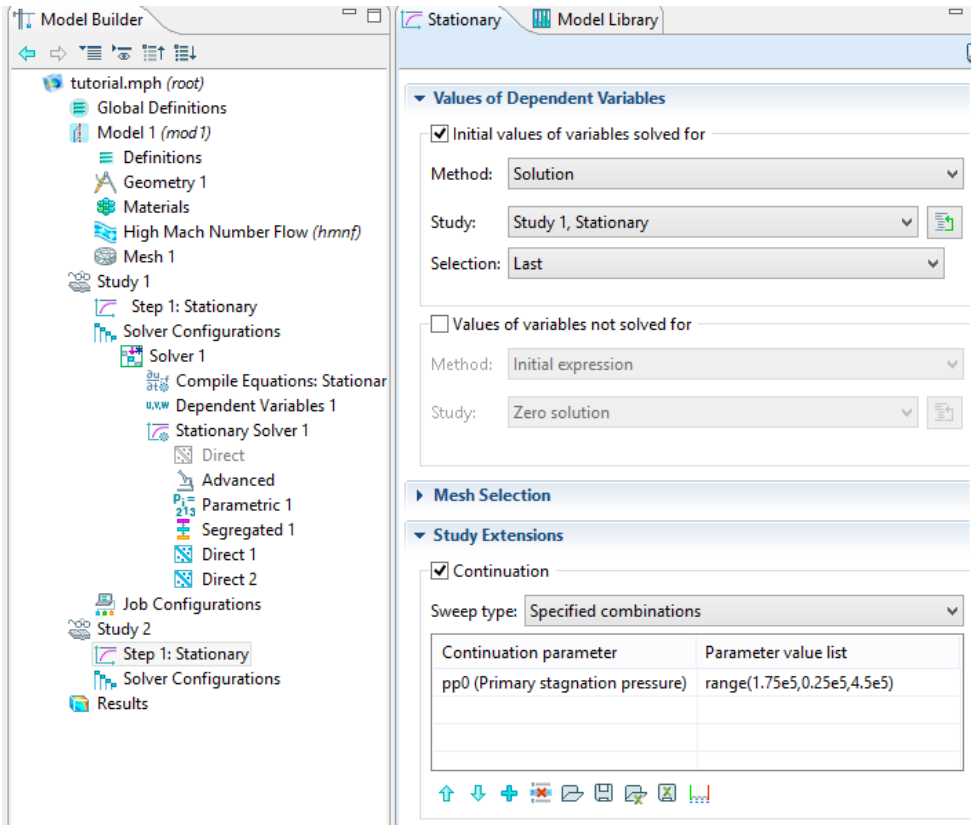

Fig. A. 11- Definition of study 2.

A.3. Postprocessing.

After solving the problem, COMSOL generates some default plots. A very useful plot is the plot of the wall resolution, which should be 11.06 for all the walls. If the result obtained is higher, then the mesh used is too coarse and must be refined. The result obtained is shown in Fig. A. 12.

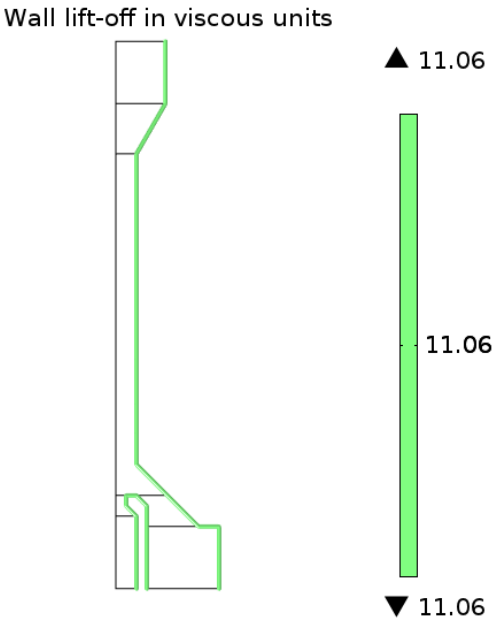

Fig. A. 12- Wall resolution obtained.

A.3.1. Computation of the mass flow

The objective of this simulation is to know the amount of mass flow obtained in the ejector under certain pressure and temperature conditions. Thus, the computation of the mass flow in the post process is mandatory.

The mass flow across an area is obtained as an integral along the area of the normal velocity to the boundary multiplied by the density.

Right click the "Derived Values" section, under "Results" and select "Integration-Line integration". Then, select the data set for which the mass flow is wanted and type "hmnf.rho*hmnf.uz*2*pi*r" as the expression to be integrated (Fig. A. 13). For the primary mass flow, the selected boundary must be the primary inlet, for the secondary, the secondary inlet, and for the mixed mass flow, the outlet (Fig. A. 7).

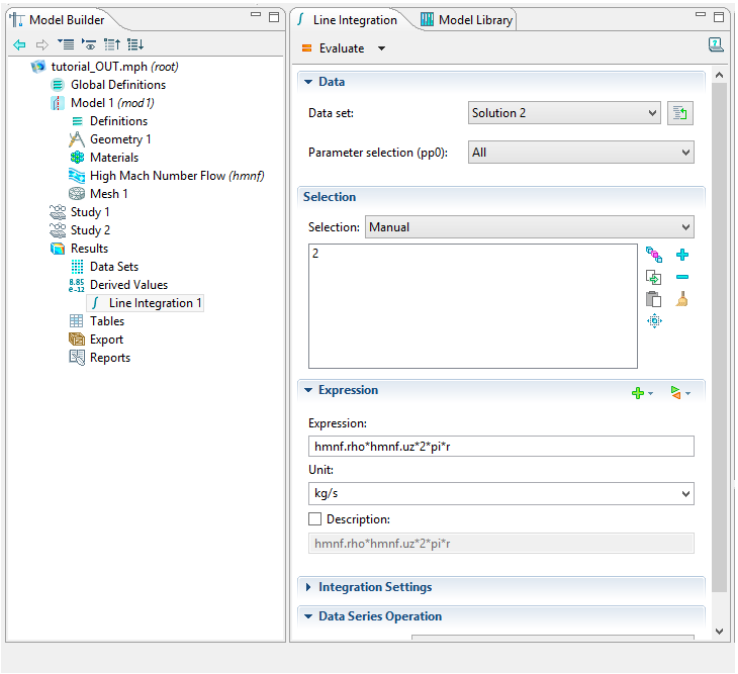

Fig. A. 13- Mass flow computation

APPENDIX B:

LABVIEW PROGRAMS

B.1. FPGA

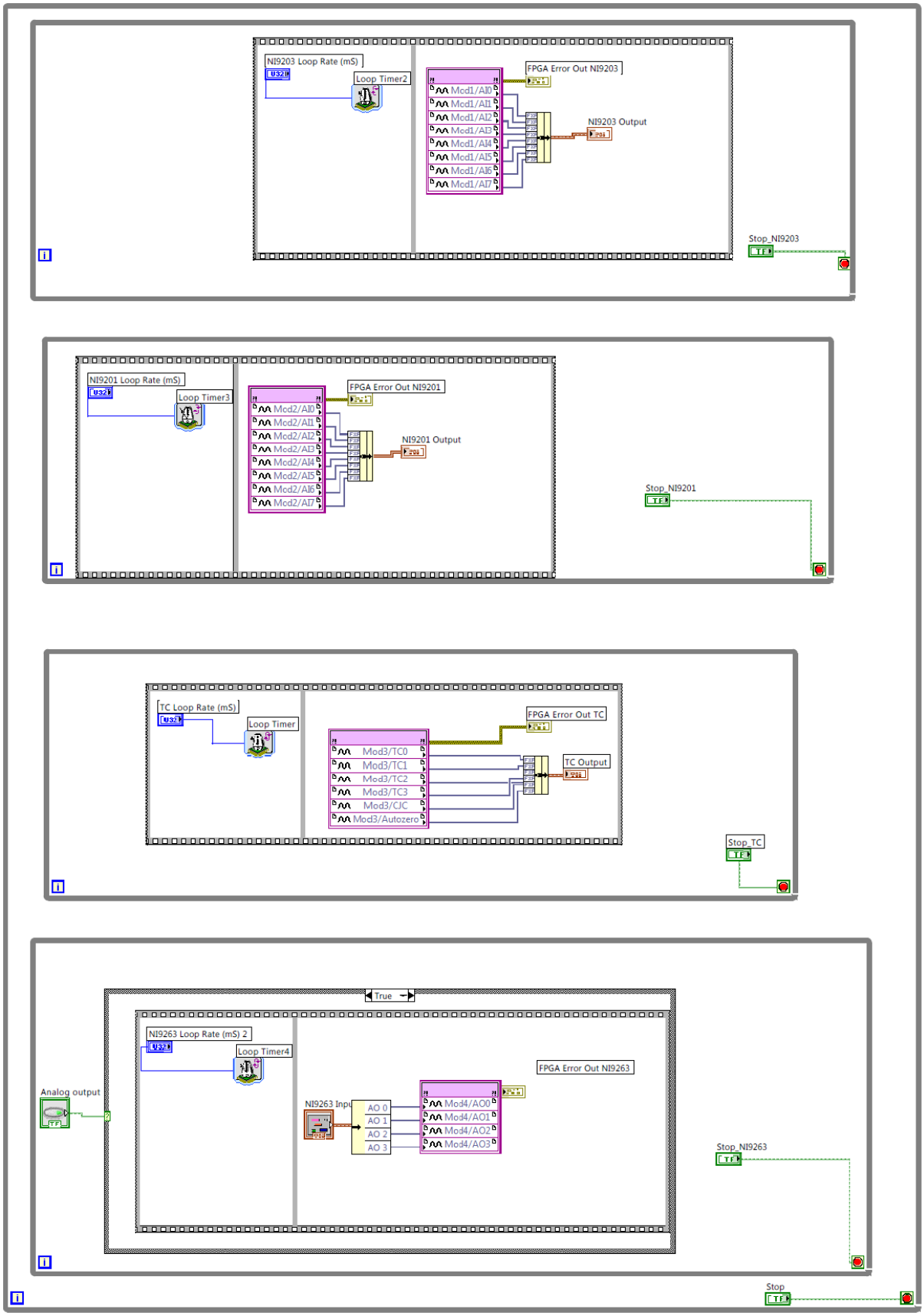
NI9203 Loop Rate (mS)
Loop Timer2
FPGA Error Out NI9203
Mod1/AI0
Mod1/AI1
Mod1/AI2
Mod1/AI3
Mod1/AI4
Mod1/AI5
Mod1/AI6
Mod1/AI7
NI9203 Output
Stop_NI9203
NI9201 Loop Rate (mS)
Loop Timer3
FPGA Error Out NI9201
Mod2/AI0
Mod2/AI1
Mod2/AI2
Mod2/AI3
Mod2/AI4
Mod2/AI5
Mod2/AI6
Mod2/AI7
NI9201 Output
Stop_NI9201
TC Loop Rate (mS)
Loop Timer
FPGA Error Out TC
Mod3/TC0
Mod3/TC1
Mod3/TC2
Mod3/TC3
Mod3/CJC
Mod3/Autozero
TC Output
Stop_TC
True
NI9263 Loop Rate (mS) 2
Loop Timer4
Analog output
FPGA Error Out NI9263
NI9263 Inpu
AO 0
AO 1
AO 2
AO 3
Mod4/AO0
Mod4/AO1
Mod4/AO2
Mod4/AO3
Stop_NI9263
Stop

B.2. RTOS

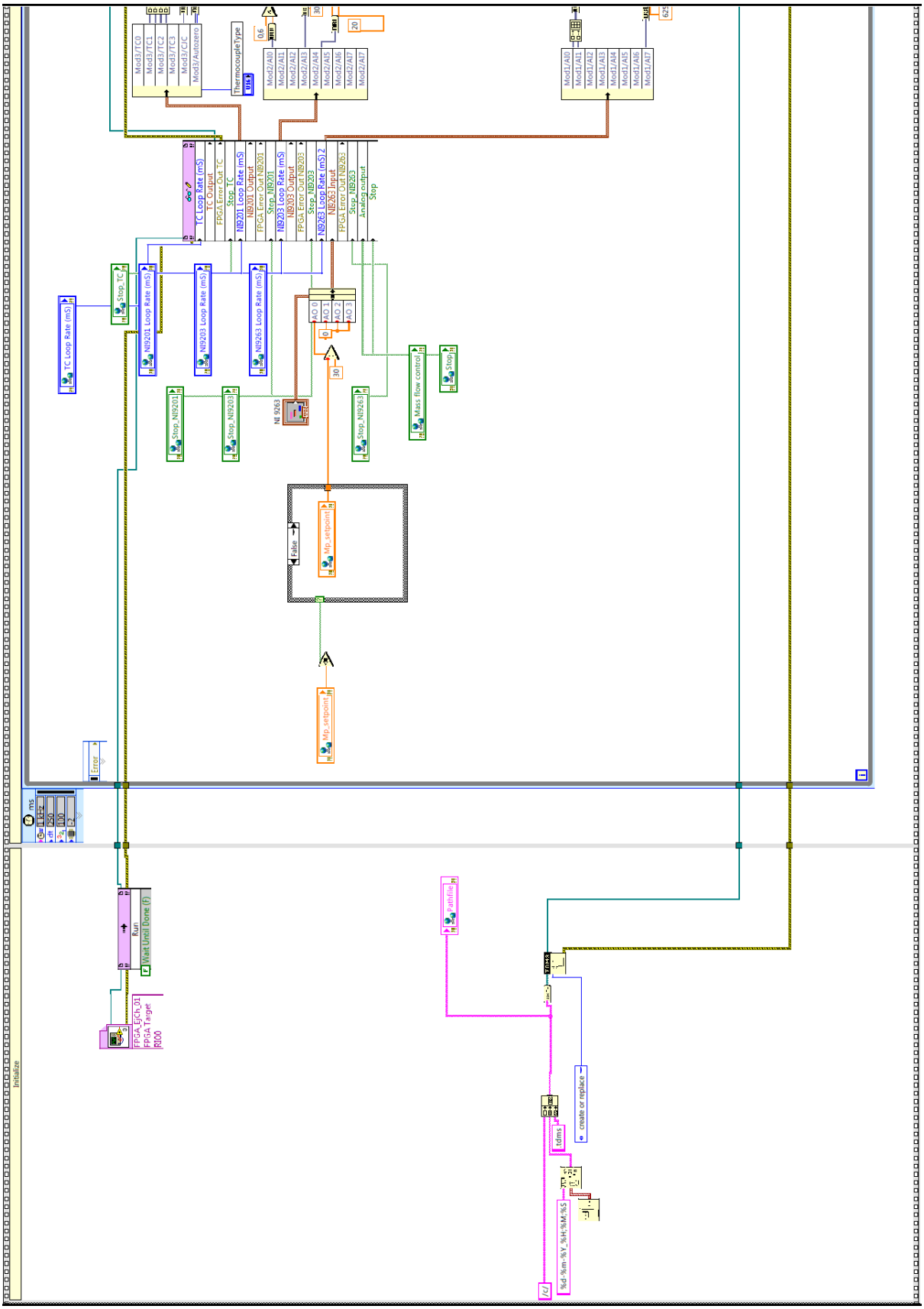
Mod3/TC0
Mod3/TC1
Mod3/TC2
Mod3/TC3
Mod3/CJC
Mod3/Autozero
ThermocoupleType
Mod2/AI0
Mod2/AI1
Mod2/AI2
Mod2/AI3
Mod2/AI4
Mod2/AI5
Mod2/AI6
Mod2/AI7
Mod1/AI0
Mod1/AI1
Mod1/AI2
Mod1/AI3
Mod1/AI4
Mod1/AI5
Mod1/AI6
Mod1/AI7
TC Loop Rate (mS)
TC Output
FPGA Error Out TC
Stop_TC
NI9201 Loop Rate (mS)
NI9201 Output
FPGA Error Out NI9201
Stop_NI9201
NI9203 Loop Rate (mS)
NI9203 Output
FPGA Error Out NI9203
Stop_NI9203
NI9263 Loop Rate (mS) 2
NI9263 Input
FPGA Error Out NI9263
Stop_NI9263
Analog output
Stop
AO 0
AO 1
AO 2
AO 3
NI 9263
Mass flow control
Stop
False
Mp_setpoint
Error
ms
Run
Wait Until Done (F)
FPGA_GCh_01
FPGA Target
RIO0
Initialize
Pathfile
create or replace
tdms
%d-%m-%Y_%Hh%Mm%Ss

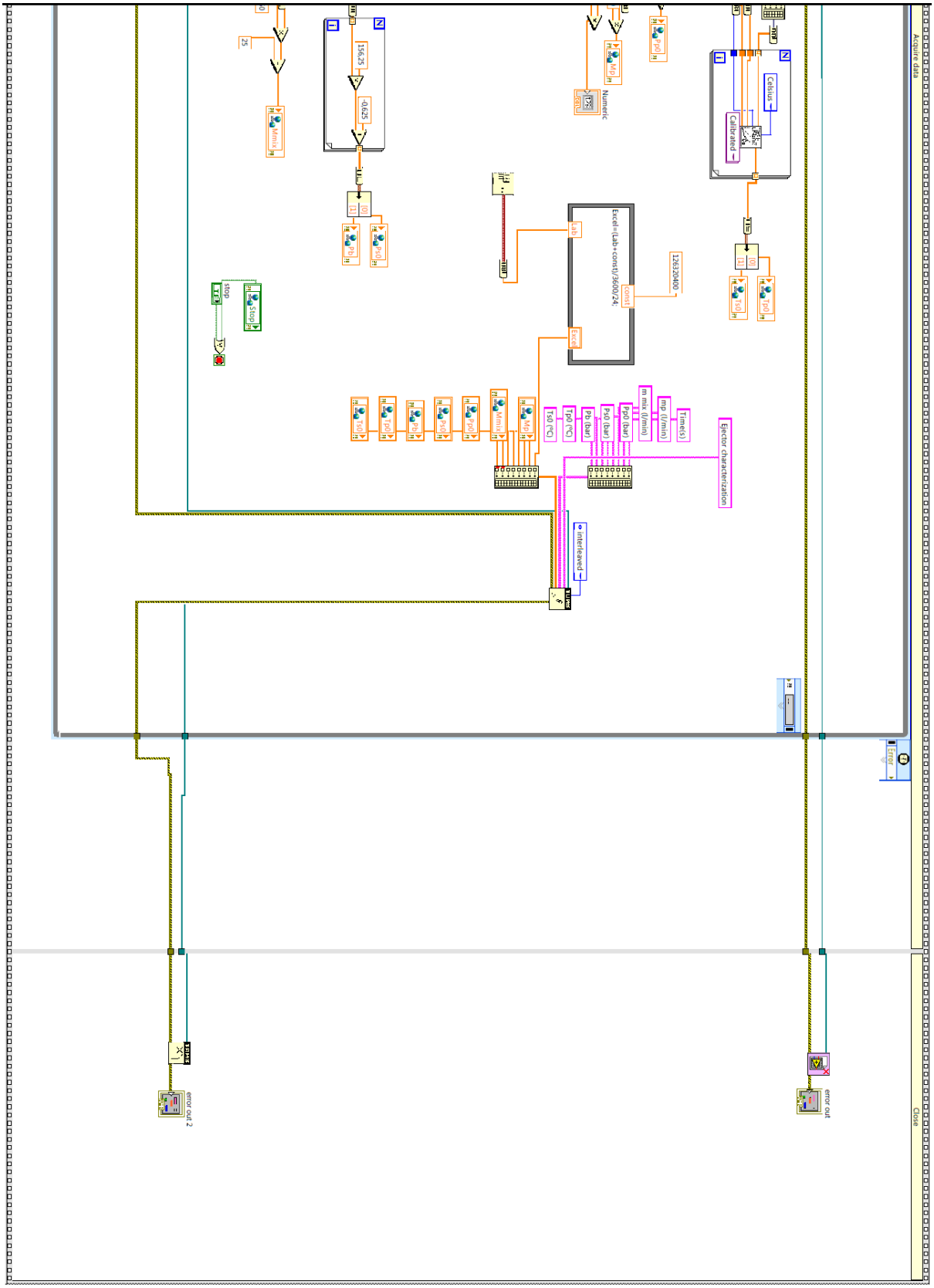
Acquire data
Close
Excel=(Lab+cons1)/3600/24;
12632400
Ejector characterization
interleaved
Numeric
Celsius
Calibrated
stop
error out
error out 2

B.3. HOST

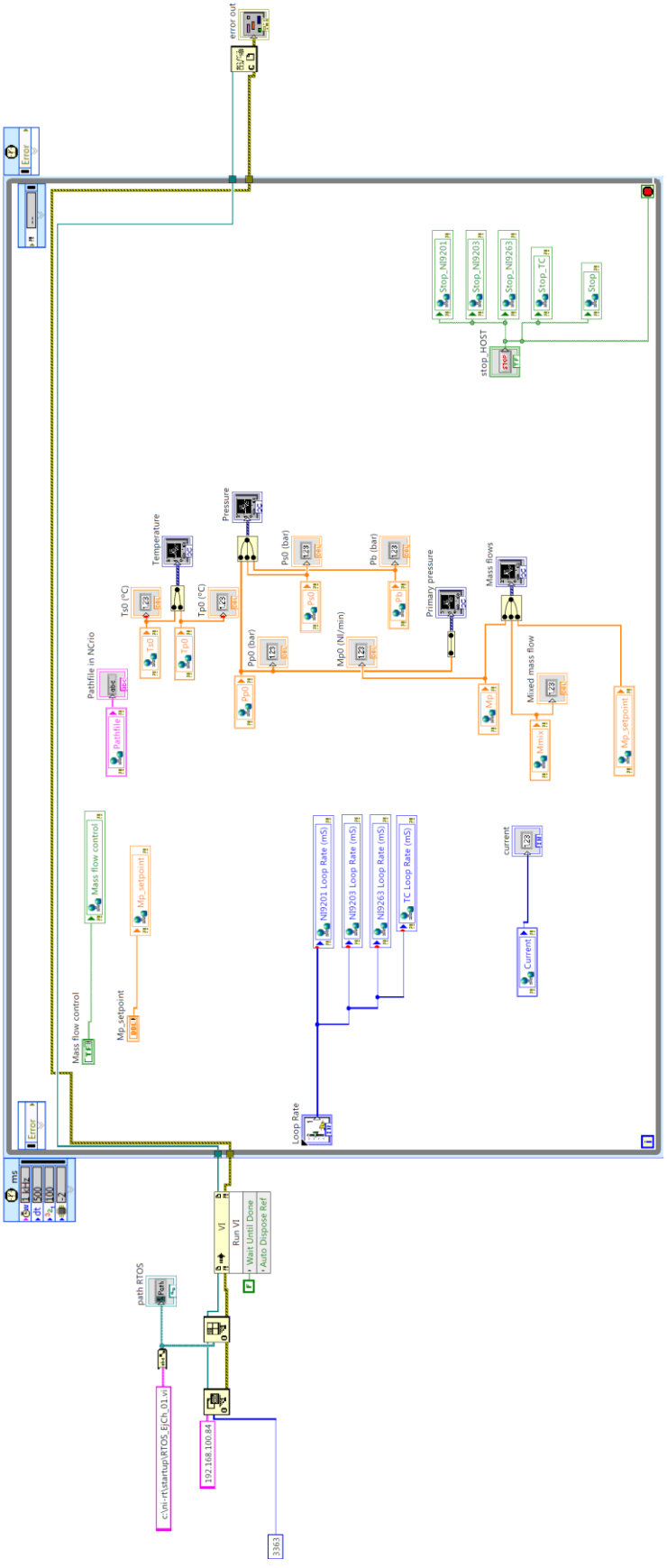
error out
Error
Stop_NI9201
Stop_NI9203
Stop_NI9263
Stop_TC
Stop
stop_HOST
Pressure
Temperature
Ts0 (°C)
Pb0 (bar)
Pb (bar)
Primary pressure
Mass flows
Mp0 (Nl/min)
Mixed mass flow
Mp_setpoint
Pathfile in NCrio
Pathfile
Mass flow control
current
NI9201 Loop Rate (mS)
NI9203 Loop Rate (mS)
NI9263 Loop Rate (mS)
TC Loop Rate (mS)
Loop Rate
ms
VI
Run VI
Wait Until Done
Auto Dispose Ref
path RTOS
Path
C:\ni-rt\startup\RTOS_EjCh_01.vi
192.168.100.84
3363

Escola Universitària d'Enginyeria
Tècnica Industrial de Barcelona
Consorci Escola Industrial de Barcelona
UNIVERSITAT POLITÈCNICA DE CATALUNYA

Budget

IMPLEMENTATION AND CHARACTERIZATION OF AN EJECTOR BASED HYDROGEN RECIRCULATION SYSTEM FOR A PEM FUEL CELL

TFG presentat per optar al títol de GRAU en
ENGINYERIA MECÀNICA
per **Xavier Corbella Coll**

Barcelona, 9 de Juny de 2015

Director: Ricardo Torres Cámara
Departament de MF
Universitat Politècnica de Catalunya (UPC)

Codirector: Miguel Allué Fantova
Departament Automatic Control
Institut de Robòtica i Informàtica Industrial (IRI/CSIC)

CONTENTS

Part 1: Budget broken down into sections 1
1.1. Valves and piping 1
1.1.1. Valves 1
1.1.2. Piping and fittings 2
1.2. Data acquisition system 2
1.3. Sensors and actuators 3
1.4. Electronics 3
1.5. Gases 3
1.6. Computer and software 4
1.6.1. Computational costs 4
1.6.2. Licenses and software 4
1.7. Support Structures 5
1.8. Ejector 5
1.9. Professional fees 6
Part 2: Total budget 7

PART 1: BUDGET BROKEN DOWN INTO SECTIONS

1.1. Valves and piping

1.1.1. Valves

Units		Unit cost	Total cost
2	10mm Stainless Steel 2-way ball valves (Hy-Lok BVH-10M-S316)	98.92 €	197.84 €
3	¼" Stainless Steel 2-way ball valves (Swagelok SS-42S4)	71.50 €	214.50 €
1	Swagelok in-line filter SS-6F-MM	61.60 €	61.60 €
1	Tee-type filter (Swagelok SS-10TF-MM-140)	65.50 €	65.50 €
1	Check valve (Swagelok SS-6C-1/3)	91.20 €	91.20 €
2	Check valve (Legris 4890 13 13)	13.96 €	27.92 €
			658.56 €

1.1.2. Piping and fittings

Units		Unit cost	Total cost
2	¼" Stainless Steel Union Tee	21.30 €	42.60 €
2	10mm Plastic Union Tee	7.20 €	14.40 €
2	¼" Stainless Steel Union Cross	38.80 €	77.60 €
2	10 mm Plastic Union Elbow	14.30 €	28.60 €
3	Connector Swagelok SS-400-1-4	6.70 €	20.10 €
24	Stainless Steel Nut	1.83 €	43.92 €
24	Stainless Steel Front Ferrule	1.04 €	24.96 €
7	Stainless Steel Plug	5.20 €	36.40 €
1	4 m of ¼" rubber pipe	3.75 €/m	15.00 €
1	2 m of Stainless Steel pipe	6.00 €/m	12.00 €
1	0.2 m of Plastic pipe	3.00 €/m	0.60 €
			316.18 €

1.2. Data acquisition system

Units		Unit cost	Total cost
1	NI cRIO 9022	3084.00 €	3084.00 €
1	Host computer	850.00 €	850.00 €
1	FPGA 9133	633.00 €	633.00 €
1	I/O Module NI9203	509.40 €	509.40 €
1	I/O Module NI9201	395.10 €	395.10 €
1	I/O Module NI9211	252.45 €	252.45 €
1	I/O Module NI9263	275.40 €	275.40 €
			5999.35 €

1.3. Sensors and actuators

Units		Unit cost	Total cost
1	150 nlpm Air Mass Flow Controller	1600.00 €	1600.00 €
1	100 nlpm Air Mass Flow Controller	1457.83 €	1457.83 €
1	Pressure Transmitter 6 bar	206.00 €	206.00 €
2	Pressure Transmitter 2.5 bar	128.11 €	256.22 €
2	Pressure regulator 10 bar	160.00 €	320.00 €
2	Thermocouple type K	2.91 €	5.82 €
			3845.87 €

1.4. Electronics

Units		Unit cost	Total cost
1	Power source	133.52 €	133.52 €
1	Signal and power wiring	23.00 €	23.00 €
			156.52 €

1.5. Gases

Units		Unit cost	Total cost
1	6000 NL of hydrogen (Air)	13.70 €/m^3	82.20 €
			82.20 €

1.6. Computer and software

1.6.1. Computational costs

Units		Unit cost	Time used	Total cost
1	ASUS laptop	1000 €		1000.00 €
1	Cluster	5700 €		5700.00 €
1	Internet	30 €/month	8 months	240.00 €
				6940.00 €

1.6.2. Licenses and software

Units		Unit cost	Time used	Total cost
1	COMSOL 4.3a	4000.00 €	400 h	2000.00 €
1	LabVIEW 2014 Embedded Control and Monitoring suite	11000.00 /year €	30 h	1833.33 €
1	SolidWorks 2014	3995.00 €	15 h	665.83 €
1	Microsoft Office 2013 Pack	119.00 €	-	119.00 €
1	Scientific database subscription	18300.00 €/year	3 months	4575.00 €
				9193.16 €

Some of the licenses are floating, so they are shared and not used all year long. Thus, their cost has been considered as the proportional cost with respect to the hours used and considering a 6 month contract for COMSOL, and a 2 months contract for SolidWorks and LabVIEW.

1.7. Support Structures

Units		Unit cost	Total cost
1	160x50mm wood board	8.00 €	8.00 €
1	1.5m of DIN rail	4.20 €/m	6.30 €
			14.30 €

1.8. Ejector

Units		Unit cost	Total cost
1	Experimental ejector	480.00 €	480.00 €
1	Nozzle 2 and Outlet 2	200.00 €	200.00 €
1	O-rings	23.83 €	23.83 €
			703.83 €

1.9. Professional fees

	Cost per hour	Hired hours	Total
Junior engineer	15.00 €/h	800 h	12000.00 €
Senior engineer	35.00 €/h	150 h	5250.00 €
			13750.00 €

The justification for the payment of salaries is:

	Junior engineer	**Senior engineer**
Accruals		
Base salary	15.00 €/h	35.00 €/h
Total accrued	12000 €	5250.00 €
Deductions		
4.7% Social Security	564.00 €	246.75 €
10 % I.R.P.F	1200.00 €	525.00 €
	10236.00 €	**4478.25 €**

PART 2:

TOTAL BUDGET

1. Valves and piping	974.74 €
2. Data acquisition system	5999.35 €
3. Sensors and actuators	3845.87 €
4. Electronics	156.52 €
5. Gases	82.20 €
6. Computer and software	16133.16 €
7. Support Structures	14.30 €
8. Ejector	703.83 €
9. Professional fees	14714.25 €
TOTAL	**42624.22 €**

Escola Universitària d'Enginyeria
Tècnica Industrial de Barcelona
Consorci Escola Industrial de Barcelona
UNIVERSITAT POLITÈCNICA DE CATALUNYA

Volume III
Technical Drawings

TREBALL DE FI DE GRAU

IMPLEMENTATION AND CHARACTERIZATION OF AN EJECTOR BASED HYDROGEN RECIRCULATION SYSTEM FOR A PEM FUEL CELL

TFG presentat per obtenir el títol de GRAU en
ENGINYERIA MECÀNICA

Per **Xavier Corbella Coll**

Barcelona, 9 de Juny de 2015

Director: Ricardo Torres Cámara
Departament de MF
Universitat Politècnica de Catalunya (UPC)

Codirector: Miguel Allué Fantova
Departament Automatic Control
Institut de Robòtica i Informàtica Industrial (IRI/CSIC)

CONTENTS

Contents
Drawing 1: Experimental Ejector
Drawing 2: Body
Drawing 3: Outlet 1
Drawing 4: Nozzle Support
Drawing 5: Nozzle 1
Drawing 6: Hexagonal Nut
Drawing 7: TS4 Ejector
Drawing 8: Outlet 2
Drawing 9: Nozzle 2

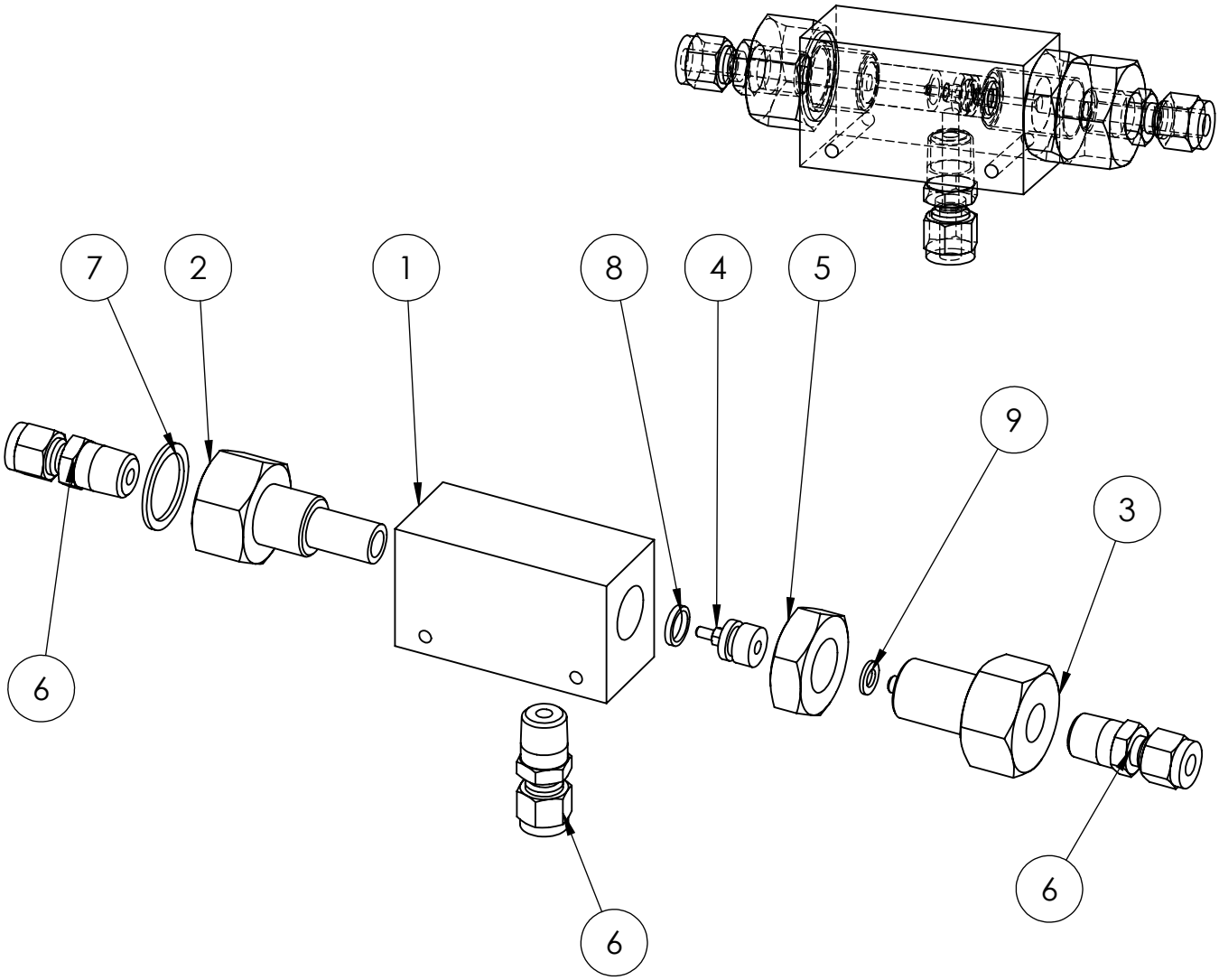

Number	Name	Amount
1	Body	1
2	Outlet 1	1
3	Nozzle Support	1
4	Nozzle 1	1
5	Hexagonal Nut	1
6	Connector SS-400-1-4	3
7	Toric Joint 1	1
8	Toric Joint 2	1
9	Toric Joint 3	1

Author: Xavier Corbella Coll (10/01/2015)

Checked:

Implementation and characterization of anejector based H2 recirculation system for a PEM fuel cell

Name of the Assembly: Experimental Ejector

Drawing nº: 1

Material: SS Type 316

Format: DIN A4

Scale: 1:2

Projection:

Escola Universitària d'Enginyeria Tècnica Industrial de Barcelona
Consorci Escola Industrial de Barcelona

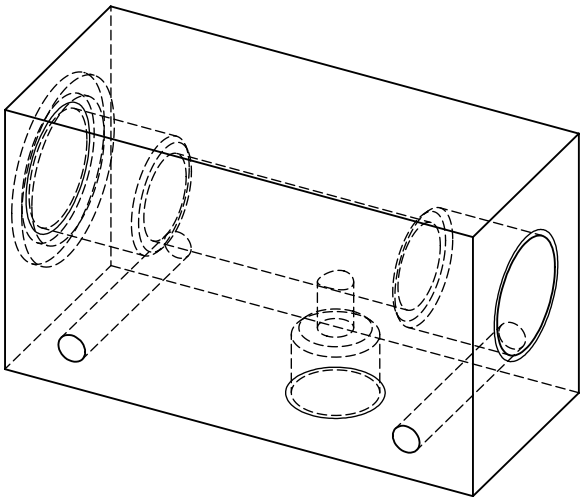

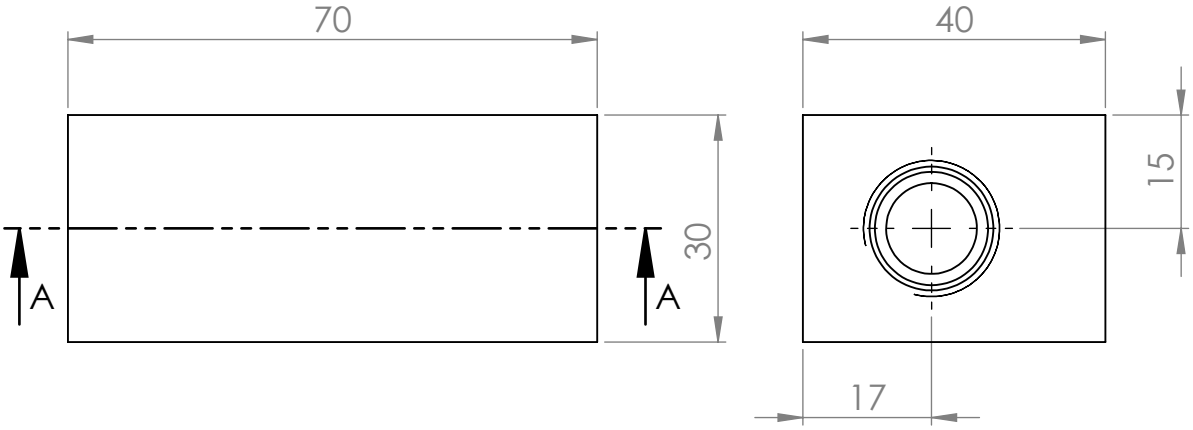

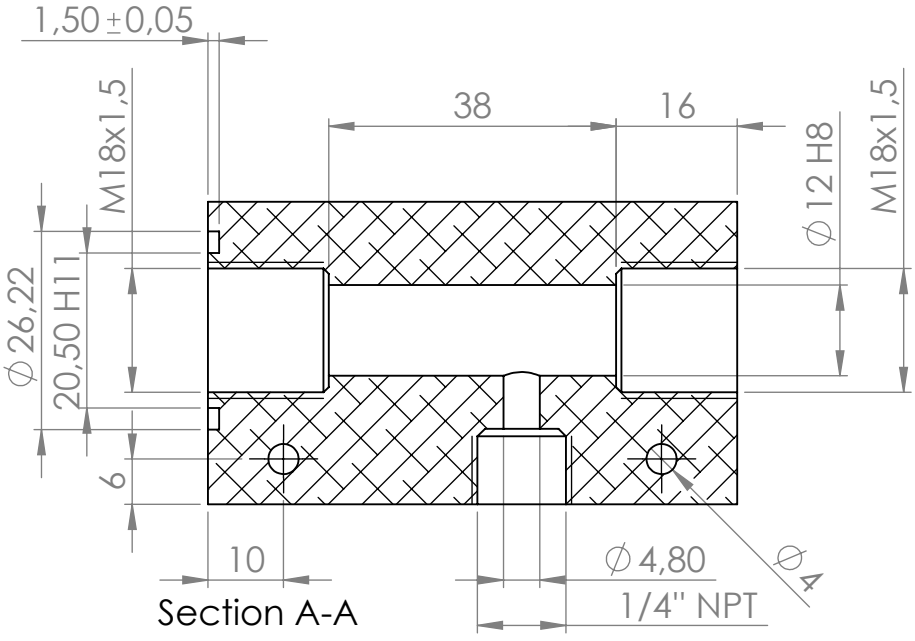

General Tolerances to ISO 2768

Author: Xavier Corbella Coll (10/01/2015) Checked:	Name of the piece: Body	Drawing nº 2
Implementation and characterization of an ejector based H2 recirculation system for a PEM fuel cell	Material: SS Type 316	
Edición de estudiante de SolidWorks. Sólo para uso académico.	Format: DIN A4 / Scale: 1:1	Projection:

Escola Universitària d'Enginyeria Tècnica Industrial de Barcelona
Consorci Escola Industrial de Barcelona

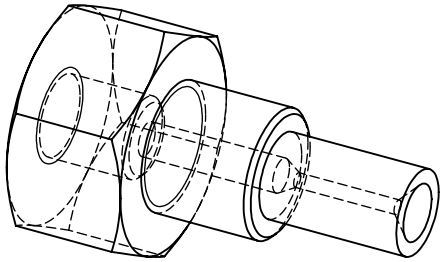

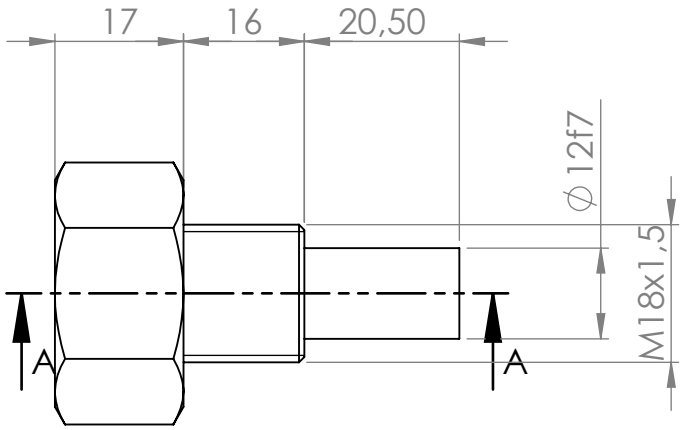

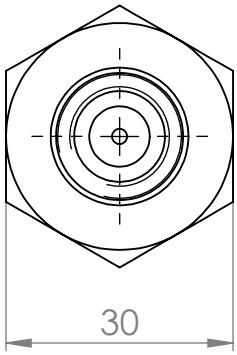

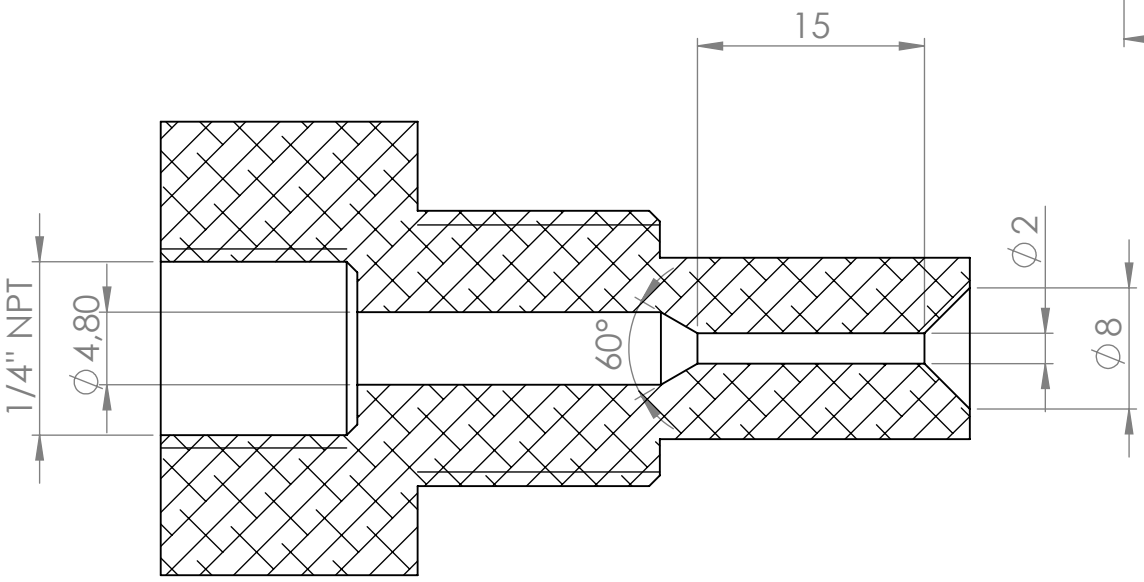

SECTION A-A
SCALE 2 : 1

General Tolerances to ISO 2768

Author: Xavier Corbella Coll (10/01/2015) Checked:	Name of the piece: Outlet 1	Drawing nº 3
Implementation and characterization of anejector based H2 recirculation system for a PEM fuel cell	Material: SS Type 316	
Edición de estudiante de SolidWorks. Sólo para uso académico.	Format: DIN A4 / Scale: 1:1	Projection:

Escola Universitària d'Enginyeria Tècnica Industrial de Barcelona
Consorci Escola Industrial de Barcelona

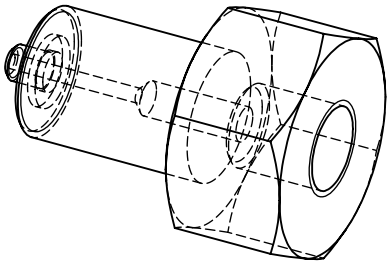

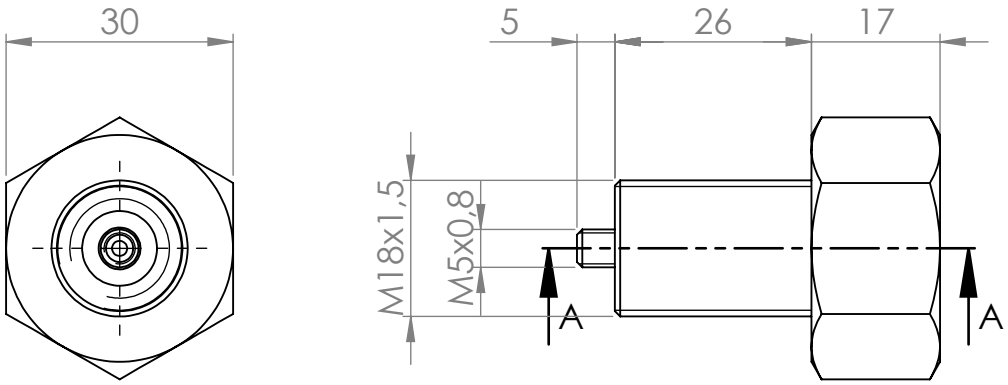

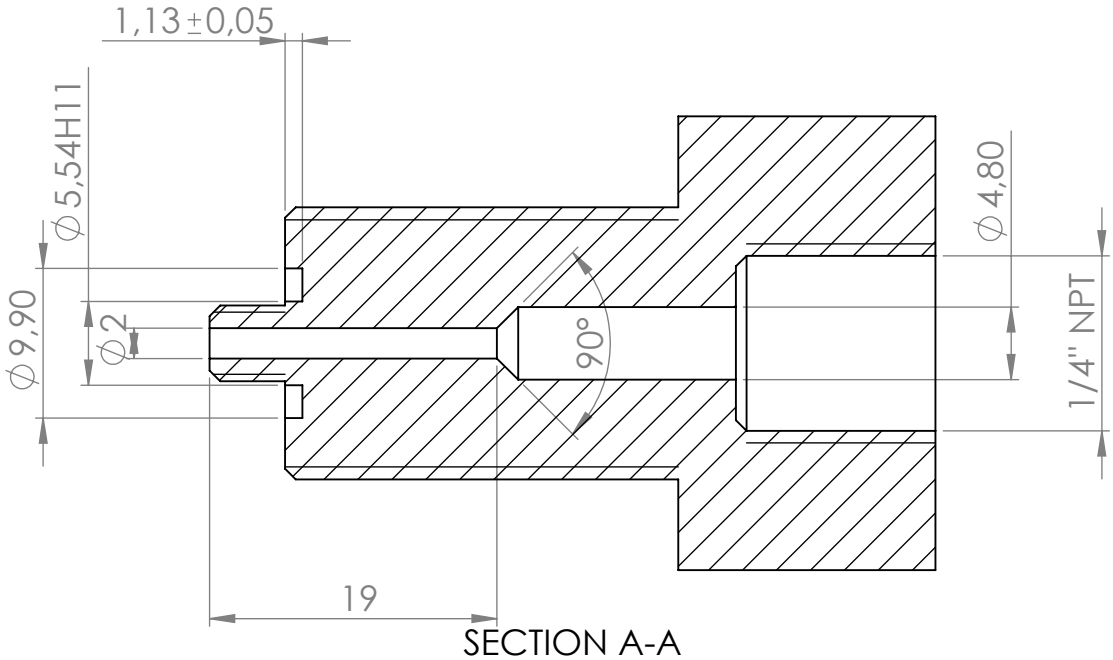

SECTION A-A
SCALE 2 : 1

General Tolerances to ISO 2768

Author: Xavier Corbella Coll (10/01/2015) Checked:	Name of the piece: Nozzle Support	Drawing nº 4
Implementation and characterization of anejector based H2 recirculation system for a PEM fuel cell	Material: SS Type 316	
Edición de estudiante de SolidWorks. Sólo para uso académico.	Format: DIN A4 / Scale: 1:1	Projection:

Escola Universitària d'Enginyeria Tècnica Industrial de Barcelona
Consorci Escola Industrial de Barcelona

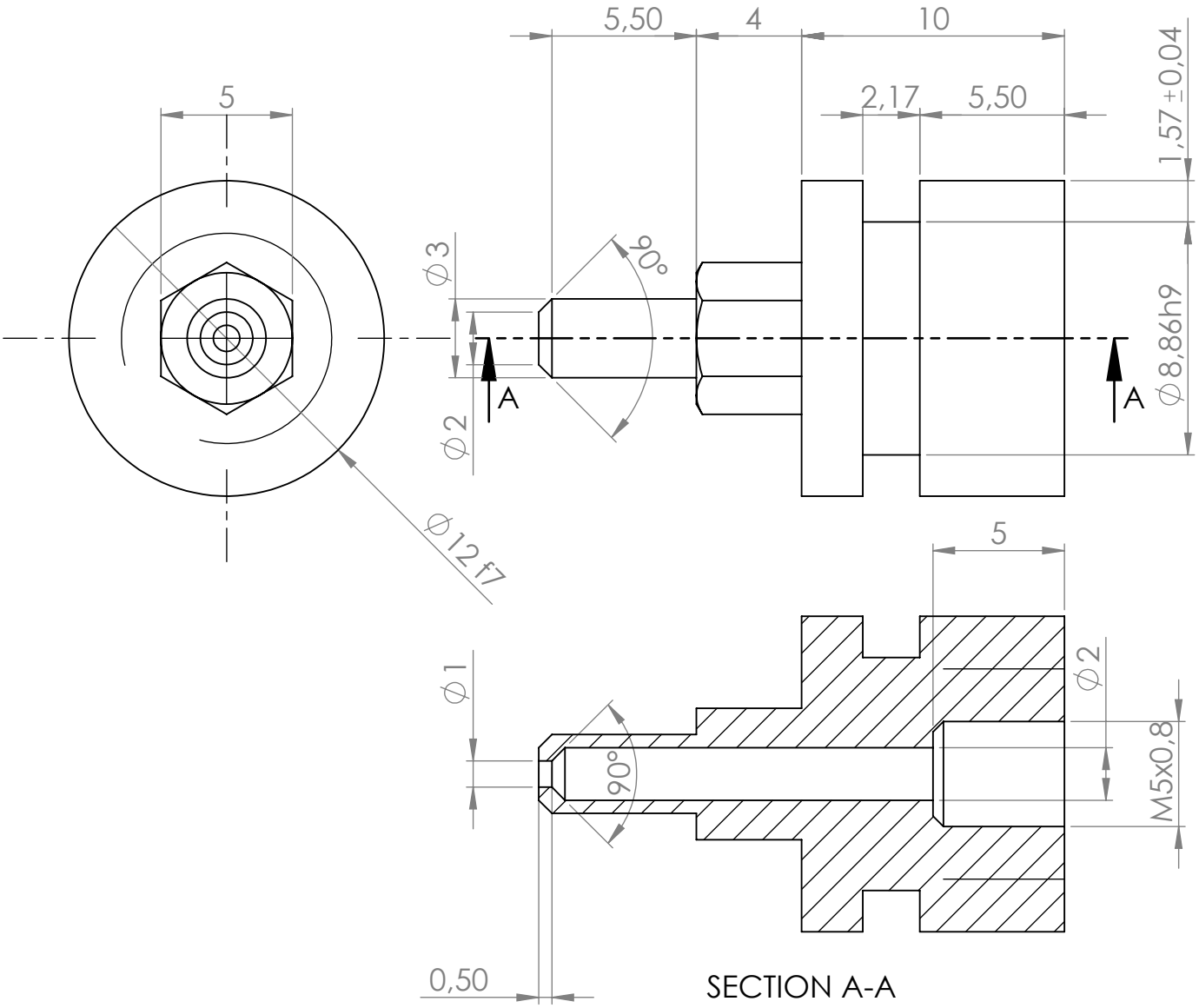

SECTION A-A

General Tolerances to ISO 2768

Author: Xavier Corbella Coll (10/01/2015) Checked:	Name of the piece: Nozzle 1	Drawing nº 5
Implementation and characterization of anejector based H2 recirculation system for a PEM fuel cell	Material: SS Type 316	
Edición de estudiante de SolidWorks. Sólo para uso académico.	Format: DIN A4 / Scale: 4:1	Projection:

Escola Universitària d'Enginyeria Tècnica Industrial de Barcelona
Consorci Escola Industrial de Barcelona

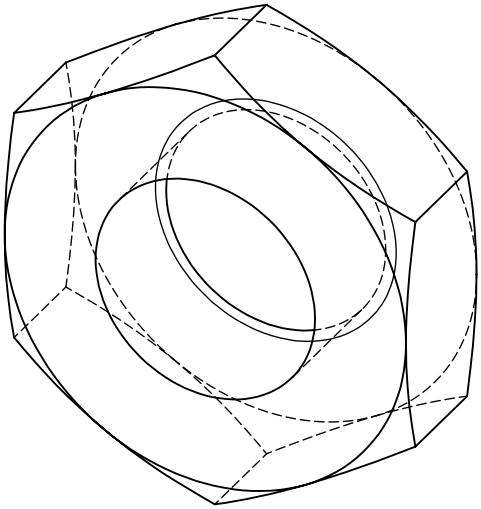

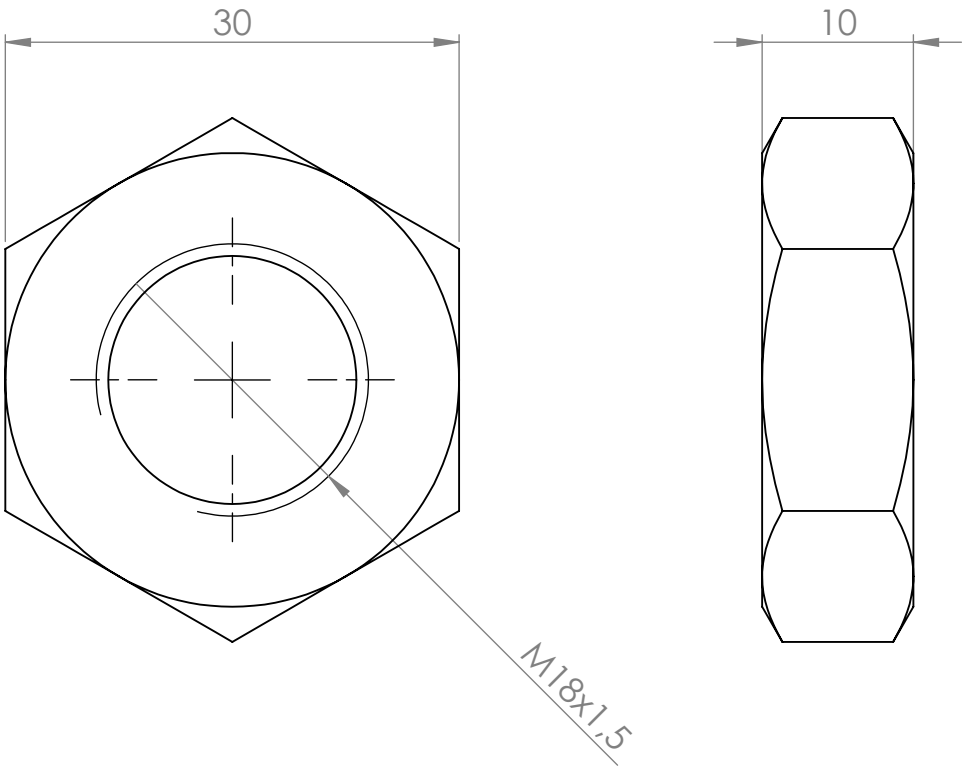

General Tolerances to ISO 2768

Author: Xavier Corbella Coll (10/01/2015) Checked:	Name of the piece: Hexagonal Nut	Drawing nº 6
Implementation and characterization of anejector based H2 recirculation system for a PEM fuel cell	Material: SS Type 316	
Edición de estudiante de SolidWorks. Sólo para uso académico.	Format: DIN A4 / Scale: 2:1 / Projection:	

Escola Universitària d'Enginyeria Tècnica Industrial de Barcelona
Consorci Escola Industrial de Barcelona

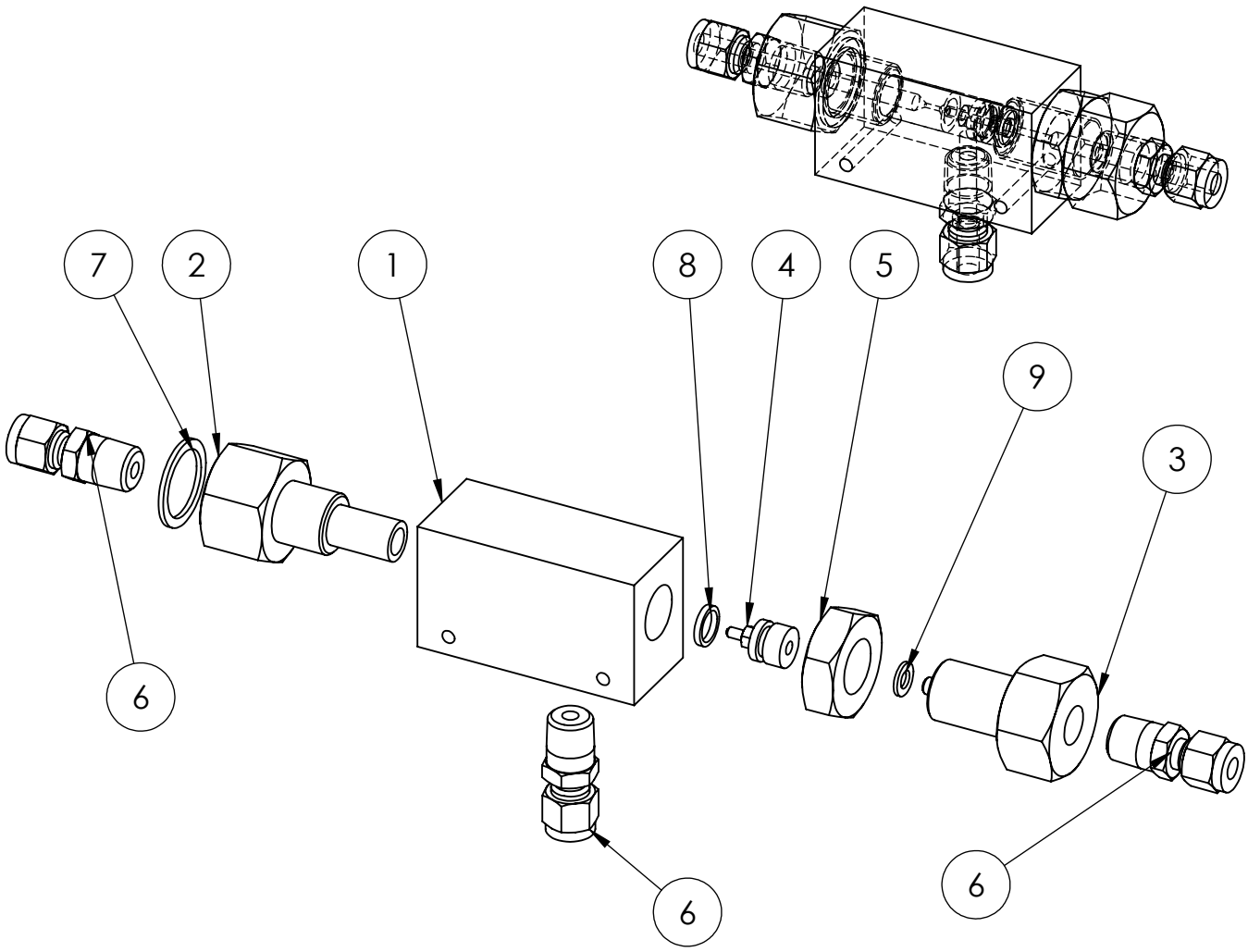

Number	Name	Amount
1	Body	1
2	Outlet 2	1
3	Nozzle Support	1
4	Nozzle 2	1
5	Hexagonal Nut	1
6	Connectors SS-400-1-4	3
7	Toric Joint 1	1
8	Toric Joint 2	1
9	Toric Joint 3	1

Author: Xavier Corbella Coll (08/05/2015)
Checked:

Implementation and characterization of anejector based H2 recirculation system for a PEM fuel cell

Name of the assembly: TS4 Ejector

Drawing nº 7

Material: SS Type 316

Format: DIN A4

Scale: 1:2

Projection:

Escola Universitària d'Enginyeria Tècnica Industrial de Barcelona
Consorci Escola Industrial de Barcelona

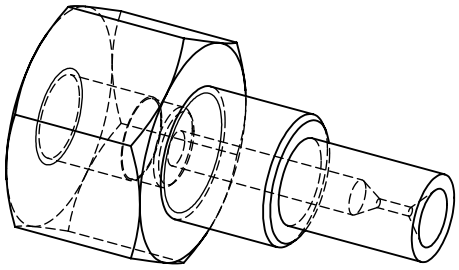

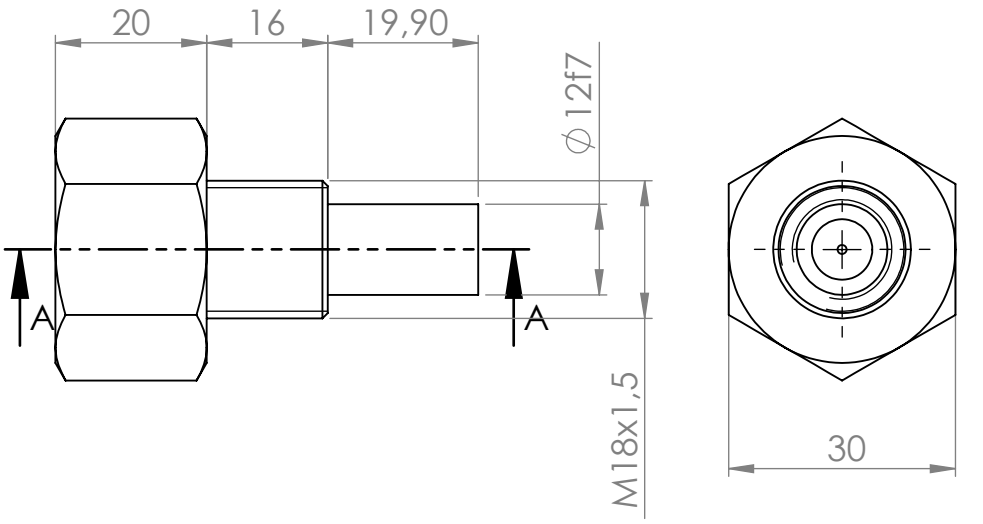

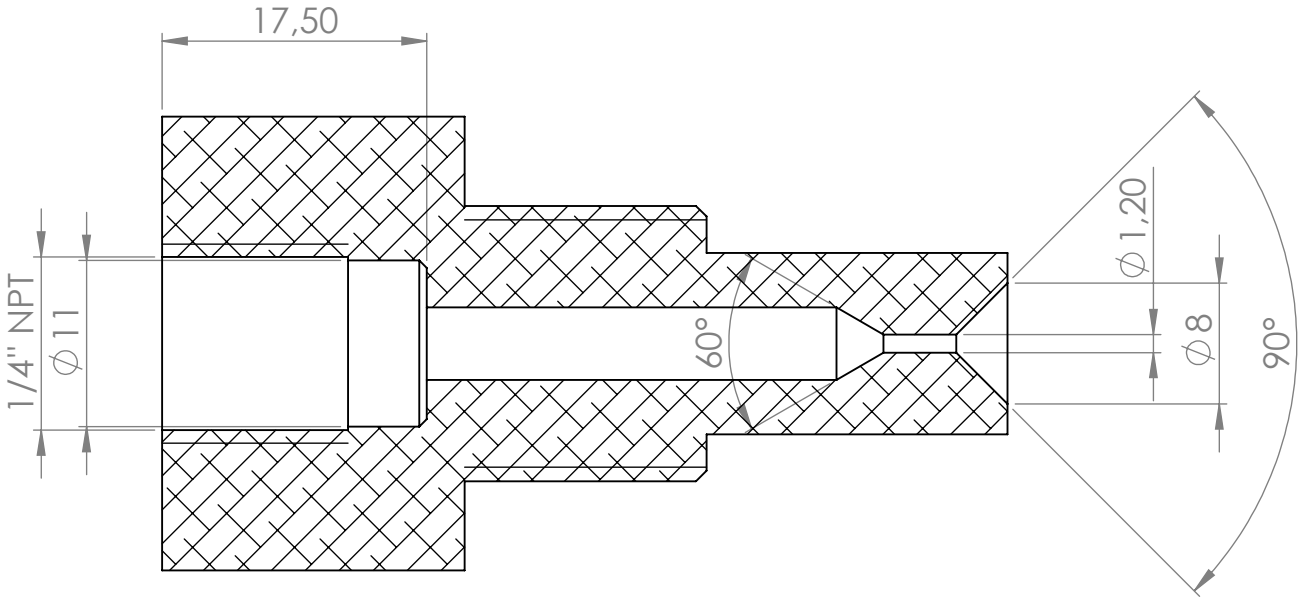

SECTION A-A
SCALE 2 : 1

General Tolerances to ISO 2768

Author: Xavier Corbella Coll (08/05/2015) Checked:	Name of the piece: Outlet 2	Drawing nº 8
Implementation and characterization of anejector based H2 recirculation system for a PEM fuel cell	Material: SS Type 316	
Edición de estudiante de SolidWorks. Sólo para uso académico.	Format: DIN A4 / Scale: 1:1	Projection:

Escola Universitària d'Enginyeria Tècnica Industrial de Barcelona
Consorci Escola Industrial de Barcelona

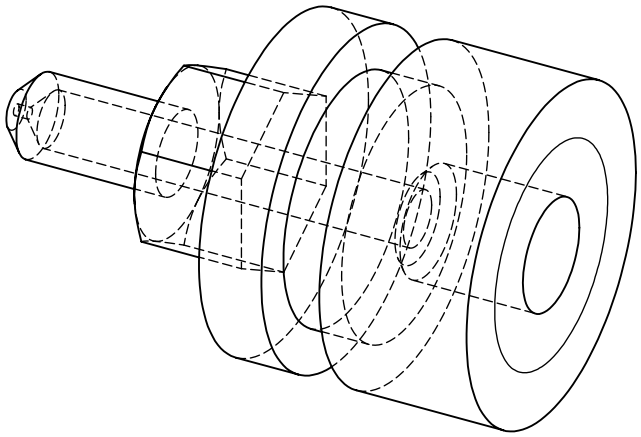

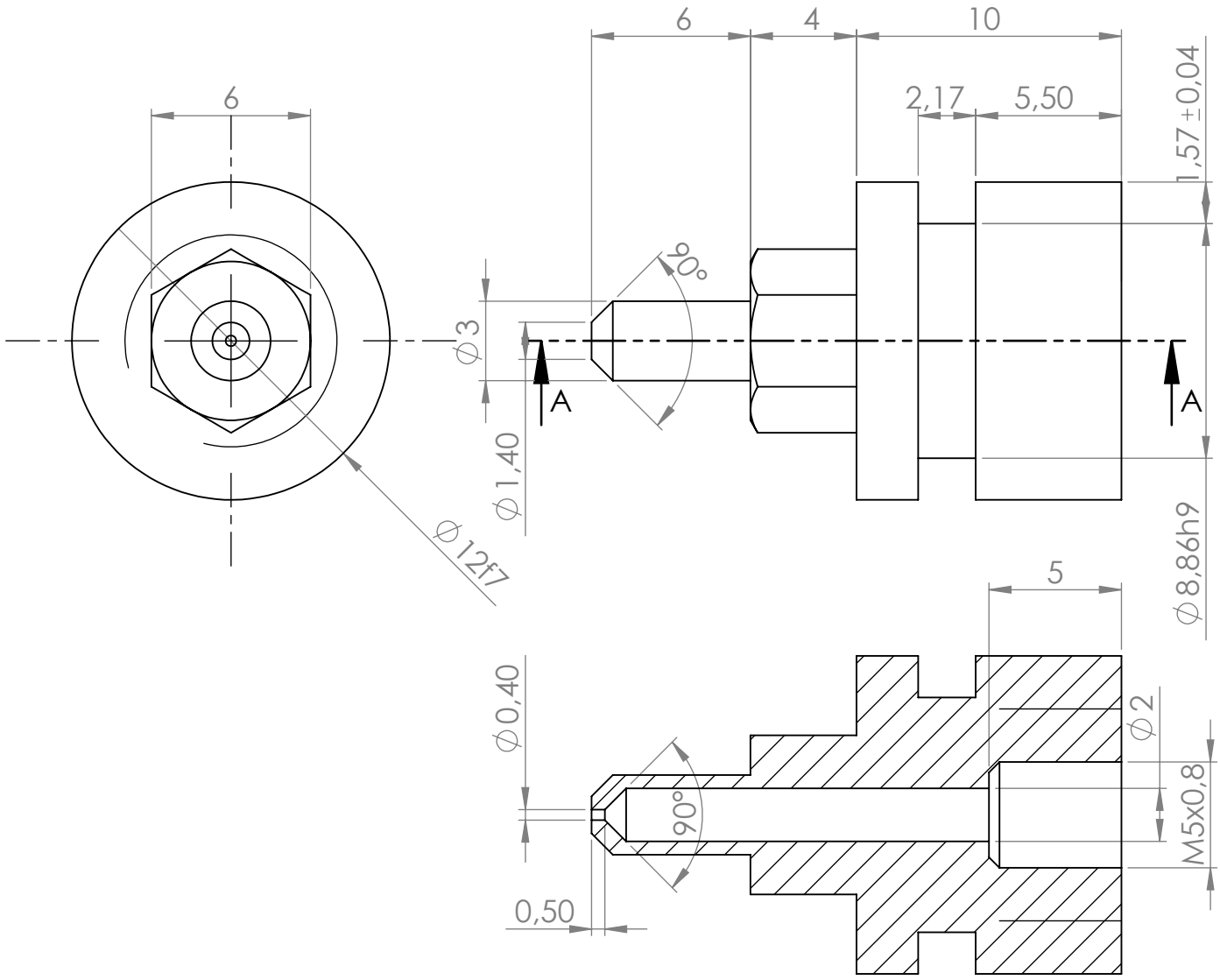

SECTION A-A

General Tolerances to ISO 2768

Author: Xavier Corbella Coll (08/05/2015) Checked:	Name of the piece: Nozzle 2	Drawing nº 9
Implementation and characterization of anejector based H2 recirculation system for a PEM fuel cell	Material: SS Type 316	
Edición de estudiante de SolidWorks. Sólo para uso académico.	Format: DIN A4 / Scale: 4:1	Projection:

Escola Universitària d'Enginyeria Tècnica Industrial de Barcelona
Consorci Escola Industrial de Barcelona